

University of Warsaw

DOCTORAL THESIS

Effects of the adsorption of harmful gas molecules on boron-based materials

Author: Supervisor:

Isabel Maria dr hab. Nevill Gonzalez

Arias-Camacho Szwacki

A thesis submitted in fulfillment of the requirements for the degree of Doctor of Philosophy

in the

Institute of Experimental Physics Faculty of Physics

May 2025

UNIVERSITY OF WARSAW

Faculty of Physics

Abstract

Doctor of Philosophy

Effects of the adsorption of harmful gas molecules on boron-based materials

by Isabel Maria Arias-Camacho

Abstract

he synthesis of graphene opened a new era in the search for new materials for nanotechnology applications. In this sense, 2D materials with a large surface-to-volume ratio, stability, and excellent electronic, thermal, transport, and mechanical properties are potentially suitable for gas sensing, chemical adsorption, and catalytic applications.

Belonging to the same family of two-dimensional mono-elemental materials, Xenes (where X represents the constitutive element), borophene, composed exclusively of boron atoms, was first theorized in the 1990s and subsequently synthesized in 2015. Since then, its outstanding physical and electronic properties have been recognized, although this promising material is still in an early stage of development. In this regard, a theoretical analysis of its properties and applications can become a starting point for further experimental research.

Boron, the metalloid element with an electronic configuration $1s^22s^22p^1$ is electron deficient. This electronic condition causes the formation of exotic bonding states, which lead to several polymorphisms, in contrast to its immediate neighbors in the periodic table, carbon and silicon. Interestingly, the corresponding two-dimensional one-atom-thick crystal can be obtained through the growth on a metal substrate such as Ag. Moreover, some studies have revealed that including transition metal atoms can stabilize borophene by electron transfer from the metal to the boron.

In this context, MBenes are two-dimensional materials that derive from their parental MAB bulk phases (where M is a transition metal, A is frequently a group IIIA-IVA element, and B is boron) and are, for this reason, regarded as relatives to MXenes which have drawn tremendous attention in recent years. MBenes exist in several stoichiometries, and the presence of transition metal atoms confers them a special robustness and magnetic properties that open new windows to the boron-based compounds.

This thesis focuses on two different classes of boron-based materials as potential candidates for gas sensing or absorption:

(i) Specific borophene polymorphs (α -sheet, buckled hexagonal, and honeycomb-like) with diverse structural and physicochemical behavior: First-principles calculations have been performed in the framework of the Density Functional Theory (DFT), to calculate the influence on the structural, electronic and magnetic properties after the adsorption of hazardous gas molecules (CO, CO₂, NO, NO₂ and NH₃) on the α -sheet, buckled hexagonal, and honeycomb-like borophenes. We have observed that the charge transfer between the molecules and the 2D structure destabilizes the bonds, producing wrinkles, which causes boron to form sp^3 hybridization instead of the sp^2 one present in the flat (or quasi-flat) borophene, a circumstance that leads to a strong bonding with the adsorbate and make this material optimal as gas adsorbent.

(ii) MBenes with M₂B₂ stoichiometry (M = Cr, Fe, and Zr): As a first step in our research, we investigated the properties of pristine MBenes, which revealed their outstanding structural strength and thermal stability as well as good conductivity. Additionally, and due to the presence of transition metal atoms in their composition, we have observed that introducing the Hubbard correction has a non-negligible influence on their electronic and magnetic ground states. Moreover, the results arising from their magnetic properties point to their use as robust magnets with high critical temperatures. From the perspective of the adsorption of both harmful molecules (CO, CO₂, NO₂, SO₂, and NH₃) and other typical molecules present in the atmosphere (H₂O, N₂ and O₂), we have found the potential use of MBenes not only as gas sensors but also as gas capturers with the consequent possibility of gas removal.

The four publications included in this dissertation form a coherent set of studies on two-dimensional boron-based materials and their interactions with small molecules, highlighting the impact of adsorption on the physicochemical properties of these systems.

Streszczenie

Synteza grafenu otworzyła nową erę w poszukiwaniu materiałów do zastosowań nanotechnologicznych. W tym kontekscie materiały 2D o dużym stosunku powierzchni do objętości, stabilności i doskonałych właściwościach elektronowych, termicznych, transportowych i mechanicznych są potencjalnie odpowiednie do wykrywania gazów, adsorpcji chemicznej i zastosowań katalitycznych.

Należący do rodziny Xenes (gdzie X reprezentuje element z układu okresowego pierwiastków) dwuwymiarowych materiałów jednoelementowych, borofen, składający się wyłącznie z atomów boru, został po raz pierwszy zaproponowany i zbadany teoratycznie w latach 90-tych, a następnie zsyntetyzowany w 2015 roku. Od tego czasu doceniono jego wyjątkowe właściwości fizyczne i elektronowe, choć ten obiecujący materiał wciąż znajduje się na wczesnym etapie poznania. W związku z tym teoretyczna analiza jego właściwości i zastosowań może stać się punktem wyjścia do dalszych badań eksperymentalnych.

Bor, pierwiastek metaloidalny o konfiguracji elektronowej 1s²2s²2p¹ ma niedobór elektronów. Ten stan elektronowy powoduje powstawanie egzotycznych wiązań, które prowadzą do istnienia licznych odmian alotropowych boru, w przeciwieństwie do jego bezpośrednich sąsiadów w układzie okresowym, węgla i krzemu. Co ciekawe, odpowiedni dwuwymiarowy kryształ o grubości jednego atomu można uzyskać poprzez wzrost na metalowym podłożu, takim jak Ag. Co więcej, niektóre badania wykazały, że włączenie atomów metali przejściowych może stabilizować borofen poprzez transfer elektronów z metalu do boru.

W tym kontekście MBenes są dwuwymiarowymi materiałami, które wywodzą się z ich macierzystych faz objętościowych MAB (gdzie M jest metalem przejściowym, A jest często pierwiastkiem z grupy IIIA-IVA, a B jest borem) i z tego powodu są uważane za krewnych MXenów, które przyciągnęły ogromną uwagę w ostatnich latach. MBeny występują w kilku stechiometriach, a obecność atomów metali przejściowych nadaje im szczególną wytrzymałość i właściwości magnetyczne, które otwierają nowe możliwości dla związków na bazie boru.

Rozprawa doktorska koncentruje się na dwóch różnych klasach materiałów na bazie boru jako potencjalnych kandydatów do wykrywania lub absorpcji gazów:

(i) Wybrane polimorfy borofenu (struktura α -sheet, struktura pofałdowana heksagonalna i struktura typu plastra miodu) o zróżnicowanej strukturze i właściwościach fizykochemicznych. Przeprowadzono obliczenia z wykorzystaniem teorii funkcjonału gęstości (DFT), aby zbadać wpływ na właściwości strukturalne, elektronowe i magnetyczne po adsorpcji potencjalnie szkodliwych cząsteczek gazu (CO, CO₂, NO, NO₂ i NH₃) na borofenach o strukturze α -sheet, heksagonalnej pofałdowanej i typu plastra miodu. Wynikiem obliczeń było między innymi to, że transfer ładunku między cząsteczkami a strukturą 2D destabilizuje wiązania, tworząc dystorsje strukturalne, co powoduje, że bor tworzy z sąsiadami hybrydyzację sp^3 zamiast sp^2 obecnej w płaskim (lub quasi-płaskim)

- borofenie, co prowadzi zarazem do silnego wiązania z adsorbatem i czyni ten materiał optymalnym jako adsorbent gazu.
- (ii) MBenes ze stechiometrią M_2B_2 (M=Cr, Fe i Zr). Jako pierwszy krok w obliczeniach komputerowych, zbadane zostały właściwości czystych MBenes, które ujawniły ich wyjątkową wytrzymałość strukturalną a także dobre przewodnictwo elektryczne. Dodatkowo, ze względu na obecność atomów metali przejściowych w ich składzie, zaobserwowane zostało, że wprowadzenie poprawki Hubbarda ma istotny wpływ na ich elektronowe i magnetyczne stany podstawowe. Co więcej, wartości momentów magnetycznych wskazują na ich możliwe zastosowanie w spintronice jako układów o wysokich temperaturach krytycznych. Z perspektywy adsorpcji zarówno szkodliwych cząsteczek (CO, CO_2 , NO_2 , SO_2 i NH_3), jak i innych typowych cząsteczek obecnych w atmosferze (H_2O , N_2 i O_2), znalezione zostało potencjalne zastosowanie MBenes nie tylko jako czujników gazu, ale także jako wychwytywaczy cząsteczek gazu z możliwością ich usuwania.

Zawarte w rozprawie cztery publikacje stanowią spójny zbiór wyników badań nad dwuwymiarowymi materiałami na bazie boru oraz ich interakcjami z małymi cząsteczkami, ukazując wpływ adsorpcji na właściwości fizykochemiczne tych układów.

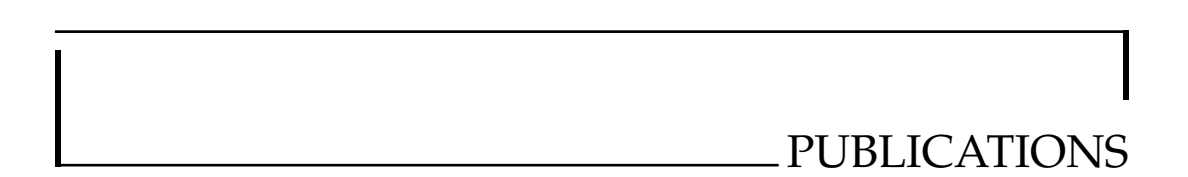
Acknowledgements

The idea of making a PhD just arose at the most suitable moment: before it, an accumulation of experiences, people and places gave me a wide perspective of the importance of science as a contribution to society. It was my very good friend Rodrigo, yet disappeared, who aimed me to perform a scientific work, and it is very sad that he will not see it concluded. However, my husband, Prof. dr. iur. Jakob Stagl at the Law Faculty and my son, Johann (the reason for all my fights) have supported me, in all senses, during these last years. It is incredible how an innocent child can comfort the soul of an adult.

But it was Prof. dr. hab. Dariusz Wasik who very wisely introduced me to my supervisor, Prof. Nevill Gonzalez Szwacki, who guided me in this adventure and, at the same time, has given me enough freedom to reach my conclusions. This mixture of scientific advice, understanding, and humanity has been crucial for this work. I am very grateful to them both for believing in me and I hope that I was at the level of their expectations. Many thanks to Teresa Szwacka for her warm and continuous support, and for helping me with the accuracy and correctness of some parts in Polish. Her presence and selfless help was always with me. I do not forget the Faculty of Physics, with special emphasis in Prof. dr hab. Wojciech Satuła and Prof. dr hab. Piotr Kossacki, for their invaluable help and for making it possible. I am also very grateful to the reviewers and the committee members for investing their time and experience in this thesis and feel very lucky for being having them.

In the Faculty, my home, I have always felt comfortable and surrounded by excellent people, but I do not forget the friends of the Polish Academy of Sciences, whose conversations about physics have been always pleasant and constructive.

Thanks to the University of Warsaw for giving me this opportunity. I am very proud to be one of its daughters. Finally, I want to thank all the people involved in this trip, colleagues, people from administration, most of them supporting and helping me in the shadows, but equally important: I was always aware that you all were here. I feel very grateful for having all these people around, thank you for bringing my dream into reality.



- 1. **Arias-Camacho, I.M.**; Gonzalez Szwacki, N. Exploring the Structural, Electronic, Magnetic, and Transport Properties of 2D Cr, Fe, and Zr Monoborides Materials 16, 5104 (2023)
- 2. **Arias-Camacho, I.M.**, Influence of the Hubbard U Parameter on the Structural, Electronic, Magnetic, and Transport Properties of Cr/Fe/Zr-Based MBenes ACS Omega 8, 47, 45003–45012 (2023)
- 3. **Arias-Camacho, Isabel M.** and Gonzalez Szwacki, Nevill *Exposure of MBenes to environmentally hazardous molecules* Surfaces and Interfaces 56, 105665 (2025)
- 4. **Isabel M. Arias-Camacho** and Nevill Gonzalez Szwacki *Borophene sheets* as potential candidates for the detection and removal of harmful gas molecules Solid State Communications 401, 115905 (2025)

List of publications not included in this thesis but resulting from collaborations in its context.

- 1. **I. M. Arias-Camacho**, A. M. León and J. Mejía-López, *Tailoring Electronic Properties on Bi*₂O₂Se under Surface Modification and Magnetic Doping J. Phys. Chem. C 128, 6, 2577–2587 (2024)
- 2. A. Araya-Barr, G. García, **I. Arias-Camacho**, C. Espinoza, Byeong-Joo Lee, E. Ramos-Moore, Second nearest neighbor modified embedded atom method interatomic potentials for TiC_xN_{1-x} ternary systems Computational Materials Science 231, 112615 (2024)

Contents

A۱	ostra	zt –	j		
A	cknov	wledgements	vi		
Pι	ıblica	ations	vii		
Li	st of	Figures	xi		
Li	st of	Tables	xi		
Li	st of	Abbreviations	xii		
Li	st of	Symbols	χv		
Ι	Ir	ntroduction	1		
	1.1	Borophene as a member of the Xenes family	1		
	1.2	MBenes	4		
	1.3	Two-dimensional materials for sensing			
	1.4	Hazardous gas molecules	10		
	1.5	Thesis structure	10		
II	M	lethodology	11		
	2.1	The Density Functional Theory	11		
		2.1.1 The Schrödinger equation	11		
		2.1.2 Computations on large systems	12		
		2.1.3 The DFT Theory	16		
	2.2	The density of states (DOS)	23		
	2.3	Bader decomposition of the charge density			
	2.4	Dynamical stability of materials and the Density Functional			
		Perturbation Theory	27		
	2.5	Determination of the Hubbard parameters	33		
	2.6	The dispersion correction DFT+D			
	2.7	Electronic Conductivity: the Boltzmann Transport Equation . 40			

	2.8	Impo	rtant parameters for the evaluation of the adsorption of	
		small	molecules	42
		2.8.1	The adsorption energy	42
		2.8.2	The recovery time	43
		2.8.3	Charge transfer between the MBene and the molecule .	44
II	I A	rticles	that compose this thesis	45
	3.1	A brie	ef introduction to the main results	45
	3.2	PAPE	R I: Borophene sheets as potential candidates for the de-	
		tection	n and removal of harmful gas molecules	47
	3.3	PAPE	R II: Exploring the Structural, Electronic, Magnetic, and	
		Trans	port Properties of 2D Cr, Fe, and Zr Monoborides	57
	3.4	PAPE	R III: Influence of the Hubbard U Parameter on the Struc-	
		tural,	Electronic, Magnetic, and Transport Properties of Cr/Fe/Z	r-
		Based	MBenes	68
	3.5	PAPE	R IV: Exposure of MBenes to environmentally hazardous	
		molec	rules	79
IV	7 N	Iain co	nclusions, challenges and outlook	95

List of Figures

1.1	Three examples of different 2D boron polymorphisms: (a) buck-	
	led triangular, (b) α -sheet and (c) honeycomb-like borophene.	2
1.2	Deintercalation of the Al layer from (CrB) ₂ Al	4
1.3	Relevant examples of 2D materials suitable for gas sensing	6
1.4	Some hazardous molecules adsorbed on the surface of the MBene.	10
2.1	Flowchart describing the DFT procedure leading to the self-	
	consistent Kohn-Sham solution	19
2.2	Example of a diatomic crystal with masses M_1 and M_2 con-	
	nected by a force constant C. The atoms are shown in their	
	fixed position and the displacements are expressed in terms of	
	u_{s-1} , u_s , u_{s+1} , for atoms M_1 and v_{s-1} , v_s , v_{s+1} , for atoms	
	M_2	28
2.3	Transversal optical and acoustic waves in a linear diatomic lattice	29
2.4	Phonon dispersion plot for a linear diatomic lattice, showing	
	the acoustic and optical branches. The constant value a in the	
	value limit $\frac{\pi}{a}$ represents the lattice constant	29
2.5	Example of a phonon dispersion in a cubic crystal, where LA	
	and TA are horizontal in the limit K_{max} . Branches LO and TO	
	coincide at $K = 0$, a consequence of the symmetry of the crystal.	30
2.6	Plot of the total energy respect to the number of electrons in	
	an atomic system in contact with a reservoir. The difference	
	between the exact result for the open system (in blue) and the	
	LDA energy (in red) are represented by the curve at the bottom	
	(in green)	35

LIST OF ABBREVIATIONS

 α -B α -sheet of borophene. AFM Anti Ferro Magnetic

buckled-BDFTbuckled sheet of borophene.Density Functional Theory

DFPT Density Functional Perturbation Theory

 $egin{array}{lll} E_{ads} & Adsorption Energy \ E_{coh} & Cohesive Energy \ E_{tot} & Total Energy \ FM & Ferro Magnetic \ \end{array}$

GGA Generalized Gradient Approximation
hc-B honeycomb-like borophene sheet.
hex-MBenes MBenes with hexagonal symmetry
LDA Local Density Approximation

ortho-MBenesMBenes with orthorrombic symmetryPBEPerdew Burke Ernzerhof approximation

SBH Schottky Barrier Height

TMTransition MetalthLayer thickness \mathbf{t}_{rec} Recovery time \mathbf{vdW} $\mathbf{van der Waals}$

LIST OF SYMBOLS

a, b and c	lattice parameters	Å
U	Hubbard parameter	eV
ν	Attempt frequency	s^{-1}
σ	Conductivity	$\Omega^{-1} \ m^{-1} \ s^{-1}$
au	Relaxation time constant	
T_c	Critical temperature	K
ω	phonon frequency	cm^{-1}
η	density of vacancies	

xvii

Dedicated to Jakob, Johann and Rodrigo. Thanks for believing in me.

CHAPTER I	
ı	
	INTRODUCTION

"NOWN for thousands of years, boron compounds (from Arabic buraq and Persian burah) have played an important role in history, from their use in mummification, in ancient Egypt, to the glassmaking process in ancient Rome. This particular element, always in combination with other elements in nature, was recognized as a substance in 1824 by Jöns Jacob Berzelius. Still, it was not until 1909 when it was first synthesized by the American chemist E. Weintraub due, to a large extent, to the fact that isolation of this element, not found uncombined on Earth and obtained predominantly from borax, is difficult to achieve in its pure form. Located between the metal beryllium and the non-metal carbon, boron possesses an electronic configuration [He]2s²2p¹, with three valence electrons in its outermost orbital and four accessible valence orbitals, resulting in an electron deficiency that leads to exotic configurations, differently from its immediate neighbors, carbon and silicon. For instance, boron can exhibit multiple bulk phases [1, 2] with diverse small clusters, two-dimensional layers, and nanotubes, many of them still unexplored.

1.1 Borophene as a member of the Xenes family

The Xene family comprises monoelemental two-dimensional compounds whose synthesis and exploitation, because of their artificial nature and stabilization issues, aspire to challenge in the coming years. Some of the potential elements are Si, Ge, Te, Sn, B, P, Se, Sb, Bi, Ga, As, Pb and Tl.

Borophene is the monoatomic layer of boron, that is, the Xene composed exclusively by boron atoms; because there are no crystals formed by borophene, it cannot be peeled of a bulk material and requires further synthesis methods. Borophene, an allotrope of boron, has been shown to be stable in several polymorphisms [3, 4, 5], showing a wide versatility due to their diversity of structural and physicochemical properties. Although Boustani reported the first news about 2D boron in 1997 [6], these structures were inspired by his early work on boron clusters. In this study, the boron atoms were arranged on a hexagonal lattice, which was later demonstrated to be buckled instead of planar: it was the buckled triangular structure.

Tang *et al.* found in 2007 [7], using first-principles calculations, that the boron sheet is a polymorphic material because it exhibits similar energies for structures with a different distribution of hexagonal vacancies.

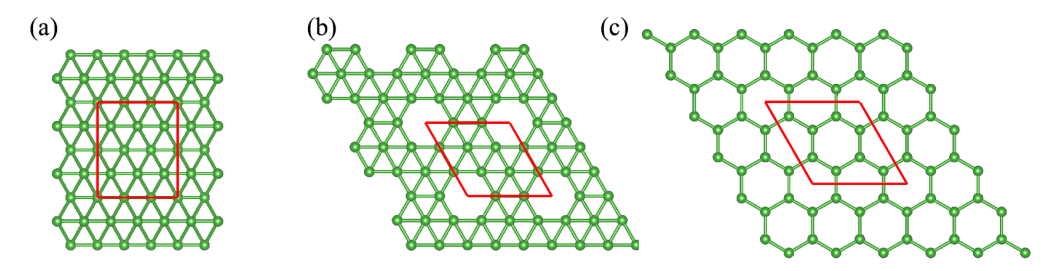


FIGURE 1.1: Three examples of different 2D boron polymorphisms: (a) buckled triangular, (b) α -sheet and (c) honeycomblike borophene.

The same authors defined the *density of vacancies* [7], η , very useful in classifying the wide number of structures:

$$\eta = \frac{\text{number of missing atoms}}{\text{number of sites in the hexagonal lattice}}$$

Compared to graphene, with its filled bonding states and empty antibonding states, free-standing honeycomb-like borophene (with $\eta=1/3$) is predicted to be unstable because it has unoccupied bonding states. The charge transfer from a metallic substrate could help to occupy such bonding states, conferring stability to the planar hexagonal lattice. An important key to achieve the desired stability is the growth on appropriate substrates of (111)—terminated surfaces of noble metals [8] and, among all, particularly the Ag (111) surface, which is, in turn, a typical template hosting a large number of Xenes. According to several theoretical predictions based on first-principles calculations, some of the borophene variants can be stabilized on

metal surfaces like Ag, Au, Al, Ti and Mg [8, 9, 10, 11]. Li *et al.* [12] achieved the pure honeycomb borophene, similar to graphene, on a Al(111) substratum using MBE. Reinforcing this idea, John *et al.* [13] also found that the adsorption of light metals on the honeycomb-like borophene can alter the electronic structure due to charge transfer, leading to a stable monolayer, a desired structure that resembles the shape of graphene.

Shortly after theoretical predictions, Piazza *et al.* [14] provided the first experimental evidence for the feasibility of a single-atom boron sheet with hexagonal vacancies, using laser ablation of a hot-pressed boron target. They named this single-atom crystal "borophene".

The first growth of atom-thick borophene was experimentally achieved by Mannix et~al.~[15] and Feng et~al.~[16] in the form of thin sheets on an Ag(111) substrate, by MBE under ultrahigh vacuum conditions. In the first case, Mannix et~al.~ obtained an image of the theoretically predicted buckled borophene using scanning tunneling microscopy (STM) and in the second case, Feng et~al.~ unveiled two allotropes with hole densities $\eta=1/6$ (named β_{12}) and $\eta=1/5$ (named χ_3 by the authors). The synthesis of borophene is currently achieved by different methods such as molecular beam epitaxy (MBE), chemical vapor deposition (CVD), or liquid-phase exfoliation. Among all, MBE is the most widely used method to produce boron monolayers on metallic substrata [17, 18, 19].

Another important polymorphism is the so-called α -sheet, the most stable form among atom-thick sheets of boron [7]. The prediction of the B₈₀ buckyball [20] was of particular interest because it was quite similar to the well-known C₆₀. This discovery was followed by the proposal of this stable α -sheet and was immediately considered a precursor of the 2D boron sheet. Its characteristic motif consists of a crossover of boron strips that produce a certain number of vacancies, in particular, $\eta = 1/9$. This circumstance allows the α -sheet to relax, remaining as a planar structure.

In comparison with theoretical predictions, only a few boron sheets have been experimentally achieved, and their synthesis remains a challenge. However, their metallic behavior and stability justify their use in applications like energy storage, sensing or information storage [21], to cite some of them.

1.2 MBenes

Beyond borophene, transition metal borides (MBs), a new class of emerging 2D materials also known as MBenes, are expected to have great potential for development in the future. Their diverse stoichiometries, like M_2B_2 , M_2B and M_3B_4 , with their corresponding structural differences, give rise to challenging physical, chemical and biological properties.

MBenes can be obtained by chemical exfoliation of their parental MAB phases, which were reported for the first time by Ade and Hillebrecht in 2015 [22]. Despite their similarity to MXenes, which originate from MAX phases, MBenes possess the advantage of adopting different stoichiometries and variable modes of sandwiching of their two-dimensional layers. Moreover, the presence of terminal groups on the synthetic surface of MBenes has not been experimentally found [23], an advantageous fact that eases the investigation of their surface behavior. Single-crystalline ternary transition metal borides, known as MAB (where M is a transition metal, A is frequently a group IIIA-IVA element and B is boron), with one-to-one stoichiometry, are either orthorhombic or hexagonal crystals with MAB and M2AB2 formulae [24], and some of them have already been experimentally synthesized like hexagonal Ti_2InB_2 [25] and orthorhombic MAIB (with M = W and Mo), M_2AlB_2 (with M = Cr, Mn and Fe). These bulk solids can be exfoliated in 2D flakes because the M-B and B-B bonds are much stronger than the A-B and A-M bonds [26, 27]. Figure 1.2 illustrates an example of the removal of the layer of element A.

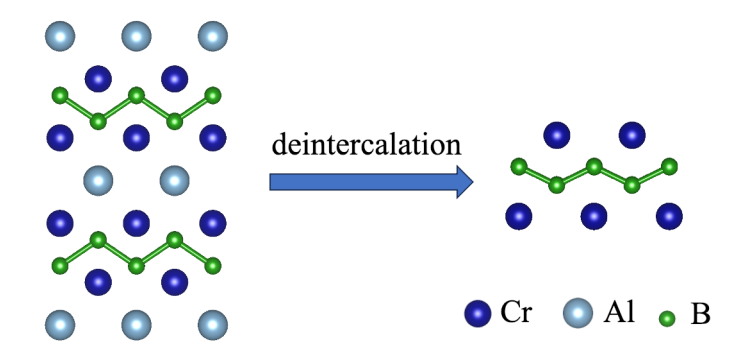


FIGURE 1.2: Deintercalation of the Al layer from (CrB)₂Al.

From these precursors, layered CrB nanosheets have been obtained by selectively HCl-etching Al layers from Cr₂AlB₂ [23, 28], a two-dimensional

MoB was synthesized by deintercalating the Al layers through partial etching of Mo₂AlB₂ [29, 30] and a bulk layered TiB structure was achieved by removing the In layer from Ti₂InB₂ through high-temperature dealloying [25]. MBenes with the chemical formula M₂B₂ present either an orthorhombic structure with *Pmma* (no. 51) space group symmetry or a hexagonal structure with *P6/mmm* (no. 191) space group symmetry, and both phases are quite different with respect to each other: while in the *Pmma* structure each atom is surrounded by six neighbors and the buckled bilayers are sandwiched between transition metal layers, the *P6/mmm* structures consist of a honeycombtype boron layer sandwiched between transition metal layers, each transition metal atom located above or below the centroid of this honeycomb structure. The existing literature contains theoretical predictions stating that Sc-, Ti-, V-, Zr-, Mo-, Hf-, Ta-and W-based MBenes are more stable in the hexagonal phase while Cr-, Mn-, Fe-, Ni-, Tc- and Ru-based MBenes are more stable in the orthorhombic phase.

Another interesting property arising from the metal atoms is magnetism, due to their half-filled d-orbitals, and this work includes some dedication to the study of the magnetic properties of Cr-, Fe- and Zr-based MBenes. Their bulk counterparts include the ferromagnetic modifications α and β of FeB and the non-magnetic CrB and ZrB compounds [31, 32, 33]. β -FeB and CrB are orthorhombic crystals with Pnma (no. 62) and Cmcm (no. 63) space group symmetries, respectively, while the structure of α -FeB is debatable [33]. Both β - FeB and CrB crystals enclose boron double-chain strips, very common motifs of all-boron nanostructures [34, 20]. The bulk of ZrB, rock-salt structured, crystallizes in cubic $Fm\bar{3}m$.

MBenes are regarded as new efficient earth-abundant materials with good biocompatibility and low toxicity that can be used for energy storage and conversion systems [35] like metal-ion batteries, capacitors, metal-air batteries, for oxygen evolution reactions (OERs), catalysis [36, 37], NO electroreduction [38], adsorption and activation of CO₂ [39], biotechnology [40], magnetic refrigeration [41], information storage devices [42] or spintronics [43, 44, 45, 46] and other electrochemical applications [47], to cite some.

1.3 Two-dimensional materials for sensing

2D materials possess outstanding properties for chemical detection by electrical transduction. Some advantages with respect to their bulk counterparts include a vast surface area with rich surface chemistry that allows enhanced

molecular interactions, good in-plane stability, or large carrier mobility, qualities that enable them as magnific detectors with high sensitivity and low detection limits. Moreover, their good conductivity favors their integration into different devices. To cite some of them, MoS₂ [48, 49], graphene, [50, 51, 52], phosphorene [53], silicene [54] or germanene [55] have been widely used in this context. The actual picture of the development of such devices is the creation of a wide collection of top-down and bottom-up experimental techniques that allow the qualities of these materials to be fine-tuned for particular applications.

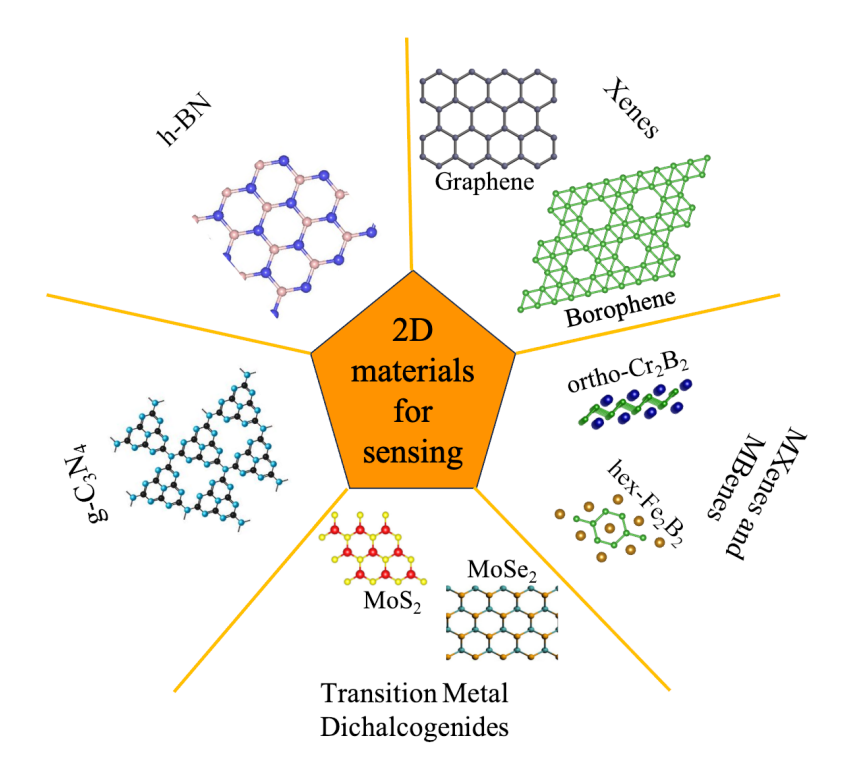


FIGURE 1.3: Relevant examples of 2D materials suitable for gas sensing.

However, this family of materials still remains an emerging field that is mostly explored through theoretical calculations, while synthesis methods are in an early stage and, for this reason, are also the subject of experimental investigations. In this sense, theoretical predictions can offer valuable insight for the future of these materials. For all these reasons, 2D materials of a few atomic layers are the focus of recent research on clean technologies [56].

The impact of harmful chemical and toxic gases on the environment and the diagnosis of human health and diseases manifest the need for efficient and robust sensing systems with the ability to detect chemical or biological analytes on the one side and to maintain sensitivity, stability and selectivity on the other side. In this sense, some 2D materials open the possibility of detecting a wide range of external species [57]. Some typical sensors are:

Gas sensors

- Chemiresistors. These sensors, easy to manufacture and operate, environmental-friendly and low cost are the most common among all the gas sensing devices. Their operating basis is the change of electrical resistance upon adsorption of gas molecules on the surface of the sensing substrate, allowing a sensitive detection.
- Conductometric sensors. They are practical and easy-to-produce sensors that can detect specific gases under typical atmospheric conditions [58, 59]. Variations in capacitance, conductivity, mass, work function, reaction kinetics, and / or optical properties are the basis for detecting the reversible interaction rate between gas molecules and the surface of the sensing material [60].
- Surface acoustic wave sensors (SAW). They constitute a new class of sensors that can detect a wide variety of gases [61, 62] and exhibit exceptional selectivity and robustness. Their working principle is the fluctuation of the physicochemical features of its surface, which affect the velocity of the acoustic wave. [63, 64]. For example, most SAW sensors can detect gases due to fluctuation in the conductive properties of the sensing material by mass loading [65].
- Schottky diodes. These devices consist of layered semiconductor heterojunctions that can detect gas molecules adsorbed on the surface of the substrate through modulation of the Fermi energy and Schottky barrier heights (SBH). The variation of the SBH causes reverse currents and the main factor affecting it is the density of adsorbed gas molecules. For this reason, these sensors show high selectivity [66].
- Electrochemical sensors. In this type of sensors, an electrode acts as a transducer element in the presence of the analyte. They are accurate sensors with high sensitivity and instantaneous response, and they are easy to use. The detection takes place upon electrochemical reactions between the analytes and the electrode surface, converting, in general, chemical concentrations into electric signals. In the specific case of gas sensing, the diffusion of the gas through a membrane leads to their

- oxidation and/or reduction on the electrode surface. To this end, important parameters that determine the efficiency of the electrodes are a vast surface area, excellent conductivity, and intrinsic redox potential.
- Wearable sensors. They have the ability to monitor human health in real time through several biomarkers present in sweat that can provide information about the physiological health of a person. Some examples of these sensors have been used in the detection of glycoprotein GP120 (HIV-1 surface protein) [67] or the detection of lactate and glucose [68].

• Electronic and optical sensors:

- Humidity sensors. Can detect the amount of water vapor in the air [69] and are widely used in the microelectronic and pharmaceutical industries, meteorology and environmental monitoring, scientific research, textile production, or agriculture, among others.
- Heavy metal ion sensing. Heavy metals, which can be found in industry and the environment, are harmful components that can enter the human body through water, air, or food, causing acute and chronic diseases [70, 71]. These elements are considered highly toxic and include chromium, mercury, lead, cadmium, thallium, arsenic, and lead. The adequate detection of these species in drinking water is, for these reasons, a crucial issue.
- Various. In the typical FET devices, there is a semiconducting channel between the drain and source electrodes and the conductivity is controlled by changing the voltage gate-to-source. In the case of the chemiresistors, the channel is sandwiched between two electrodes without the gate. The conductance of chemiresistors or FET devices changes when the material of the channel is exposed to foreign species, being the advantage of 2D materials, as their atom-thick surface is very effective for sensing purposes [72].
- Fluorescent sensors. Although the majority of 2D materials are not able to emit fluorescence, they can however work as flourescent dye quenchers, that is, they can quench flourescent signals, which is their working principle. Their detection capability is based on the decrease or increase of fluorescent signals due to the interactions between the material and the analytes [73].

- Surface-enhanced Raman spectroscopy-related sensors. They are an ultrasensitive method for molecule detection, but their fabrication is still a challenge.
- **Human chemical signal monitoring.** The human body produces signals that can be evaluated with non-invasive and cost-effective devices. They consist of a receptor that exhibits good selectivity toward selected biomarkers and a transducer that converts this chemical information into a quantifiable signal. Depending on the origin of the chemical signals, they can be used for sweat analysis, breath gas detection, and saliva detection, allowing personalized healthcare evaluation and detection and evaluation of illnesses.

• Biomedical and health care sensors:

- Single-cell detection. Distinguish healthy from unhealthy cells,
 which play an important role in diagnosis[74].
- DNA sensing. They are based on the rapid detection of DNA molecules at extremely low concentrations. PCR (polymerase chain reaction) is one of the most famous and has been widely used [75].
- Protein sensing. Which are ultra-fast, sensitive and small biosensors that detect proteins in real time.
- Cancer diagnosis and treatment (photothermal and chemotherapy). In the world of biosensors, 2D materials are increasing importance in the early detection of carcinoma cells. For example, graphene-based fluorescent probes can identify tumors with high specificity and deliver therapeutic drugs.
- Optogenetic sensing. In this sense, graphene shows good biocompatibility, mechanical robustness, good electrical and thermal conductivity, adaptability, tunable photonic properties and wide wavelength refraction [76]. Such advantages allow for the adequate treatment of several neurological diseases such as schizophrenia or Parkinson.
- Ophthalmology sensing. 2D materials are helpful in this field because some of them are wearable, biocompatible, and environmentally stable. Smart, wearable contact lenses have been developed to detect diabetes and glaucoma by evaluating glucose in tears and intraocular pressure [77].

1.4 Hazardous gas molecules

Short-lived climate forcers (SLCFs) are chemically and physically active substances that have a relatively short lifetime in the atmosphere (typically less than two decades) and can be air pollutants that affect the climate [78] through different environmental effects. They can be either radiatively active or influence other radiatively active compounds through chemistry. Direct SLCFs include methane, ozone, short-lived halogenated compounds, and aerosols. Indirect SLCFs include chemically reactive gases like nitrogen oxides, CO, nonmethane volatile organic compounds, SO₂, and NH₃. They can either have an anthropogenic origin or be emitted from natural systems. The growth of industry and cities requires the development of new materials capable not only of adsorbing and detecting contaminants such as CO, NH₃, NO₂, and SO₂, but also of producing and storing green energy to help decarbonize industry and combat pollution.

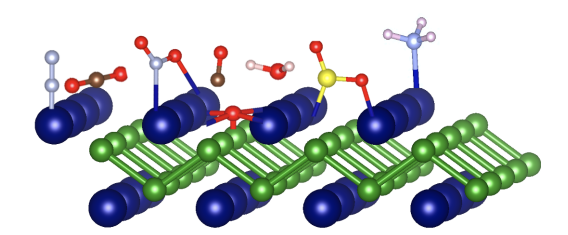
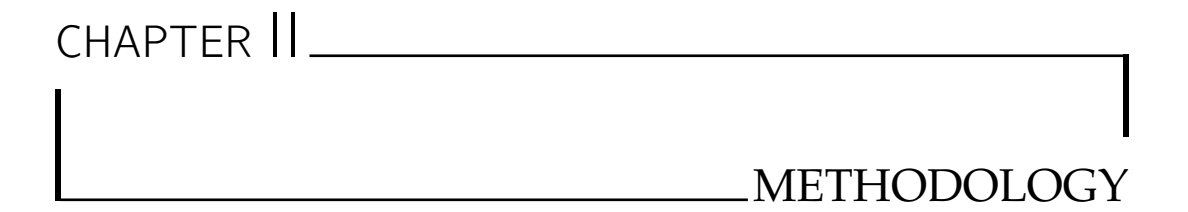


FIGURE 1.4: Some hazardous molecules adsorbed on the surface of the MBene.

1.5 Thesis structure

Before going into the main conclusions of this thesis, a detailed description of the methodologies employed is developed, not only as justification but also to better understand. Once the parameters and approximations involved have been adjusted to the requirements of this study, the results of the investigation are presented. This thesis comprises four articles derived from research based on boron-based materials with potential applications as sensors and capturers for harmful gas molecules. This work, mainly based on the essential analysis and comprehension of physicochemical phenomena, but with another side facing a potential application toward the protection of society and environment, comes to final conclusions and a promising outlook, which are summarized at the end of this work.



2.1 The Density Functional Theory

The following section describes how quantum-mechanical simulations of large systems are performed.

2.1.1 The Schrödinger equation

The fundamental equation in quantum-mechanical calculations is the Schrödinger equation:

$$E\Psi = \hat{H}\Psi$$
,

In this expression, \hat{H} is the Hamiltonian operator of the system and E is the energy eigenvalue for a particular wave function, Ψ . In the case of one-dimensional systems with only one particle and a single potential, this equation offers a simple solution adopting the form:

$$E\Psi(\vec{r}) = \left[\frac{-\hbar\nabla^2}{2m} + V(\vec{r})\right]\Psi(\vec{r}),$$

The first term of this expression represents the kinetic energy of the particle, and the second term represents a potential "felt" by the particle. As mentioned above, this equation can be solved analytically for simple cases,

but working with three-dimensional systems with several particles increases the complications, making necessary the use of approximations:

2.1.2 Computations on large systems

Some approximation methods for solving the Schrödinger equation in systems more complex than the hydrogen atom, like solids or molecules, are described below.

The Born-Oppenheimer approximation

This approach considers the positions of the nuclei as "frozen", based on the idea that neutrons or protons are around 1800 heavier than electrons (whose response to changes in the system is much faster). Under this assumption, the Schrödinger equation becomes the following for a system in which multiple nuclei interact with multiple electrons:

$$E\Psi(\vec{r}) = \left[\frac{-\hbar}{2m} \sum_{i=1}^{N} \nabla_{i}^{2} + \sum_{i=1}^{N} V(\vec{r}_{i}) + \sum_{i=1}^{N} \sum_{j < i} U(r_{i}, r_{j})\right] \Psi(\vec{r}),$$

The first term corresponds to the kinetic energy of each electron, the second term is the interaction energy between the atomic nuclei and each electron and the third term is the interaction energy between different electrons (most complicated term to compute). In this Hamiltonian, E is the ground state energy of the electrons and the wave function, for each of the N electrons, is a function of each of the coordinates.

The Hartree-Fock method

This method calculates everything from the wave functions that were specified at the beginning.

1. Independent electrons

To make things easier with the electron-electron interaction, a model of independent electrons is introduced, assuming that each electron behaves independently and "feels" the interaction with the other electrons as an average. The corresponding Hamiltonian is written:

$$\hat{H} = \left[\frac{-\hbar}{2m} \sum_{i=1}^{N} \nabla_i^2 + \sum_{i=1}^{N} V(\vec{r}_i) + \sum_{i=1}^{N} V_H(\vec{r}_i)\right],$$

where the Hartree potential, V_H , replaces, with an average value, the exact electron-electron interaction :

$$V_H(\vec{r}) = e^2 \int \frac{n(\vec{r})}{|\vec{r} - \vec{r'}|} d^3(\vec{r'})$$

being $n(\vec{r})$ the electron density.

The condition:

$$h\chi = E\chi$$

is satisfied by the solutions of the Schrödinger equation to this Hamiltonian. In this equation, h is the one-electron Hamiltonian, E is the energy and the eigenfunctions, χ , are the spin orbitals.

2. The Hartree product

If the total Hamiltonian is the sum of the operators of each electron, the eigenfunctions are the products of the one-electron spin orbitals:

$$\Psi(\vec{x}_1, \vec{x}_2, ..., \vec{x}_N) = x_{j1}(\vec{x}_1) x_{j2}(\vec{x}_2) ... x_{jN}(\vec{x}_N),$$

That is, by the Hartee product, the wavefunction of a many-particle system is given as a combination wavefunctions of the individual particles. Bacuase it assumes that the particles are independent, it is inherently mean-field and the sum of the energies of the spin orbitals, $E = E_{j1} + ... + E_{jN}$, is the energy of the total wave function.

Although the Hartree product has the advantage of its simplicity, it is, however, not satisfactory for fermions, like electrons, because it does not fulfill all the criteria for wave functions (the resulting wave function is not antisymmetric). To overcome this issue, an antisymmetric wave function is mathematically described by means of the Slater determinant.

3. The principle of anti-symmetry and Slater's determinant The sign of the wavefunctions of electrons, since they are fermions, must change sign if two electrons change place with each other. It is known as the principle of antisymmetry. In this case, the total wave function can be written as a Slater determinant of the single-electron [79] wave functions. For example, in the case of two electrons:

$$\Psi(\vec{x}_1, \vec{x}_2) = \frac{1}{\sqrt{2}} det[\chi_j(\vec{x}_1) \chi_j(\vec{x}_2) \chi_k(\vec{x}_1) \chi_k(\vec{x}_2)] = \frac{1}{\sqrt{2}} [\chi_j(\vec{x}_2) - \chi_k(\vec{x}_1)],$$

this the total wave function satisfies the anti-symmetry principle. Moreover, the indistinguishability between electrons and their vanishing if two electrons have the same coordinates, or if two of the wave functions of an electron are the same, are other important properties. In this sense, the Slater determinant also satisfies the conditions of the Pauli exclusion principle.

Summarizing, the Slater determinant ensures that the solution to the Schrödinger equation will include the exchange interaction but it is not the only electronic correlation. To achieve an adequate accuracy, more conditions are needed. As an example, the electrons interact with each other and do not "feel" an average potential.

4. **The Hartree-Fock procedure** Under the assumption that the positions of the atomic nuclei are fixed, the Schrödinger equation to determine the wave function of the N interacting electrons is:

$$E_j \chi_j(\vec{x}) = \left[\frac{-\hbar}{2m} \sum_{i=1}^N \nabla_i^2 + \sum_{i=1}^N V(\vec{r}_i) + \sum_{i=1}^N V_H(\vec{r}_i)\right] \chi_j(\vec{x}),$$

The full eigenfunction is obtained from the combination of the solutions to this equation into a single Slater determinant. Than is, the total wave function is formed from the Slater determinant of the N lowest energy spin orbitals of the single-electron equation. But the spin orbitals must be defined firstly to solve the single-electron equation. To this end, a finite set of functions, which can be summed to approximate the exact spin orbitals, is defined:

$$\chi_j(\vec{x}) = \sum_{i=1}^K \alpha_{i,j} \phi_i(\vec{x})$$

The set of functions $\phi_1(\vec{x})$, $\phi_2(\vec{x})$... $\phi_K(\vec{x})$ is called the *basis set* and the spin orbitals are expanded in this basis. All the information necessary to perform a Hartree-Fock calculation is now available. The procedure is described as follows:

(a) An initial estimate of spin orbitals is performed:

$$\chi_j(\vec{x}) = \sum_{i=1}^K \alpha_{i,j} \phi_i(\vec{x})$$

specifying the expansion coefficients $\alpha_{i,j}$.

- (b) The electron density $n(\vec{r'})$, is defined from the estimation of the spin orbitals.
- (c) The single-electron equations for the spin orbitals are solved using the electron density from the previous step, .
- (d) If the spin orbitals found in step (c) are consistent with the orbitals used in step (b) they are solutions to the Hartree-Fock problem. Otherwise, a new estimate of these spin orbitals should be made, going back to step (b).
- Methods beyond Hartree-Fock Although the Hartree-Fock method provides an accurate description for the exchange of electrons, it does not correctly describe the electron correlations (how electrons influence each other).
 - (a) The Hartree-Fock limit The Hartree-Fock limit [80] would be the calculated energy of N electrons if it were possible to use an infinite basis set in the Hartree-Fock calculations. Because the electron correlation is not correctly described in Hartree-Fock, this energy is not the same as the energy of the real wave function. In fact, the electron correlation energy is the difference between the energy of the real, non-relativistic, ground state and the Hartree-Fock limit. In this regard, some part of the electronic correlation is included in more sophisticated methods. A common description of the electron correlation consists on mixing in the wave function of some configurations in which electrons have been excited from lower energy to higher energy orbitals.

(b) Single determinant methods

These methods, formally known as *post-Hartree-Fock* methods, use a single Slater determinant as the reference wave function and excitations are obtained from this wave function. They include

- the Møller-Plesset (MP) perturbation theory [81], the Configuration Interaction (CI) and the quadratic configuration interaction approach (QCI) [82], each of them presenting different variants.
- (c) Multiple determinant methods In these methods, the reference wave function is defined by more than one Slater determinant and include the multiconfigurational self-consistent field (MRDCI) [83] and the N-electron valence state perturbation theory (NEVPT) methods.

2.1.3 The DFT Theory

The DFT theory is more advantageous respect to the aforementioned methods in the sense that, instead of starting with a few wave functions to subsequently determine other parameters from them, DFT starts with an electron density and determines parameters, including the wave functions, from this density. The basis of this theory is two mathematical theorems proved by Kohn and Hohenberg [84] and the derivation of a set of equations by Kohn and Sham in the mid-1960s [85].

- 1. **Kohn and Hohenberg's first theorem** *The ground-state energy state of the Schrödinger's equation is a unique functional of the electron density.*The meaning of this theorem is that the electron density of the ground-state determines uniquely all properties, including the wave function and the energy of the ground state. The Schrödinger equation for the ground-state can then be calculated with only three spatial coordinates, the electron density, instead of a function of 3N variables, as the wave function. Moreover, this theorem proves that there is a density functional that can be used to solve the Schrödinger equation, but adds nothing about which functional it is.
- 2. **Kohn and Hohenberg's second theorem** *The electron density that minimizes the energy of the overall functional is the true electron density corresponding to the full solution to the Schrödinger equation.*If the true functional is known, the electron density could be varied until the functional is minimized, offering a procedure for finding the relevant electron density. One form of writing the functional is to describe it in terms of single-electron wave functions:

$$E[\Psi_i] = E_{Known}[\Psi_i] + E_{XC}[\Psi_i],$$

The first term can be written analytically and second term is the exchange-correlation. The known terms are the electron kinetic energies, the Coulomb interaction between electrons and nuclei, the Coulomb interactions between pairs of electrons and the Coulomb interactions between pairs of nuclei. Then:

$$E_{known} \Psi_i = \frac{-\hbar^2}{m} \sum_i \int \Psi_i^* \nabla_i^2 \Psi_i d^3 r + \int V(\vec{r}) n(\vec{r}) d^3 r + \frac{e^2}{2} \int \int \frac{n(\vec{r}) n(\vec{r'})}{|\vec{r} - \vec{r'}|} d^3 r d^3 r' + E_{ion},$$

Where E_{ion} is the Coulomb interaction between the pairs of nuclei. The problem of expressing the exchange-correlation functional in a useful form was solved by Kohn and Sham. They demonstrated that the correct electron density can be found by solving a set of equations, each equation considering only a single electron. These equations are know as the *Kohn-Sham equations*:

$$\left[rac{-\hbar^2}{2m} + V(\vec{r}) + V_H(\vec{r}) + V_{XC}
ight]\Psi_i(\vec{r}) = \epsilon_i \Psi_i(\vec{r}).$$

It is similar to the equation used in the Hartee-Fock procedure. In the case of the Kohn-Sham equations, the Hartree potential describes the Coulomb repulsion between one particular electron and the total electron density defined by all electrons. The Hartree potential also includes a self-interaction, as the considered electron is also part of the total electron density, and is a corrected term for the exchange-correlation potential.

The exchange-correlation potential is defined as the functional derivative of the exchange-correlation energy:

$$V_{XC} = \frac{\delta E_{XC}(\vec{r})}{n(\vec{r})}.$$

3. The DFT procedure

Using the Kohn-Sham equations and the electron density, the standard procedure for a DFT calculation would be:

- (a) Definition of an initial trial electron density, $n(\vec{r})$
- (b) Determination of the defined Kohn-Sham equations using this trial electron density, to find the single-particle wave functions, $\Psi_i(\vec{r})$
- (c) Calculation of the electron density defined by the single-particle Kohn-Sham wave function from the previous step,

$$n_{KS}(\vec{r}) = 2\sum_{i} \Psi_{i}^{*}(\vec{r})\Psi_{i}(\vec{r}),$$

(d) Comparison between the calculated electron density, $n_{KS}(\vec{r})$, with the electron density used when solving the Kohn-Sham equations, $n(\vec{r})$. If both densities are the same, then this is the electron density of the ground-state and can be used to calculate the total energy. If the two densities are different, the trial electron density must be updated and process would return to step (b).

Figure 2.1 shows a flowchart describing this procedure. Commonly, the initial electron density consists of a superposition of atomic charge densities. After each iteration, a comparison is made between the new and old electron densities. If they differ less than a certain specified criterion, the solution is considered as converged and new ionic positions are calculated. A new comparison is made between the energies of the new and the previous ionic positions and if they also differ less than a specified criterion, the energy is considered converged, ending the loop and arriving at the solution.

- 4. **Exchange-correlation functionals** The next paragraphs describe some of the most used functionals related with the exchange-correlation term.
 - (a) The Local Density Approximation Functional (LDA)

This functional treats the electron density locally and assumes that it is evenly distributed, like in a uniform electron gas, where the exchange-correlation-range potential is exactly known. It gives us a method to completely define the Kohn-Sham equations, but does not solve the Schrödinger equation, as it does not use the exact [86]

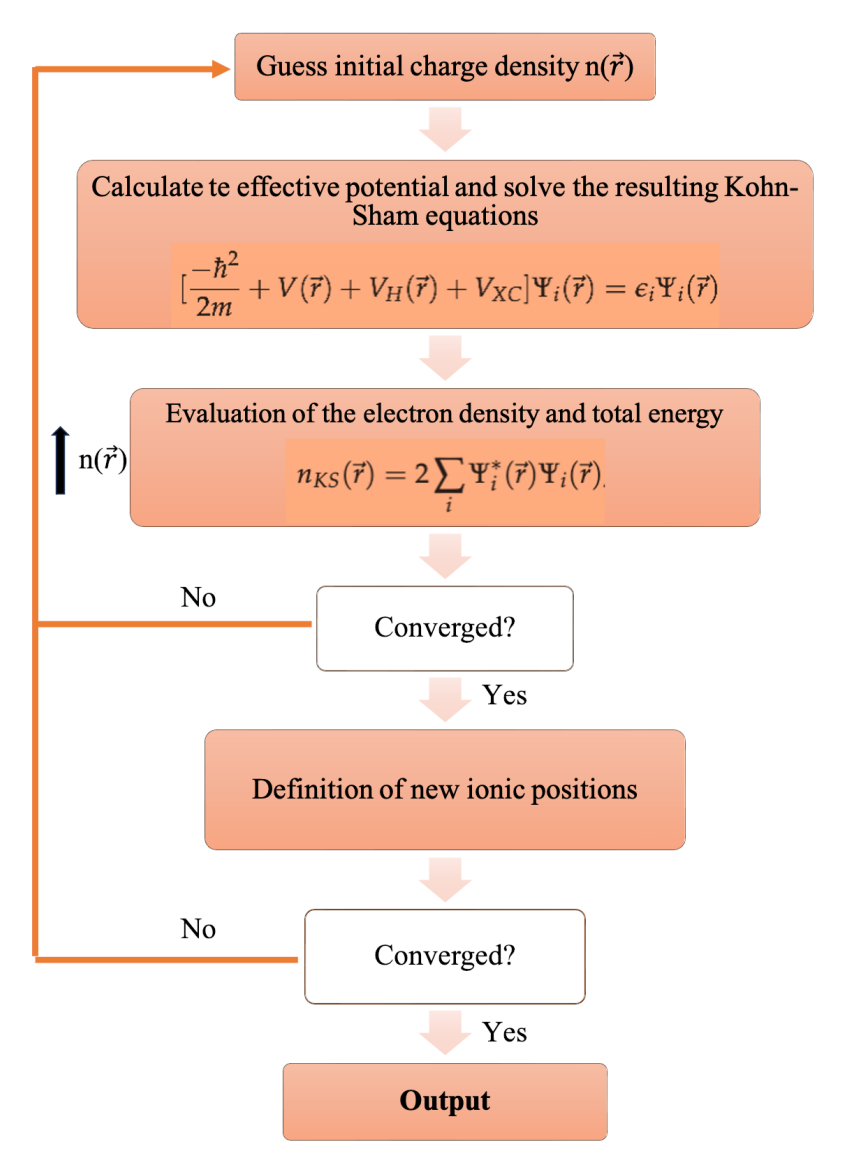


FIGURE 2.1: Flowchart describing the DFT procedure leading to the self-consistent Kohn-Sham solution.

exchange-correlation functional. The definiton for the exchange-correlation potential in LDA is:

$$E_{xc}^{LDA}[n] = \int n(\vec{r}) \epsilon_{xc}(n(\vec{r})) d(\vec{r}),$$

where n is the electron density and ϵ_{xc} is the exchange-correlation energy per particle in the homogeneous electron gas of charge density n.

(b) Generalized Gradient Approximation Functionals (GGA)

Due to the fact that LDA assumes that the density is the same at

all points in space, it shows a tendency to underestimate the exchange energy and to overestimate the correlation energy. To account for the inhomogeneity of the true electron density and correct this issues, information about the local electron density and the local density gradient is often included. It is known under the name of *generalized gradient approximations* (GGA) [87, 88, 89] and looks like this [79]:

$$E_{xc}^{LDA}[n\uparrow,n\downarrow] = \int n(\vec{r})\epsilon_{xc}(n\uparrow,n\downarrow,|\nabla n\uparrow|,|\nabla n\downarrow|,...)d\vec{r} =$$

$$\int n(\vec{r})\epsilon_{x}^{hom}(n)F_{xc}(n\uparrow,n\downarrow,|\nabla n\uparrow|,|\nabla n\downarrow|,...)d\vec{r},$$

where F_{xc} is dimensionless and ϵ_x^{hom} is the exchange energy of the non-polarized gas. There is a spin scaling relation for the exchange:

$$E_x[n\uparrow,n\downarrow] = \frac{1}{2}[E_x[2n\uparrow] + E_x[2n\downarrow],$$

where $E_x[n]$ is the exchange energy for a non-polarized system of density $n(\vec{r})$. Thus, the exchange

 $F_x(n, |\nabla n|)$ only has to be considered non-polarized. It is natural to work in terms of dimensionless reduced density gradients of m-th order which can be defined as:

$$s_m = \frac{|\nabla^m n|}{n(2k_F)^m}$$

The lowest order terms in the expansion of F_x have been calculated analytically [90]:

$$F_x = 1 + \frac{10}{81}s_1^2 + \frac{146}{2025}s_2^2 + \dots,$$

The GGA functionals can achieve accurate results for fundamental states.

(c) The PBE functional

Another widely used functional, when talking about solids, is the

Perdew-Burke-Ernzerhof (PBE) [91, 90] functional. The PBE is most probably the simplest GGA functional. The PBE functional for the exchange is given by a simple form of the enhancement factor F_x [79]. This form is chosen as $F_x(0) = 1$ (recovers the local approximation) and $F_x = cte$ for large s,

$$F_{x}(s) = 1 + \kappa - \frac{\kappa}{\left(1 + \frac{\mu s^{2}}{\kappa}\right)},$$

where $\kappa = 0.804$ is chosen to satisfy the Lieb-Oxford limit. A value of $\mu = 0.21951$ is assigned to recover the linear response form of the local approximation (i.e., to cancel the correlation term), to be in better agreement with quantum Monte Carlo calculations. This choice violates the known expansion for small s with the argument of a better fit of the functional. The form of the correlation is expressed as the local correlation plus an additional term, both dependent on gradients and spin polarization [91]:

$$E_c^{GGA-PBE}[n\uparrow,n\downarrow] = \int d^3r n [\epsilon_c^{hom}(r_s,\zeta) + H(r_s,\zeta,t)]$$

where $\zeta=\frac{(n\uparrow,n\downarrow)}{n}$ is the spin polarization, r_s is the local value of the density parameter, and t is a dimensionless gradient $t=\frac{|\nabla n|}{2\phi nk_{TF}}$

5. Post-DFT methods

(a) **Hybrid functionals** They are more advanced GGA potentials where additional variables (for example, higher-order density gradients) are incorporated and combined with some accurate Hartree-Fock [92] energy of exchange method. They are constructed as linear combinations of the exact Hartree-Fock exchange functional and some number of explicit exchange-correlation density functionals. The exact Hartree-Fock exchange functional has the following form:

$$E_x^{HF} = -\frac{1}{2} \sum_{i,1} \int \int \psi_i^*(\vec{r}_1) \psi_j^*(\vec{r}_2) \frac{1}{r_{12}} \psi_j(\vec{r}_1) \psi_i(\vec{r}_2) d\vec{r}_1 d\vec{r}_2$$

Hybrid functionals make use of spatially localized basis functions and not extended basis functions, like plane waves, although in recent years they have begun to be implemented in plane wave codes. These hybrid functionals are sometimes impractical for materials calculations, as they can significantly increase computational time.

(b) Functional HSE06

It is a specific hybrid functional designed for solids [93, 94]. In the particular case of diamond, it is almost free from electron self-interaction error due to the compensation between Hartree-Fock and GGA exchange errors, thus providing defect levels and defect-related electronic transitions close to the experimental values [95]. It incorporates 25% of the exact Hartree-Fock exchange with a screened Coulomb potential (screening length $0.2~{\rm \AA}^{-1}$). The exchange-correlation potential for HSE06 results:

$$E_{xc}^{wPBEh} = aE_x^{HF,SR}(w) + (1-a)E_x^{PBE,SR}(w) + E_x^{PBE,LR}(w) + E_c^{PBE}$$

where a is the mixing parameter (0.25 for HSE06) and w is the screening length (0.2 for HSE06). This equation consists of short-range (SR) and long-range (LR) terms of the exact exchange plus a correlation term from the PBE. By setting w = 0 is obtained the hybrid PBE0 functional.

(c) The GW approach

This approximation calculates the electron self-energy and is suitable for studying properties of excited states in extended systems. In this approximation, the electron self-energy is the product of the one-particle Green's function and the screened Coulomb interaction. The resulting band structures and band gaps are generally closer to the measured values than those obtained purely with the Kohn-Sham DFT [96, 97, 98]. A G0W0 calculation is the simplest and most computationally efficient GW calculation. It calculates quasi-particle energies from a single GW iteration, neglecting all off-diagonal elements of the self-energy and using a Taylor expansion of the self-energy around the DFT energies.

(d) **Bethe-Salpeter Equation (BSE)** It can be described as the last step in a three-step process. The first step consists of a ground-state

DFT calculation that solves the Kohn-Sham equations. In a second step, the band-structure energies of the quasiparticle calculated in the GW approximation are obtained. In a third step, the BSE equation is used to compute the optical response function (i.e., the frequency-dependent dielectric function) including excitonic effects [99, 100, 101].

2.2 The density of states (DOS)

The energy levels of an electron belonging to a gas of free and independent electrons can be specified by the wave vector \vec{k} and a spin quantum number s with, in absence of a magnetic field, independent energies. The expression describing it:

$$\varepsilon(\vec{k}) = \frac{\hbar^2 k^2}{2m}.$$

The distribution function must satisfy in the ground state (T = 0) that:

$$f_{ks} = 1 \text{ for } \varepsilon(\vec{k}) < \varepsilon_F$$

 $f_{ks} = 0 \text{ for } \varepsilon(\vec{k}) > \varepsilon_F$.

Only levels $\varepsilon(\vec{k}) \leqslant \varepsilon_F$ are occupied in the ground state. The limit of this distribution function is, as the temperature tends to zero:

$$f_{ks} = 1 \text{ for } \varepsilon(\vec{k}) < \mu$$

 $f_{ks} = 0 \text{ for } \varepsilon(\vec{k}) > \mu$.

The limit of the chemical potential must satisfy, for consistency, $\mu = \varepsilon_F$.

Although the chemical potential is equal to the Fermi energy to a high degree of accuracy for metals up to room temperature, this statement is not completely true for accurate calculations and they must be distinguished to avoid misunderstandings.

In Fermi-Dirac statistics, the calculation of the electronic contribution to the specific heat at constant volume of a metal is defined by:

$$c_V = \frac{dQ}{dT}\Big|_V = \frac{T}{V}\left(\frac{\partial S}{\partial T}\right)_V = \left(\frac{\partial u}{\partial T}\right)_V \text{ with } u = \frac{U}{V}.$$

In this set of equations, S is the entropy and u is the density of internal energy. On the other side, the *Fermi function* for Fermi-Dirac statistics, $f_{F-D}(\varepsilon)$, is the mean number of electrons in the one-electron level of energy ε , which leads to a total number of electrons, N:

$$N = \sum_{i} = f_{F-D}(\varepsilon_i) = \sum_{i} \frac{1}{e^{\beta(\varepsilon_i - \mu)} + 1}.$$

From this expression, N is a function of the temperature (as $\beta = K_B T$) and the chemical potential, μ .

In the independent electron approximation, the internal energy U is the sum over the *Fermi function*, $(f_{F-D}(\varepsilon(\vec{k})))$, $\varepsilon(\vec{k})$ times $\varepsilon(\vec{k})$, that is:

$$U = 2\sum_{\vec{k}} \varepsilon(\vec{k}) f_{F-D}(\varepsilon(\vec{k}))$$

The energy density u is obtained when both sides of this equation are divided by the volume V:

$$u = \frac{U}{V} = \int \frac{d\vec{k}}{4\pi^3} \varepsilon(\vec{k}) f_{F-D}(\varepsilon(\vec{k}))$$

In a similar form, dividing N by V and replacing the quantum state i by the wave vector for free electrons, \vec{k} , the electronic density results:

$$n = \frac{N}{V} = \int \frac{d\vec{k}}{4\pi^3} f_{F-D}(\varepsilon(\vec{k})).$$

where the integrand now depends on \vec{k} only through the electronic energy $\varepsilon(\vec{k}) = \frac{\hbar^2 k^2}{2m}$ Evaluating the integral in spherical coordinates and changing the variables from \vec{k} to ε :

$$\int \frac{d\vec{k}}{4\pi^3} F(\varepsilon(\vec{k})) = \int_0^\infty \frac{k^2 dk}{\pi^2} F(\varepsilon(\vec{k})) = \int_{-\infty}^\infty d\varepsilon g(\varepsilon) F(\varepsilon).$$

 $g(\varepsilon)$, a significant function called *energy density of states* or simply *density of states* (DOS), is the number of one-electron level between energies ε to $\varepsilon + d\varepsilon$:

$$g(\varepsilon) = \frac{1}{2\pi^2} \left(\frac{2m}{\hbar^2}\right)^{\frac{3}{2}} \sqrt{\varepsilon}$$
, for $\varepsilon > 0$;
 $g(\varepsilon) = 0$ for $\varepsilon < 0$;.

Considering that $k_F = (3\pi^2 n)^{1/3}$ and $\varepsilon = \frac{\hbar^2 k_F^2}{2m} g(\varepsilon)$ at zero temperature, $g(\varepsilon)$ can be written as:

$$g(\varepsilon) = \frac{3}{2} \frac{n}{\varepsilon_F} \left(\frac{\varepsilon}{\varepsilon_F}\right)^{\frac{1}{2}}$$
, for $\varepsilon > 0$;
 $g(\varepsilon) = 0$ for $\varepsilon < 0$;.

The DOS at the Fermi energy is a quantity of particular importance, given by:

$$g(\varepsilon) = \frac{mk_F}{\hbar^2 \pi^2} = \frac{3}{2} \frac{n}{\varepsilon_F}.$$

2.3 Bader decomposition of the charge density

In this work is crucial the determination of the charge transfer between atoms, as many properties of the material are strongly related to it. The main difficulty in the estimation of this magnitude is that the atomic charges in solids are not observables and cannot be defined by means of quantum mechanics, because the electronic charge density results a continuum. The proposals to solve this questions consist of either using electronic orbitals or only the charge density. One typical orbital based method is the Mulliken analysis, which employs basis functions which are centered on atoms. In this method, the charge associated with these functions is assigned to that atom. Although this way of calculating the partial charges on an atom is efficient and fast, it however depends on the election of the basis set. To avoid this drawback, Bader proposed an approach based on the charge density [102], independent

of the choice of the basis set. In this method, the *Bader regions* divide the space by surfaces which run through charge density minima, where the electron density has no component normal to the surface. The total charge of one atom is estimated then by integrating the electronic density contained in a Bader region where a nucleus of an atom can be found, and adding possibly the electronic charge of nearby regions that do not have a nucleus. Although the first algorithms developed for the Bader analysis were complex and required computational efforts, Henkelmann *et al.* presented an efficient and robust method that uses exclusively steepest ascent trajectories confined to the grid points. The advantage of this method is that the required operations per grid point, in this algorithm, does not depend on the number of atoms and the size of the grid and the computational cost is linear respect to the number of grid points.

The methodology is summarized below. The charge density points are assumed to form a lattice and each grid point must be associated to a Bader region. It is done by finding a path of steepest ascent in the charge density. If $\vec{r}(i,j,k)$ is the Cartesian vector to the grid point (i,j,k), the move is made in the direction which maximizes the charge density gradient, ∇n , calculated along the possible directions toward adjacent grid points.

$$\nabla n(i,j,k) \cdot \hat{r}(di,dj,dk) = \frac{\Delta n}{|\Delta \vec{r}|},$$

where the values $\{-1,0,1\}$ are assigned to di,dj and dk excluding di = di = dk = 0 and

$$\Delta n = n(i+di, j+dj, k+dk) - n(i, j, k),$$

is the change in charge density and

$$|\Delta \vec{r}| = |\vec{r}(i+di,j+dj,k+dk) - \vec{r}(i,j,k)|,$$

is the change in distance. They are computed between neighbors. Following the given definition, the steepest ascent step $\vec{r}(di,dj,dk)$ is the one that maximize the positive values of $\nabla n(i,j,k)$ and it is considered a charge density maximum in absence of positive values.

Finally, by summing over the grid points contained in a Bader region, the total electronic charge in this region can be evaluated. This algorithm is very efficient in the sense that each point requires a fixed amount of work.

2.4 Dynamical stability of materials and the Density Functional Perturbation Theory

[103]

A *phonon* is defined as a unit of vibrational energy as a result of oscillating atoms in a crystal. According to quantum mechanics, this vibrational energy is a multiple of a basic amount of energy (quantum) and is proportional to the frequency ω . In this sense, phonons can be considered as packets of energy or particles of heat with energy $\epsilon = (n + \frac{1}{2})\hbar\omega$. Together with electrons, they constitute the two most important elementary excitations/particles in solids.

When a material is heated, its atoms oscillate at specific frequencies and the resulting wave (or phonon) travels through the crystal. The way to describe the elastic vibrations in a crystal is via the dependence of the frequency of an elastic wave, ω with respect to the wave vector, k, known as phonon dispersion. In solids with two or more atoms per unit cell, this phonon dispersion exhibits two branches known as acoustic branch and optic branch. As a result, there are longitudinal acoustic modes (LA) transversal acoustic modes (TA), longitudinal optic modes (LO) and transversal optic models (TO). The number of branches is determined by the number of atoms in the unite cell, N, existing 3 acoustic branches and 3N-3 optic branches. To illustrate this idea, an example with a cubic crystal composed by two different atoms of mass M_1 and M_2 , respectively, with a distance a between identical planes (and not between nearest-neighbor planes) is developed below. Let's consider waves propagating in a direction of symmetry for which one plane contains one kind of atoms. Under the assumption that each plane is interacting exclusively with nearest-neighbors, and that the force constants are identical between the neighboring atomic planes, then:

$$M_1 \frac{d^2 u_s}{dt^2} = C(v_s + v_{s-1} - 2u_s),$$

 $M_2 \frac{d^2 v_s}{dt^2} = C(u_{s+1} + u_s - 2v_s),$

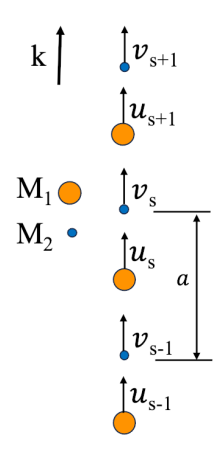


FIGURE 2.2: Example of a diatomic crystal with masses M_1 and M_2 connected by a force constant C. The atoms are shown in their fixed position and the displacements are expressed in terms of u_{s-1} , u_s , u_{s+1} , ... for atoms M_1 and v_{s-1} , v_s , v_{s+1} , ... for atoms M_2 .

possible solutions are $u_s = ue^{is\vec{k}a}e^{-i\omega t}$ and $v_s = ve^{is\vec{k}a}e^{-i\omega t}$. Substituting them in the equations, it results:

$$-\omega^{2} M_{1} u = Cv[1 + e^{-ika}] - 2Cu,$$

$$-\omega^{2} M_{2} v = Cu[1 + e^{ika}] - 2Cv,$$

then:

$$det \begin{vmatrix} 2C - M_1 \omega^2 & -C[1 + e^{-ika}] \\ -C[1 + e^{ika}] & 2C - M_2 \omega^2 \end{vmatrix} = 0$$

that is

$$M_1 M_2 \omega^4 - 2C(M_1 + M_2)\omega^2 + 2C^2(1 - coska) = 0,$$

Let's consider two limits for *k*:

• $ka \ll 1$ (small ka), then $cos(ka) \simeq 1 - \frac{1}{2}k^2a^2 + ...$

$$\omega^2 \simeq 2C \left(\frac{1}{M_1} + \frac{1}{M_2} \right)$$
 — optical branch

$$\omega^2 \simeq \frac{\frac{1}{2}C}{M_1 + M_2} k^2 a^2 - \text{acoustic branch}$$

• $-\frac{\pi}{a} \leqslant k \leqslant \frac{\pi}{a}$ for such limits:

$$\omega^2 = \frac{2C}{M_1}$$
 – acoustic branch $\omega^2 = \frac{2C}{M_2}$ – optical branch

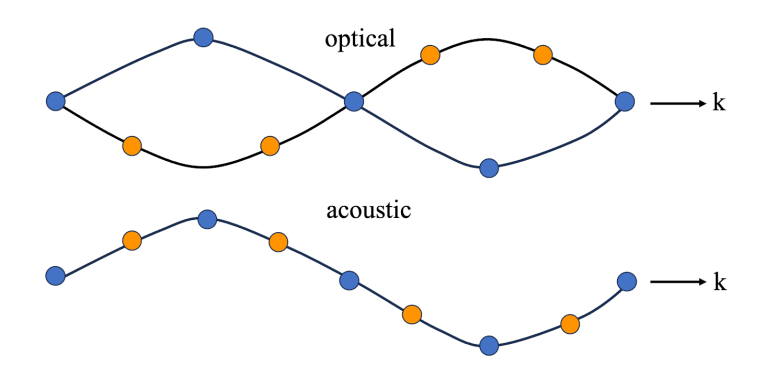


FIGURE 2.3: Transversal optical and acoustic waves in a linear diatomic lattice

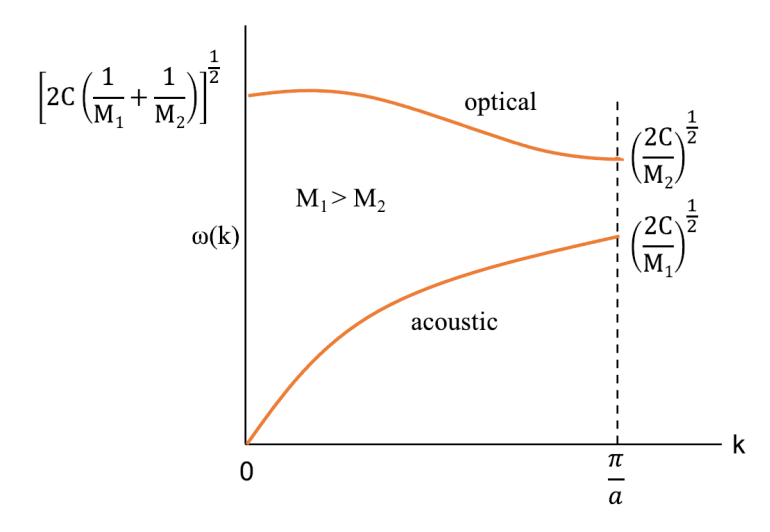


FIGURE 2.4: Phonon dispersion plot for a linear diatomic lattice, showing the acoustic and optical branches. The constant value a in the value limit $\frac{\pi}{a}$ represents the lattice constant.

Now arises the question: why the value of ω^2 is so important for the analysis of the stability? The reason is that, if the structure is (or results) unstable, ω^2 will be negative and hence, ω will result imaginary, meaning that

the crystal will spontaneously transform in another structure more stable. In this regard, we are looking for structures without imaginary frequencies in their dispersion relation of phonons.

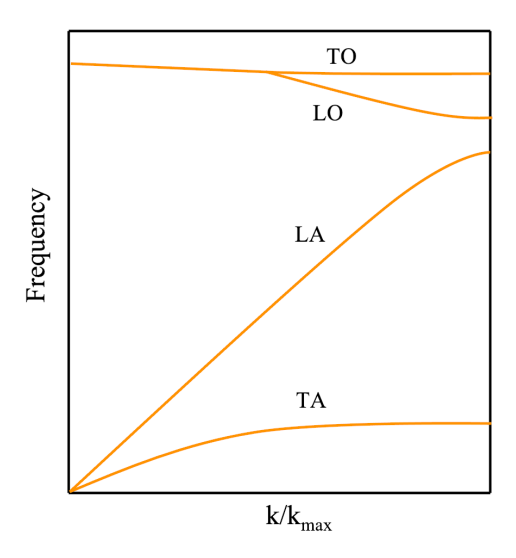


FIGURE 2.5: Example of a phonon dispersion in a cubic crystal, where LA and TA are horizontal in the limit K_{max} . Branches LO and TO coincide at K=0, a consequence of the symmetry of the crystal.

The dynamical stability of a system is an important factor to consider when looking for a suitable material for specific purposes. This information is provided by the vibrational properties obtained from their electronic structure. From all of these possible properties, the behavior of the phonon dispersion is mandatory when starting to work with a new compound. The classical experimental way to measure such properties is the infrared and Raman spectroscopy, but also the inelastic neutron scattering, which provide accurate information of vibrational spectra. In this sense, the theoretical estimation of properties like displacement patterns or frequencies plays an important role in materials modeling due to the information contained on the atomic and electronic structure. The implementation consists of considering a system near its equilibrium, where the Hamiltonian is reduced to a system of independent oscillators that are called *normal modes*. The corresponding displacement patterns, U_I^{α} for the α th Cartesian component of the Ith atom, and frequencies, ω , are given by:

$$\sum_{J,\beta} (C_{IJ}^{\alpha\beta} - M_I \omega^2 \delta_{IJ} \delta_{\alpha\beta}) U_J^{\beta} = 0, \text{ with } C_{IJ}^{\alpha\beta} = \frac{\partial^2 E(\{\vec{R}\})}{\partial R_I^{\alpha} \partial R_J^{\beta}} = -\frac{\partial F_I^{\alpha}}{\partial R_I^{\beta}}$$

where $C_{IJ}^{\alpha\beta}$ is the matrix of the *interatomic force constants* (IFCs), $\{\vec{R}\}$ is the set of nuclear coordinates and \vec{F}_I are the forces calculated via the Hellmann-Feynmann theorem applied to the Born-Oppenheimer Hamiltonian.

The direct computation of the interatomic force constants can be performed using density-functional perturbation theory. In this context, their explicit expression is obtained by differentiating the forces with respect to the nuclear coordinates:

$$\frac{\partial^2 E(\{\vec{R}\})}{\partial \vec{R_I} \partial \vec{R_I}} = \int \frac{\partial n(\vec{r})}{\partial \vec{R_I}} \frac{\partial V_{\{\vec{r}\}}(\vec{r})}{\partial \vec{R_I}} d\vec{r} + \delta_{ij} \int n(\vec{r}) \frac{\partial^2 V_{\{\vec{R}\}}(\vec{r})}{\partial \vec{R_I} \partial \vec{R_I}} d(\vec{r}) + \frac{\partial^2 E_N(\{\vec{R}\})}{\partial \vec{R_I} \partial \vec{R_I}},$$

the ground-state charge density, $n(\vec{r})$ and its linear response to a distortion, $\partial n(\vec{r})/\partial \vec{R}_I$, of the nuclear geometry, are needed, then, for the calculation of the interatomic force constants.

Let's then suppose an atom I in a perfect crystal and located, in turn, in the lth unit cell. Its position is:

$$\vec{R}_I = \vec{R}_l + \tau_s = l_1 \vec{a}_1 + l_2 \vec{a}_2 + l_3 \vec{a}_3 + \tau_s$$

where \vec{R}_l , the position of the lth cell in the Bravais lattice, is a sum of three primitive translation vectors \vec{a}_1 , \vec{a}_2 and \vec{a}_3 , and τ_s is the equilibrium position of the sth atom in this unit cell, then:

$$\psi_n(\vec{r}) \equiv \psi_{\nu,\vec{k}}(\vec{r}), \quad \psi_{\nu,\vec{k}}(\vec{r} + \vec{R}_l) = e^{i\vec{k}\cdot\vec{R}_l}\psi_{\nu,\vec{k}}(\vec{r})$$

where k is a wave vector in the first Brillouin zone and ν corresponds to a band index.

In crystalline solids, *phonons* (or normal modes) are defined by a mode index ν and a wave vector \vec{q} , resulting in phonon frequencies, $\omega(\vec{q})$, and displacements, $U_s^{\alpha}(\vec{q})$ evaluated as:

$$\sum_{t,\beta} \left(\tilde{C}_{st}^{\alpha\beta}(\vec{q}) - M_s \omega^2(\vec{q}) \delta_{st} \delta_{\alpha\beta} \right) U_t^{\beta}(\vec{q}) = 0$$

where $\tilde{C}_{st}^{\alpha\beta}(\vec{q})$ is the so-called *dynamical matrix*, which is the Fourier transform of real-space *interatomic force constants*, IFCs, that is:

$$\tilde{C}_{st}^{\alpha\beta}(\vec{q}) = \sum_{l} e^{-i\vec{q}\cdot\vec{R}_{l}} C_{st}^{\alpha\beta}(\vec{R}_{l}), \text{ with } C_{st}^{\alpha\beta}(l,m) \equiv \frac{\partial^{2}E}{\partial u_{s}^{\alpha}(l)\partial u_{t}^{\beta}(m)} = C_{st}^{\alpha\beta}(\vec{R}_{l} - \vec{R}_{m}),$$

Where the atom s in cell l is displaced $\vec{u}_s(l)$ from its equilibrium position, that is, $\vec{R}_I = \vec{R}_l + \tau_s + \vec{u}_s(l)$. We can see that, due to translational invariance, the dependence of real-space IFCs on m and l is exclusively through $\vec{R}_l - \vec{R}_m$.

However, because the displacement of one atom breaks the translational symmetry of the infinite periodic system, these derivatives must be formulated in a different way. If $u_s(q)$ is the amplitude of a lattice distortion of wave-vector \vec{q} and N_c are the unit cells, then:

$$\tilde{C}_{st}^{\alpha\beta}(\vec{q}) = \frac{\partial^2 E}{\partial u_s^{*\alpha}(\vec{q}) \partial u_t^{\beta}(\vec{q})},$$

with
$$u_s(l) = u_s(\vec{q})e^{i\vec{q}\cdot\vec{R}_l}$$

It means that, unless $\vec{q}=0$, this equation loses the periodicity in the frozen-phonon approach. To deal with this difficulty, the calculation of IFCs for $\vec{q}\neq 0$ requires a big *supercell* for a perturbation of wave-vector \vec{q} . However, because the computational cost increases as the cube of the size of this supercell (approximately), this frozen-phonon approach is limited to a small increase of the unit cell or to phonons with $\vec{q}=0$.

The dynamical matrix can be expressed in two components, the ionic and the electronic:

$$\tilde{C}_{st}^{\alpha\beta}(\vec{q}) = ^{el} \tilde{C}_{st}^{\alpha\beta}(\vec{q}) + ^{ion} \tilde{C}_{st}^{\alpha\beta}(\vec{q}),$$

with

$${}^{el}\tilde{C}_{st}^{\alpha\beta}(\vec{q}) = \frac{1}{N_c} \left[\int \left(\frac{\partial n(\vec{r})}{\partial u_s^{\alpha}(\vec{q})} \right)^* \frac{\partial V_{\{\vec{R}\}}(\vec{r})}{\partial u_t^{\beta}(\vec{q})} d\vec{r} + \delta_{st} \int n(r) \frac{\partial V_{\{\vec{R}\}}}{\partial u_s^{*\alpha}(\vec{q}=0) u_t^{\beta}(\vec{q}=0)} d(r) \right],$$

The ionic contribution is independent of the electronic structure and the second term of $^{el}\tilde{C}_{st}^{\alpha\beta}(\vec{q})$ is feasible to evaluate because it is only dependent on

the charge density of the system without perturbation. Then, is the first term which depends on the linear response of the charge-density to the lattice distortion, with a perturbing potential:

$$\frac{\partial V_{\{\vec{R}\}}(\vec{r})}{\partial \vec{u}_s(\vec{q})} = -\sum_{l} \frac{\partial v_s(\vec{r} - \vec{R}_l - \tau_s)}{\partial \vec{r}} e^{i\vec{q} \cdot \vec{R}_l}$$

The DFPT equations are linear respect to the perturbing potential, an advantage in comparison with the frozen-phonon technique. This method allows the calculation of the dynamical matrix for any \vec{q} without the need to introduce supercells, and real-space ICFs are obtained by means of discrete Fourier transforms. The dynamical matrices are calculated on a uniform \vec{q} -grid in the Brillouin Zone:

$$\vec{q}_{l_1,l_2,l_3} = l_1 \frac{\vec{b}_1}{N_1} + l_2 \frac{\vec{b}_2}{N_2} + l_3 \frac{\vec{b}_3}{N_3},$$

with l_1 from 0 to N_1 - 1, l_2 from 0 to N_2 - 1 and l_3 from 0 to N_3 - 1, integers and $\vec{b_1}$, $\vec{b_2}$ and $\vec{b_3}$ primitive translation vectors in the reciprocal lattice. IFCs in real space are obtained via a discrete Fourier transform $\tilde{C}_{st}^{\alpha\beta}(\vec{q}_{l_1,l_2,l_3}) \to C_{st}^{\alpha\beta}(\vec{R}_{l_1,l_2,l_3})$ where all the \vec{R} -vectors are contained in a real-space grid in a supercell with primitive translation vectors $N_1\vec{a}_1, N_2\vec{a}_2, N_3\vec{a}_3$:

$$\vec{R}_{l_1,l_2,l_3} = l_1 \vec{a}_1 + l_2 \vec{a}_2 + l_3 \vec{a}_3$$

Finally, the calculated interatomic force constants are used to easily calculate the dynamical matrices by the Fourier transform for any vector \vec{q} that was not included in the original reciprocal-space grid, a procedure called *Fourier interpolation*.

2.5 Determination of the Hubbard parameters

It is well known that a big problem with *ab initio* calculations is that they do not correctly describe the electronic properties of strongly correlated systems. One of the most famous failures associated with this issue is the inability of both the local spin density approximation (LDA) and the spin-polarized generalized gradient approximation (σ -GGA) to predict the insulating nature of some transition metal oxides (TMO), and to give a proper estimation of the

band gap. To overcome this problem, great efforts have been put into the development of new approaches that can accurately describe such systems. In this direction, Anisimov *et al.* [104, 105, 106] introduced the LDA+U approach, which notably improved the results for several strongly correlated systems with respect to LSDA or σ -GGA and, in turn, motivated the implementation of more sophisticated theoretical approaches.

One classical way to treat the Hubbard correction would be to take some proven values and mix them with (when they are available) experimental results. Alternatively, in the present work, the Hubbard parameters for the transition metal d orbitals have been determined using the linear response approach [107], which is based on the density-functional perturbation theory (DFPT) [108, 109]. With this method, independent of the basis set employed in the calculation, the Hubbard parameter U can be computed from the second-order derivative of the energy.

In the following, the parameter J that describes the magnetic interaction will be either set to zero or mimicked by redefining the U parameter as $U_{eff} = U - J$ [110].

LDA or GGA approaches can quite well reproduce the total energy between different states if the orbital occupation is constrained to have integer values [111]. A good approximation to recover the physical situation would be adding a correction to the total energy given by LDA, which disappears for an integer number of electrons and eliminates the curvature of the energy profile of LDA (caused by a quadratic term not canceled adequately in the exchange-correlation term, which arises from the Hartree energy) in every interval with fractional occupations. It is achieved if the value of the *U* parameter is set equal to the curvature of the energy profile of LDA or GGA.

However, in solids, the hybridization of localized orbitals with the crystal can lead to fractional occupations. In this case, the LDA/GGA energy contains such effects coming from hybridization and, to deal with this problem, a linear response approach is used to evaluate the U parameters. The first step to approaching this calculation is to compute U using a constrained density functional [112, 113, 114]. The total energy is a function of the localized-level occupations of the "Hubbard" sites:

$$E[\{q_I\}] = \min_{n(\vec{r}),\alpha_I} \left\{ E[n(\vec{r})] + \sum_I \alpha_I(n_I - q_I) \right\},\,$$

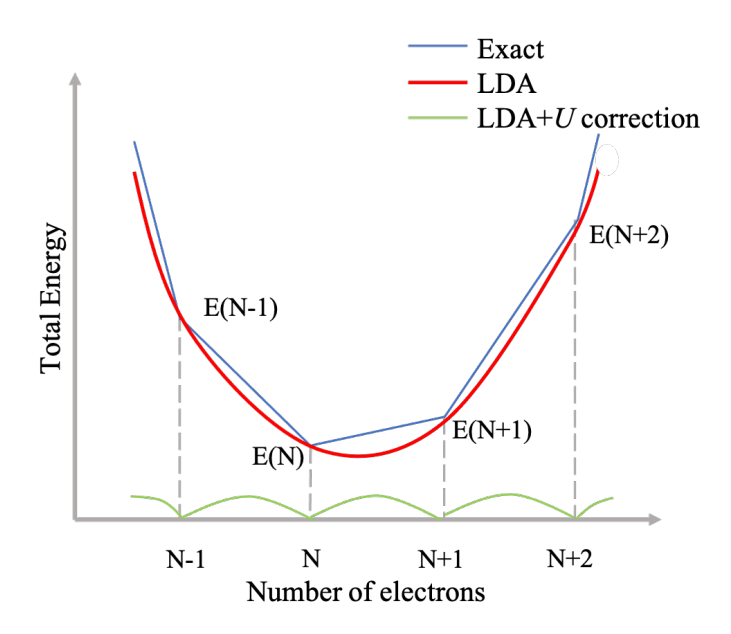


FIGURE 2.6: Plot of the total energy respect to the number of electrons in an atomic system in contact with a reservoir. The difference between the exact result for the open system (in blue) and the LDA energy (in red) are represented by the curve at the bottom (in green).

With this expression, the curvature of the total energy can thus be numerically computed with respect to the variation of the occupation of an isolated site around the unconstrained values $\{n_I^{(0)}\}$. This equation uses Lagrange multipliers α_I to constrain site occupations n_I .

Moreover, if the total energy of a non-interacting Kohn-Sham problem corresponding to the same system is calculated:

$$E^{KS}[\{q_I\}] = \min_{n(\vec{r}), \alpha_I} \left\{ E^{KS}[n(\vec{r})] + \sum_{I} \alpha_I^{KS}(n_I - q_I) \right\},$$

The rehybridization of localized orbitals with other degrees of freedom, caused by the variation of the site occupation, also produces a nonlinear change in the energy of the system. This kind of curvature arising from the rehybridization exists also in the interacting case, and it is independent of the Hubbard U of the interacting system. That is the reason why it should be removed from the total curvature:

$$U = \frac{\partial^2 E[\{q_I\}]}{\partial q_I^2} - \frac{\partial^2 E^{KS}[\{q_I\}]}{\partial q_I^2},$$

The Janak theorem [115] proves that the second-order derivative of the total energy can be expressed as a first-order derivative of the localized eigenvalue. In the present approach, the eigenvalue of the isolated atom is represented by the Lagrange multiplier, which enforces the level occupation [116], that is:

$$\frac{\partial E[\{q_J\}]}{\partial q_I} = -\alpha_I, \ \frac{\partial^2 E[\{q_J\}]}{\partial q_I^2} = -\frac{\partial \alpha_I}{\partial q_I},$$

$$\frac{\partial E^{KS}[\{q_J\}]}{\partial q_I} = -\alpha_I^{KS}, \ \frac{\partial^2 E^{KS}[\{q_J\}]}{\partial q_I^2} = -\frac{\partial \alpha_I^{KS}}{\partial q_I}.$$

The advantage of this method is that the contribution of the band structure $(-\partial \alpha_I^{KS}/\partial q_I)$ is subtracted from the curvature but the U parameter is calculated in the same system in which it will be applied, making environmental screening more realistic.

In real calculations, the α_I 's become independent variables by means of a Legendre transform:

$$E[\{\alpha_I\}] = \min_{n(\vec{r})} \left\{ E[n(\vec{r})] + \sum_I \alpha_I(n_I) \right\},\,$$

$$E^{KS}[\{\alpha_I^{KS}\}] = \min_{n(\vec{r})} \left\{ E^{KS}[n(\vec{r})] + \sum_{I} \alpha_I^{KS}(n_I) \right\}.$$

The density response functions of the interacting and non-interacting systems with respect to the localized perturbations are defined as:

$$\chi_{IJ} = \frac{\partial^2 E}{\partial \alpha_I \partial \alpha_J} = \frac{\partial n_I}{\partial \alpha_J},$$

$$\chi_{IJ}^0 = \frac{\partial^2 E^{KS}}{\partial \alpha_I^{KS} \partial \alpha_I^{KS}} = \frac{\partial n_I}{\partial \alpha_I^{KS}}.$$

Then, the *U* parameter corresponding to site *I* is expressed as:

$$U_I = \left(-\frac{\partial \alpha^I}{\partial q_I}\right) - \left(-\frac{\partial \alpha_I^{KS}}{\partial q_I}\right) = (\chi_0^{-1} - \chi^{-1})_{II},$$

where the density response functions χ_0^{-1} and χ^{-1} are obtained from numerical derivatives. To this end, the method uses a sufficiently large supercell in which the occupation of a specific site is changed while the other side occupation remains unchanged. The process starts with the calculation of a self-consistent potential performing a well-converged LDA calculation for the unconstrained system with $\alpha_I = 0$ for all sites. Starting with this potential, small positive and negative shifts of the potential are added to each non-equivalent Hubbard site J. The variation of the occupation n_I for all sites in the supercell is then computed:

- (i) the Kohn-Sham potential is let to adjust self-consistently to screen optimally the localized perturbation
- (ii) not allowing this screening

The derivatives calculated in (i) and (ii) give the matrices χ_{IJ} and χ_{IJ}^0 respectively. This approach to compute the Hubbard U parameters based on DFPT is implemented in QE in the HP code [117, 118].

2.6 The dispersion correction DFT+D

In this section, an overview of the London-dispersion correction is presented [119]. It is well known that the London-dispersion interactions are nonlocal and behave asymptotically in the form:

$$E_{\rm disp} \propto -\frac{C_6}{R_6}$$

where C_6 is the sixth-order dispersion coefficient and R is the distance.

In this regard, it is clear that conventional Density Functional Theory cannot describe these interactions because the long-range tail of the dispersion energy, proportional to $\frac{1}{R_6}$, is not captured by the DFT approximations. Although empirical corrections were first tested in the 1990s, it was not until the 2000s that modern and accurate semiclassical corrections appeared. Among all these corrections, this section will consider the DFT-D3 approach. However, it is worthwhile to start with a brief explanation of its predecessor, DFT+D2 [120]. This correction accounts for a dispersion contribution for all pairs of atoms in a system, in the form of the London formula mentioned above:

$$E_{\mathrm{disp}}^{\mathrm{DFT\text{-}D2}} = -rac{1}{2} s_6 \sum_{A
eq B} rac{C_6^{AB}}{R_{AB}^6} f_{\mathrm{damp}}^{\mathrm{DFT\text{-}D2}}(R_{AB}),$$

where the factor $\frac{1}{2}$ prevents double counting, s_6 is a scaling parameter, C_6^{AB} represents the isotropic averaged sixth-order dispersion coefficient for a pair of atoms AB and $f_{\rm damp}^{\rm DFT-D2}$ is a damping function that establishes a seamless connection between the short- and long-range regions (in the following "medium-range region") with the form:

$$f_{\text{damp}}^{\text{DFT-D2}}(R_{AB}) = \frac{1}{1 + e^{-20(R_{AB}/R_r - 1)}}$$

In this definition, R_r is the sum of van der Waals radii, and the election of the exponent 20 guarantees larger corrections at intermediate distances in comparison with previous corrections.

The global scaling factor s_6 is empirically adjusted for every density functional approximation, by fitting to a set of non-covalent interaction energies. The value of s_6 will depend on the chosen functional, that is, attractive functionals deliver lower values of s_6 whereas repulsive functionals require values for s_6 larger than unity. The dispersion coefficient is empirical and is obtained as a geometric mean from the specific coefficients of each element, C_6^A and C_6^B :

$$C_6^{AB} = \sqrt{C_6^A C_6^B},$$

This correction supposed not only a crucial contribution to DFT but also provided a better description of noncovalent interactions. However, despite these advantages, this approach soon revealed some drawbacks. For example, the C_6 coefficients and the van der Waals radii had been determined only for the main group elements, whereas the 3d transition metals and the 4d transition metals were assigned the values for scandium and yttrium, respectively. The problem goes further because the dispersion coefficients C_6 were estimated by free atom calculations in the gas phase, ignoring effects such as hybridizations. In fact, some studies related to charged and neutral alkaline compounds have reported problems when using this approximation [121]. That is the reason for the development of the DFT-D3 correction, which overcomes the above-mentioned issues and is applicable to the 94 first

elements of the periodic table. The most remarkable difference with respect to the DFT-D2 approach is that the dispersion coefficients are now fully flexible and dependent on the system. This approximation includes a three-body component of the dispersion energy, $E_{\rm disp}$, in the form:

$$E_{\text{disp}}^{\text{DFT-D3}} = -\frac{1}{2} \sum_{A \neq B} \sum_{n=6,8} s_n \frac{C_n^{AB}}{R_{AB}^n} f_{\text{damp},n}^{\text{DFT-D3}}(R_{AB})$$

expression dependent on two multipole terms: the first one, the sixth-order term with isotropic dispersion coefficients (C_6^{AB}) and the second one an eighth-order term with dispersion coefficients (C_8^{AB}), designed to consider medium-range effects. Although terms of higher order were tested, these were shown to be negligible and absorbed by the s_8 scale factor.

The damping functions were originally proposed by Chai and Head-Gordon, but showed numerical stability for high-order miltipole terms that suited very well for DFT-D3 [121].

For the sixth-order term, the damping function adopts the form:

$$f_{\text{damp,6}}^{\text{DFT-D3}}(R_{AB}) = \frac{1}{1 + 6(R_{AB}/s_{r,6}R_0^{AB})^{-\alpha_6}}$$

whereas, for the eighth-order term:

$$f_{\text{damp,8}}^{\text{DFT-D3}}(R_{AB}) = \frac{1}{1 + 6(R_{AB}/R_0^{AB})^{-(\alpha_6+2)}}$$

On the other hand, the dispersion coefficients in DFT-D3 depend on the system and are calculated as follows:

$$C_8^{AB} = 3C_6^{AB} \sqrt{Q_A Q_B},$$

with

$$Q_A = \frac{1}{2} \sqrt{Z_A} \frac{\langle r^4 \rangle_A}{\langle r^2 \rangle_A},$$

being Z the nuclear charge, and $\langle r^4 \rangle_A$ and $\langle r^2 \rangle_A$ are the expectation values of the quadrupole- and the dipole-moment type, respectively, derived

from the atomic densities. These values were calculated once and subsequently tabulated for every element. The employment of this technique provides a good estimation of the higher-order coefficients, in a few percent of their accurate values. Posterior versions of DFT-D3 use the same dispersion coefficients but differ in the damping functions. The impact of the three-body terms on the computational cost scales from $0(N_{\rm atoms}^2)$ to $0(N_{\rm atoms}^3)$, but is still negligible comparing with the overall cost of a DFT calculation.

2.7 Electronic Conductivity: the Boltzmann Transport Equation

Let us denote, for each band, the quasi-particles' energies and their derivatives as Fourier sums:

$$\tilde{\varepsilon}_k = \sum_{\Lambda} C_A \sum_{R \in \Lambda} e^{i\vec{k}\cdot\vec{R}},$$

$$\nabla \tilde{\varepsilon}_k = i \sum_{\Lambda} C_A \sum_{R \in \Lambda} \vec{R} e^{(i\vec{k} \cdot \vec{R})},$$

here, Λ represents a set of symmetry-equivalent lattice vectors. Shankland [122, 123, 124] had the idea that, by minimizing a roughness function under the assumption that the quasi-particle (and derivatives) energies were exactly reproduced, the coefficients could be obtained. Then, the number of coefficients C should be larger than the number of calculated points. It is equivalent to minimizing the Lagrangian with respect to the Fourier coefficient (C_R):

$$I = \frac{1}{2} \sum_{\vec{k}} C_{\vec{k}} \rho_{\vec{k}} + \sum_{\vec{k}} \left[\lambda_{\vec{k}} (\varepsilon_{\vec{k}} - \tilde{\varepsilon}_{\vec{k}}) + \sum_{\alpha} \lambda_{\alpha, \vec{k}} \nabla_{\alpha} (\varepsilon_{\vec{k}} - \tilde{\varepsilon}_{\vec{k}}) \right],$$

In this equation, the Lagrange multipliers $\lambda_{\vec{k}}$ and $\lambda_{\alpha,\vec{k}}$, are chosen to ensure that the constraints (quasi-particle and derivative energies exactly reproduced) are fulfilled. The index α represents the Cartesian indexes, indicating that each calculated derivative $\nabla \varepsilon_{\vec{k}} = -\langle \psi_{\vec{k}} | \vec{p} | \psi_{\vec{k}} \rangle$, obtained from the elements of the intra-band optical matrix [125, 126], adds three Lagrange multipliers. In the BoltzTraP code, the roughness function is taken from Pickett *et al.* [127]:

$$\rho_{\vec{R}} = \left(1 - c_1 \frac{R}{R_{min}}\right)^2 + \left(c_2 \frac{R}{R_{min}}\right)^6.$$

The rigid-band approximation (RBA) assumes that doping a system or changing the temperature does not change the band structure. In this approach, the carrier concentration in a semiconductor is related to the density of states as follows:

$$n(\varepsilon) = \int \sum_{b} \delta(\varepsilon - \varepsilon_{b,\vec{k}}) \frac{d\vec{k}}{8\pi^{3}},$$

for a given μ and T, b running over bands, by calculating the deviation with respect to charge neutrality:

$$c(\mu, T) = N - \int n(\varepsilon) f^{(0)}(\varepsilon; \mu, T) d\varepsilon.$$

where $f^{(0)}$ is the Fermi distribution function and N is the nuclear charge. If the Fermi level is found in the band gap under the charge neutrality condition, at T=0, it would become a semiconductor n-type if μ is moved into the conduction bands and a semiconductor p-type if μ is moved into the valence bands.

The Boltzmann Transport equation describes the behavior of a system out of equilibrium in terms of a balance between the scattering in and out of each possible state with scalar scattering rates [128].

The transport distribution function arises from the linearized Boltzmann Transport equation under the rigid-band approximation:

$$\sigma(\varepsilon,T) = \int \sum_b \vec{v}_{b,\vec{k}} \otimes \vec{v}_{b,\vec{k}} \tau_{b,\vec{k}} \delta(\varepsilon - \varepsilon_{b,\vec{k}}) \frac{d\vec{k}}{8\pi^3}$$

The moments of the generalized transport coefficients are calculated from this distribution function:

$$\mathcal{L}^{(\alpha)}(\mu;T) = q^2 \int \sigma(\varepsilon,T) (\varepsilon - \mu)^{\alpha} \Biggl(-\frac{\partial f^{(0)}(\varepsilon;\mu,T)}{\partial \varepsilon} \Biggr) d\varepsilon,$$

The charge current is then calculated from:

$$j_e = \mathcal{L}^{(0)} \vec{E} + \frac{\mathcal{L}^{(1)}}{qT} (-\nabla T)$$

in the zero temperature gradient experimental situation, the conductivity is obtained by:

$$\sigma = \mathcal{L}^{(0)}$$

the group velocities can be directly obtained from the \vec{k} -space derivatives of the quasi-particle energies, $\nabla \tilde{\epsilon}_k = i \sum_{\Lambda} C_{\Lambda} \sum_{R \in \Lambda} \vec{R} e^{(i\vec{k} \cdot \vec{R})}$.

In the BoltzTrap2 code the interpolated quasi-particle energies are assumed to be independent from parameters like the Fermi level and the temperature, and this interpolation does not need to be repeated (only the integration) to evaluate thermoelectric coefficients for different temperatures or doping levels. The interpolation of quai-particle energies is once and for all, avoiding the duplication of work when interpolating a τ dependent on the temperature.

2.8 Important parameters for the evaluation of the adsorption of small molecules

Up to this point, the theory behind the diverse approaches, used in the calculations, has been described. In this section, some physical parameters, important for the study of the adsorption phenomena, are defined.

2.8.1 The adsorption energy

In the process of adsorption, the interaction between the adsorbent and the molecule is stabilized by the so called adsorption energy. This energy describes in some way the feasibility and the spontaneity of the interaction, that is, when it adopts a negative value, this process will be spontaneous and, on the contrary, a positive value is an indicator of a repulsive interaction. Attending to the magnitude of the adsorption energy, the adsorption can be considered either chemisorption (covalent bonding) or physisorption (van der Waals forces). It is important to note that the efficiency of the substratum adsorbing a specific gas is an indication that this substratum is more

sensitive toward this gas, with a high negative value of the adsorption energy. From this perspective, this adsorbent may be a feasible material for the fabrication of a gas sensor.

The adsorption energy between the molecule and the pristine material is evaluated in this work by:

$$E_{ads} = E_{substratum + molecule} - E_{substratum} - E_{molecule}$$

In this expression, $E_{substratum+molecule}$ represents the total energy corresponding to the whole substratum/molecule system, $E_{substratum}$ is the total energy of the pristine substratum and $E_{molecule}$ is the total energy of the isolated molecule. This definition gives negative values for the energetically favorable adsorptions.

2.8.2 The recovery time

The recovery time, t_{rec} , is also another important descriptor because it is an estimation of the recovery performance of the sensor. It gives us an idea of the time needed by the sensor, in absence of the gas, to pass from a certain response (e.g., 90 % of the maximum response when the gas is injected) to a certain percentage of it (e.g., 10 %) when the gas is removed, and it is calculated as:

$$t_{rec} = \nu^{-1} e^{-E_{ads}/k_B T}$$

here, ν is the so-called *attempt frequency*, k_B is the Boltzmann constant (in eV/K) and T is the Temperature (in K). The theoretical estimation of the attempt frequency is a laborious process and would need a study apart, as it involves a combination of DFT+U, Nudge Elastic Band method, phonon calculations and the transition state theory, whereas, experimentally, the recovery time of a sensor is usually determined applying thermal effects. It is the reason why, in the literature, it is normally taken between 10^{11} and 10^{13} s⁻¹. From the dependence of this magnitude with the adsorption energy, E_{ads} , it is clear that the larger the interaction strength between the substratum and the molecule, the higher the recovery time. It is important to remark that this quantity must be interpreted carefully, because it gives an estimation and does not accurately measure the time required by the sensor

to be recovered. The reason is that the molecules undergo adsorption and desorption processes simultaneously, which are in dynamical equilibrium, making complicated the exact determination of this value. Nevertheless, it is a valuable parameter to elucidate if a material has a better use as sensor or as gas capturer.

2.8.3 Charge transfer between the MBene and the molecule

In parallel to E_{ads} , the charge transfer between the pristine material and the molecule is computed as:

$$\Delta \rho = \rho_{substratum + molecule} - \rho_{substratum} - \rho_{molecule}$$

This quantity is important to know if the substratum is acting as an acceptor (accepting electrons from the molecule) or as a donor (giving electrons to the molecule) and also to understand the electronic behavior of the interaction.



3.1 A brief introduction to the main results

Knowledge, but also sustainable development and the protection of environment and biodiversity, are inherent features of science. In the last decades, the rapid growth of industry and cities has unavoidably led to the increase of pollution which impact directly on the quality of living creatures, as well as on our own planet. Although many efforts are put on reverting this situation, we are still far from a satisfactory solution. It is through a committed collaboration between the scientific community that we can imagine an auspicious future for next generations. Among all the threatening substances delivered by the human activity, Short-lived climate forcers (SLCFs) are pollutants that have a relatively short lifetime in the atmosphere and impact the climate. They are classified under different criteria, but one of the most conventional way is to separate them into radiatively active or influential on other radiatively active compounds through chemistry. The so-called direct SLCFs include methane, ozone, short-lived halogenated compounds, and aerosols, while *indirect SLCFs* include chemically reactive gases like nitrogen oxides, CO, non-methane volatile organic compounds, SO₂, and NH₃. In this regard, 2D materials with large surface area, with a rich surface chemistry, can favor interactions with molecules, enabling these materials to work as highly sensitive sensors even at low gas concentrations. Two-dimensional boron-based materials constitute an emerging family and are gaining interest thanks to their unique physical and chemical properties, becoming ideal candidates in applications for sensing, reducing, and adsorbing pollutants.

As newbies in the world of *flats*, their related works are still mainly predictive, although some of them start to be synthesized and demonstrate to be stable. Borophene, with its beautiful polymorphisms, has been thoroughly studied since its discovery. Up to date, an important theoretical and experimental development has been invested in this material. The first article of this thesis, based on these preliminary works, demonstrates the great capability of borophene for gas sensing and capturing.

Thanks to all the efforts put on these mono elemental compounds, no much time was needed for the emergence of MBenes, which are two-dimensional transition metal borides. In parallel to MXenes, they are predicted to be obtained from their parental MAB phases. The achievement of these compounds, present in diverse stoichiometries and cristalline structures, and with the peculiarities introduced by the metal ions, opens new perspectives in their use as nanodevices. But before starting with their potential as substrata for the above mentioned applications, a rigorous study concerned to their suitability for such purposes must be done. In the second article, a thorough evaluation of the structural, electronic, magnetic and transport properties of MBenes with M_2B_2 stoichiometry (with M = Cr, Fe and Zr), points to promising and robust materials with diverse facets. The third article is a follow up to the second, and deals with a classical problem of DFT: the consideration of MBenes as high correlated systems, due to the inclusion of partially occupied 3d orbitals from the transition metals. The use of the Density Functional Perturbation Theory for obtaining the customized Hubbard parameters for each system, and their subsequent introduction, shows that the inclusion of this correction is not negligible when the transition metals are Cr and Fe, but practically negligible for the Zr-based MBene.

Once all the cards are on the table, the fourth article tries to put in practice the ability of MBenes as potential candidates for gas sensing and removal. To this end, several parameters involved have been evaluated in depth to analyze the influence of small molecules on the physicochemical properties of the substrata. Their behavior under the adsorption of small molecules will describe the Cr and Fe-based MBenes as sensors, whereas the Zr-based MBene will act as a gas capturer. The novelty introduced by the present thesis is the perspective of Fe and Zr-based MBenes as gas sensors/capturers, and the Cr-based MBene as sensor for these specific molecules, establishing the foundations for further research in this direction.

3.2 PAPER I: Borophene sheets as potential candidates for the detection and removal of harmful gas molecules

This article explores the potential of different structures of borophene, specifically the α -sheet, buckled hexagonal, and honeycomb-like forms, for the detection and capture of five common harmful gas molecules: CO, CO₂, NO, NO₂, and NH₃. But prior to evaluating the influence of small molecules on borophene, it is necessary to perform a preliminary study of the pristine materials. All these forms show high cohesive energies, highlighting the robustness of the compounds, and their electronic structure indicates that, while the α and buckled borophenes are dominated by the out-of-plane orbitals (p_z), in-plane orbitals ($s+p_x+p_y$) stand out in the honeycomb sheet. This circumstance makes the honeycomb-type borophene unstable, in contrast to graphene. This drawback can be, however, overcome, by growing this hexagonal planar structure on a metal, where the electron transfer from the metal can stabilize this boron layer.

Concerning the effects of adsorption on the structure, a surface disturbance occurs, which is more remarkable in the honeycomb sheet, most probably due to a destabilization of the sp^2 bonding of the flat borophene to form sp^3 hybridization instead.

On the side of the molecules, the results reveal that only CO_2 is physisorbed on the α -sheet and the rest of molecules result chemisorbed on the surface, reaching NO and NO_2 the largest values of adsorption energy, in accordance to similar works. In fact, compared with other two-dimensional materials, the adsorption values for molecules on borophene are appreciably higher. These results are related, via an Arrhenius-type equation (the *recovery time*), with the recovery capacity of the sensor after the adsorption. It depends exponentially on the adsorption energy and gives an idea of how much time needs the substratum to be recovered, meaning that the most suitable results correspond to moderate values of this energy. The present study reveals that CO and NO on the α -sheet and CO_2 and NH_3 on buckled borophene present acceptable recovery times as sensors.

The particularities of such interactions are also present in their electronic behavior, whose density of states reveal that the free-standing NO molecule, with magnetic nature, is able to influence the magnetism of the whole system,

and the NO₂ molecule switches its paramagnetic nature into nonmagnetic after adsorption, with the exception of NO₂ on buckled borophene. Other important peculiarities are the tendencies of the charge transfer, as it normally happens from borophene to the molecules, and only ammonia is acting as a donor of electrons to borophene. The metallic nature of borophene is a good quality for sensing, and, in this sense, all of the analyzed sheets show large values, demonstrating their good conductive properties. The buckled sheet exhibits, indeed, the largest deviations between the borophene/molecule systems and the related pristine sheet, with good selectivity toward the ammonia molecule. Finally, the article intends to elucidate if there is a influence in the magnetism after the adsorption of the small molecules. The answer is that, in fact, magnetism arises from the electron transference between the substrata and the above-mentioned molecules, NO and NO₂.

These findings suggest that borophene has promising applications in sensing and removing hazardous gases.



Contents lists available at ScienceDirect

Solid State Communications

journal homepage: www.elsevier.com/locate/ssc



Borophene sheets as potential candidates for the detection and removal of harmful gas molecules

Isabel M. Arias-Camacho*, Nevill Gonzalez Szwacki

University of Warsaw, Faculty of Physics, Pasteura 5, Warsaw, PL-02093, Poland

ARTICLE INFO

Communicated by François Peeters

Keywords:
First-principles calculations
Borophene
Adsorption of molecules
Gas sensing and removal

ABSTRACT

The synthesis of graphene marked the beginning of a new era for two-dimensional materials, celebrated for their exceptional properties and wide-ranging applications. Among the emerging mono-elemental Xenes family, borophene – composed entirely of boron atoms – stands out due to its exotic bonding states, which give rise to diverse polymorphs and versatile applications. This study focuses on three distinct borophene structures: the buckled hexagonal, the α -sheet, and the honeycomb-like forms, each characterized by unique boron densities. Their potential for detecting and capturing five harmful gas molecules (CO, CO₂, NO, NO₂, and NH₃) is thoroughly assessed. The novelty of this work lies in analyzing the interactions between these gases and the well-known α -sheet and honeycomb-like borophene, while using the buckled form as a reference. The results indicate that borophene holds significant promise for applications in hazardous gas sensing and removal.

1. Introduction

The increasing presence of hazardous gases in the atmosphere, driven by industrial growth and traffic, necessitates the development of novel technologies for their effective detection and capture, even at trace concentrations. Two-dimensional materials offer promising possibilities in this regard due to their remarkable physical and chemical properties, including high in-plane mobility, robust mechanical strength, and large surface-to-volume ratios. Gas molecule adsorption, which can involve charge transfer by acting as donors or acceptors, alters the electronic properties of these materials, leading to measurable changes in electrical conductivity—a principle that underpins the operation of gas sensors. Among these materials, the emerging mono-elemental family of Xenes has gained attention. This group includes graphene [1,2], MoS₂ [3,4], phosphorene [5], silicene [6], germanene [7], borophene [8], and heterostructures like borophene/MoS₂ [9].

Borophene, a unique member of the Xenes family, consists entirely of boron atoms and was first predicted theoretically using first-principles calculations by Tang et al. in 2007 [10]. Its experimental realization came later, as thin sheets were synthesized on an Ag(111) substrate under ultra-high vacuum conditions by Mannix et al. [11]. Boron, with its electronic configuration $2s^22p^1$, exhibits distinct polymorphisms [12] in planar and quasi-planar forms, enabling a diverse range of applications due to structural differences.

A key metric for classifying borophene structures is the *density of vacancies* or hole density [10], defined as:

 $\eta = \frac{\text{number of missing atoms}}{\text{number of sites in the hexagonal lattice}}$

Among the various borophene polymorphs, the α -sheet ($\eta=1/9$) is the most stable [10], closely related to the B₈₀ fullerene [13]. Its structure comprises clusters of seven boron atoms, with one central atom lying nearly planar with a surrounding hexagonal chain. The crossover of boron strips creates vacancies that relax the lattice, allowing the α -sheet to maintain its planar structure.

Conversely, honeycomb-like borophene ($\eta=1/3$) is predicted to be unstable due to unoccupied bonding states [10], unlike graphene, whose filled bonding states and empty antibonding states ensure planar stability. Nevertheless, stabilizing this structure is possible through bonding state occupation. Zenitani et al. [14] identified a graphene-like honeycomb borophene layer in MgB₂, exhibiting superconducting properties. Other approaches have stabilized honeycomb borophene on aluminum surfaces via Molecular Beam Epitaxy (MBE) [15], where charge transfer from the metal stabilized the boron layer. Zhang et al. [16] demonstrated that this hexagonal structure could achieve higher energetic stability when adsorbed on metal surfaces. Additionally, alkali or alkaline earth metal adsorption has been shown to stabilize the structure by transferring electrons to the σ and π bands [17].

In this study, we perform first-principles calculations to explore the interaction between five toxic industrial gases (CO, CO₂, NO,

E-mail addresses: isabel.arias@fuw.edu.pl (I.M. Arias-Camacho), gonz@fuw.edu.pl (N.G. Szwacki).

^k Corresponding author.

 NO_2 , and NH_3) and three borophene polymorphisms: *buckled-B*, α -B, and *honeycomb-B* (*hc-B*). The exceptional physicochemical properties of borophene, including its metallicity, flexibility, and chemically interactive surface, make it a promising material for gas sensing and capture.

2. Methods

First-principles calculations were conducted within the Density Functional Theory (DFT) framework, employing a local-spin-density approximation and the generalized gradient-corrected PBE exchange-correlation functional [18]. Projector augmented wave (PAW) pseudopotentials [19] were implemented via the Quantum ESPRESSO (QE) package [20]. The electronic wave functions were expanded in planewave basis sets with an energy cutoff of 60 Ry, ensuring accurate total energy (E_{tot}) evaluations. For Brillouin Zone (BZ) sampling, a Monkhorst–Pack Γ -centered k-point grid of $16 \times 16 \times 1$ was used for geometry optimization and $32 \times 32 \times 1$ for density of states (DOS) calculations, with Gaussian smearing set to 0.02 Ry.

The pristine borophene sheets included a unit cell of eight boron atoms for α -B, a $2 \times 2 \times 1$ supercell of eight atoms for hc-B, and a $3 \times 2 \times 1$ supercell of 12 atoms for buckled-B. A vacuum space of 20 Å was introduced along the normal direction to prevent interactions between adjacent layers. Geometries (pristine and molecule-adsorbed systems) were optimized until residual forces were below 0.3 eV/Å, with a total energy convergence threshold of 10^{-5} Ry. Honeycomb-like symmetry was enforced during optimization to address the hc-B sheet's instability against in-plane shear. Spin-polarized calculations were also performed to explore potential magnetic effects.

The structural characterization included evaluating the cohesive energy per atom:

$$E_{coh} = \frac{E_{\text{B-sheet}} - n_{\text{B}} E_{\text{B}}}{n_{\text{B}}},$$

where $E_{\text{B-sheet}}$ is the total energy of the borophene sheet, E_{B} is the energy of an isolated spin-polarized boron atom, and n_{B} is the number of boron atoms in the unit cell.

The adsorption energy (E_{ads}) between the molecule and the pristine borophene sheets was determined as:

$$E_{ads} = E_{\text{B-sheet/mol}} - E_{\text{B-sheet}} - E_{\text{mol}},$$

where $E_{\text{B-sheet/mol}}$ is the total energy of the borophene sheet with the adsorbed molecule, $E_{\text{B-sheet}}$ is the total energy of the pristine sheet, and E_{mol} is the total energy of the isolated molecule. Negative E_{ads} values indicate favorable adsorption.

Van der Waals interactions were accounted for using the dispersion-corrected DFT-D3 framework [21], incorporating three-body terms for accurate predictions. Recovery time (t_{rec}) , an indicator of sensor performance, was calculated as:

$$t_{rec} = v^{-1} e^{-E_{ads}/k_B T},$$

where k_B is the Boltzmann constant (eV/K), T is the temperature (300 K), and ν is the attempt frequency (10¹² s⁻¹) [22–25].

Charge transfer during adsorption was analyzed via Bader charge calculations [26], and differential charge density was computed as:

$$\Delta \rho = \rho_{\text{B-sheet/mol}} - \rho_{\text{B-sheet}} - \rho_{\text{mol}},$$

where $\rho_{\text{B-sheet/mol}}$ represents the charge of the combined system, and $\rho_{\text{B-sheet}}$ and ρ_{mol} correspond to the charges of the pristine borophene and isolated molecule, respectively.

Electron conductivity was calculated using the BoltzTrap2 code [27, 28] within the constant relaxation time approximation, assuming $\tau = 0.8 \times 10^{-14}$ s. Visualizations of the structures and charge distributions were generated using the VESTA software [29].

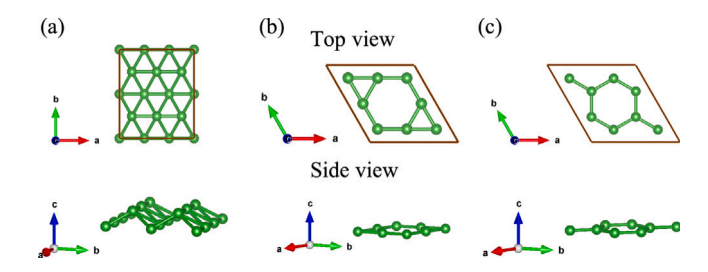


Fig. 1. Top and side views of the optimized pristine borophene layers: (a) *buckled-B*, (b) α -B, and (c) hc-B.

Table 1 Cohesive energies (E_{coh} , in eV), lattice parameters (a and b, in Å), and B–B bond lengths (d_{B-B} , in Å) for pristine borophene structures.

Present work	E_{coh} (eV)	a (Å)	b (Å)	$d_{\mathrm{B-B}}$ (Å)
buckled-B	5.83	1.61	2.87	1.62-1.87
<i>α</i> -B	5.92	5.06	5.06	1.69-1.71
hc-B	5.04	2.92	2.92	1.68
Other works	E _{coh} (eV)	a (Å)	b (Å)	$d_{\mathrm{B-B}}$ (Å)
buckled-B	5.70 ^a 6.00 ^b	1.62 ^c	2.87 ^c	1.61-1.89 ^a 1.60-1.86 ^b
α-В	6.11 ^b	5.07 ^e	5.07 ^e	1.66-1.69 ^b
hc-B	4.96 ^a 5.25 ^b	2.92^{d}	2.92^{d}	1.68a 1.67b

- a Ref. [30].
- ^b Ref. [10].
- c Ref. [31].
- d Ref. [17].
- e Ref. [32].

3. Results and discussion

3.1. Pristine α -B, buckled-B, and hc-B

Fig. 1 presents the optimized unit cells of pristine α -B, buckled-B, and hc-B sheets. The corresponding cohesive energies (E_{coh}), lattice parameters (a and b), and B–B bond lengths ($d_{\rm B-B}$) are summarized in Table 1. These values agree with previous studies [10,17,30–32], validating the accuracy of the optimized structures and providing a solid foundation for further investigations.

Among the configurations studied, α -B exhibits the highest cohesive energy (5.92 eV), making it the most stable 2D boron structure. This stability arises from a synergistic combination of two-center and three-center bonds [33].

The second most stable configuration is *buckled-B*, with a cohesive energy of 5.83 eV. Its stability stems from the relaxation of a flat triangular sheet into a buckled structure, which incorporates both inplane and out-of-plane electronic states, enhancing binding strength. The calculated buckling amplitude of 0.89 Å aligns well with prior reports [10,13].

The hc-B structure is the least stable, with a cohesive energy of 5.04 eV. This lower stability is attributed to the partial occupancy of inplane sp^2 bonding states, explaining why honeycomb-like boron, unlike carbon, does not favor this configuration.

Fig. 2 shows the projected density of states (PDOS) for the three configurations, all exhibiting metallic behavior. The p orbitals dominate at the Fermi level, consistent with previous studies [34,35]. For α -B and buckled-B, the p_z orbitals dominate, while the hc-B structure shows a greater contribution from in-plane orbitals ($s + p_x + p_y$), in agreement with prior findings [10].

3.2. Adsorption of molecules on borophene

To identify the most favorable adsorption sites for various molecules, several nonequivalent initial positions were considered based on the symmetry of each borophene layer (see Fig. 3). For *buckled-B*, four

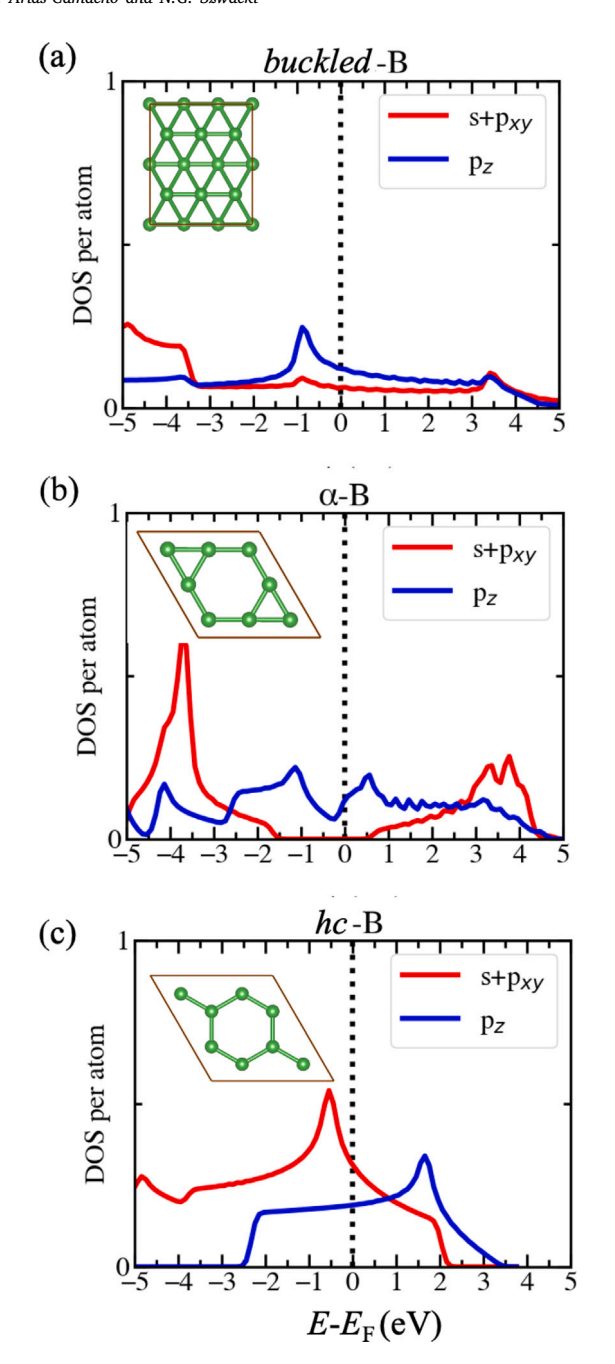


Fig. 2. PDOS of pristine structures: (a) *buckled-B*, (b) α -B, and (c) *hc-B*. The red curve represents in-plane (s, p_x , p_y) contributions, while the blue curve shows out-of-plane (p_z) contributions. The vertical black dotted line indicates the Fermi level (E_F). (For interpretation of the references to color in this figure legend, the reader is referred to the web version of this article.)

unique positions were evaluated, while α -B had twelve and hc-B three, corresponding to top (T), bridge (B), and hollow (H) sites. Additionally, both vertical orientations – with O or C/N atoms directed toward the surface – were tested for diatomic molecules like CO and NO. Molecules were placed horizontally or vertically relative to the borophene surface, yielding eleven possible arrangements for each system. Following structural optimization, the most stable adsorption sites revealed distinct differences between the three borophene types and the studied molecules. These optimized configurations are illustrated in Figs. 4, 5, and 6, while the corresponding adsorption energy values are summarized in Tables S1, S2, and S3.

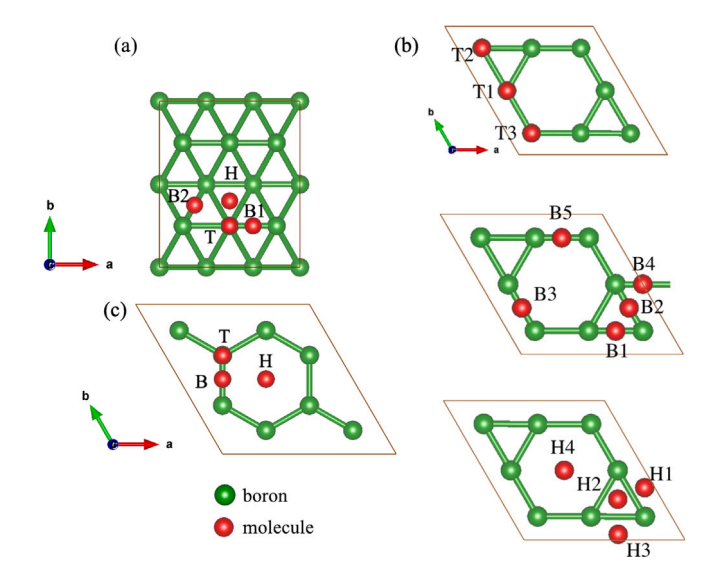


Fig. 3. Starting non-equivalent positions of the molecules on (a) buckled-B, (b) α -B, and (c) hc-B.

The adsorption energies, minimum distances between the molecule and borophene, charge transfers, and recovery times for all configurations are shown in Table 2. Chemisorption is identified when adsorption energies exceed 0.2 eV, and the molecule-boron distance is less than 3.0 Å, consistent with previous studies [31,36,37]. Based on these criteria, α -B demonstrates the weakest adsorption energies among the three borophene types, followed by buckled-B with moderate values. These moderate interactions ensure that the α -B and buckled-B lattices experience minimal structural distortions, primarily limited to boron atoms directly involved in the adsorption. This localized deformation, characterized by slight out-of-plane displacements, results from strong N-B or C-B interactions, as reported in analogous studies [38-40]. Such deformations often induce sp^3 hybridization in boron, replacing the sp^2 hybridization characteristic of pristine borophene, strengthening the molecule-surface interaction and enhancing adsorption energy. Similar behavior has also been observed in silicene [6].

Interestingly, only CO_2 on $\alpha\text{-B}$ remains physisorbed, maintaining a distance of 3.54 Å from the boron layer, while all other molecules undergo chemisorption. In contrast, hc-B exhibits strong chemisorption with adsorption energies exceeding 2.3 eV, capable of dissociating NO and NO_2 . This dissociation forms surface compounds through electronsharing bonds. For instance, the charge transfer analysis reveals that boron atoms bonded to N and O lose more than one electron each, while N and O atoms gain two and one electron(s), respectively. Similarly, NO_2 dissociates into NO and O, with the oxygen atoms receiving charge from nearby boron atoms. This makes hc-B suitable for O_2 production and for removing harmful gases.

Fig. 7 illustrates the relationship between adsorption energy and hole density (η) in the borophene sheets. hc-B, with the highest vacancy density ($\eta=1/3$), exhibits the strongest adsorption energies and the largest variation among molecular species. Conversely, α -B ($\eta=1/9$) and buckled-B ($\eta=0$) show more moderate adsorption patterns, suggesting that a lower vacancy density enhances the sensor properties of borophene.

From a molecular perspective, CO consistently adsorbs vertically, with the carbon atom closest to the surface, while NO attaches horizontally. On *buckled-B*, NO forms N–B and O–B bonds, with an N–O bond length of 1.40 Å, which enhances adsorption strength. CO₂, typically linear in its free-standing state, bends upon interacting with *buckled-B* (123.7°) and *hc-B* (114.25°), while maintaining its linear geometry on α -B. NO₂ preferentially adsorbs with oxygen atoms covalently bonded to boron on α -B and *buckled-B*, whereas dissociation occurs on *hc-B*,

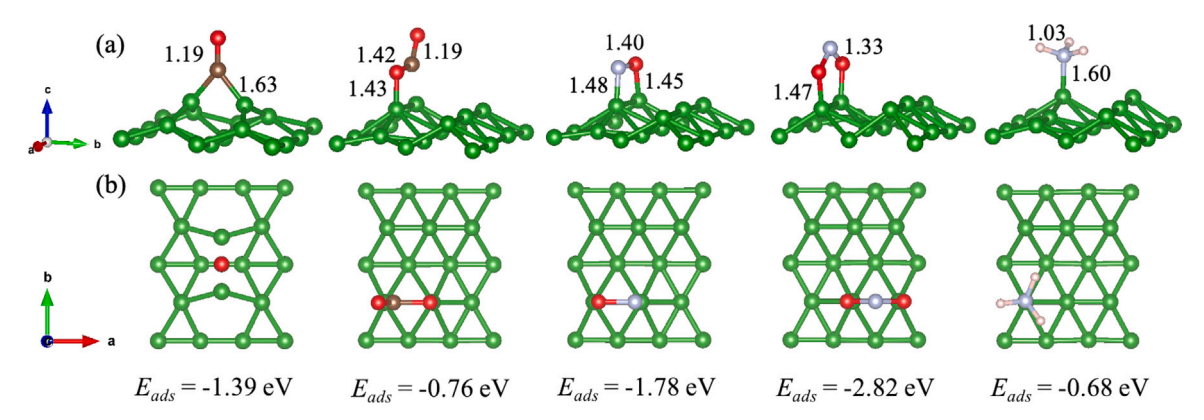


Fig. 4. Side (a) and top (b) views of molecular adsorption on buckled-B, highlighting atomic interactions. Boron atoms are depicted in green, oxygen in red, carbon in brown, nitrogen in light blue, and hydrogen in light pink. (For interpretation of the references to color in this figure legend, the reader is referred to the web version of this article.)

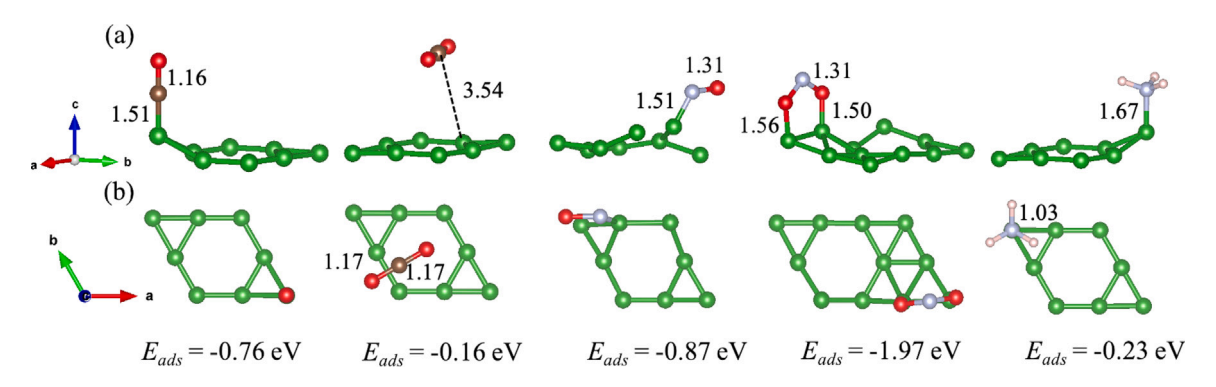


Fig. 5. Side (a) and top (b) views of molecular adsorption on α -B, highlighting atomic interactions. Boron atoms are depicted in green, oxygen in red, carbon in brown, nitrogen in light blue, and hydrogen in light pink. (For interpretation of the references to color in this figure legend, the reader is referred to the web version of this article.)

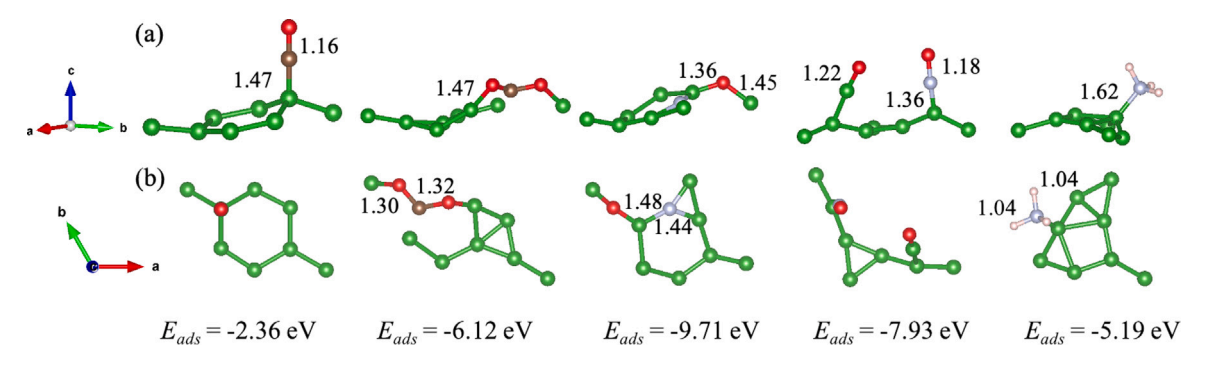
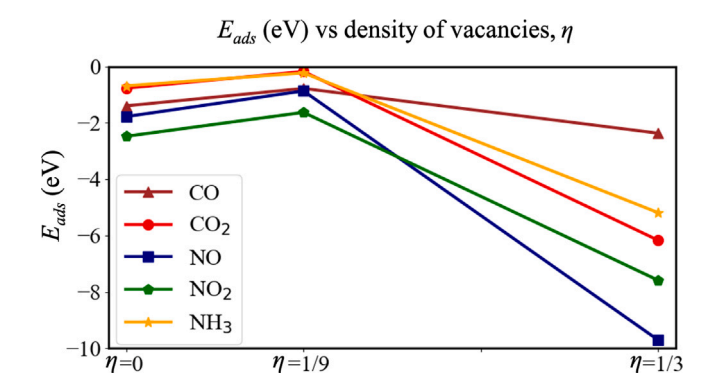


Fig. 6. Side (a) and top (b) views of molecular adsorption on hc-B, highlighting atomic interactions. Boron atoms are depicted in green, oxygen in red, carbon in brown, nitrogen in light blue, and hydrogen in light pink. (For interpretation of the references to color in this figure legend, the reader is referred to the web version of this article.)



 $\textbf{Fig. 7.} \ \ \textbf{Comparison of the adsorption energies with respect to the density of vacancies of each boron layer.}$

with N bonding directly to boron. For NH₃, nitrogen consistently bonds atop a boron atom, with bond lengths of 1.60–1.67 Å, larger than those observed for NO and NO₂.

The recovery times, shown in Table 2, provide insight into the potential for recycling borophene sensors. At 300 K, CO and NO on α -B and CO₂ and NH₃ on *buckled*-B exhibit favorable recovery times, enabling effective sensor regeneration (see Fig. 8).

Compared to other 2D materials, borophene generally exhibits higher adsorption energies, as shown in Table 3. While graphene and MoS_2 show weaker interactions, borophene's adsorption energies approach those of borophene/ MoS_2 heterostructures, demonstrating its potential as an advanced material for molecular adsorption.

3.3. Electronic properties

This section examines the influence of molecular adsorption on the electronic properties of borophene sheets. The projected density of

Table 2 Adsorption energy (E_{ads} , in eV), minimum borophene-molecule distance ($d_{\rm B-mol.}$, in Å), charge transfer (CT, in e), and recovery time (t_{rec}) for the most stable adsorption configurations of borophene/molecule systems.

Boroph.	sheet	CO	CO_2	NO	NO_2	NH_3
buckled-B	E_{ads}	-1.40	-0.77	-1.78	-2.48	-0.69
	$d_{\mathrm{B-mol.}}$	1.63	1.43	1.45	1.47	1.60
	CT	-0.78	-1.19	-1.31	-1.11	+0.03
	t_{rec}	years	10.1 s	years	years	0.32 s
α-В	E_{ads}	-0.78	-0.18	-0.87	-1.63	-0.23
	$d_{\mathrm{B-mol.}}$	1.51	3.54	1.51	1.50	1.63
	CT	-0.43	-0.02	-1.15	-1.02	-0.04
	t_{rec}	10.5 s	0.97 ns	8 min	years	7.6 ns
hc-B	E_{ads}	-2.37	-6.13	-9.71	-7.59	-5.19
	$d_{\mathrm{B-mol.}}$	1.47	1.47	-	-	1.62
	CT	-0.43	-1.59	-3.58	-1.87	+0.02
	t_{rec}	years	years	years	years	years

Table 3 Comparison of reported adsorption energies (E_{ads} , in eV) for various molecules on representative 2D materials, highlighting the adsorption performance of borophene relative to other systems.

Material	CO	CO_2	NO	NO_2	NH_3
buckled-B ^j	-0.76	-0.90	-4.04	-2.84	-1.96
buckled-B ^a	-1.38	-0.36	-1.79	-2.32	-1.75
β_{12} -B ^{klm}	-1.19	-0.18	-1.17	-1.31	-0.94
χ_3 -B ^{kn}	-0.44		-0.95	-1.80	-1.11
$(\beta_{12} + \chi_3) - B^k$			-2.20	-1.89	-1.13
			-1.93	-2.14	-1.48
Boroph./MoS ₂ ^b	-1.15	-0.64	-1.47	-2.12	-1.52
MoS_2^{ef}	-0.44	-0.33	-0.56	-0.14	-0.16
Graphene ^{cdj}	-0.01	-0.05	-0.03	-0.07	-0.03
Phosphoreneg	-0.32	-0.41	-0.86	-0.62	-0.50
Silicene ^h	-0.18	-0.04	-0.35	-1.37	-0.60
Germanene ⁱ	-0.16	-0.10	-0.51	-1.08	-0.44

- a Ref. [41].
- ^b Ref. [9].
- c Ref. [1].
- d Ref. [2].
- e Ref. [3].
- f Ref. [4].
- h Ref. [6].
- ⁱ Ref. [7].
- ^j Ref. [31]. ^k Ref. [42].
- ¹ Ref. [43].
- m Ref. [38].
- ⁿ Ref. [40].

states (PDOS) of boron atoms (with s and p states represented in light and dark green, respectively) and adsorbed molecules (with s and p states in orange and red, respectively) is shown in Figs. S1(a), S1(b), and S1(c), where the Fermi level is set to zero. A Bader charge analysis was also conducted to quantify charge transfer between the molecules and borophene sheets. Due to spin-polarized calculations, four systems exhibit magnetic behavior: NO on all borophene sheets and NO $_2$ on buckled-B, necessitating the presentation of both spin channels for these cases.

For CO adsorption, hybridization occurs between the p states of the molecule and boron atoms at the Fermi level for α -B, whereas this interaction is negligible for buckled-B and hc-B. In contrast, CO_2 adsorption results in energy levels far from the Fermi level, reflecting its weak interaction with the surface and minimal impact on electronic properties. However, on hc-B, CO_2 adsorption induces a shift from metallic to semiconducting behavior, a notable transformation.

NO adsorption is unique due to its asymmetric density of states across spin channels, resulting in magnetic behavior. The p states of

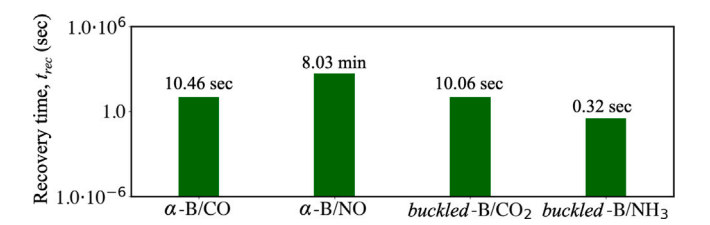


Fig. 8. Recovery times for selected borophene/molecule systems under optimal conditions, highlighting the potential for efficient sensor regeneration.

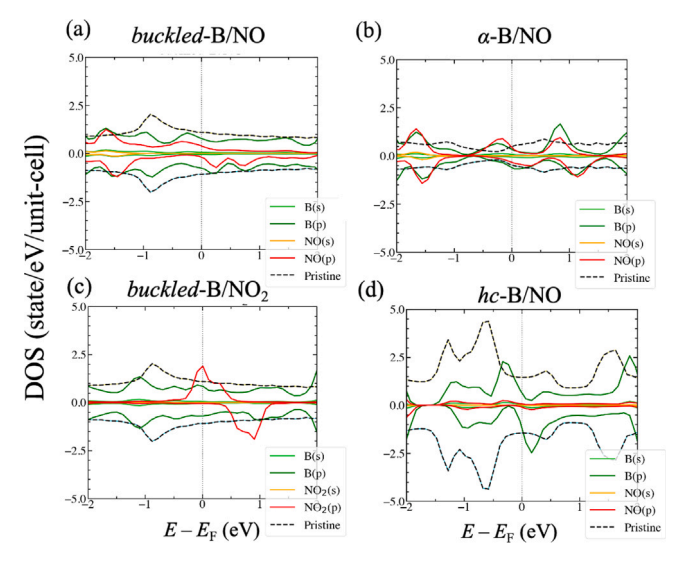


Fig. 9. Density of states (DOS) of pristine borophene sheets and PDOS of magnetic borophene/molecule systems: (a) buckled-B/NO, (b) α -B/NO, (c) buckled-B/NO₂, and (d) hc-B/NO. Red lines represent the molecule's p states, while green lines denote boron p states. Dashed lines correspond to pristine borophene sheets. (For interpretation of the references to color in this figure legend, the reader is referred to the web version of this article.)

NO hybridize with boron p states at the Fermi level, as shown in Figs. 9(a) and 9(b). Furthermore, NO dissociation on hc-B causes a displacement of boron p contributions (see Fig. 9(d)). In the case of NO₂, paramagnetic behavior transitions to nonmagnetic occur upon adsorption, except on buckled-B, where the Fermi level aligns with a peak in the molecule's majority spin density (see Fig. 9(c)). NH₃, however, shows minimal contribution at the Fermi level, with its states located at deeper energy levels.

The Bader charge analysis results are presented in Table 2, where a negative sign indicates that the molecule gains electrons from borophene. Notably, $\mathrm{NH_3}$ is an exception, acting as a donor on <code>buckled-B</code> and <code>hc-B</code>, with a small charge transfer consistent with previous studies [9,38,39,42]. The relationship between charge transfer and adsorption energy is visualized in Fig. 10, demonstrating that stronger interactions correlate with higher charge transfer.

Charge acceptor molecules, such as NO and NO₂, exhibit higher charge transfer, particularly on hc-B, compared to the donor molecule NH₃. Differential charge density plots, shown in Fig. 11, provide further insight into charge redistribution during adsorption. Yellow regions represent charge accumulation, while blue regions indicate depletion. For example, NH₃ on buckled-B (see Fig. 11(a)) shows charge depletion near the molecule, while CO on α -B (see Fig. 11(b)) and NO on α -B (see Fig. 11(c)) demonstrate significant charge accumulation around the molecules. Notably, NO₂ adsorption on hc-B (see Fig. 11(d)) reveals extensive charge redistribution due to its strong interaction.

The influence of adsorption on conductivity is illustrated in Fig. 12, showing the average in-plane conductivity $\sigma = (\sigma_{xx} + \sigma_{yy})/2$ after

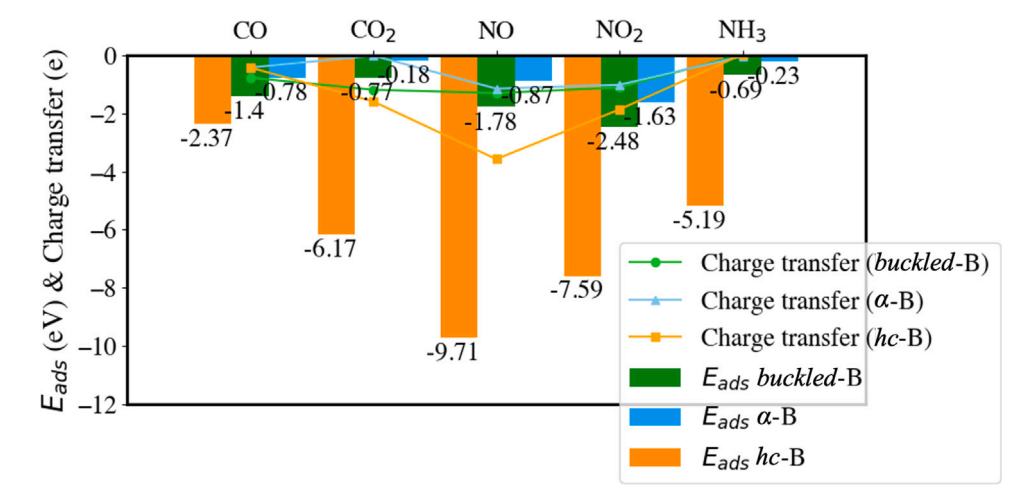


Fig. 10. Adsorption energies (in eV) and charge transfer (in e) for borophene/molecule systems, highlighting the correlation between interaction strength and charge transfer.

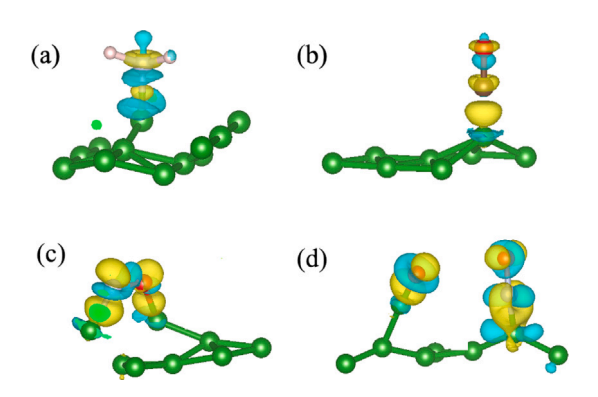


Fig. 11. Differential charge density, $\rho_{\rm Borophene/molecule}(\vec{r}) - \rho_{\rm Borophene}(\vec{r}) - \rho_{\rm molecule}(\vec{r})$, for: (a) buckled-B/NH₃, (b) α-B/CO, (c) α-B/NO, and (d) hc-B/NO₂. Yellow and blue regions indicate charge accumulation and depletion, respectively, with isosurfaces at 0.07 e/Å³. (For interpretation of the references to color in this figure legend, the reader is referred to the web version of this article.)

molecular interaction. Pristine borophene exhibits excellent conductive properties, with conductivity values of $1.35\cdot 10^{20}$ for α -B, $2.85\cdot 10^{20}$ for buckled-B, and $5.24\cdot 10^{19}$ (1/ $\Omega\cdot m\cdot s$) for hc-B. Among the systems studied, buckled-B shows the most significant deviations in conductivity, particularly after NH $_3$ adsorption, while hc-B remains largely unaffected. α -B displays intermediate sensitivity, with notable changes upon CO $_2$ and NO adsorption, making it highly selective for these molecules. Similarly, buckled-B shows strong selectivity for NH $_3$, supported by its favorable recovery time.

3.4. Magnetism

As discussed in Section 3.3, four systems exhibit magnetic properties, a notable deviation from the nonmagnetic behavior of pristine borophene sheets. This suggests that magnetism arises from electron transfer between the borophene layers and specific adsorbed molecules. Spin-polarized calculations for isolated molecules confirmed that most molecules possess a net magnetic moment of zero, except for NO and NO_2 , whose ground states are magnetic, each with a total magnetic moment of 1 $\mu_{\rm B}$.

This magnetic behavior is evident in the PDOS plots (Figs. S1(a), S1(b), and S1(c)), where a broadening of peaks around the Fermi level reflects electron withdrawal from borophene. Interestingly, NO_2 exhibits a transition from paramagnetic behavior in its gaseous state to nonmagnetic behavior upon adsorption on α -B and hc-B, whereas

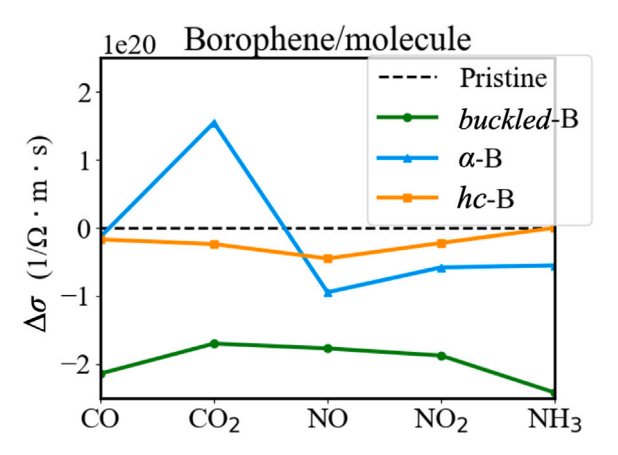


Fig. 12. Changes in conductivity, $\sigma=(\sigma_{xx}+\sigma_{yy})/2$, after molecular adsorption relative to pristine borophene values, highlighting sensitivity and selectivity for specific molecules.

its magnetic properties persist on <code>buckled-B</code>. A similar paramagnetic-to-nonmagnetic transition was reported by Yu et al. [42] for NO and NO₂ adsorption on β_{12} and χ_3 defective borophene. Additionally, Ta et al. [39] observed that NO₂ becomes spin-unpolarized when adsorbed on β_{12} borophene.

This study's spin-polarized calculations reveal that molecular adsorption induces different magnetic moments for the systems analyzed. The total magnetic moments are calculated as 0.46 $\mu_{\rm B}$ for α -B/NO, 0.57 $\mu_{\rm B}$ for buckled-B/NO, 0.39 $\mu_{\rm B}$ for buckled-B/NO₂, and 0.78 $\mu_{\rm B}$ for hc-B/NO. Notably, some boron atoms near the adsorption sites exhibit slight spin polarization.

The charge transfer values for these systems, as shown in Table 2, are among the highest observed in this study, with -1.15, -1.31, -1.11, and -3.58 electrons transferred for α -B/NO, buckled-B/NO, buckled-B/NO, respectively. These substantial charge transfers further highlight the strong interaction between these molecules and borophene. Despite these significant interactions, the total magnetic moments induced by these systems remain relatively small.

4. Summary

In this work, the adsorption of hazardous gas molecules on α -B, buckled-B, and hc-B has been comprehensively studied, focusing on their structural, electronic, and magnetic properties.

Upon adsorption, the CO molecule consistently bonds in a normal orientation to the surface, with the carbon atom directed toward the

borophene layer. In contrast, CO_2 aligns parallel to the substrate, forming bonds exclusively between boron and oxygen atoms. NO undergoes strong chemisorption parallel to the sheets, while NO_2 adsorbs facedown with its oxygen atoms bonded to boron. The NH_3 molecule consistently bonds with its nitrogen atom atop a boron atom.

Compared to other two-dimensional materials, borophene demonstrates high adsorption energies and significant charge transfer, making it a highly effective adsorbent for gas molecules.

Among the three borophene polymorphs, hc-B exhibits the highest adsorption energies. However, this comes at the cost of severe lattice distortion following adsorption, limiting its suitability for gas sensing and making it more appropriate as a gas capturer. To mitigate this drawback, using a metallic substrate that can share electrons with boron may enhance its stability. On the other hand, α -B and buckled-B display moderate adsorption energies, preserving their original structures post-adsorption. These characteristics make α -B and buckled-B more suitable for gas sensing applications, with α -B showing good selectivity for CO $_2$. The gas sensor performance of buckled-B is highly responsive to adsorbed molecules, though its selectivity could benefit from further optimization. Overall, the sensing capabilities improve as the density of vacancies in borophene decreases.

In terms of electronic properties, NO and NO $_2$ exhibit the largest charge transfer with the borophene sheets, acting as strong acceptors and inducing magnetism in the system after adsorption. Notably, the hc-B/CO $_2$ system displays semiconducting behavior, despite the pristine sheet being metallic. Conversely, NH $_3$ acts as a donor, transferring minimal charge to the buckled-B and hc-B sheets.

These findings suggest that 2D borophene holds significant promise as a substrate for gas sensors targeting molecules such as CO_2 and NO , as well as a highly efficient gas capturer for molecules like NO_2 . The strong interactions and large charge transfers between borophene and polar gas molecules underscore its potential as a sensitive adsorbent in gas sensing and capture applications.

CRediT authorship contribution statement

Isabel M. Arias-Camacho: Writing – original draft, Visualization, Validation, Methodology, Investigation, Conceptualization. **Nevill Gonzalez Szwacki:** Writing – review & editing, Supervision, Investigation, Conceptualization.

Declaration of competing interest

The authors declare that they have no known competing financial interests or personal relationships that could have appeared to influence the work reported in this paper.

Acknowledgments

We gratefully acknowledge the Polish high-performance computing infrastructure, PLGrid, for granting access to the LUMI supercomputer, operated by the EuroHPC Joint Undertaking and hosted by CSC (Finland) in collaboration with the LUMI consortium, under project number PLL/2023/05/016755. Additionally, we acknowledge the use of computational resources provided through grant No. GB80-23 at the Interdisciplinary Center for Mathematical and Computational Modelling (ICM), University of Warsaw, Poland.

Appendix A. Supplementary data

Supplementary material related to this article can be found online at https://doi.org/10.1016/j.ssc.2025.115905.

Data availability

Data will be made available on request.

References

- [1] O. Leenaerts, B. Partoens, F.M. Peeters, Adsorption of H₂O, NH₃, CO, NO₂, and NO on graphene: A first-principles study, Phys. Rev. B 77 (2008) 125416, http://dx.doi.org/10.1103/PhysRevB.77.125416.
- [2] Y. Liu, J. Wilcox, CO₂ adsorption on carbon models of organic constituents of gas shale and coal, Environ. Sci. Technol. 45 (2011) 809–814, http://dx.doi.org/ 10.1021/es102700c.
- [3] A. Shokri, N. Salami, Gas sensor based on MoS₂ monolayer, Sensors Actuators
 B: Chem. 236 (2016) 378–385, http://dx.doi.org/10.1016/j.snb.2016.06.033.
- [4] B. Cho, M.G. Hahm, M. Choi, J. Yoon, A.R. Kim, Y.-J. Lee, S.-G. Park, J.-D. Kwon, C.S. Kim, M. Song, Y. Jeong, K.-S. Nam, S. Lee, T.J. Yoo, C.G. Kang, B.H. Lee, H.C. Ko, P.M. Ajayan, D.-H. Kim, Charge-transfer-based gas sensing using atomic-layer MoS₂, Sci. Rep. 5 (2015) 8052, http://dx.doi.org/10.1038/srep08052.
- [5] L. Kou, T. Frauenheim, C. Chen, Phosphorene as a superior gas sensor: Selective adsorption and distinct I–V response, J. Phys. Chem. Lett. 5 (2014) 2675–2681, http://dx.doi.org/10.1021/jz501188k.
- [6] J. wen Feng, Y. jie Liu, H. xia Wang, J. xiang Zhao, Q. hai Cai, X. zhang Wang, Gas adsorption on silicene: A theoretical study, Comput. Mater. Sci. 87 (2014) 218–226, http://dx.doi.org/10.1016/j.commatsci.2014.02.025.
- [7] W. Xia, W. Hu, Z. Li, J. Yang, A first-principles study of gas adsorption on germanene, Phys. Chem. Chem. Phys. 16 (2014) 22495–22498, http://dx.doi. org/10.1039/C4CP03292F.
- [8] P. Kumar, G. Singh, R. Bahadur, Z. Li, X. Zhang, C. Sathish, M.R. Benzigar, T. Kim Anh Tran, N.T. Padmanabhan, S. Radhakrishnan, J.C. Janardhanan, C. Ann Biji, A. Jini Mathews, H. John, E. Tavakkoli, R. Murugavel, S. Roy, P.M. Ajayan, A. Vinu, The rise of borophene, Prog. Mater. Sci. 146 (2024) 101331, http://dx.doi.org/10.1016/j.pmatsci.2024.101331.
- [9] J. Shen, Z. Yang, Y. Wang, L.-C. Xu, R. Liu, X. Liu, The gas sensing performance of borophene/MoS₂ heterostructure, Appl. Surf. Sci. 504 (2020) 144412, http: //dx.doi.org/10.1016/j.apsusc.2019.144412.
- [10] H. Tang, S. Ismail-Beigi, Novel precursors for boron nanotubes: The competition of two-center and three-center bonding in boron sheets, Phys. Rev. Lett. 99 (2007) 115501, http://dx.doi.org/10.1103/PhysRevLett.99.115501.
- [11] A.J. Mannix, X.-F. Zhou, B. Kiraly, J.D. Wood, D. Alducin, B.D. Myers, X. Liu, B.L. Fischer, U. Santiago, J.R. Guest, et al., Synthesis of borophenes: Anisotropic, two-dimensional boron polymorphs, Science 350 (2015) 1513–1516.
- [12] E.S. Penev, S. Bhowmick, A. Sadrzadeh, B.I. Yakobson, Polymorphism of two-dimensional boron, Nano Lett. 12 (2012) 2441–2445.
- [13] N. Gonzalez Szwacki, Boron fullerenes: A first-principles study, Nanoscale Res. Lett. 3 (2) (2007) http://dx.doi.org/10.1007/s11671-007-9113-1.
- [14] Y. Zenitani, J. Akimitsu, J. Nagamatsu, N. Nakagawa, T. Muranaka, Super-conductivity at 39K in magnesium diboride, Nature 410 (2001) 63–64, http://dx.doi.org/10.1038/35065039.
- [15] W. Li, L. Kong, C. Chen, J. Gou, S. Sheng, W. Zhang, H. Li, L. Chen, P. Cheng, K. Wu, Experimental realization of honeycomb borophene, Sci. Bull. 63 (2018) 282–286.
- [16] L.Z. Zhang, Q.B. Yan, S.X. Du, G. Su, H.J. Gao, Boron sheet adsorbed on metal surfaces: structures and electronic properties, Phys. Chem. C 116 (2012) 18202–18206.
- [17] D. John, B. Nharangatt, R. Chatanathodi, Stabilizing honeycomb borophene by metal decoration: a computational study, J. Mater. Chem. C 7 (2019) 11493–11499.
- [18] J.P. Perdew, K. Burke, M. Ernzerhof, Generalized gradient approximation made simple, Phys. Rev. Lett. 77 (1996) 3865–3868, http://dx.doi.org/10.1103/ PhysRevLett.77.3865.
- [19] P.E. Blöchl, Projector augmented-wave method, Phys. Rev. B 50 (1994) 17953–17979, http://dx.doi.org/10.1103/PhysRevB.50.17953.
- [20] P. Giannozzi, S. Baroni, N. Bonini, M. Calandra, R. Car, C. Cavazzoni, D. Ceresoli, G.L. Chiarotti, M. Cococcioni, I. Dabo, A.D. Corso, S. de Gironcoli, S. Fabris, G. Fratesi, R. Gebauer, U. Gerstmann, C. Gougoussis, A. Kokalj, M. Lazzeri, L. Martin-Samos, N. Marzari, F. Mauri, R. Mazzarello, S. Paolini, A. Pasquarello, L. Paulatto, C. Sbraccia, S. Scandolo, G. Sclauzero, A.P. Seitsonen, A. Smogunov, P. Umari, R.M. Wentzcovitch, QUANTUM ESPRESSO: a modular and open-source software project for quantum simulations of materials, J. Phys.: Condens. Matter. 21 (39) (2009) 395502. http://dx.doi.org/10.1088/0953-8984/21/39/395502.
- [21] S. Grimme, J. Antony, S. Ehrlich, H. Krieg, A consistent and accurate ab initio parametrization of density functional dispersion correction (DFT-D) for the 94 elements H-Pu, J. Chem. Phys. 132 (2010) 154104, http://dx.doi.org/10.1063/ 1.3382344.
- [22] X. Zhang, Z. Chen, D. Chen, H. Cui, J. Tang, Adsorption behaviour of SO₂ and SOF₂ gas on Rh-doped BNNT: a DFT study, Mol. Phys. 118 (2020) e1580394, http://dx.doi.org/10.1080/00268976.2019.1580394.
- [23] H. Cui, X. Zhang, G. Zhang, J. Tang, Pd-doped MoS₂ monolayer: A promising candidate for DGA in transformer oil based on DFT method, Appl. Surf. Sci. 470 (2019) 1035–1042, http://dx.doi.org/10.1016/j.apsusc.2018.11.230.
- [24] D. Chen, X. Zhang, J. Tang, H. Cui, Y. Li, Noble metal (Pt or Au)-doped monolayer MoS_2 as a promising adsorbent and gas-sensing material to SO_2 , SOF_2 and SO_2F_2 : a DFT study, Appl. Phys. A 124 (2018) 194, http://dx.doi.org/10. 1007/s00339-018-1629-y.

- [25] A. Shukla, G. Sharma, S. Krishnamurty, Functionalized Mo₂BX₂ (X=H, OH, O) MBenes as a promising sensor, capturer and storage material for environmentally toxic gases: A case study of 1T and 2H phase, Appl. Surf. Sci. 615 (2023) 156299, http://dx.doi.org/10.1016/j.apsusc.2022.156299.
- [26] G. Henkelman, A. Arnaldsson, H. Jónsson, A fast and robust algorithm for Bader decomposition of charge density, Comput. Mater. Sci. 36 (3) (2006) 354–360, http://dx.doi.org/10.1016/j.commatsci.2005.04.010.
- [27] G.K. Madsen, J. Carrete, M.J. Verstraete, BoltzTraP2, a program for interpolating band structures and calculating semi-classical transport coefficients, Comput. Phys. Comm. 231 (2018) 140–145, http://dx.doi.org/10.1016/j.cpc.2018.05.010.
- [28] S.H. Mir, V.K. Yadav, J.K. Singh, Recent advances in the carrier mobility of two-dimensional materials: A theoretical perspective, ACS Omega 5 (24) (2020) 14203–14211, http://dx.doi.org/10.1021/acsomega.0c01676.
- [29] K. Momma, F. Izumi, VESTA 3 for three-dimensional visualization of crystal, volumetric and morphology data, J. Appl. Crystallogr. 44 (6) (2011) 1272–1276, http://dx.doi.org/10.1107/S0021889811038970.
- [30] K.C. Lau, R. Pandey, Stability and electronic properties of atomisticallyengineered 2D boron sheets, J. Phys. Chem. C 111 (2007) 2906.
- [31] T. Liu, Y. Chen, M. Zhang, L. Yuan, C. Zhang, J. Wang, J. Fan, A first-principles study of gas molecule adsorption on borophene, AIP Adv. 7 (2017) 125007.
- [32] X.-F. Zhou, X. Dong, A.R. Oganov, Q. Zhu, Y. Tian, H.-T. Wang, Semimetallic two-dimensional boron allotrope with massless Dirac Fermions, Phys. Rev. Lett. 112 (2014) 085502, http://dx.doi.org/10.1103/PhysRevLett.112.085502.
- [33] K.C. Lau, Y.K. Yap, R. Pandey, Boron and boron carbide materials: Nanostructures and crystalline solids, in: B-C-N Nanotubes and Related Nanostructures, Springer New York, 2009, pp. 271–291, http://dx.doi.org/10.1007/9781441900869_9.
- [34] B. Peng, H. Zhang, H. Shao, Y. Xu, R. Zhang, H. Zhu, The electronic, optical, and thermodynamic properties of borophene from first-principles calculations, J. Mater. Chem. C 4 (2016) 3592–3598, http://dx.doi.org/10.1039/C6TC00115G.

- [35] J.C. Alvarez-Quiceno, R.H. Miwa, G.M. Dalpian, A. Fazzio, Oxidation of free-standing and supported borophene, 2D Mater. 4 (2017) 025025, http://dx.doi.org/10.1088/2053-1583/aa55b6.
- [36] X. Zhang, X. Pu, Y. Chen, X. Gu, Di Xu, S. Zhang, Characterization of high concentration Ga-doped ZnO nano-powders prepared by sol-gel combustion, Mater. Lett. 112 (2013) 129–132, http://dx.doi.org/10.1016/j.matlet.2013.08. 096
- [37] H. ping Zhang, X. gang Luo, X. yang Lin, X. Lu, Y. Leng, H. tao Song, Density functional theory calculations on the adsorption of formaldehyde and other harmful gases on pure, Ti-doped, or N-doped graphene sheets, Appl. Surf. Sci. 283 (2013) 559–565, http://dx.doi.org/10.1016/j.apsusc.2013.06.145.
- [38] C.-S. Huang, A. Murat, V. Babar, E. Montes, U. Schwingenschlögl, Adsorption of the gas molecules NH₃, NO, NO₂, and CO on borophene, J. Phys. Chem. C 122 (2018) 14665–14670, http://dx.doi.org/10.1021/acs.jpcc.8b03811.
- [39] L.T. Ta, I. Hamada, Y. Morikawa, V.A. Dinh, Adsorption of toxic gases on borophene: surface deformation links to chemisorptions, RSC Adv. 11 (2021) 18279–18287, http://dx.doi.org/10.1039/D1RA02738G.
- [40] J.-X. Duan, Y.-P. Tian, C.-B. Wang, L.-L. Zhang, First-principles study of χ₃-borophene as a candidate for gas sensing and the removal of harmful gases, Nanomaterials 13 (2023) 2117, http://dx.doi.org/10.3390/nano13142117.
- [41] V. Shukla, J. Wärnå, N.K. Jena, A. Grigoriev, R. Ahuja, Toward the realization of 2D borophene based gas sensor, J. Phys. Chem. C 121 (2017) 26869–26876, http://dx.doi.org/10.1021/acs.jpcc.7b09552.
- [42] X. Yu, F. Chen, Z. Yu, Y. Li, Computational study of borophene with line defects as sensors for nitrogen-containing gas molecules, ACS Appl. Nano Mater. 3 (2020) 9961–9968, http://dx.doi.org/10.1021/acsanm.0c01975.
- [43] X. Tan, H.A. Tahini, S.C. Smith, Borophene as a promising material for charge-modulated switchable CO₂ capture, ACS Appl. Mater. Interfaces 9 (2017) 19825–19830, http://dx.doi.org/10.1021/acsami.7b03676.

3.3 PAPER II: Exploring the Structural, Electronic, Magnetic, and Transport Properties of 2D Cr, Fe, and Zr Monoborides

Although at an early stage of investigation, transition metal borides, MBenes, with their wide range of possible two-dimensional structures, are regarded as promising materials due to their challenging properties and possibilities of applications. The introduction of 3d electrons coming from the transition metals, confer not only stability but also a magnetic character that convert them, in some cases, in robust magnets. In this article, the density functional theory constitutes the framework for the study of the structural, electronic, magnetic and transport properties of stoichiometric M₂B₂ compounds (with M = Cr, Fe and Zr), which can adopt either orthorhombic or hexagonal structures (ortho- and hex-MBenes respectively). To ensure the stability and robustness of the selected MBenes, an evaluation of their cohesive energies together with the phonon dispersion has been performed, confirming that all of them are stable and can be grown under certain conditions. In principle, the orthorhombic Cr and Fe-MBenes are more energetically favorable while the hexagonal form of Zr₂B₂ prevails, but the results for both phases are so close in cohesive energies that, at high temperatures, ortho-MBenes might transform into hex-MBenes. Another desired quality of MBenes is their metallicity, proven by all their electronic band structures, with partially occupied bands crossing the Fermi level for both spin channels. Their corresponding densities of states reveal the predominance of d orbitals of the metals at this energy level. In addition, the orthorhombic MBenes exhibit anisotropy of the conductivity tensor, differently from the hexagonal MBenes, which are isotropic in this sense, but in any case they reach high values that make these materials valuable as electronic nanodevices. To conclude with this study, the critical temperature (Curie or Néel temperature), T_c , has been calculated in the mean-field approximation by means of the energy difference between the ferromagnetic and antiferromagnetic configurations, describing ortho-Fe₂B₂ as a room-temperature robust magnet.

Now that things are clearer, the results of this paper open the possibility of going further in research, considering MBenes as potential candidates for sensing and catalytic processes.





Article

Exploring the Structural, Electronic, Magnetic, and Transport Properties of 2D Cr, Fe, and Zr Monoborides

Isabel M. Arias-Camacho D and Nevill Gonzalez Szwacki *D

Faculty of Physics, University of Warsaw, Pasteura 5, PL-02093 Warsaw, Poland; isabel.arias@fuw.edu.pl * Correspondence: gonz@fuw.edu.pl; Tel.: +48-22-55-32-797

Abstract: Compared to other 2D materials, MBenes are at an early stage of investigation in terms of both experimental and theoretical approaches. However, their wide range of possible 2D structures leads to novel and challenging properties and consequent applications. From all the possible stoichiometries, we performed a theoretical study of orthorhombic and hexagonal M_2B_2 MBenes within the framework of density functional theory. We found that both symmetries of Cr_2B_2 , Fe_2B_2 , and Zr_2B_2 show metallic behavior and could be grown under certain conditions as they were demonstrated to be dynamically stable. Moreover, the values of the magnetic moment observed, in specific ferromagnetic cases exceeding $2.5~\mu_B/M_2B_2$, make them suitable as robust 2D magnets. Our findings represent an important step in the understanding of MBenes and open several windows to future research in fields like energy conversion and storage, sensing, catalysis, biochemistry, and nanotechnology, among others.

Keywords: transition metal borides; MBenes; energy conversion and storage; 2D magnets



Citation: Arias-Camacho, I.M.; Gonzalez Szwacki, N. Exploring the Structural, Electronic, Magnetic, and Transport Properties of 2D Cr, Fe, and Zr Monoborides. *Materials* **2023**, *16*, 5104. https://doi.org/10.3390/ ma16145104

Academic Editor: Dominique de Caro

Received: 31 May 2023 Revised: 12 July 2023 Accepted: 16 July 2023 Published: 20 July 2023



Copyright: © 2023 by the authors. Licensee MDPI, Basel, Switzerland. This article is an open access article distributed under the terms and conditions of the Creative Commons Attribution (CC BY) license (https://creativecommons.org/licenses/by/4.0/).

1. Introduction

Transition metal borides (MBs) can be regarded as new efficient earth-abundant materials for energy storage/conversion systems, including metal-ion batteries, metal-air batteries, capacitors, oxygen evolution reactions (OERs), and other electrochemical fields [1]. Single-crystalline ternary transition metal borides (MAB phases, where M are transition metals, A are *p*-block elements, and B is boron) were first reported in 2015 by Ade and Hillebrecht and recently gained attention as promising layered materials [2]. Their two-dimensional counterparts (MBenes) can be obtained from the chemical exfoliation of the MAB phases. It is noted that MBenes possess different stoichiometries and variable modes of 2D layer sandwiching compared to the corresponding MXenes [3].

The MAB phases with M and B with one-to-one stoichiometry are orthorhombic and hexagonal crystals with the chemical formulae of MAB and M₂AB₂ [3]. Experimentally, orthorhombic MAlB (M = Mo and W), M₂AlB₂ (M = Cr, Mn, and Fe), and hexagonal Ti₂InB₂ [4] have already been synthesized. The MAB phases are promising candidates for obtaining new 2D MBenes. A 2D MoB was reported to have been obtained by the partial etching of Mo₂AlB₂ phases through the deintercalation of Al layers from the ordered stacking faults region [5,6]. Selectively HCl-etching Al layers from Cr₂AlB₂ yielded bulk-layered CrB nanosheets [7,8]. Removal of the indium layer through the high-temperature dealloying of Ti₂InB₂ yielded a bulk-layered TiB structure [4]. To date, however, the synthesis of individual single-layer MBenes has not been realized.

The present work concerns computational studies of the structural, energetic, electronic, and transport properties of selected MBene compounds with M = Cr, Fe, and Zr. Some of the investigated 2D structures have been proven to be stable in previous studies [9]. The studied MBenes present either an orthorhombic structure (ortho-MBenes) with Pmma (no. 51) space group symmetry or a hexagonal structure (hex-MBenes) with P6/mmm (no. 191) space group symmetry. In the Pmma structures, each atom is surrounded by

Materials 2023, 16, 5104 2 of 10

six neighbors, and the buckled bilayers are sandwiched between transition metal (TM) layers. On the other hand, in the P6/mmm structures, the honeycomb-type boron layer is sandwiched between two TM layers on both sides, and every TM atom is located above or below the centroid of the honeycomb structure.

The bulk counterparts of our metal monoboride nanosheets are the ferromagnetic α and β modifications of FeB and the nonmagnetic CrB and ZrB compounds, all widely studied, both experimentally and theoretically [10–12]. The structure of α -FeB is debatable [12], whereas β -FeB and CrB are orthorhombic crystals with Pnma (no. 62) and Cmcm (no. 63) space group symmetries, respectively. The ZrB solid is rock-salt-structured and crystallizes in a cubic $Fm\overline{3}m$ (no. 225) space group symmetry. The β -FeB and CrB solids exhibit very interesting structures since both enclose boron double-chain (BDC) stripes which are very common motifs of all-boron nanostructures [13,14].

The purpose of this work is to understand the origin of the physical properties of MBene (M = Cr, Fe, and Zr) compounds, as well as to identify features that may affect the transport properties of these compounds.

2. Computational Approach

First-principles spin-polarized calculations were performed within the framework of density functional theory (DFT) within the generalized gradient corrected approximation of Perdew-Burke-Ernzerhof (PBE) [15] for the exchange-correlation functional, using projector plane-wave (PAW) pseudopotentials [16] as implemented in the Quantum ESPRESSO (QE) suite of codes [17]. Every unit cell consists of two atoms of boron and two atoms of the TM. To avoid interactions between adjacent MBenes, we considered an empty space of thickness 15 Å along the normal direction. Optimized geometries were reached allowing the unit cell shape, volume, and the ions to relax until the residual forces on the atoms were less than 0.3 meV/Å and the total energy (E_{tot}) convergence was set to 10^{-5} Ry. We expanded the electronic wave functions and charge density in plane-wave basis sets with an energy cutoff of 70 and 700 Ry, respectively, while the Γ -centered k-point grid in the Brillouin zone, in the Monkhorst–Pack scheme, was set to $12 \times 12 \times 1$ for the geometry optimization and $24 \times 24 \times 1$ for the DOS calculations, with Gaussian smearing of 0.02 Ry; these values ensure the accuracy of E_{tot} . All the structures were considered to be initially spin-polarized and, in order to determine the magnetic ground states of each, we calculated two magnetic configurations—one ferromagnetic (FM) and one antiferromagnetic (AFM)—to reach the most energetically favorable.

For the structural characterization of the studied systems, an important descriptor we use is the cohesive energy per atom (E_{coh}); that is, the difference in energy between E_{tot} of the compound and the sum of the total energies of the isolated atoms,

$$E_{coh} = (E[M_2B_2] - n_B E[B] - n_M E[M]) / (n_B + n_M),$$
(1)

which means the released energy when a compound dissociates into isolated free atoms, where M represents the TM atom, $E[M_2B_2]$ is the E_{tot} of the MBene, E[B] and E[M] are the total energies of the isolated atoms (B and TM atoms), and n_B and n_M are the numbers of boron and TM atoms per unit cell, respectively, directly obtained from the spin-polarized calculations. The phonon-dispersion curves were obtained by means of density functional perturbation theory (DFPT), calculating the dynamical matrices in the linear response approach on a q-point grid of $4 \times 4 \times 1$. The transport integrals were computed using Boltzmann transport theory and a constant scattering rate model [18]. The charge transfer was obtained by Bader analysis [19] and all the visualizations were performed using the Visualization for Electronic and STructural Analysis (VESTA) software [20].

3. Results and Discussion

3.1. Structure and Stability

Since boron is electron deficient, it is expected that a mixture with TM atoms will lead to stable structures. As mentioned above, among all the possible MBenes, we focused on

Materials 2023, 16, 5104 3 of 10

those which possess either orthorhombic or hexagonal M_2B_2 structures, which are shown in Figure 1. After a full structural optimization, we found that the unit cells of ortho-MBenes became almost rectangular with a>b when the TM was Fe or Cr (a/b is 1.005 and 1.013 for chromium and iron, respectively), whereas a< b for ortho- Zr_2B_2 (a/b=0.94). All the cell parameters are described in Table 1 and compared with other literature reports.

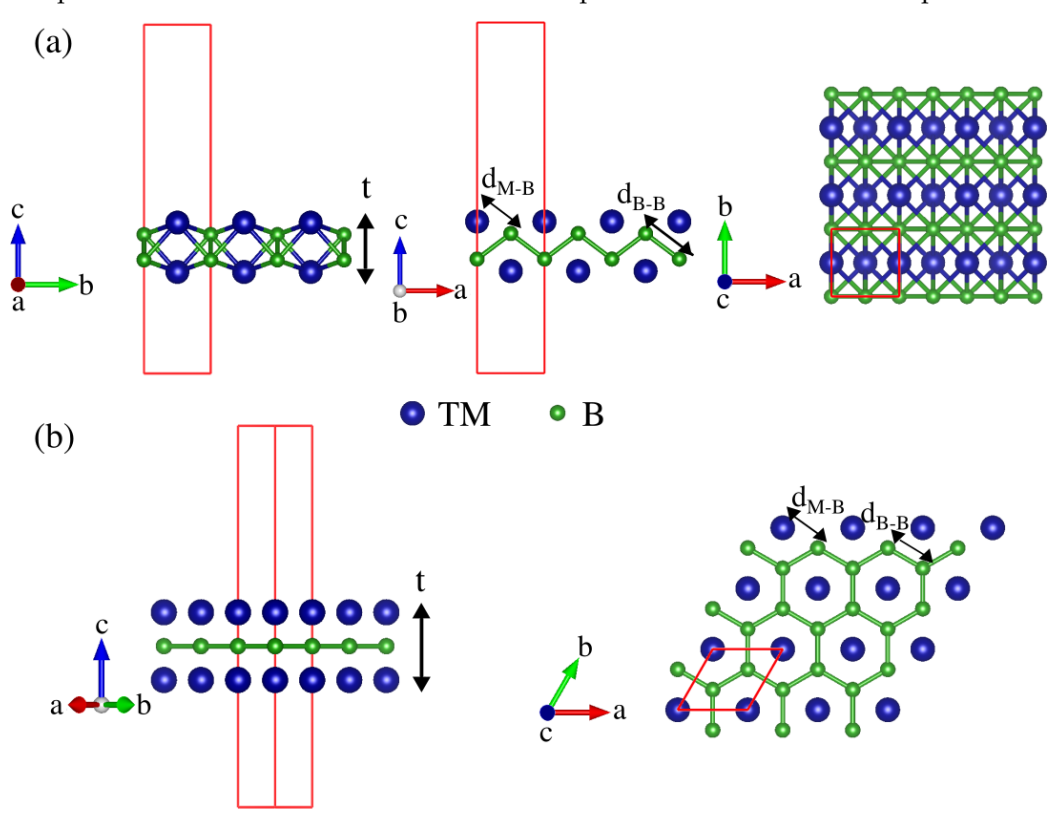


Figure 1. Side (**left**) and top (**right**) views of the (**a**) ortho-MBene and (**b**) hex-MBene structures of M_2B_2 corresponding to *Pmma* and *P6/mmm* symmetries, respectively. The unit cells used in the calculations are shown in red.

The E_{coh} and phonon dispersion curves are good indicators of the bond strength and dynamical stability of the materials. The dynamical matrix gives us the frequency $\omega(\mathbf{q})$ whose square is negative when there exist instabilities for a particular phonon mode with \mathbf{q} (imaginary frequencies), which means that this mode does not generate the restoring force needed by the lattice vibrations and could take the structure away from the original configuration. The results of our calculations are summarized in Table 2 and in Figure 2.

Table 1. Lattice parameters (a and b), boron–boron distance (d_{B-B}), TM–boron distance (d_{M-B}), and thickness of the 2D structure (t) for Cr_2B_2 , Fe_2B_2 , and Zr_2B_2 . The d_{B-B} , d_{M-B} , and t parameters are defined in Figure 1. All the values are in Angstroms (Å) and, for comparison purposes, the data in brackets are taken from the literature.

	Cr_2B_2		Fe_2B_2		$\mathbf{Zr}_2\mathbf{B}_2$	
	Pmma	P6/mmm	Pmma	P6/mmm	Pmma	P6/mmm
а	2.885 (2.860 ⁴) (2.930 ⁵)	2.919 (2.921 ¹) (2.926 ²)	2.823 (2.800 ⁴) (2.770 ⁵)	2.913	3.084 (3.07 ⁷)	3.159 (3.144 ¹) (3.160 ²) (3.134 ³)

Materials **2023**, 16, 5104 4 of 10

Tal	1 1		-		
13	n	Δ		1 1	nnt

	Cr_2B_2		Fe_2B_2		$\mathbf{Z}\mathbf{r}_{2}\mathbf{B}_{2}$	
	2.870	2.919	2.787	2.913	3.281	3.159
b	$(2.850^{\ 4})$ $(2.870^{\ 5})$	(2.921 ¹) (2.926 ²)	(2.680 ⁴) (2.820 ⁵)		(3.27 ⁷)	(3.144^{1}) (3.160^{2}) (3.134^{3})
	1.810	1.685	1.813	1.682	1.721	1.824
$d_{\mathrm{B-B}}$		$(1.689^{\ 2})$			(1.71^{7})	(1.825^{2}) (1.891^{3})
$d_{ ext{M-B}}$	2.10 (2.11 ⁴)	2.15	2.04 (2.05 ⁴)	2.15	2.46 (2.43 ⁷)	2.49 (2.49 ³)
	2.122	2.662	2.134	2.680	2.817	3.382
t		(2.651 ¹) (2.639 ²)	(2.13 ⁶)		(2.84^{7})	(3.391 ¹) (3.380 ²) (3.385 ³)

¹ Ref. [21]. ² Ref. [22]. ³ Ref. [23]. ⁴ Ref. [24]. ⁵ Ref. [25]. ⁶ Ref. [26]. ⁷ Ref. [27].

Table 2. Cohesive energy (E_{coh}), highest frequency at the Γ point (ν), and charge transfer from TM to B (Δq) for Cr₂B₂, Fe₂B₂, and Zr₂B₂. The values in bold are to highlight the structure with higher E_{coh} .

	Cr_2B_2		Fe_2B_2		$\mathbf{Zr}_2\mathbf{B}_2$	
	Pmma	P6/mmm	Pmma	P6/mmm	Pmma	P6/mmm
E_{coh} (eV)	6.222	6.201	6.901	6.830	8.050	8.087
ν (cm ⁻¹)	762.45	1003.50	772.74	976.01	928.02	744.12
Δq (e)	-0.76	-0.61	-0.37	-0.40	-1.17	-0.86

All our MBenes exhibit large E_{coh} values ranging from 6.222 to 8.087 eV, as shown in Table 2, which means they present strong internal binding and good stability. Moreover, our results are in good agreement with previous works. For instance, Zhang et al. [28] obtained a value of 6.30 eV for ortho- Cr_2B_2 . For the sake of comparison, we also computed the diamond structure of carbon using the same optimization parameters, resulting in a E_{coh} of 7.757 eV, which is a comparable value to that of other theoretical and experimental reports [29]. Interestingly, other studies have noted a dependence of the structure stability with the atomic mass of the TM [22], a fact that is also reproduced in our results, hex- Zr_2B_2 being the MBene with the highest E_{coh} (8.087 eV). From a structural point of view, Cr_2B_2 and Fe_2B_2 prefer to adopt orthorhombic structures, whereas Zr_2B_2 accommodates better to the hexagonal one. However, the orthorhombic and hexagonal phases are close in energy (within some tens of meV), and, according to recent reports [9,30], ortho-MBenes might transform into hex-MBenes at high temperatures.

On the one hand, calculations of the phonon frequencies reveal that some small imaginary frequencies appear in the surroundings of the Γ point for orthorhombic Cr_2B_2 and Zr_2B_2 as shown on the left panel of Figure 2. On the other hand, none of the hexagonal structures have imaginary frequencies as shown on the right panel of Figure 2. Similar dynamical instabilities as for ortho-MBenes have been reported for freestanding 2D structures in previous works [25,31]. These studies have concluded that the out-of-plane acoustic mode, ZA, is responsible for such instabilities, which are against the long-wavelength transversal waves that could be fixed by defects like grain boundaries or ripples [32].

The highest values of the frequencies at the Γ -point are collected in Table 2. All the frequencies are higher than 740 cm $^{-1}$. Starting with the orthorhombic structures, the highest optical frequency at Γ -point increases with the atomic number of the TM atom; that is, Cr, Fe, and Zr, in that order. These results are very close to those found in the literature [24]. Since the optical frequency is an indicator of the bond strength, Zr_2B_2 is more stable than Cr_2B_2 and Fe_2B_2 . The trend is, however, the opposite for hex-mBenes, meaning that the

Materials 2023, 16, 5104 5 of 10

highest frequency at the Γ -point corresponds to the TM atom which has the smallest atomic number, in this case Cr, and decreases for Fe and Zr. We can conclude that the studied MBenes are stable and could be grown experimentally under certain conditions.

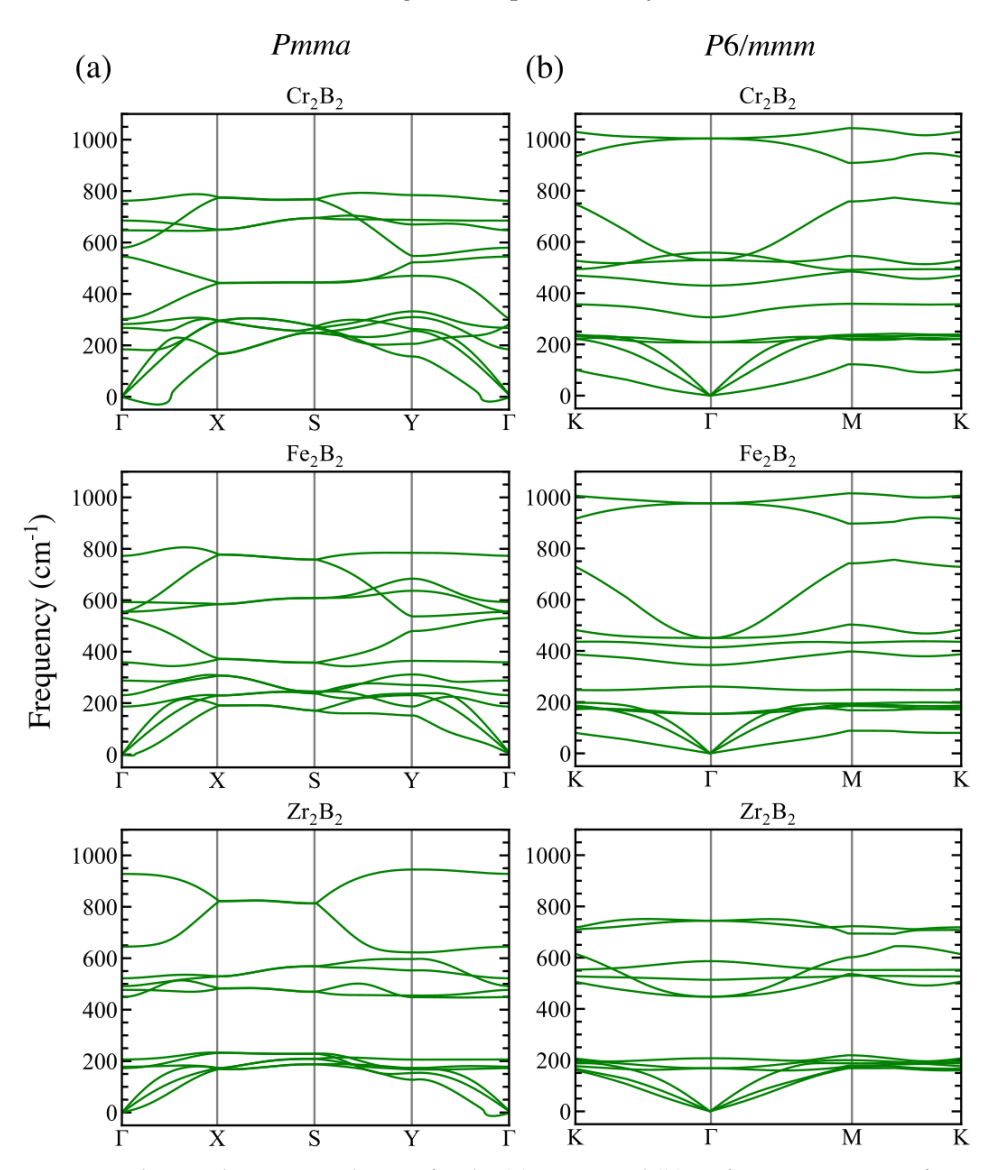


Figure 2. Phonon dispersion relations for the (a) Pmma and (b) P6/mmm structures of Cr_2B_2 , Fe_2B_2 , and Zr_2B_2 .

3.2. Electronic Properties

To understand the electronic behavior of the MBenes involved in our study, we calculated the spin-polarized band structure, the density of states (DOS), and the projected density of states (PDOS) for the studied systems. The results of these calculations are shown in Figures 3 and 4 for ortho-MBenes and hex-MBenes, respectively. Looking at the band structure and DOS, we may conclude that there are no band gaps between the valence band (VB) and the conduction band (CB) for any of the studied structures, which means that all the systems are metallic with partially occupied bands crossing the Fermi level (for the majority and the minority spin channels). This metallic character of the pristine MBenes has also been reported in other works [33]. In all cases, the p orbitals of boron are deep in energy (ranging from -8 to -2 eV approximately) and, in the orthorhombic structures, partially hybridize with the d orbitals of the TM. Near the Fermi level, the PDOS for both symmetries of Cr_2B_2 and Fe_2B_2 is dominated by the d orbitals of Cr and Cr and Cr respectively (see the right panels of (a) and (b) in Figures 3 and 4). Whereas, hybridization between

Materials 2023, 16, 5104 6 of 10

the p and d orbitals of Zr occurs at the Fermi level of Zr_2B_2 (see the right panels of (c) in Figures 3 and 4). The contribution of the majority states at the Fermi level of ortho- Fe_2B_2 is very small, whereas an equal contribution of the minority and majority states is observed in hex- Fe_2B_2 and also in both symmetries of Zr_2B_2 . Finally, the contribution of the majority states is larger than that of the minority states at the Fermi level for Cr_2B_2 .

According to our Bader analysis, the charge transfer, Δq , always occurs from the TMs to the boron atoms. This is shown in Table 2 where we present the values of Δq for all the studied cases. The obtained values are in agreement with other reports (e.g., $\Delta q = -0.34e$ for ortho-Fe₂B₂, as reported in ref. [26]). In general, considering both the *Pmma* and *P6/mmm* structures, the largest charge transfer occurs between Zr and B, whereas Fe is the TM for which the charge transfer to B is the smallest one.

The conductivity results are shown in Figure 5. They reveal anisotropy of the conductivity tensor for the ortho-MBenes, especially for the case of ortho- Zr_2B_2 for which the direction perpendicular to the BDC is clearly the preferred one, whereas for ortho- Fe_2B_2 , the conductivity is higher along the BDC. On the other hand, the hex-MBenes are isotropic with respect to conductivity. It is also worth highlighting that the orthorhombic Fe_2B_2 and Zr_2B_2 present the highest conductivity values among all the studied cases.

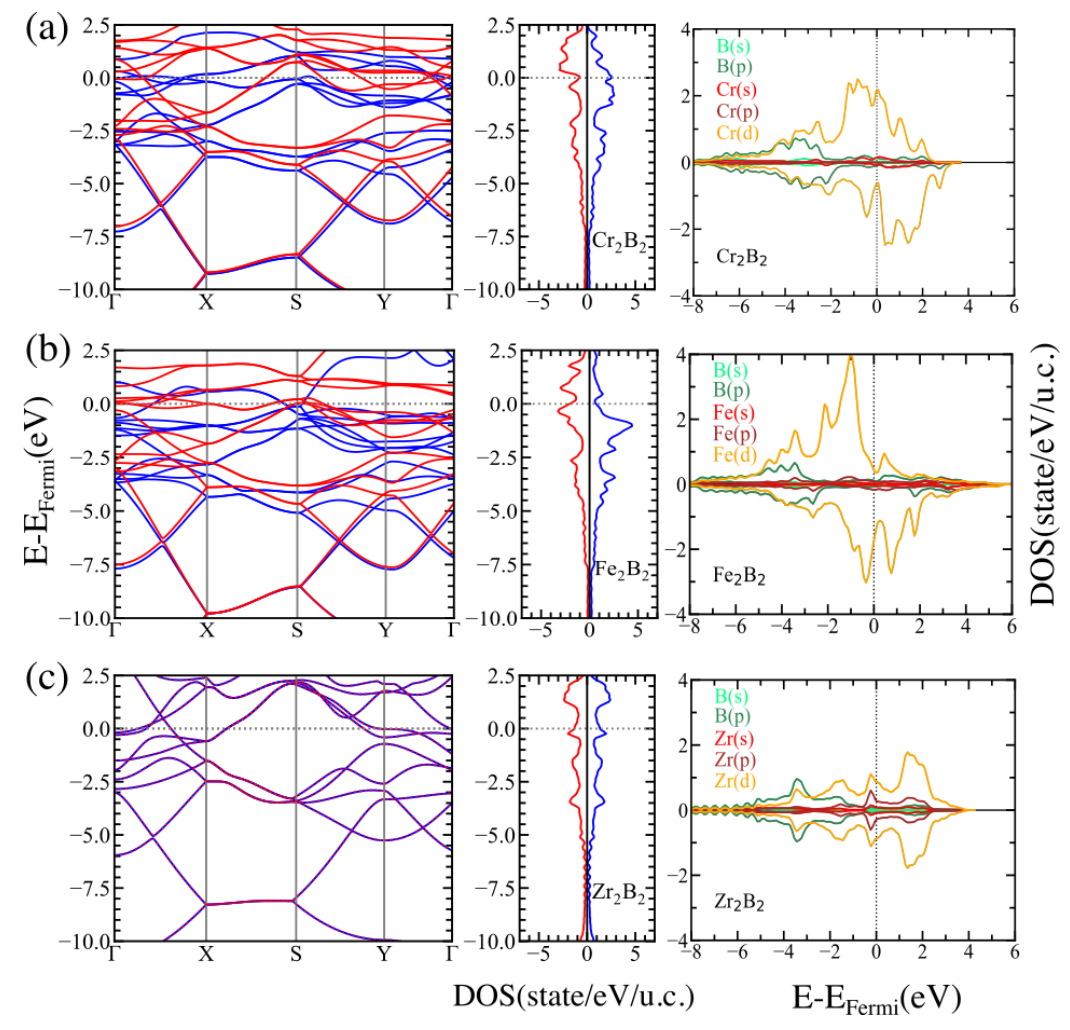


Figure 3. Electronic band structure (**left**) and DOS (**center**) for the majority (blue) and minority (red) spin states, and orbital-resolved PDOS (**right**) for the *Pmma* structures of (**a**) Cr_2B_2 , (**b**) Fe_2B_2 , and (**c**) Zr_2B_2 .

Materials 2023, 16, 5104 7 of 10

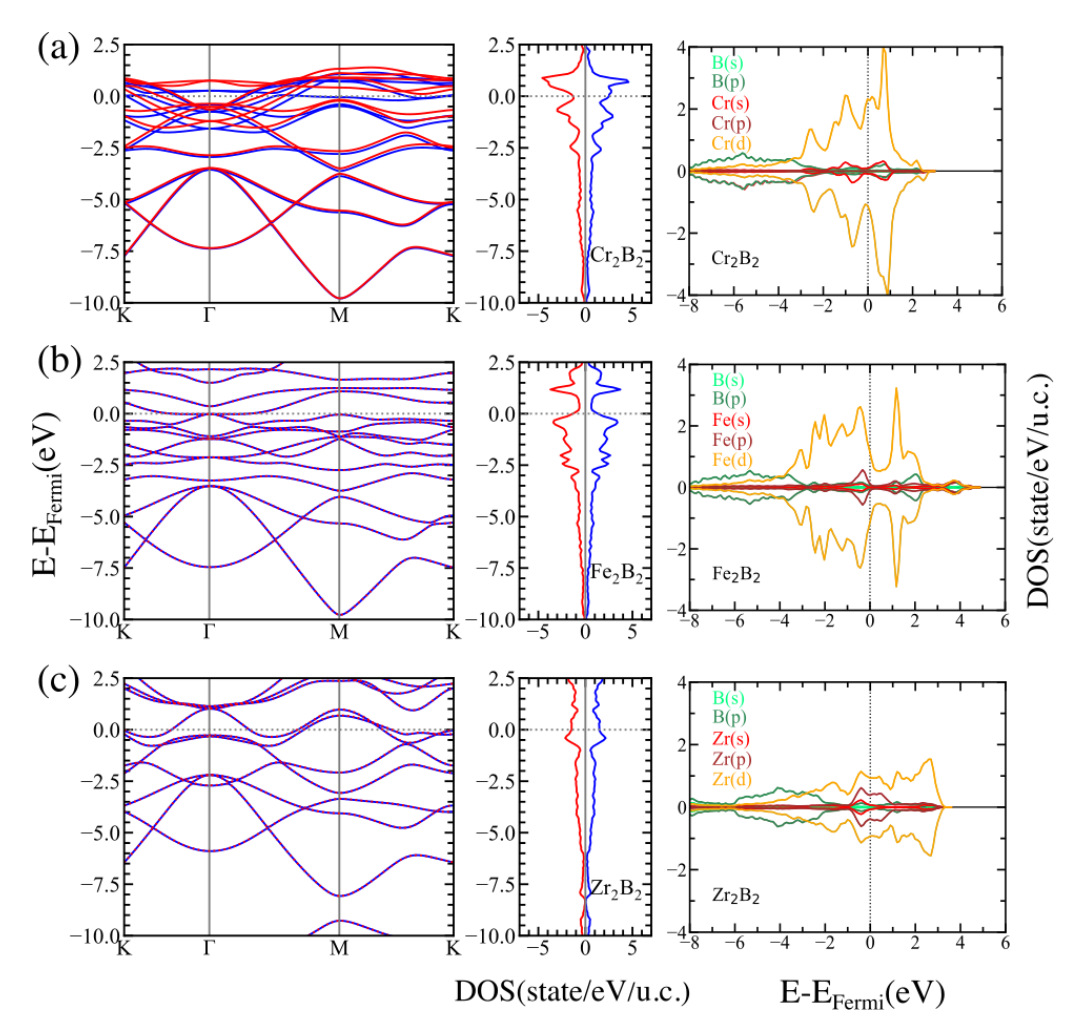


Figure 4. Electronic band structure and DOS for the majority (blue) and minority (red) spins, and orbital-resolved projected density of states (PDOS) for the P6/mmm structures of (a) Cr_2B_2 , (b) Fe_2B_2 , and (c) Zr_2B_2 .

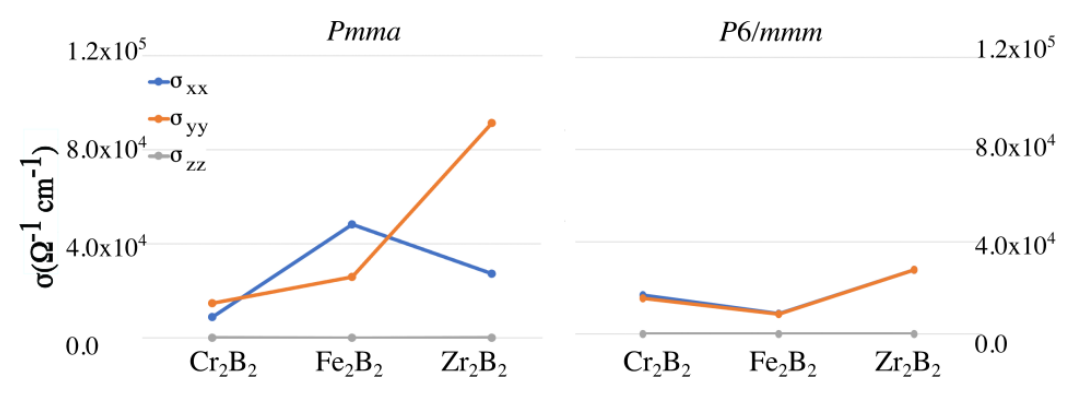


Figure 5. Components of the conductivity tensor for the *Pmma* (**left**) and P6/mmm (**right**) structures of Cr_2B_2 , Fe_2B_2 , and Zr_2B_2 .

3.3. Magnetic Properties

The origin of magnetism in these types of materials arises from the d orbitals of the TM atoms. Both FM and AFM configurations have been suggested to determine the ground state. The results of our calculations are summarized in Table 3. Among all the considered structures, only the hex-Fe₂B₂ resulted in an AFM ground state since the E_{tot} value of the FM state is 46.84 meV higher in energy. On the other hand, ortho-Fe₂B₂ exhibited an FM ground state in accordance with previous reports [34]. However, a more detailed analysis, that

Materials 2023, 16, 5104 8 of 10

also included the next nearest neighbors and was performed using DFT combined with the Monte Carlo method, revealed that ortho-Fe₂B₂ actually has a stable columnar AFM ground state [26]. In the particular case of Cr₂B₂, both structures result in an FM arrangement of the magnetic moments. In general, the total energy difference, $\Delta E_{\rm FM-AFM}$, between the FM and AFM configurations is always higher in absolute value for the orthorhombic structures (-104.38 and -108.12 eV for Cr₂B₂ and Fe₂B₂, respectively,) than for the hexagonal ones (-0.29 and 46.84 eV for Cr₂B₂ and Fe₂B₂, respectively) indicating that, in the latter case, the magnetic ordering may not be preserved at room temperature. Both orthorhombic Cr₂B₂ and Fe₂B₂ structures show an FM ground state with a magnetic moment over $2.5~\mu_{\rm B}$ per unit cell, a suitable behavior for robust 2D magnets. Interestingly, the boron atoms are also slightly polarized for those cases for which the TM–boron distances ($d_{\rm M-B}$) are the shortest (see Table 1). Finally, Zr₂B₂ MBenes exhibit non-magnetic behavior.

The energy difference $\Delta E_{\text{FM-AFM}} = E_{\text{FM}} - E_{\text{AFM}}$ can be used to evaluate the exchange interaction, J_{NN} , between TM atoms at the nearest neighbor (NN) positions. The exchange energy for a system of interacting atomic moments, \mathbf{S}_i , can be described by the Heisenberg model:

$$E_{tot} = E_0 - \frac{1}{2} \sum_{i \neq j} J_{ij} \mathbf{S}_i \cdot \mathbf{S}_j, \tag{2}$$

where E_0 is the total energy excluding spin–spin interactions and in our case $S_i = S_j = S$. For ferromagnetically or antiferromagnetically coupled TM ions at NN positions $-2J_{\text{NN}}S^2 = \Delta E_{\text{FM-AFM}}$. The critical temperature (Curie or Néel temperature), T_c , in the mean field approximation (MFA) can be estimated from

$$T_c \simeq \frac{2}{3}k_{\rm B} \cdot \left(J_{\rm NN}S^2\right) = \frac{1}{3}k_{\rm B} \cdot |\Delta E_{\rm FM-AFM}|.$$
 (3)

The T_c values are collected in Table 3. As can be seen from the table, we obtain a considerably large value of $T_c = 418$ K for ortho-Fe₂B₂. However, as mentioned above, a more accurate investigation [26] predicts an AFM ground state with $T_c = 115$ K. Interestingly, our calculations predict an AFM ground state for hex-Fe₂B₂ with $T_c = 181$ K.

Table 3. Total magnetic moment (μ_{tot}), magnetic moment of the TM atoms (μ_{TM}), magnetic moment induced on the boron atoms (μ_B), magnetic ground state (MGS), the total energy difference between the FM and the AFM configurations (ΔE_{FM-AFM}), and the critical temperature (T_c) estimated using Equation (3) for Cr_2B_2 , Fe_2B_2 , and Zr_2B_2 .

	Cr_2B_2		Fe_2B_2		$\mathbf{Zr}_2\mathbf{B}_2$	
	Pmma	P6/mmm	Pmma	P6/mmm	Ртта	P6/mmm
μ_{tot} ($\mu_{\rm B}$ /unit cell)	2.56	0.63	2.69	0.00	0.00	0.00
μ_{TM} ($\mu_{\mathrm{B}}/\mathrm{ion}$)	1.03	0.31	1.26	2.06/-2.06	0.00	0.00
μ_{B} ($\mu_{\mathrm{B}}/\mathrm{ion}$)	-0.05	-0.01	-0.05	0.00	0.00	0.00
MGS	FM	FM	FM	AFM	Non-magnetic	Non-magnetic
$\Delta E_{\text{FM-AFM}}$ (meV/unit cell)	-104.38	-0.29	-108.12	46.84	-	-
T_c (K)	403	1	418	181	-	-

4. Summary and Conclusions

In summary, we carried out a comparison between the structural, electronic, magnetic, and transport properties for orthorhombic and hexagonal phases of a selected group of MBenes, Cr_2B_2 , Fe_2B_2 and Zr_2B_2 , that are usually considered separately in the literature. Although there are several theoretical reports that have predicted the stability of the studied MBenes, to our knowledge, hex- Fe_2B_2 is shown for the first time in this work to be

Materials 2023, 16, 5104 9 of 10

dynamically stable. Experimentally the most studied MBenes are those composed of early TMs, whereas those composed of late TMs (like iron) remain to be synthesized.

We observe that, from an energetic point of view, the larger the atomic weight is, the higher the E_{coh} is, which means that Zr_2B_2 possesses the strongest bonds. However, despite the small difference between the E_{coh} values of the orthorhombic and hexagonal structures of each MBene, both phases can exist theoretically. This assumption is reinforced by the calculation of the corresponding phonon dispersion plots that predict stable behavior of all the MBenes. Furthermore, the metallic character of our pristine MBenes makes them efficient materials for charge transport, and therefore are competitive 2D materials for electronic, sensing, or electrocatalytic purposes. We predicted that, for both symmetries of Cr_2B_2 , the contribution of the majority spin states would be larger than that of the minority spin states at the Fermi level, leading to an FM ground state and opening the possibility of their use in information magnetic storage.

This understanding of the properties of the studied materials, together with the acknowledgment that, within the same framework, both orthorhombic and hexagonal phases are feasible and different in their properties, creates the possibility of going further in our research to consider them as potential candidates for sensing and catalytic processes. Although there exists some parallelism with MXenes, MBenes are emerging 2D materials that are expected to have great development potential in the future, due to their diverse stoichiometries and, as a consequence, structural differences and new challenging physical, chemical, and biological properties. The biggest difference for MBenes is that some of them can potentially exist in both orthorhombic and hexagonal phases.

Author Contributions: Conceptualization, I.M.A.-C. and N.G.S.; methodology, I.M.A.-C.; validation, I.M.A.-C.; investigation, I.M.A.-C. and N.G.S.; writing and original draft preparation, I.M.A.-C.; writing, review, and editing, N.G.S.; visualization, I.M.A.-C.; supervision, N.G.S. All authors have read and agreed to the published version of the manuscript.

Funding: This research received no external funding.

Acknowledgments: The use of supercomputers at the Interdisciplinary Centre for Mathematical and Computational Modelling (ICM) at the University of Warsaw is gratefully acknowledged.

Conflicts of Interest: The authors declare no conflict of interest.

References

- 1. Akopov, G.; Yeung, M.T.; Kaner, R.B. Rediscovering the Crystal Chemistry of Borides. *Adv. Mater.* **2017**, 29, 1604506. [CrossRef] [PubMed]
- 2. Ade, M.; Hillebrecht, H. Ternary Borides Cr_2AlB_2 , Cr_3AlB_4 , and Cr_4AlB_6 : The First Members of the Series $(CrB_2)_nCrAl$ with n = 1, 2, 3 and a Unifying Concept for Ternary Borides as MAB-Phases. *Inorg. Chem.* **2015**, 54, 6122–6135. [CrossRef] [PubMed]
- 3. Carlsson, A.; Rosen, J.; Dahlqvist, M. Theoretical predictions of phase stability for orthorhombic and hexagonal ternary MAB phases. *Phys. Chem. Chem. Phys.* **2022**, 24, 11249–11258. [CrossRef] [PubMed]
- 4. Wang, J.; Ye, T.N.; Gong, Y.; Wu, J.; Miao, N.; Tada, T.; Hosono, H. Discovery of hexagonal ternary phase Ti₂InB₂ and its evolution to layered boride TiB. *Nat. Commun.* **2019**, *10*, 2284. [CrossRef]
- 5. Alameda, L.T.; Moradifar, P.; Metzger, Z.P.; Alem, N.; Schaak, R.E. Topochemical Deintercalation of Al from MoAlB: Stepwise Etching Pathway, Layered Intergrowth Structures, and Two-Dimensional MBene. *J. Am. Chem. Soc.* **2018**, *140*, 8833–8840. [CrossRef]
- Alameda, L.T.; Lord, R.W.; Barr, J.A.; Moradifar, P.; Metzger, Z.P.; Steimle, B.C.; Holder, C.F.; Alem, N.; Sinnott, S.B.; Schaak, R.E. Multi-Step Topochemical Pathway to Metastable Mo₂AlB₂ and Related Two-Dimensional Nanosheet Heterostructures. *J. Am. Chem. Soc.* 2019, 141, 10852–10861. [CrossRef]
- 7. Zhang, H.; Xiang, H.; zhi Dai, F.; Zhang, Z.; Zhou, Y. First demonstration of possible two-dimensional MBene CrB derived from MAB phase Cr₂AlB₂. *J. Mater. Sci. Technol.* **2018**, *34*, 2022–2026. [CrossRef]
- 8. Zhang, H.; Dai, F.Z.; Xiang, H.; Wang, X.; Zhang, Z.; Zhou, Y. Phase pure and well crystalline Cr₂AlB₂: A key precursor for two-dimensional CrB. *J. Mater. Sci. Technol.* **2019**, *35*, 1593–1600. [CrossRef]
- 9. Khazaei, M.; Wang, J.; Estili, M.; Ranjbar, A.; Suehara, S.; Arai, M.; Esfarjani, K.; Yunoki, S. Novel MAB phases and insights into their exfoliation into 2D MBenes. *Nanoscale* **2019**, *11*, 11305–11314. [CrossRef]
- 10. Barinov, V.A.; Dorofeev, G.A.; Ovechkin, L.V.; Elsukov, E.P.; Ermakov, A.E. Structure and magnetic properties of the α-FeB phase obtained by mechanical working. *Phys. Status Solidi (a)* **1991**, *123*, 527–534. [CrossRef]

Materials 2023, 16, 5104 10 of 10

11. Zhao, X.; Li, L.; Bao, K.; Zhu, P.; Tao, Q.; Ma, S.; Cui, T. Insight the effect of rigid boron chain substructure on mechanical, magnetic and electrical properties of β-FeB. *J. Alloys Compd.* **2022**, *896*, 162767. [CrossRef]

- 12. Saldaña, F.I.; Defoy, E.; Janisch, D.; Rousse, G.; Autran, P.O.; Ghoridi, A.; Séné, A.; Baron, M.; Suescun, L.; Godec, Y.L.; et al. Revealing the Elusive Structure and Reactivity of Iron Boride α-FeB. *Inorg. Chem.* **2023**, *62*, 2073–2082. [CrossRef] [PubMed]
- 13. Gonzalez Szwacki, N.; Sadrzadeh, A.; Yakobson, B.I. B₈₀ Fullerene: An Ab Initio Prediction of Geometry, Stability, and Electronic Structure. *Phys. Rev. Lett.* **2007**, *98*, 166804. [CrossRef] [PubMed]
- 14. Szwacki, N.G. Boron Fullerenes: A First-Principles Study. Nanoscale Res. Lett. 2007, 3, 49. [CrossRef]
- 15. Perdew, J.P.; Burke, K.; Ernzerhof, M. Generalized Gradient Approximation Made Simple. *Phys. Rev. Lett.* **1996**, 77, 3865–3868. [CrossRef]
- 16. Blöchl, P.E. Projector augmented-wave method. Phys. Rev. B 1994, 50, 17953–17979. [CrossRef]
- 17. Giannozzi, P.; Baroni, S.; Bonini, N.; Calandra, M.; Car, R.; Cavazzoni, C.; Ceresoli, D.; Chiarotti, G.L.; Cococcioni, M.; Dabo, I.; et al. QUANTUM ESPRESSO: A modular and open-source software project for quantum simulations of materials. *J. Phys. Condens. Matter* 2009, 21, 395502. [CrossRef]
- 18. Himmetoglu, B.; Janotti, A. Transport properties of KTaO₃ from first-principles. *J. Phys. Condens. Matter* **2016**, *28*, 065502. [CrossRef]
- Henkelman, G.; Arnaldsson, A.; Jónsson, H. A fast and robust algorithm for Bader decomposition of charge density. Comput. Mater. Sci. 2006, 36, 354–360. [CrossRef]
- 20. Momma, K.; Izumi, F. VESTA 3 for three-dimensional visualization of crystal, volumetric and morphology data. *J. Appl. Crystallogr.* **2011**, 44, 1272–1276. [CrossRef]
- 21. Bo, T.; Liu, P.F.; Xu, J.; Zhang, J.; Chen, Y.; Eriksson, O.; Wang, F.; Wang, B.T. Hexagonal Ti₂B₂ monolayer: A promising anode material offering high rate capability for Li-ion and Na-ion batteries. *Phys. Chem. Chem. Phys.* **2018**, 20, 22168–22178. [CrossRef] [PubMed]
- 22. He, Q.; Li, Z.; Xiao, W.; Zhang, C.; Zhao, Y. Computational investigation of 2D 3*d*/4*d* hexagonal transition metal borides for metal-ion batteries. *Electrochim. Acta* **2021**, 384, 138404. [CrossRef]
- 23. Yuan, G.; Bo, T.; Qi, X.; Liu, P.F.; Huang, Z.; Wang, B.T. Monolayer Zr₂B₂: A promising two-dimensional anode material for Li-ion batteries. *Appl. Surf. Sci.* **2019**, *480*, 448–453. [CrossRef]
- 24. Mir, S.H.; Yadav, V.K.; Singh, J.K. Efficient CO₂ Capture and Activation on Novel Two-Dimensional Transition Metal Borides. *ACS Appl. Mater. Interfaces* **2022**, *14*, 29703–29710. [CrossRef]
- 25. Dou, M.; Li, H.; Yao, Q.; Wang, J.; Liu, Y.; Wu, F. Room-temperature ferromagnetism in two-dimensional transition metal borides: A first-principles investigation. *Phys. Chem. Chem. Phys.* **2021**, 23, 10615–10620. [CrossRef]
- 26. Ozdemir, I.; Kadioglu, Y.; Yüksel, Y.; Ümit Akıncı.; Üzengi Aktürk, O.; Aktürk, E.; Ciraci, S. Columnar antiferromagnetic order of a MBene monolayer. *Phys. Rev. B* **2021**, *103*. [CrossRef]
- 27. Qi, S.; Fan, Y.; Zhao, L.; Li, W.; Zhao, M. Two-dimensional transition metal borides as highly efficient N₂ fixation catalysts. *Appl. Surf. Sci.* **2021**, *536*, 147742. [CrossRef]
- 28. Zhang, B.; Zhou, J.; Guo, Z.; Peng, Q.; Sun, Z. Two-dimensional chromium boride MBenes with high HER catalytic activity. *Appl. Surf. Sci.* **2020**, *500* 144248. [CrossRef]
- 29. Shin, H.; Kang, S.; Koo, J.; Lee, H.; Kim, J.; Kwon, Y. Cohesion energetics of carbon allotropes: Quantum Monte Carlo study. *J. Chem. Phys.* **2014**, *140*, 114702. [CrossRef]
- 30. Xu, T.; Wang, Y.; Xiong, Z.; Wang, Y.; Zhou, Y.; Li, X. A Rising 2D Star: Novel MBenes with Excellent Performance in Energy Conversion and storage. *Nano-Micro Lett.* **2022**, *15*, 6. [CrossRef]
- 31. Şahin, H.; Cahangirov, S.; Topsakal, M.; Bekaroglu, E.; Akturk, E.; Senger, R.T.; Ciraci, S. Monolayer honeycomb structures of group-IV elements and III-V binary compounds: First-principles calculations. *Phys. Rev. B* **2009**, *80*, 155453. [CrossRef]
- 32. Fasolino, A.; Los, J.H.; Katsnelson, M.I. Intrinsic ripples in graphene. Nat. Mater. 2007, 6, 858–861. [CrossRef] [PubMed]
- 33. Zhang, B.; Zhou, J.; Sun, Z. MBenes: Progress, challenges and future. J. Mater. Chem. A 2022, 10, 15865–15880. [CrossRef]
- 34. Guo, Z.; Zhou, J.; Sun, Z. New two-dimensional transition metal borides for Li ion batteries and electrocatalysis. *J. Mater. Chem. A* **2017**, *5*, 23530–23535. [CrossRef]

Disclaimer/Publisher's Note: The statements, opinions and data contained in all publications are solely those of the individual author(s) and contributor(s) and not of MDPI and/or the editor(s). MDPI and/or the editor(s) disclaim responsibility for any injury to people or property resulting from any ideas, methods, instructions or products referred to in the content.

3.4 PAPER III: Influence of the Hubbard U Parameter on the Structural, Electronic, Magnetic, and Transport Properties of Cr/Fe/Zr-Based MBenes

This article is a sequel of the previous one and treats the classical problem of DFT when dealing with the strongly correlated electrons in the *d* orbitals of the transition metals. Finding a correct treatment of these systems seems to be not obvious because the different mechanisms influence the determination of the physical and chemical properties, which is crucial in the search for further technological applications. Inclusion of d electrons is expected to stabilize the structures, since boron is electron-deficient. However, it is known that LDA or GGA fail in the correct management of self-interaction of the partially occupied Kohn-Sham (KS) orbitals and make necessary, to solve this problem, the determination of the corresponding correction. The Hubbard parameter, U, has been calculated for each particular system by means of the density functional perturbation theory (DFPT), described in the previous section of the methodology, resulting in important values for Cr- and Fe-based MBenes (with *U* ranging between 4.2 and 5.0 eV) and in a small value for Zr_2B_2 (U = 1.8 eV). Under the introduction in such a correction, all the possible structures associated with the M₂B₂ stoichiometry, i.e., orthorhombic and hexagonal, remain feasible as in the previous work, although the more energetically favorable configurations are changed since all the compounds become preferably hexagonal, indicating that the inclusion of the correction has a strong influence on their stability. Also, the electronic properties are influenced by *U* because the Coulombian repulsion, expected by the consideration of this term, increases the separation of the bands in the surroundings of the Fermi level and, in relation with the transport properties, while the conductivity takes place along the boron chain in ortho-Fe₂B₂ under U = 0, it is the opposite when $U \neq 0$ and the same can be said for ortho-Cr₂B₂ which changes the direction in which conductivity occurs. Finally, the effect of *U* increases, in general, the critical temperature values, T_c , highlighting MBenes as excellent candidates for high N'eel temperature antiferromagnetic spintronics.

Influence of the Hubbard *U* Parameter on the Structural, Electronic, Magnetic, and Transport Properties of Cr/Fe/Zr-Based MBenes

Published as part of ACS Omega virtual special issue "Jaszowiec 2023".

Isabel M. Arias-Camacho*



Downloaded via 137.101.87.150 on December 2, 2023 at 14:58:51 (UTC). See https://pubs.acs.org/sharingguidelines for options on how to legitimately share published articles.

Cite This: ACS Omega 2023, 8, 45003–45012

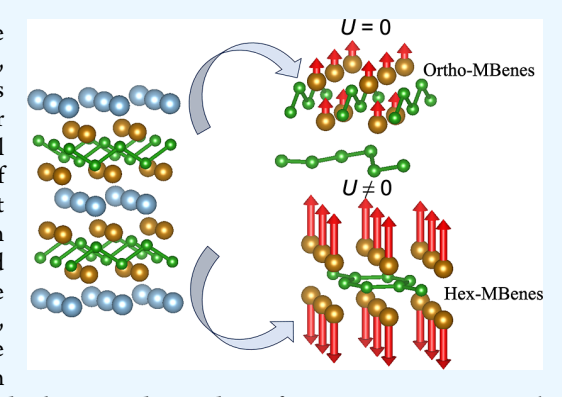


ACCESS I

III Metrics & More

Article Recommendations

ABSTRACT: Although relatively new, MBenes are gaining prominence due to their outstanding mechanical, electronic, magnetic, and chemical properties, and they are predicted to be good electrodes for catalytic processes as well as robust 2D magnets with high critical temperatures, to mention some of their intriguing attributes. From all their multiple stoichiometries, a theoretical study of their orthorhombic and hexagonal phases in the framework of density-functional theory is performed in this work. The results suggest that their properties are strongly dependent on the initial conditions considered in the theoretical approach and must be treated with caution. However, and independently of these factors, all of them are demonstrated to be energetically stable, show a metallic behavior, and exhibit, in specific cases, large magnetic moments per unit cell, exceeding 6.5 $\mu_{\rm B}$ in the case of the orthorhombic-type ${\rm Cr_2B_2}$, making them suitable as robust 2D magnets with



room critical temperature. These findings represent an important step toward a better understanding of MBenes, opening several windows to future research in energy conversion and storage, sensing, catalysis, biotechnology, or spintronics.

■ INTRODUCTION

The purpose of this work is to understand, with a computational approach, the origin of the structural, electronic, magnetic, and transport properties of selected transition metal (TM) monoborides, also known as MBenes (M = Cr, Fe, and Zr), as well as to identify features that may affect the transport properties of these compounds. All these MBenes, some of them already proven to be stable by previous study, present good structural stability and some of them exhibit robust magnetism, as well. 2D MBenes are present in a variety of stoichiometries $(M_2B_2, M_2B_3, and M_3B_4)$. The chosen structures for the MBenes described here possess M2B2 stoichiometry, which can be either orthorhombic (in the following, ortho-MBenes) with Pmma (no. 51) space group symmetry or hexagonal (in the following, hex-MBenes) with P6/mmm (no. 191) space group symmetry. In the Pmma structures, each atom is surrounded by six neighbors, and the buckled boron bilayers are sandwiched between the TM layers. On the other hand, in the P6/mmm structures, the honeycomb, graphene-like, boron layer is sandwiched between two TM layers on both sides, with every TM atom located above or below the centroid of the honeycomb structure. Their bulk counterparts, all widely studied both experimentally and theoretically, $^{2-4}$ are the ferromagnetic (FM) α and β modifications of FeB and the nonmagnetic (NM) CrB and ZrB compounds. The structure of α -FeB is debatable, whereas β -FeB and CrB are orthorhombic crystals with *Pnma*

(no. 62) and Cmcm (no. 63) space group symmetries, respectively. The ZrB solid is rock-salt structured and crystallizes in cubic Fm3m (no. 225) space group symmetry. The β -FeB and CrB solids exhibit very interesting structures since both enclose boron double-chain stripes which are very common motives of all-boron nanostructures. 5,6 Parallel to MAX phases in MXenes, MBenes can be obtained by removing the element A by chemical etching from their parental MAB phases. Ade and Hillebrecht were the first to identify MBenes as derivatives of MXenes in 2015. Since then, a lot of efforts have been done in the search of boron-based 2D materials with excellent charge carrier mobility, versatile chemical activity, magnificent specific surface area or good mechanical strength, well-desired characteristics in a lowdimensional material. Although relatively young and in process of being explored,8 synthesized,9 and understood, the TM monoborides present a high potential in diverse applications like energy conversion and storage, 10 catalysis, 11,12 NO electroreduction, 13 adsorption and activation of CO2, 14 biotechnol-

Received: August 31, 2023 Revised: October 27, 2023 Accepted: November 1, 2023 Published: November 16, 2023





ogy, 15 magnetic refrigeration, 16 information storage devices, 17 or spintronics, $^{18-21}$ among others. It was thought for several years that the long-range magnetic order was not possible in 2D materials due to thermal fluctuations.²² However, contradicting the predictions of the Mermin-Wagner theorem, the magnetic anisotropy energy originating on the spin orbit coupling can shield this effect, confirming consequently the existence of 2D magnets. Nevertheless, most of them, like CrI_3^{24} or $Fe_3GeTe_2^{25}$ show low critical temperatures (\approx 45 and 130 K, respectively), reason why the achievement of materials with higher critical temperatures remains a challenge for their use in magnetic storage devices and spintronics. In the recent years, several research studies involving MBenes point in this direction. 18,20 Another issue to deal with is the consideration (or not) of the correction introduced by the Hubbard parameter, U, which accounts appropriately for the strongly correlated electrons in the d orbitals of the TMs. Both approaches are found in the literature, almost equally, when diverse properties of the 2D TM monoborides are studied. However, the differences in the results of both methodologies can lead to completely different conclusions, for example, in the final magnetic ground state (MGS) or the most stable geometry, which in specific cases become the opposite the one to the other. Then, a correct treatment of the initial premises seems not obvious.²⁰ Following these premises, this paper intends to elucidate how the different mechanisms influence in the determination of the physical and chemical properties, crucial in the search of further technological applications. This work is structured in the following parts. In the first section, the structures of the selected MBenes are computed to determine the Hubbard parameters for each of them based on their optimized geometries and MGSs. Once obtained, the stability, conductivity, and electronic and magnetic properties will be compared and discussed in both contexts: with and without the correction, to end with the main conclusions and a view into their future applications.

■ COMPUTATIONAL APPROACH

In the framework of the density-functional theory (DFT), firstprinciples spin-polarized calculations have been performed, within the generalized gradient-corrected approximation of Perdew-Burke-Ernzerhof (PBE)²⁶ for the exchange-correlation functional, using projector plane-wave pseudopotentials²⁷ implemented in the Quantum ESPRESSO (QE) suite of codes.²⁸ Every unit cell contains two atoms of the TM and two atoms of boron, with an empty space of thickness of 15 Å along the normal direction to avoid interactions between adjacent MBenes. The optimization of geometries has been done, allowing the unit cell shape, volume, and the ions to relax until the residual forces on the atoms have been less than 0.3 meV/Å and the total energy convergence has been set to $10^{-5}\,$ Ry. The electronic wave functions and the charge density have been expanded in plane-wave basis sets with energy cutoffs of 70 and 700 Ry, respectively, while the Γ -centered k-point grid in the Brillouin zone, in the Monkhorst-Pack scheme, has been set to $12 \times 12 \times 1$ for the geometry optimizations and $24 \times 24 \times 1$ for the density of state (DOS) calculations, with a Gaussian smearing of 0.02 Ry; the accuracy of the total energy is ensured by these values. To determine the most energetically favorable MGS of each structure, two collinear calculations, one FM and one antiferromagnetic (AFM), have been used. The geometry relaxations of the 2D structures have been performed with PBE, and the magnetic and electronic properties have been calculated

using both PBE and PBE+U. An important descriptor used for the structural characterization is the cohesive energy per atom $(E_{\rm coh})$, that is, the difference in energy between the total energy of the compound and the sum of the total energies of the isolated atoms

$$E_{\rm coh} = (n_{\rm B}E[{\rm B}] + n_{\rm M}E[{\rm M}] - E[{\rm M}_2{\rm B}_2])/(n_{\rm B} + n_{\rm M})$$
 (1)

which is the released energy when a compound dissociates into isolated free atoms, where M represents the TM atom, $E[M_2B_2]$ is the total energy of the MBene, E[B] and E[M] are the total energies of the isolated atoms (B and TM atoms), and $n_{\rm B}$ and $n_{\rm M}$ are the numbers of boron and TM atoms per unit cell, respectively, directly obtained from the spin-polarized calculations. The transport integrals have been computed using the Boltzmann transport theory²⁹ and a constant scattering rate model (the inverse of relaxation time was taken to be 0.1 eV), and a Bader analysis has been used to obtain the charge transfer. The visualizations have been performed using the Visualization for Electronic and STructural Analysis (VESTA) software.³⁰

■ RESULTS AND DISCUSSION

Structure. It is expected that a mixture between boron and TM atoms will stabilize the structures since boron is electron deficient. Among all the possible stoichiometries of MBenes, we have focused on the orthorhombic (ortho-) and hexagonal (hex-) M_2B_2 structures, as shown in Figure 1.

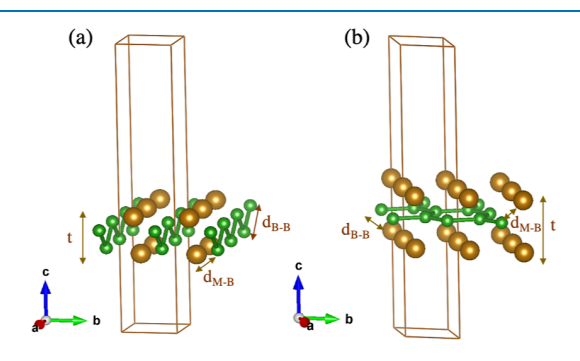


Figure 1. (a) Ortho-MBene and (b) hex-MBene structures of M_2B_2 corresponding to *Pmma* and *P6/mmm* symmetries, respectively. The unit cells used in the calculations are shown in brown.

In our previous work, ³¹ we have performed a full structural optimization to determine the structural parameters of our unit cells, finding that the unit cells of ortho-MBenes become almost rectangular with a > b when the TM is Fe or Cr (a/b is 1.005 and 1.013 for chromium and iron, respectively), whereas a < b for ortho-Zr₂B₂ (a/b = 0.94). The lattice parameters, a = 2.885 and b = 2.870 Å for ortho-Cr₂B₂, a = 2.823 and b = 2.787 Å for ortho-Fe₂B₂, and a = 3.084 and b = 3.281 Å for ortho-Zr₂B₂; a = b = 2.919 Å for hex-Cr₂B₂, a = b = 2.913 Å for hex-Fe₂B₂, and a = b = 3.159 Å for hex-Zr₂B₂, have been compared to and are in good agreement with the values found in the literatures. ^{11,14,17,19,32–34} The distances between the TMs and the boron atoms are always larger for the hexagonal systems (ranging between 2.15 and 2.49

larger for the hexagonal systems (ranging between 2.15 and 2.49 Å) than those for the orthorhombic systems (between 2.04 and 2.46 Å), with the bigger distances corresponding to Zr_2B_2 MBenes.

Determination of the *U* **Parameter.** The Hubbard *U* parameter is introduced in highly correlated systems due to the fact that LDA or GGA inadequately treats the self-interaction of the partially occupied Kohn–Sham (KS) orbital. In solids, it is

even more complicated because the hybridization of localized orbitals can produce fractional occupations, causing the total energy to contain such effects from hybridization. In this work, we determine the Hubbard parameters for the TM d orbitals using the linear response approach³⁵ based on the density-functional perturbation theory (DFPT). Mithin this framework, the Hubbard parameters can be computed from the second-order derivative of the energy. The total energy as a function of the localized orbital occupation q_I of Hubbard site I is given by

$$E(\{q_{\rm I}\}) = \min_{\rho, \alpha_{\rm I}} \{E_{\rm DFT}[\rho] + \sum_{\rm I} \alpha_{\rm I}(n_{\rm I} - q_{\rm I})\}$$
 (2)

where ρ is the charge density and $\alpha_{\rm I}$ is the Lagrange multiplier (that acts as a perturbation potential) employed to constrain the site occupation $n_{\rm I}$ which is the occupation of the localized states in the d orbital of site I. It is more convenient to work with the Legendre transform of eq 2, which leads to a modified energy functional that depends on $\{\alpha_{\rm I}\}$

$$E(\{\alpha_{\rm I}\}) = \min_{\rho} \{E_{\rm DFT}[\rho] + \sum_{\rm I} \alpha_{\rm I} n_{\rm I}\}$$
(3)

Then, the total energy as a function of on-site occupations n_1 is given via a Legendre transform

$$\mathcal{E}(\{n_{\mathrm{I}}\}) = E(\{\alpha_{\mathrm{I}}\}) - \sum_{\mathrm{I}} \alpha_{\mathrm{I}} n_{\mathrm{I}}$$

from which the second derivative can be evaluated with

$$\frac{\partial^2 \mathcal{E}}{\partial n_{\rm I} \partial n_{\rm J}} = -\frac{\partial \alpha_{\rm I}}{\partial n_{\rm J}} \tag{4}$$

Similarly, the second derivative of the total energy for the noninteracting system evaluated through KS equations can be obtained from

$$\frac{\partial^2 E^{KS}}{\partial n_I^{KS} \partial n_J^{KS}} = -\frac{\partial \alpha_I^{KS}}{\partial n_J^{KS}} \tag{5}$$

The effective interaction parameter U of site I can be calculated as a difference of the above-defined second derivatives of the energy of the interacting and noninteracting systems with respect to electronic occupation

$$U_{\rm I} = \left(-\frac{\partial \alpha_{\rm I}}{\partial n_{\rm I}}\right) - \left(-\frac{\partial \alpha_{\rm I}^{\rm KS}}{\partial n_{\rm I}^{\rm KS}}\right) \tag{6}$$

This approach to compute the Hubbard U parameters based on DFPT is implemented in QE in the HP code. ^{38,39}

Table 1 describes the values for Cr_2B_2 and Fe_2B_2 that are higher than those for Zr_2B_2 . Such values of U are found to be similar to other works, ^{20,21} so the consistency of these results is assumed. However, in order to perform a suitable comparison using the same parameter for both MGSs, the values of the second column (FM) were chosen as a criterion.

Ground-State Energetics. A high cohesive energy, $E_{\rm coh}$, indicates a high bond strength and hence a good thermodynamic stability. The cohesive energies of all the systems involved here have been calculated using eq 1. The corresponding results are shown in the second column of Table 2.

All our MBenes exhibit large cohesive energies ranging from 6.222 to 8.087 eV if U = 0 and from 4.466 to 7.178 eV after using the corresponding value of U, and they are similar to those found in the literature. All of them present strong internal binding

Table 1. Hubbard Parameters Calculated Using DFPT^a

	F	M	AF	M
MBene	U_{TM1}	U_{TM2}	U_{TM1}	U_{TM2}
ortho-Cr ₂ B ₂	4.297	4.297	6.682	6.806
hex-Cr ₂ B ₂	5.000	5.000	4.995	4.995
ortho- Fe_2B_2	4.346	4.279	4.651	4.556
hex-Fe ₂ B ₂	4.232	4.231	4.009	4.010
ortho- Zr_2B_2	1.792	1.792	1.792	1.792
hex-Zr ₂ B ₂	1.802	1.802	1.802	1.802

"FM and AFM indicate the ferro- and antiferromagnetic ground states, respectively, and TM1 and TM2 correspond to each transition metal in the unit cell.

Table 2. Cohesive Energies (E_{coh}) for the Orthorhombic and Hexagonal Structures of Cr_2B_2 , Fe_2B_2 , and Zr_2B_2

	E	coh
MBene	<i>U</i> = 0	$U \neq 0$
ortho- Cr_2B_2	6.222	4.539
hex-Cr ₂ B ₂	6.201	4.558
ortho- Fe_2B_2	6.901	6.235
$hex-Fe_2B_2$	6.830	6.264
ortho- Zr_2B_2	8.050	7.579
$\text{hex-Zr}_2\text{B}_2$	8.087	7.615

and good stability, although, in general, the cohesive energies for U=0 are always higher. To check the consistency of our values, we have computed the carbon diamond structure with the same parameters used in the optimization, resulting an $E_{\rm coh}$ of 7.757 eV, comparable to other experimental and theoretical work. Moreover, Zhang et al. 2 reported a cohesive energy of 6.30 eV for ortho- Cr_2B_2 , which is close to our 6.22 eV when U=0.

The dependence of the structure stability with the atomic mass of the TM observed earlier 33 is also present in our results, being hex-Zr₂B₂ the MBene with the highest $E_{\rm coh}$ (8.087 eV). Moreover, in a previous work, 31 we have calculated the phonon dispersion of all the orthorhombic and hexagonal stoichiometries which have resulted dynamically stable with frequencies over 740 cm $^{-1}$, in agreement to other studies. 13,21,34

Interestingly, a remarkable difference between the two approaches employed is observed between the most energetically favorable geometries (which have been indicated in bold for more clarity): under the approximation with U = 0, Cr_2B_2 and Fe₂B₂ prefer orthorhombic configurations, as other works also predict, 1,32,43 whereas Zr₂B₂ suits better the hexagonal structure from the point of view of the cohesive energy. The picture changes when $U \neq 0$, for which all the structures become preferably hexagonal, indicating that the introduction of the correction has a strong influence on the stability. The existing attempts to obtain MBenes from ternary MAB phases have used ortho-MAB phases as precursor to synthesize MoB and CrB ortho-MBenes, with the result of poor quality, due to the complete dissolution of the parent phases or the partial etching of Al. 7,44-47 On the other side, new attempts are focused on the fabrication of hex-MAB phases as a promising phase toward hex-MBenes.⁴⁸ In this sense, up to date, there are scarce experimental results that can firmly confirm the adoption of the one or the other structure, and big efforts into this direction are still ongoing. 49,5

It should be noted that both orthorhombic and hexagonal structures are very close in energy (some tens of eV), and investigations based on the nudged elastic band method have

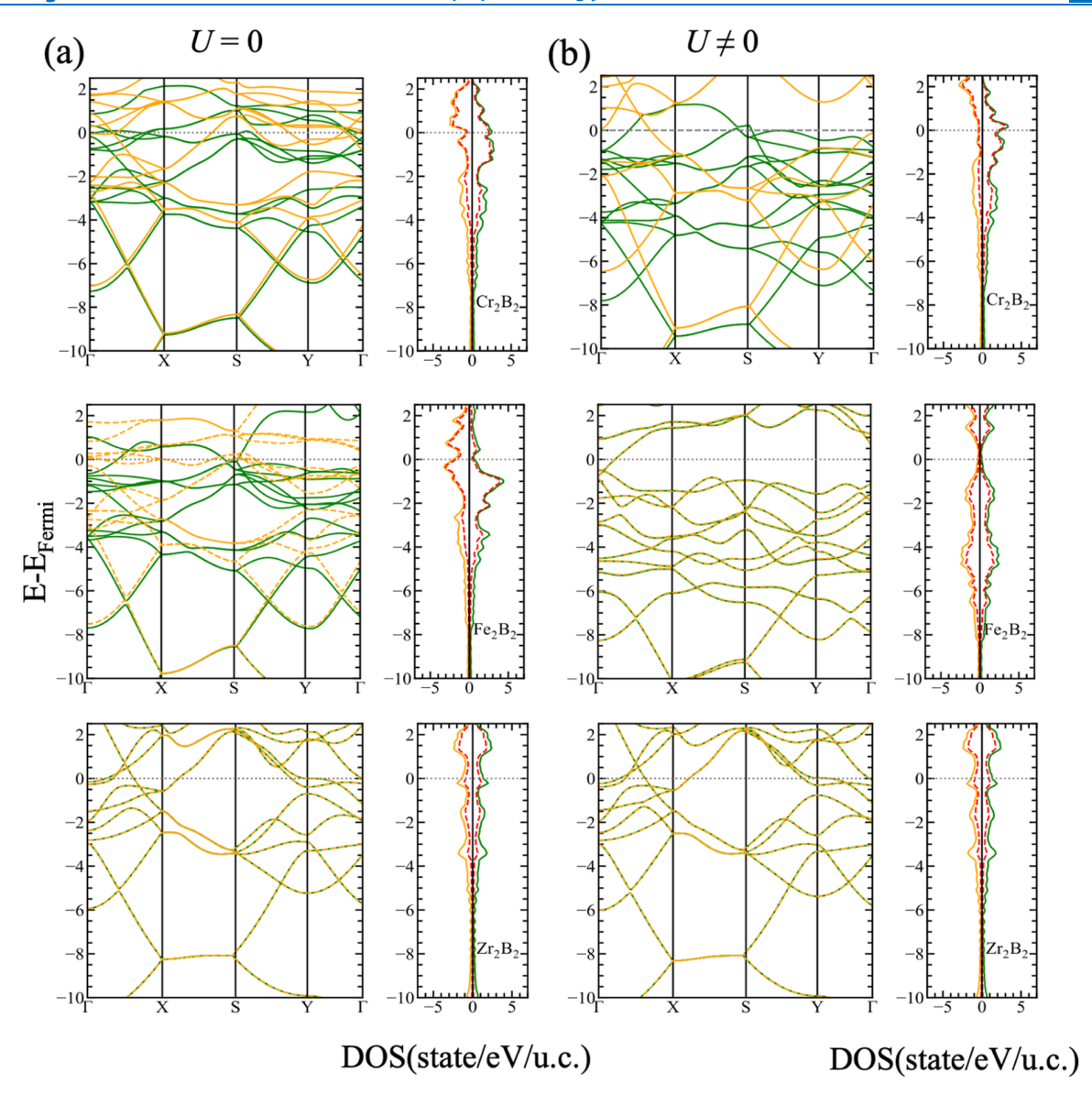


Figure 2. Comparison between the electronic band structure and DOS for the majority (green) and minority (orange) spins of the Pmma structures of Cr_2B_2 , Fe_2B_2 , and Zr_2B_2 using (a) DFT and (b) DFT+U. The dotted red line indicates the contribution of the TM-d orbitals.

determined that the small energy barrier, between 0.2 and 0.4 eV per atom, could lead to the transformation of the ortho-MBenes into hex-MBenes at high temperatures. 1,10

Electronic and Transport Properties. The calculated spin-polarized band structures, DOSs, and projected densities of states (PDOSs) including U = 0 and $U \neq 0$ are shown in Figures 2 and 4 for both orthorhombic and hexagonal structures, respectively. As expected, 9,11,21,40 the behavior of these MBenes is always metallic, with no band gaps between the valence band and the conduction band, but with partially occupied bands crossing the Fermi level for the majority and minority spin channels. For clarity, the d states of the TMs have been plotted together with the total DOS, highlighting their major contribution at the Fermi level. The effect of introducing U becomes clearly visible after a comparison of the respective spin-polarized band structures, where the Coulombian repulsion expected by the introduction of the term increases the separation of the bands in the surroundings of the Fermi level.

The total DOS predicts the FM ground states for ortho- Cr_2B_2 and ortho- Fe_2B_2 with an asymmetry at the Fermi level between the two spin channels that transforms into AFM, in the case of ortho- Fe_2B_2 , when U is used in the calculation of the electronic properties. It is also observed that only one band is crossing the Fermi level, which lies in a minimum of the DOS, and curiously, the systematic research of Dou et al. reported that ortho- Cr_2B_2 is a FM metal, while the ortho- Fe_2B_2 monolayer is a typically AFM semiconductor. Taking this result into consideration, some modifications like the addition of functional groups like OH, F, and O would allow to tailor the electronic properties for subsequent applications.

Figure 3 plots simultaneously the p orbitals of boron and the d orbitals of the TM for the ortho-structures. When U = 0, it is clear that the Fermi level is dominated by the d states of the metals, and the p states of boron are negligible. Deep in energies (approximately in a range between -8 and -2 eV) are found the p states of boron, which partially hybridize with the d states of the TM and demonstrate the existing interaction between the

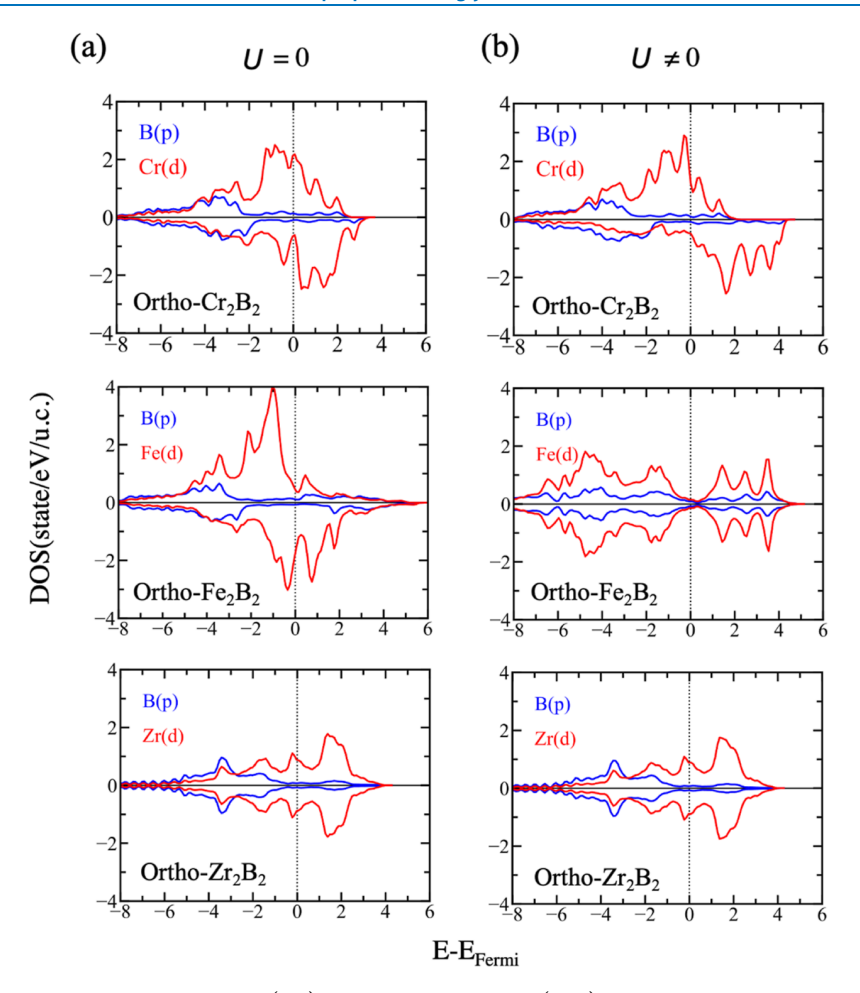


Figure 3. PDOS corresponding to the d states of the TM (red) and the p states of boron (blue) of the *Pmma* structures of Cr_2B_2 , Fe_2B_2 , and Zr_2B_2 using (a) DFT and (b) DFT+U.

TM and B atoms. The introduction of U dramatically changes the electronic properties of the materials and switches ortho-Fe₂B₂ into an AFM ground state. Focusing on the latter, here the p states of the boron shift toward the Fermi level, increasing their importance. Zr_2B_2 behaves as a nonmagnetic material, and the consideration of its own small U value does not introduce remarkable changes. Around the Fermi level, the d orbitals of Zr predominate, but the p orbitals of Zr also become relevant, showing a nonperfect hybridization with a similar behavior.

The governing ground states of the hex-MBenes when U is considered are all AFM, which can be deduced from the band structures depicted in Figure 4, with the exception of hex- Zr_2B_2 which behaves again like nonmagnetic. Again, the p states of boron (Figure 5) are shifted toward the vicinity of the Fermi level, where, interestingly, the population of the d states is strongly diminished after including the correction.

Generally speaking about ortho-MBenes, the components of the conductivity are strongly dependent on the in-plane directions, revealing their anisotropy (Figure 6). There are noticeable differences in the behavior of each MBene and also depending on the physical treatment adopted. While the conductivity takes place along the boron chain in ortho-Fe₂B₂, it is the opposite in Zr_2B_2 . When $U \neq 0$, on the other hand, it is for ortho-Cr₂B₂ that the conductivity happens along the boron chain instead. From the point of view of the conductivity, hex-MBenes are isotropic, presenting Zr_2B_2 the highest values among all.

Magnetic Properties. The electron deficiency and low electronegativity of boron distinguish MBenes with intriguing magnetic properties. Some of the MBenes predicted as feasible exhibit robust metallic magnetism higher than 3 $\mu_{\rm B}$ per TM atom and Curie temperatures over room temperature. Some studies suggest, moreover, that the critical temperatures can even be elevated under a careful selection of functional groups. 18,19,51 To determine the MGS, two collinear configurations have been performed: one FM and another AFM, which consist of keeping the same spin alignment within each plane of metals. The results suggest a superexchange interaction because due to the large distances between the d orbitals, a direct overlap between them seems to be little realistic. Considering this, the d orbitals hybridize with the ligand atoms, that is, the 2p orbitals of boron, and hence, the magnetic interaction takes place between nonneighboring magnetic ions (TM) mediated by neighboring nonmagnetic ions (B). For such a magnetic interaction, the MGSs, which can be either FM or AFM, are empirically determined by the rules of Goodenough-Kanamori-Anderson⁵²⁻⁵⁴ based on the symmetry and the electron occupancy of the overlapping atomic orbitals. The magnetic moments of the boron atoms shown in Table 3 show that they are slightly polarized, demonstrating that magnetism in these cases is mediated by them.

The two possible scenarios that emerge from the inclusion (or not) of the U parameter reach different conclusions, an effect found in a similar work¹⁸ where a thorough calculation with the

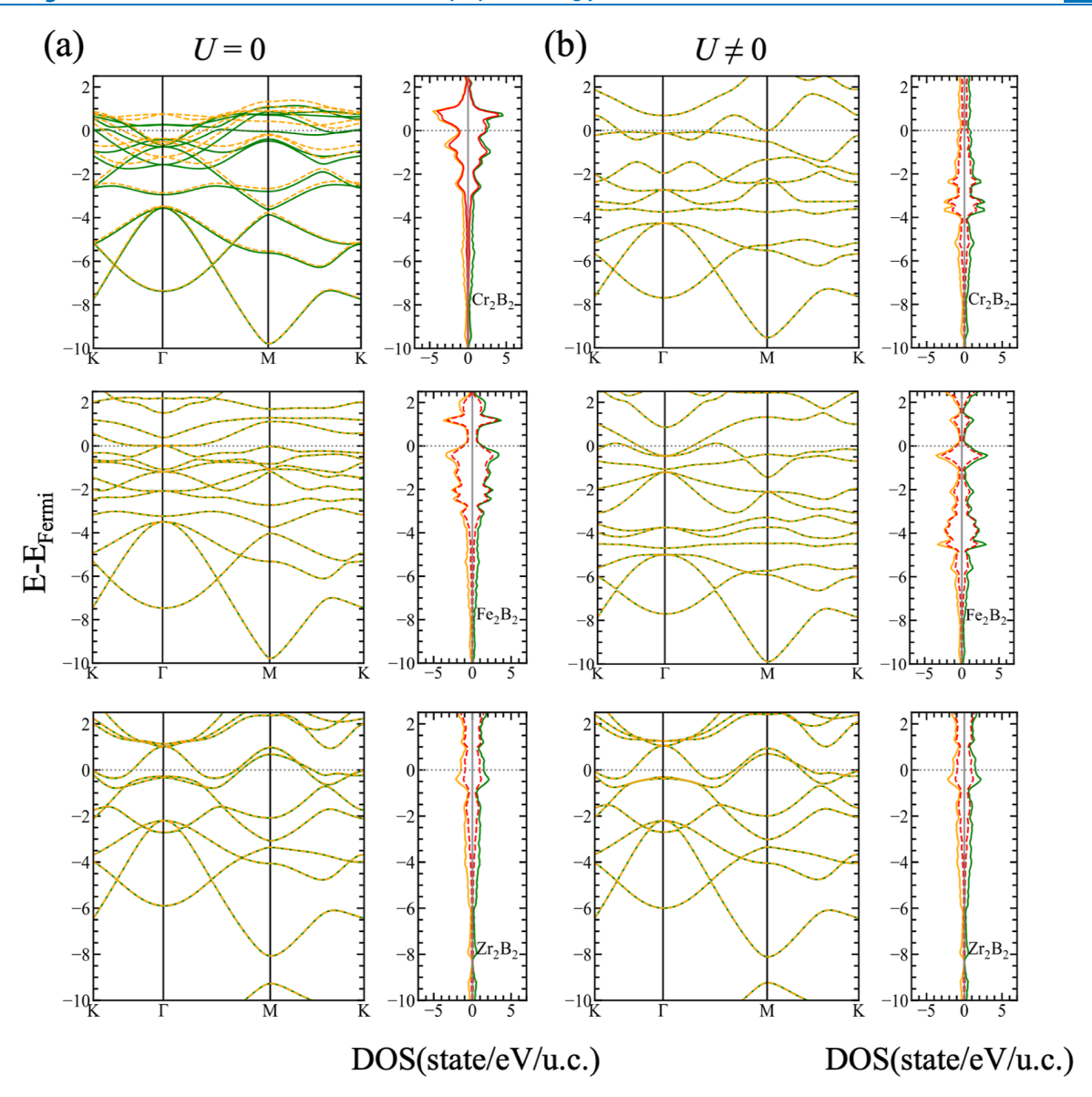


Figure 4. Comparison between the electronic band structure and DOS for the majority (green) and minority (orange) spins of the P6/mmm structures of Cr_2B_2 , Fe_2B_2 , and Zr_2B_2 using (a) DFT and (b) DFT+U. The dotted red line indicates the contribution of the TM-d orbitals.

increase in values of U produced a change in the MGSs of the same material. Excluding U, only hex-Fe2B2 adopted an AFM ground state, with an $E_{\rm coh}$ of the FM state being 46.84 meV smaller (Table 3) than that of the AFM state. However, ortho-Fe₂B₂ has a larger E_{coh} when the TM atoms arrange ferromagnetically, an effect observed before. 55 Both orthorhombic and hexagonal structures of Cr₂B₂ result FM. Orthorhombic Cr₂B₂ and Fe₂B₂ with FM ordering possess magnetic moments over 2.5 $\mu_{\rm B}$ per formula unit, indicating a suitable behavior as robust 2D magnets, but Zr₂B₂ exhibits nonmagnetic properties. The introduction of U causes the AFM states predominate over the FM states, and only ortho-Cr₂B₂ remains FM with a magnetic moment of 6.39 $\mu_{\rm B}$, very close to the 6.10 and 6.49 $\mu_{\rm B}$ values reported by Zhang et al., ⁴² after setting U = 4 eV for their calculations and U = 3 eV by Dou et al., 17 respectively, whereas the AFM behavior of ortho-Fe₂B₂ considering $U \neq 0$ is in accordance to other works. The Bader charge analysis confirms that magnetism in these compounds arises from the d-electrons of the TM atoms.

According to Table 3, the charge transference always happens from the TM to the boron atoms, with Zr being the metal for which the charge transference is larger. These values are in agreement to other works. ^{18,19} Considering the Pauli exclusion principle together with Hund's rules, the theoretical predicted magnetic moment of freestanding Cr, with electronic configuration [Ar] 3d⁴ 4s², would be 4 $\mu_{\rm B}$, whereas for iron, with electronic configuration [Ar] 3d⁶ 4s², it will result in 3 $\mu_{\rm B}$. As the calculated magnetic moments per metal ion are 2.79 and 3.23 $\mu_{\rm B}$ for ortho- and hex-Cr₂B₂, respectively, and 2.31 and 2.59 $\mu_{\rm B}$ for ortho- and hex-Fe₂B₂, we can conclude that the transference of one electron from the TM to the boron atom leads to the obtained magnetic moment and is, therefore, consistent with these results.

Attending to the results in Table 4, the large energy difference will increase the critical temperature beyond room temperature, a well-desired property for spintronic applications as mentioned above.

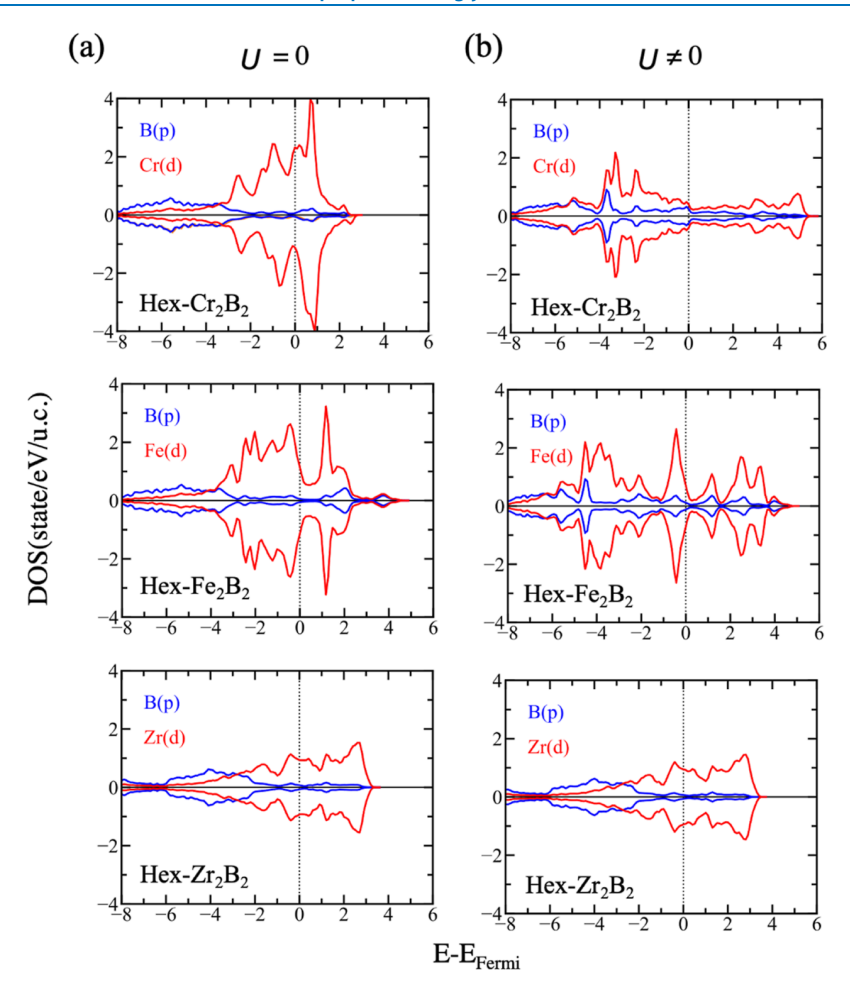


Figure 5. PDOS corresponding to the d states of the TM (red) and the p states of boron (blue) of the P6/mmm structures of Cr_2B_2 , Fe_2B_2 , and Zr_2B_2 using (a) DFT and (b) DFT+U.

The exchange interaction, $J_{\rm NN}$, between the TM atoms at the nearest-neighbor (NN) positions can be evaluated with the energy difference $\Delta E_{\rm FM-AFM} = E_{\rm FM} - E_{\rm AFM}$. It is well-known that the exchange energy for a system of interacting atomic moments can be described by the Heisenberg model

$$E_{\text{tot}} = E_0 - \frac{1}{2} \sum_{i \neq j} J_{ij} \mathbf{S}_i \cdot \mathbf{S}_j$$
 (7)

where E_0 is the total energy excluding spin—spin interactions and in our case $S_i = S_j = S$. For ferromagnetically or antiferromagnetically coupled TM ions at NN positions, $-2J_{\rm NN}S^2 = \Delta E_{\rm FM-AFM}$. Considering ferromagnetically or antiferromagnetically coupled TM ions at NN positions, $-2J_{\rm NN}S^2 = \Delta E_{\rm FM-AFM}$. On the other side, the critical temperature (Curie or Néel temperature), T_c is described in the mean field approximation (MFA) as

$$T_{\rm c} \simeq \frac{2}{3k_{\rm B}} \cdot (J_{\rm NN}S^2) = \frac{1}{3k_{\rm B}} \cdot |\Delta E_{\rm FM-AFM}|$$
 (8)

Although MFA usually overestimates the transition temperature for 2D magnets in $\approx\!20\%$ or, what is more, is dependent on the coordination number, however, this approximation is able to establish an upper limit of T_c at small computational cost.

Using eq 8, the resulting T_c values are collected in Table 4. As can be seen from the table, without the Hubbard correction, we obtain a considerably large value of $T_c = 418$ K for ortho-Fe₂B₂.

However, as mentioned above, a more accurate investigation ¹⁹ predicts an AFM ground state with $T_{\rm c}$ = 115 K. Interestingly, the calculations predict an AFM ground state for hex-Fe₂B₂ with $T_{\rm c}$ = 181 K. Adding the Hubbard correction, the MGS of ortho-Fe₂B₂ turns to AFM with an important energy difference. Other study ¹⁷ computed even a higher difference for AFM ortho-Fe₂B₂, but using a smaller value of U = 3 eV, whereas their value for FM ortho-Cr₂B₂ is closer.

In this same direction, and having in mind that the current findings point out to high critical temperatures, much efforts are being done in finding MBenes for high Néel temperature AFM spintronics.²⁰

CONCLUSIONS

In the present work, the energetic, electronic, magnetic, and transport properties of selected MBenes have been systematically computed from two different perspectives (U=0 and $U\neq 0$) to be subsequently described, compared, and discussed. The findings reveal that the consideration or not of the Hubbard correction is not trivial and leads, in some cases, even to opposite results. Because the use of the parameter U is controversial, a thorough comparison with the experimental work is necessary to clarify which theoretical approach is the most suitable to describe the systems. The resulting values of U are typical of those found in previous studies for Cr_2B_2 and Fe_2B_2 . In the particular case of Zr_2B_2 , U is considerably smaller, and hence,

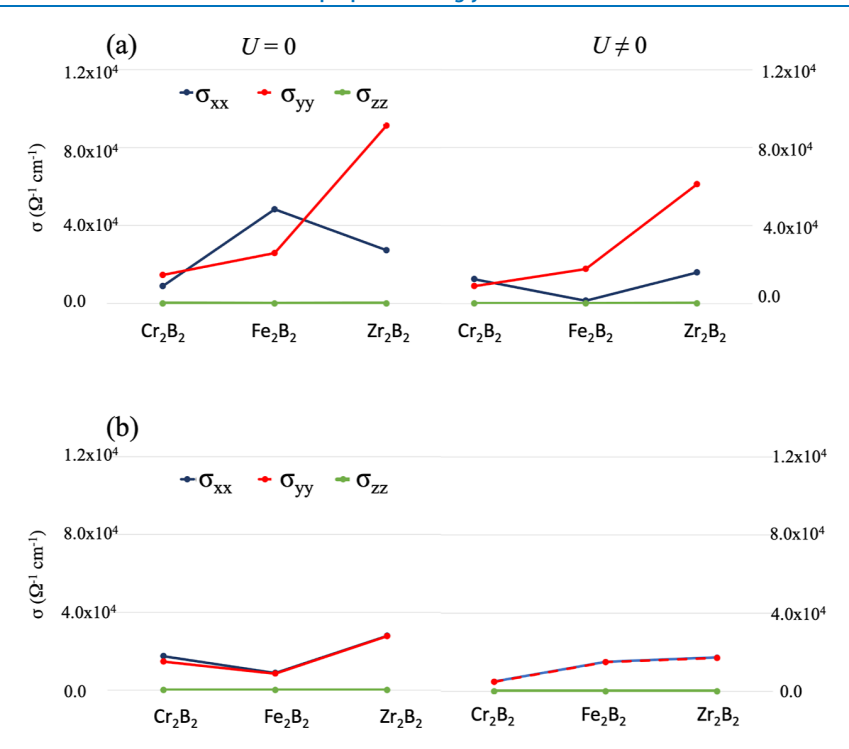


Figure 6. Components of the conductivity tensor for the (a) Pmma and (b) P6/mmm structures of Cr_2B_2 , Fe_2B_2 , and Zr_2B_2 considering U = 0 (left) and $U \neq 0$ (right).

Table 3. Charge Transfer from TM to B (Δq), Total Magnetic Moment (μ_{tot}) per Unit Cell, Magnetic Moment of the TM Atom ($\mu_{TM/ion}$), and Magnetic Moment of the Boron Atoms ($\mu_{B/ion}$) in Cr_2B_2 , Fe_2B_2 , and Zr_2B_2

	Δ	A q	$\mu_{ m tot}$	$(\mu_{ m B})$	$\mu_{ m TM/io}$	$_{ m on} (\mu_{ m B})$	$\mu_{ m B/ior}$	$(\mu_{\rm B})$
MBene	U = 0	$U \neq 0$	<i>U</i> = 0	$U \neq 0$	U = 0	$U \neq 0$	<i>U</i> = 0	$U \neq 0$
ortho-Cr ₂ B ₂	-0.76	-0.82	2.56	6.39	1.03	2.79	-0.05	-0.22
hex-Cr ₂ B ₂	-0.61	-0.63	0.63	0.00	0.31	±3.23	-0.01	0.00
ortho- Fe_2B_2	-0.37	-0.48	2.69	0.00	1.26	±2.31	-0.05	±0.08
hex-Fe ₂ B ₂	-0.40	-0.41	0.00	0.00	±2.06	±2.59	0.00	0.00
ortho- Zr_2B_2	-1.17	-1.17	0.00	0.00	0.00	0.00	0.00	0.00
$hex-Zr_2B_2$	-0.86	-0.86	0.00	0.00	0.00	0.00	0.00	0.00

Table 4. MGS, Energy Difference, $\Delta E_{\text{FM-AFM}}$, between the FM and AFM Configurations, and Critical Temperature, T_c , of Cr_2B_2 , Fe_2B_2 , and Zr_2B_2

	M	GS	$\Delta E_{ ext{FM-AF}}$	M (meV)	$T_{\rm c}$	(K)
MBene	U = 0	$U \neq 0$	U = 0	$U \neq 0$	U = 0	$U \neq 0$
ortho-Cr ₂ B ₂	FM	FM	-104.38	-140.93	413	545
hex-Cr ₂ B ₂	FM	AFM	-0.29	+46.61	1	180
ortho- Fe_2B_2	FM	AFM	-108.12	+540.66	418	2091
hex-Fe ₂ B ₂	AFM	AFM	+46.84	+581.53	181	2249
ortho- Zr_2B_2	NM	NM				
$\text{hex-Zr}_2\text{B}_2$	NM	NM				

this MBene maintains its properties unaffected with respect to the case of U = 0. The prevailing structures from an energetic point of view are orthorhombic for Cr_2B_2 and Fe_2B_2 and hexagonal for Zr_2B_2 , whereas all of them become preferably hexagonal if high values for U are assumed. Also, the electronic properties are affected by such changes with a general decrease of states at the Fermi level, a situation reflected in the results for the conductivity. Up to this point, such discrepancies can influence the subsequent analysis for adsorption or catalytic processes, to give some examples. Moreover, the magnetic

properties are strongly influenced by the value of U. The original MGS for U=0, predominantly FM (except for hex-Fe₂B₂, with an AFM ground state), becomes mostly AFM after the inclusion of the corresponding Hubbard parameter (except for ortho-Cr₂B₂ which remains FM) reaching a high magnetic moment of 6.39 $\mu_{\rm B}$ per formula unit, a desirable quality as a robust 2D magnet. Finally, the present calculations give rise to high critical temperatures, one of the reasons why MBenes are currently in the spotlight, opening the possibility of their use in room-temperature spintronics. In any case, it is clear that independently of the initial premises, all the MBenes are energetically stable, show a good conductive behavior, and, in some cases, are robust 2D magnets with high critical temperatures.

AUTHOR INFORMATION

Corresponding Author

Isabel M. Arias-Camacho — Faculty of Physics, University of Warsaw, Warsaw PL-02-093, Poland; ⊚ orcid.org/0009-0001-5704-6996; Email: Isabel.Arias@fuw.edu.pl

Complete contact information is available at: https://pubs.acs.org/10.1021/acsomega.3c06539

Notes

The author declares no competing financial interest.

ACKNOWLEDGMENTS

The use of supercomputers at the Interdisciplinary Center for Mathematical and Computational Modelling (ICM) at the University of Warsaw is gratefully acknowledged.

REFERENCES

- (1) Khazaei, M.; Wang, J.; Estili, M.; Ranjbar, A.; Suehara, S.; Arai, M.; Esfarjani, K.; Yunoki, S. Novel MAB phases and insights into their exfoliation into 2D MBenes. *Nanoscale* **2019**, *11*, 11305–11314.
- (2) Barinov, V. A.; Dorofeev, G. A.; Ovechkin, L. V.; Elsukov, E. P.; Ermakov, A. E. Structure and magnetic properties of the α-FeB phase obtained by mechanical working. *Phys. Status Solidi A* **1991**, *123*, 527–534.
- (3) Zhao, X.; Li, L.; Bao, K.; Zhu, P.; Tao, Q.; Ma, S.; Cui, T. Insight the effect of rigid boron chain substructure on mechanical, magnetic and electrical properties of β -FeB. *J. Alloys Compd.* **2022**, 896, 162767.
- (4) Igoa Saldaña, F.; Defoy, E.; Janisch, D.; Rousse, G.; Autran, P.-O.; Ghoridi, A.; Séné, A.; Baron, M.; Suescun, L.; Le Godec, Y.; Portehault, D. Revealing the Elusive Structure and Reactivity of Iron Boride α -FeB. *Inorg. Chem.* **2023**, *62*, 2073–2082.
- (5) Gonzalez Szwacki, N.; Sadrzadeh, A.; Yakobson, B. I. B₈0 Fullerene: An Ab Initio Prediction of Geometry, Stability, and Electronic Structure. *Phys. Rev. Lett.* **2007**, *98*, 166804.
- (6) Gonzalez Szwacki, N. Boron Fullerenes: A First-Principles Study. Nanoscale Res. Lett. 2007, 3, 49.
- (7) Ade, M.; Hillebrecht, H. Ternary Borides Cr_2AlB_2 , Cr_3AlB_4 , and Cr_4AlB_6 : The First Members of the Series $(CrB_2)_nCrAl$ with n=1,2,3 and a Unifying Concept for Ternary Borides as MAB-Phases. *Inorg. Chem.* **2015**, 54, 6122–6135.
- (8) Yousaf, A.; Gilliam, M. S.; Chang, S. L. Y.; Augustin, M.; Guo, Y.; Tahir, F.; Wang, M.; Schwindt, A.; Chu, X. S.; Li, D. O.; et al. Exfoliation of Quasi-Two-Dimensional Nanosheets of Metal Diborides. *J. Phys. Chem. C* 2021, 125, 6787–6799.
- (9) Zhang, B.; Zhou, J.; Sun, Z. MBenes: progress, challenges and future. J. Mater. Chem. A 2022, 10, 15865–15880.
- (10) Xu, T.; Wang, Y.; Xiong, Z.; Wang, Y.; Zhou, Y.; Li, X. A Rising 2D Star: Novel MBenes with Excellent Performance in Energy Conversion and storage. *Nano-Micro Lett.* **2023**, *15*, 6.
- (11) Qi, S.; Fan, Y.; Zhao, L.; Li, W.; Zhao, M. Two-dimensional transition metal borides as highly efficient N₂ fixation catalysts. *Appl. Surf. Sci.* **2021**, *536*, 147742.
- (12) He, C.; Wang, J.; Fu, L.; Zhao, C.; Huo, J. Associative vs. dissociative mechanism: Electrocatalysis of nitric oxide to ammonia. *Chin. Chem. Lett.* **2022**, *33*, 1051–1057.
- (13) Xiao, Y.; Shen, C. Transition-Metal Borides (MBenes) as New High-Efficiency Catalysts for Nitric Oxide Electroreduction to Ammonia by a High-Throughput Approach. *Small* **2021**, *17*, 2100776.
- (14) Mir, S. H.; Yadav, V. K.; Singh, J. K. Efficient CO₂ Capture and Activation on Novel Two-Dimensional Transition Metal Borides. ACS Appl. Mater. Interfaces **2022**, *14*, 29703–29710.
- (15) Jakubczak, M.; Szuplewska, A.; Rozmysłowska-Wojciechowska, A.; Rosenkranz, A.; Jastrzębska, A. M. Novel 2D MBenes—Synthesis, Structure, and Biotechnological Potential. *Adv. Funct. Mater.* **2021**, *31*, 2103048.
- (16) Romero-Muniz, C. e. a.; Law, J. Y.; Moreno-Ramírez, L. M.; Díaz-García, Á.; Franco, V. Using a computationally driven screening to enhance magnetocaloric effect of metal monoborides. *J. Phys. Energy* **2023**, *5*, 024021.
- (17) Dou, M.; Li, H.; Yao, Q.; Wang, J.; Liu, Y.; Wu, F. Roomtemperature ferromagnetism in two-dimensional transition metal borides: A first-principles investigation. *Phys. Chem. Chem. Phys.* **2021**, 23, 10615–10620.
- (18) Wang, S.; Miao, N.; Su, K.; Blatov, V. A.; Wang, J. Discovery of intrinsic two-dimensional antiferromagnets from transition-metal borides. *Nanoscale* **2021**, *13*, 8254–8263.

- (19) Ozdemir, I.; Kadioglu, Y.; Yüksel, Y.; Akıncı, Ü.; Aktürk, O. Ü.; Aktürk, E.; Ciraci, S. Columnar antiferromagnetic order of a MBene monolayer. *Phys. Rev. B* **2021**, *103*, 144424.
- (20) Abdullahi, Y. Z.; Vatansever, Z. D.; Aktürk, E.; Akıncı, Ü.; Aktürk, O. Ü. Novel two-dimensional CrXB₂ (X = Cr, Ru) metal for high Néel temperature antiferromagnetic spintronics. *J. Solid State Chem.* **2021**, 302, 122427.
- (21) Xing, S.; Zhou, J.; Zhang, B.; Sun, Z. Magnetic Superexchange Induced Quantum Phase Transition in Cr_2B_2 MBene. *J. Phys. Chem. C* **2022**, *126*, 14275–14282.
- (22) Mermin, N. D.; Wagner, H. Absence of ferromagnetism or antiferromagnetism in one-or two-dimensional isotropic Heisenberg models. *Phys. Rev. Lett.* **1966**, *17*, 1133–1136.
- (23) Lee, J.-U.; Lee, S.; Ryoo, J. H.; Kang, S.; Kim, T. Y.; Kim, P.; Park, C.-H.; Park, J.-G.; Cheong, H. Ising-Type Magnetic Ordering in Atomically Thin FePS₃. *Nano Lett.* **2016**, *16*, 7433–7438.
- (24) Huang, B.; Clark, G.; Navarro-Moratalla, E.; Klein, D. R.; Cheng, R.; Seyler, K. L.; Zhong, D.; Schmidgall, E.; McGuire, M. A.; Cobden, D. H.; Yao, W.; Xiao, D.; Jarillo-Herrero, P.; Xu, X. Layer-dependent ferromagnetism in a van der Waals crystal down to the monolayer limit. *Nature* **2017**, *546*, 270–273.
- (25) Fei, Z.; Huang, B.; Malinowski, P.; Wang, W.; Song, T.; Sanchez, J.; Yao, W.; Xiao, D.; Zhu, X.; May, A. F.; Wu, W.; Cobden, D. H.; Chu, J. H.; Xu, X. Two-dimensional itinerant ferromagnetism in atomically thin Fe_3GeTe_2 . *Nat. Mater.* **2018**, *17*, 778–782.
- (26) Perdew, J. P.; Burke, K.; Ernzerhof, M. Generalized Gradient Approximation Made Simple. *Phys. Rev. Lett.* **1996**, *77*, 3865–3868.
- (27) Blöchl, P. E. Projector augmented-wave method. *Phys. Rev. B: Condens. Matter Mater. Phys.* **1994**, *50*, 17953–17979.
- (28) Giannozzi, P.; Baroni, S.; Bonini, N.; Calandra, M.; Car, R.; Cavazzoni, C.; Ceresoli, D.; Chiarotti, G. L.; Cococcioni, M.; Dabo, I.; et al. QUANTUM ESPRESSO: a modular and open-source software project for quantum simulations of materials. *J. Phys.: Condens.Matter* **2009**, *21*, 395502.
- (29) Himmetoglu, B.; Janotti, A. Transport properties of KTaO₃ from first-principles. *J. Phys.: Condens. Matter* **2016**, *28*, 065502.
- (30) Momma, K.; Izumi, F. VESTA 3 for three-dimensional visualization of crystal, volumetric and morphology data. *J. Appl. Crystallogr.* **2011**, *44*, 1272–1276.
- (31) Arias-Camacho, I.; Gonzalez Szwacki, N. Exploring the Structural, Electronic, Magnetic, and Transport Properties of 2D Cr, Fe, and Zr Monoborides. *Materials* **2023**, *16*, 5104.
- (32) Bo, T.; Liu, P.-F.; Xu, J.; Zhang, J.; Chen, Y.; Eriksson, O.; Wang, F.; Wang, B.-T. Hexagonal Ti_2B_2 monolayer: a promising anode material offering high rate capability for Li-ion and Na-ion batteries. *Phys. Chem. Chem. Phys.* **2018**, 20, 22168–22178.
- (33) He, Q.; Li, Z.; Xiao, W.; Zhang, C.; Zhao, Y. Computational investigation of 2D 3d/4d hexagonal transition metal borides for metalion batteries. *Electrochim. Acta* **2021**, *384*, 138404.
- (34) Yuan, G.; Bo, T.; Qi, X.; Liu, P. F.; Huang, Z.; Wang, B. T. Monolayer Zr_2B_2 : A promising two-dimensional anode material for Liion batteries. *Appl. Surf. Sci.* **2019**, *480*, 448–453.
- (35) Cococcioni, M.; de Gironcoli, S. Linear response approach to the calculation of the effective interaction parameters in the LDA + U method. *Phys. Rev. B: Condens. Matter Mater. Phys.* **2005**, 71, 035105.
- (36) Timrov, I.; Marzari, N.; Cococcioni, M. Hubbard parameters from density-functional perturbation theory. *Phys. Rev. B* **2018**, *98*, 085127.
- (37) Timrov, I.; Marzari, N.; Cococcioni, M. Self-consistent Hubbard parameters from density-functional perturbation theory in the ultrasoft and projector-augmented wave formulations. *Phys. Rev. B* **2021**, *103*, 045141.
- (38) Hsu, H.; Umemoto, K.; Cococcioni, M.; Wentzcovitch, R. First-principles study for low-spin LaCoO₃ with a structurally consistent Hubbard *U. Phys. Rev. B: Condens. Matter Mater. Phys.* **2009**, 79, 125124
- (39) Timrov, I.; Marzari, N.; Cococcioni, M. HP A code for the calculation of Hubbard parameters using density-functional perturbation theory. *Comput. Phys. Commun.* **2022**, 279, 108455.

- (40) Jia, J.; Li, B.; Duan, S.; Cui, Z.; Gao, H. Monolayer MBenes: prediction of anode materials for high-performance lithium/sodium ion batteries. *Nanoscale* **2019**, *11*, 20307–20314.
- (41) Shin, H.; Kang, S.; Koo, J.; Lee, H.; Kim, J.; Kwon, Y. Cohesion energetics of carbon allotropes: Quantum Monte Carlo study. *J. Chem. Phys.* **2014**, *140*, 114702.
- (42) Zhang, B.; Zhou, J.; Guo, Z.; Peng, Q.; Sun, Z. Two-dimensional chromium boride MBenes with high HER catalytic activity. *Appl. Surf. Sci.* **2020**, *500*, 144248.
- (43) Hu, T.; Wang, M.; Wang, X.; Zhou, Y.; Li, C. Unraveling surface functionalization of $Cr_2B_2T_2$ (T = OH, O, Cl, H) MBene by first-principles calculations. *Comput. Mater. Sci.* **2021**, *199*, 110810.
- (44) Alameda, L. T.; Holder, C. F.; Fenton, J. L.; Schaak, R. E. Partial Etching of Al from MoAlB Single Crystals To Expose Catalytically Active Basal Planes for the Hydrogen Evolution Reaction. *Chem. Mater.* **2017**, 29, 8953–8957.
- (45) Alameda, L. T.; Moradifar, P.; Metzger, Z. P.; Alem, N.; Schaak, R. E. Topochemical Deintercalation of Al from MoAlB: Stepwise Etching Pathway, Layered Intergrowth Structures, and Two-Dimensional MBene. J. Am. Chem. Soc. 2018, 140, 8833–8840.
- (46) Alameda, L. T.; Lord, R. W.; Barr, J. A.; Moradifar, P.; Metzger, Z. P.; Steimle, B. C.; Holder, C. F.; Alem, N.; Sinnott, S. B.; Schaak, R. E. Multi-Step Topochemical Pathway to Metastable Mo₂AlB₂ and Related Two-Dimensional Nanosheet Heterostructures. *J. Am. Chem. Soc.* **2019**, *141*, 10852–10861.
- (47) Zhang, H.; Xiang, H.; Dai, F. z.; Zhang, Z.; Zhou, Y. First demonstration of possible two-dimensional MBene CrB derived from MAB phase Cr₂AlB₂. *J. Mater. Sci. Technol.* **2018**, *34*, 2022–2026.
- (48) Miao, N.; Gong, Y.; Zhang, H.; Shen, Q.; Yang, R.; Zhou, J.; Hosono, H.; Wang, J. Discovery of Two-dimensional Hexagonal MBene HfBO and Exploration on its Potential for Lithium-Ion Storage. *Angew. Chem., Int. Ed.* **2023**, *62*, No. e202308436.
- (49) Bury, D.; Jakubczak, M.; Purbayanto, M. A. K.; Rybak, M.; Birowska, M.; Wójcik, A.; Moszczyńska, D.; Eisawi, K.; Prenger, K.; Presser, V.; Naguib, M.; Jastrzębska, A. M. Wet-Chemical Etching and Delamination of MoAlB into MBene and Its Outstanding Photocatalytic Performance. *Adv. Funct. Mater.* **2023**, 2308156.
- (50) Bhaskar, G.; Gvozdetskyi, V.; Batuk, M.; Wiaderek, K. M.; Sun, Y.; Wang, R.; Zhang, C.; Carnahan, S. L.; Wu, X.; Ribeiro, R. A.; et al. Topochemical Deintercalation of Li from Layered LiNiB: toward 2D MBene. J. Am. Chem. Soc. 2021, 143, 4213–4223.
- (51) Jiang, Z.; Wang, P.; Jiang, X.; Zhao, J. MBene (MnB): a new type of 2D metallic ferromagnet with high Curie temperature. *Nanoscale Horiz.* **2018**, *3*, 335–341.
- (52) Goodenough, J. B. Theory of the Role of Covalence in the Perovskite-Type Manganites [La, M(II)]MnO₃. Phys. Rev. **1955**, 100, 564–573
- (53) Kanamori, J. Crystal Distortion in Magnetic Compounds. *J. Appl. Phys.* **1960**, *31*, S14–S23.
- (54) Anderson, P. W. New Approach to the Theory of Superexchange Interactions. *Phys. Rev.* **1959**, *115*, 2–13.
- (55) Guo, Z.; Zhou, J.; Sun, Z. New two-dimensional transition metal borides for Li ion batteries and electrocatalysis. *J. Mater. Chem. A* **2017**, *5*, 23530–23535.

3.5 PAPER IV: Exposure of MBenes to environmentally hazardous molecules

In the previous articles, the analysis of the stability, electronic, transport, and magnetic properties of pristine MBenes has demonstrated that they possess good qualities as gas sensors or gas capturers, and now it is time to investigate their potential for such applications. The novelty of this work is the use of Cr, Fe and Zr-based MBenes for these purposes because to date, only other research is centered on Cr_2B_2 as sensor of specific organic molecules.

Another novelty respect to previous works arises from the nature of the interaction between a surface and a molecule which involves, among others, the van der Waals forces, which must be accounted for. In this new stage of the investigation, a new approximation include them. For better accuracy, the DFT-D3 correction formulated by Grimme *et al.* [121] has been shown to provide more accurate results by containing three-body terms. Both calculations, with and without the dispersion correction, have described the same trends in the adsorption with only a small increase in the adsorption energies, on the order of a hundredth of eV (consistent with similar works).

However, the results show that molecules are more likely to adsorb on top of metal ions and that the character of such interactions is predominantly chemisorption, with the exception of the CO₂ molecule, which is physisorbed in most cases. In general terms and among the three compounds, the highest values of the adsorption energy are achieved for Zr₂B₂, suggesting that it is more suitable as a gas capturer than Fe₂B₂ or Cr₂B₂. The molecules exhibiting the strongest interactions are precisely those with the ability to form several bonds with the metal atoms of the surface, such as NO₂ or SO₂, and due to the relationship between recovery time and adsorption energy, the recovery of these three MBenes after chemisorption will not be feasible in the short term, limiting the use of the substrata as adsorbers in these specific cases. Moreover, Cr₂B₂ suffers a distortion of its original lattice caused by strong interactions that can become not only a handicap but also a challenge with respect to its reusability as a gas sensor.

Bader analysis reveals that charge transfer occurs predominantly from MBene to gas molecules and displays a correlation between the charge transfer and the adsorption strength, with the exception of NH₃ on the Fe-based MBene where the molecule behaves as a donor: it demonstrates that the

MBene substratum behaves not only as donor but also as acceptor. In addition, analysis of conductivity provides a wider picture pointing to Fe_2B_2 as the substratum with the largest deviations between the pristine sheet and the MBene/molecule system.

In terms of magnetism, the molecular magnetic moments are almost zero when attached to the MBene surface, except for the SO_2 molecule on Cr_2B_2 . However, the total magnetic moments of the MBene/molecule systems have significantly increased in most cases.

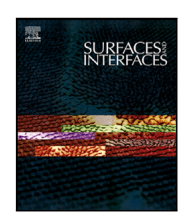
On the basis of these findings, this article concludes that Cr-, Fe-, and Zr-based MBenes could be considered as potential substrata for the detection/capture of gas molecules, potentially paving the way for designing sensor nanodevices based on these materials.



Contents lists available at ScienceDirect

Surfaces and Interfaces





Exposure of MBenes to environmentally hazardous molecules

Isabel M. Arias-Camacho, Nevill Gonzalez Szwacki *

Faculty of Physics, University of Warsaw, Pasteura 5, Warsaw, PL-02093, Poland

ARTICLE INFO

Keywords: Greenhouse gases MBenes First-principles calculations Sensors

ABSTRACT

2D materials are receiving attention due to their high surface-to-volume ratio and stability, making them potentially useful for gas sensing, chemical adsorption, and catalytic applications. MBenes, in particular, are of interest because of their excellent electronic, thermal, transport, mechanical, and physicochemical properties, which make them highly capable of adsorbing small molecules. In this study, we conducted first-principles calculations to investigate the adsorption of eight molecules: CO, CO_2 , H_2O , NH_3 , NO_2 , SO_2 , O_2 , and N_2 . We aimed to assess the potential of Cr_2B_2 , Fe_2B_2 , and Zr_2B_2 as gas adsorbents or gas sensors. Our investigation systematically examined optimal adsorption sites, charge transfer, electronic structure, and magnetism under different theoretical approaches to understand the mechanisms governing the interaction between gas molecules and the MBene substrate. To our knowledge, this is the first time that the potential of Cr_2B_2 , Fe_2B_2 , and Zr_2B_2 MBenes as sensors is evaluated for such collection of gas molecules. Our findings point out that Cr/Fe/Zr-based MBenes are suitable substrates for detecting and capturing gas molecules and can be used to fabricate nanotechnology-based sensors.

1. Introduction

Short-lived climate forcers (SLCFs) have a relatively short lifetime in the atmosphere and can be air pollutants impacting the climate [1]. They can be either radiatively active or influence other radiatively active compounds through chemistry. Direct SLCFs include methane, ozone, short-lived halogenated compounds, and aerosols. Indirect SLCFs include chemically reactive gases like nitrogen oxides, CO, non-methane volatile organic compounds, SO_2 , and NH_3 . The growth of industry and cities requires the development of new materials capable of adsorbing and detecting hazardous contaminants such as CO, NH_3 , NO_2 , and SO_2 . These materials could also be used in green energy production and storage to help decarbonize industry and combat pollution.

In this regard, 2D materials possessing a high surface-to-volume ratio due to their large lateral size and small thickness of a few atomic layers are the focus of recent research on clean technologies [2]. This large surface area, with its rich surface chemistry, favors interactions with molecules, which enables these materials to work as highly sensitive sensors even at low gas concentrations. Moreover, their good conductivity favors their integration into different devices.

MBenes, an emerging family of two-dimensional (2D) transition metal borides, are gaining interest thanks to their unique physical and chemical properties, becoming ideal candidates in applications such as catalysts, electrodes for Li/Na-ion batteries, or sensors, among others.

Other advantages of MBenes are their metallicity and stability in humid environments, high oxidation resistance, and corrosion resistance [3,4]. In this sense, implementing MBenes for sensing, reducing, and adsorbing pollutants is the focus of current research. Xiao et al. [5] have centered their research on 11 different MBenes for $\rm CO_2$ electroreduction (conversion of oxide fuel into a metal form). Moreover, Mir et al. [6] have found them advantageous for the adsorption of molecules, as they do not need surface passivation to be stabilized. Besides that, vacancies have also been found as potential active sites for adsorption [7].

MBenes were first theoretically predicted, but shortly afterward, MoB [8], $\mathrm{Ti}_2\mathrm{B}_2$ [9] and $\mathrm{Cr}_2\mathrm{B}_2$ [10] have been experimentally synthesized by exfoliation of a parent bulk MAB phase, where A, frequently a group IIIA–IVA element, is the removed layer, B is boron and M is the transition metal [6,8,10–12]. The bulk can be exfoliated into 2D flakes because the M–B and B–B bonds are much stronger than the A–B and A–M bonds [13,14]. However, the existing studies are fundamentally theoretical, as the experimental synthesis is still ongoing. To date, density functional theory (DFT)-based calculations predict several MBenes as stable in the hexagonal, tetragonal, and orthorhombic structures and stoichiometries like $\mathrm{M}_2\mathrm{B}_2$, $\mathrm{M}_2\mathrm{B}$, and $\mathrm{M}_3\mathrm{B}_4$, thanks to the electronic deficiency of boron that leads to exotic bonding states [4,13,15–17]. Surface functionalization can influence the electronic properties of the sensor, as demonstrated by Guo et al. [18] who found that Fe₂B₂(OH)₂ and Fe₂B₂F₂ behave as semiconductors whereas Fe₂B₂O₂ is metallic.

E-mail address: gonz@fuw.edu.pl (N. Gonzalez Szwacki).

^{*} Corresponding author.

There is no experimental evidence of the presence of terminal groups in the synthetic surface of MBenes [10].

Given these advantages, many efforts must be put into their large-scale production, which today is a challenge and is in an early stage of development. Different synthesis methods are being investigated in this direction, such as chemical and mechanical exfoliation, CVD, sputtering, or thermal fragmentation, to find a more efficient way of production, reducing costs and manufacturing times [4]. Another important consideration is the extent to which the production impacts the environment because one of the typical etchants used is HF, which is considered highly hazardous, toxic, and corrosive. More research is still needed to assess and overcome their environmental and health impact. Attempts to address this issue are, for example, the development of a fluorine-free hydrothermal-assisted alkaline solution etching method [19] or the use of the sputtering technique to grow Mo₂B₂ from a Mo₂AlB₂ film [20].

In the present study, based on first-principles calculations, we study the effects of several hazardous molecules, CO, CO $_2$, H $_2$ O, NH $_3$, NO $_2$, SO $_2$, O $_2$, and N $_2$ on Cr/Fe/Zr-based M $_2$ B $_2$ MBenes, to understand the adsorption mechanisms and to determine their influence on the properties of the MBene/molecule system. To this end, first, we will start with a brief study of the pristine MBenes to follow with the effects on their properties after the adsorption of the small molecules.

2. Computational methodology

Our first-principles calculations have been performed within the framework of the density functional theory (DFT) using the Quantum ESPRESSO (QE) suite of codes [21]. The Perdew-Burke-Ernzerhof (PBE) [22] gradient corrected exchange-correlation functional is used combined with the projector plane-wave (PAW) pseudopotentials [23, 24]. To ensure the accuracy of the total energy, E_{tot} , the electronic wave functions have been expanded in plane-wave basis sets with an energy cutoff of 60 Ry while the Brillouin Zone (BZ) has been sampled with a Γ -centered k-point grid of $12 \times 12 \times 1$ mesh points for the geometry optimization and 24 × 24 × 1 for the DOS calculations, in the Monkhorst-Pack scheme, with Gaussian smearing of 0.02 Ry (the convergence tests of E_{tot} respect to the energy cutoff and the k-point grid are shown in Fig. A.11). The unit cell of the pristine structures (a $2 \times 2 \times 1$ supercell) consists of eight boron atoms and eight atoms of the transition metals Cr, Fe, and Zr. A vacuum space of 15 Å along the normal direction is used, to avoid interactions between adjacent MBenes. The cell has been allowed to relax until the residual forces on the atoms were less than 0.3 meV/Å. The convergence threshold for E_{tot} was set to 10^{-5} Ry. For optimizing the structures with the molecules, the residual force and the E_{tot} convergence thresholds have been set to 3 meV/Å and 10⁻⁴ Ry, respectively. Moreover, the Hubbard U correction has been applied due to the inaccuracy of LDA or GGA in describing the self-interaction of the partially occupied Kohn-Sham (KS) orbitals. A $\it U$ equal to 4.3, 4.3, and 1.8 eV is taken for the Cr-, Fe-, and Zr-based MBenes, respectively, as calculated in our previous work [16] utilizing the linear response approach [25] based on the density functional perturbation theory (DFPT) [26,27]. The DFT+U approach is implemented in QE in the HP code [28].

Van der Waals (vdW) interactions are not properly accounted for by standard local and semilocal density functional approximations (LDA or GGA). In this sense, including such dispersion effects is crucial to accurately describe systems with important intermolecular interactions, like weakly-bonded systems. Therefore, to account for the van der Waals forces, a dispersion-corrected framework (DFT-D3) [29] is used. Davis et al. demonstrated that, in opposition to D2 and optPBE dispersion corrections, the D3 correction (which correction contains three-body terms) gives, in some cases, more accurate results [30,31].

The cohesive energy per atom, E_{coh} , for the pristine structures, that is, the released energy when the compound dissociates into isolated free atoms, has been calculated as:

$$E_{coh} = (E_{\rm M_2B_2} - n_{\rm B}E_{\rm B} - n_{\rm M}E_{\rm M})/(n_{\rm B} + n_{\rm M}),$$

being M the TM atom, $E_{\rm M_2B_2}$ is the $E_{\rm tot}$ of the MBene, $E_{\rm B}$ and $E_{\rm M}$ are the total energies of the isolated atoms (boron and transition metal atoms), and $n_{\rm B}$ and $n_{\rm M}$ are the numbers of boron and TM atoms per unit cell, respectively, directly obtained from the spin-polarized calculations.

Similarly, the adsorption energy, E_{ads} , between the molecule and the pristine MBenes has been evaluated from:

$$E_{ads} = E_{M_2B_2 + \text{molecule}} - E_{M_2B_2} - E_{\text{molecule}},$$

where $E_{\rm M_2B_2+molecule}$ is the total energy of the system MBene + molecule, $E_{\rm M_2B_2}$ is the total energy of the pristine sheet and $E_{\rm molecule}$ is the total energy of the isolated molecule. From this definition, negative E_{ads} values lead to energetically favorable adsorptions.

Another important descriptor is the recovery time, \mathbf{t}_{rec} , which estimates the recovery performance of the sensor and is calculated as:

$$t_{rec} = v^{-1} e^{-E_{ads}/k_B T},$$

where k_B is the Boltzmann constant in eV/K, T is the temperature, set as 300 K in the present work, and ν is the attempt frequency taken as $10^{12}~{\rm s}^{-1}$ based on previous works [17,32–34].

The charge transferred between the MBene and the molecule during the interaction was obtained by performing Bader analysis [35]. Of our interest is the charge difference computed as:

$$\Delta \rho = \rho_{\text{M}_2\text{B}_2 + \text{molecule}} - \rho_{\text{M}_2\text{B}_2} - \rho_{\text{molecule}},$$

being $ho_{M_2B_2+molecule}$ the charge of the complete system substrate+molecule, $ho_{M_2B_2}$ the charge of the corresponding pristine sheet and $ho_{molecule}$ the charge of the isolated molecule.

For all structures, spin-polarized calculations are performed, and four different magnetic configurations, one ferromagnetic (FM) and three antiferromagnetic (AFM) (see Fig. B.12), have been considered to determine the most energetically favorable.

To calculate the electron conductivity, we have used the BoltzTrap2 code [36,37] in the constant relaxation time approximation framework (the relaxation time constant τ is approximated as 0.8×10^{-14} s). Finally, all the visualizations were performed using the Visualization for Electronic and STructural Analysis (VESTA) software [38].

3. Results and discussion

3.1. Structural, electronic, and magnetic properties of pristine MBenes

In Fig. 1, we show the minimal energy configurations and the electronic structure of the pristine MBenes after structural optimization. In contrast to MXenes, MBenes can be stabilized without the need for surface passivation [10], which implies an advantage in investigating the behavior of their surfaces [46] under different chemical or physical processes. Each MBene presents an orthorhombic structure with Pmma (no. 51) space group symmetry, where six neighbors surround each atom. The buckled bilayers of boron are sandwiched between transition metal (TM) layers. The resulting lattice parameters and cohesive energies are shown in Table 1 and qualitatively, and also in some cases quantitatively, agree with other works [6,15,16,39-43]. The MBene's thickness (th) is obtained from the vertical distance between the capping TM layers. The shortest TM-B distance corresponds to Fe₂B₂ (2.090 Å) and the largest distance, to Zr₂B₂ (2.479 Å). The cohesive energies are 5.040 eV/atom for Cr₂B₂, 5.328 eV/atom for Fe₂B₂, and 7.295 eV/atom for Zr₂B₂. Those large values are an indication of a high bond strength and help to determine that the structure has a good thermodynamic stability [47]. Moreover, the values are close in magnitude to those reported for MXenes [48]. The results differ from those of our previous works [15,16] because, in the present study, we have used the Hubbard U correction and a different unit cell size. However, the trends (e.g., increasing E_{coh} from Cr_2B_2 to Zr_2B_2) and the order of magnitudes are very close to those reported before. Furthermore, we

Table 1 Lattice parameters a and b (in Å), thickness (th, in Å), distance between TM and boron (TM–B, in Å), distance between boron and boron (B–B, in Å), and cohesive energy (E_{coh} , in eV).

	MBene a					b						th				d _{TM} -	-B			$d_{\mathrm{B-B}}$		E_{coh}							
This work	Cr ₂ B ₂ 2.8	384				2.870						3.071				2.35				1.605		5.05							
	Fe ₂ B ₂ 2.8	304				2.812						2.385				2.09				1.771		5.33							
	Zr_2B_2 3.0	084				3.281						2.838				2.48				1.720		7.30							
Other works	s Cr ₂ B ₂ 2.8	885 [15] 2	2.860 [6] 2.930	[39]	2.870	[15]	2.850	[6] :	2.870	[39]	2.122	[15]			2.10	[15]	2.11 [[6]	1.810	[15]	6.22	[15]	4.54	[16]	4.79	[40]	6.30	[41]
	Fe ₂ B ₂ 2.8	323 [1 <mark>5</mark>] 2	2.800 [6] 2.770	[39]	2.787	[15]	2.680	[6]	2.820	[39]	2.134	[15]	2.130	[42]	2.04	[15]	2.05 [[6]	1.813	[15]	6.90	[15]	6.24	[16]	4.72	[40]	5.60	[42]
	Zr_2B_2 3.0	084 [1 <mark>5</mark>] 3	3.07 [4	3]		3.281	[15]	3.27 [43]			2.817	[15]	2.840	[43]	2.46	[15]	2.43 [[43]	1.721	[15]	8.05	[15]	7.58	[16]	7.74	[44]	7.75	[45]

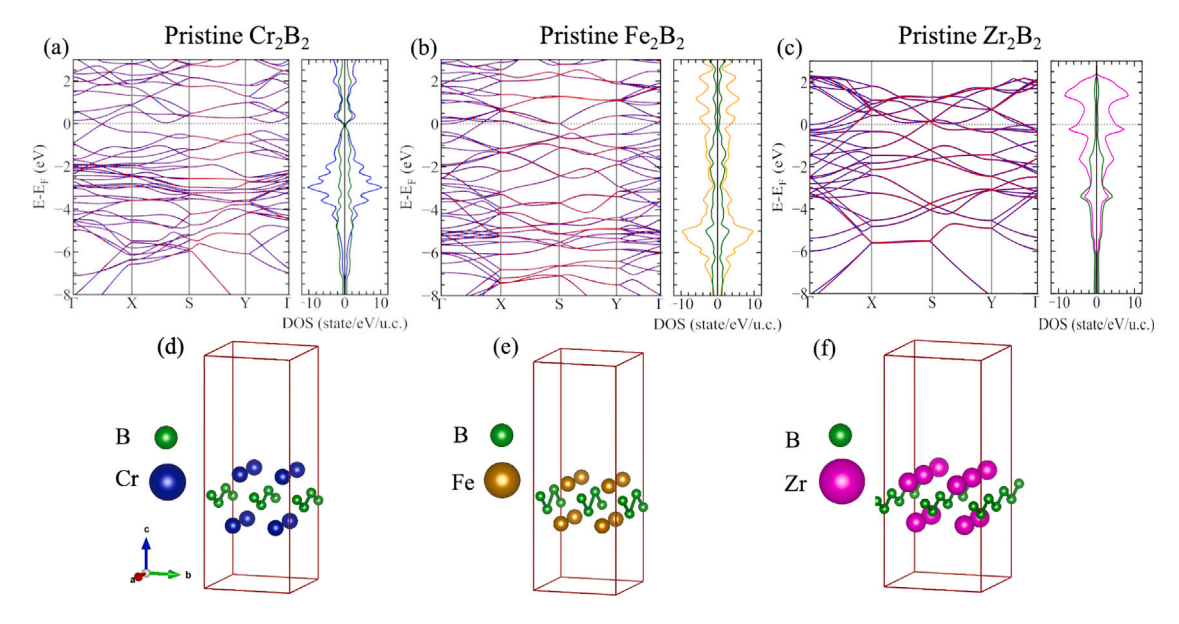


Fig. 1. (a-c) Band structure and projected density of states (PDOS) of the studied pristine MBenes. Majority and minority spin bands are plotted in blue and red, respectively. Boron's contribution to the PDOS is represented in green, and Cr, Fe, and Zr are represented in blue, orange, and magenta, respectively. The Fermi energy in the plots has been set to zero. (d-f) Minimum energy configurations of the pristine MBenes. (For interpretation of the references to color in this figure legend, the reader is referred to the web version of this article.)

corroborated in our previous work [15] the dynamic stability of the studied structures. Mir et al. [6] also confirmed the nonexistence of imaginary frequencies in the phonon dispersion relation.

The electronic properties of our pristine MBenes have been studied considering the spin-polarized projected density of states (PDOS) and the band structure is shown in Fig. 1. This study concludes that all the pristine compounds are metallic, with partially occupied bands crossing the Fermi level, in accordance with previous findings [7]. However, Cr_2B_2 is semimetallic with a very small overlap between the bottom of the conduction band (CB) and the top of the valence band (VB).

Moreover, from the Bader analysis, we conclude that the charge transfer always occurs from the metal (which loses nearly one electron) to the boron ion, whose charge increases from three to around four electrons. Also, the resulting high conductivity values of the pristine MBenes are similar to those found in the literature [6]. The averaged values between the σ_{xx} and σ_{yy} components are $7.60\times10^{19},\,1.12\times10^{20},\,$ and $1.07\times10^{20}\,\,\Omega^{-1}\cdot m^{-1}\cdot s^{-1}$ for Cr_2B_2 , Fe_2B_2 and Zr_2B_2 , respectively. Turning to magnetic properties, our results show that both Cr- and Febased MBenes have adopted an antiferromagnetic (AFM) ground state but with two different arrangements, shown in Fig. 2, of the atomic magnetic moments, whereas the Zr-based MBene remains nonmagnetic. The absolute values of the magnetic moments of Cr and Fe are 3.55 and 2.64 $\mu_{\rm B}$, respectively, and there is also some polarization in the boron chains of 0.02 and 0.07 $\mu_{\rm B}$, respectively.

3.2. Adsorption of hazardous molecules on orthorhombic MBenes

3.2.1. Structural behavior and adsorption energies

Taking into consideration the symmetry of the unit cell, we have established four starting configurations to set the molecules (Fig. 3):

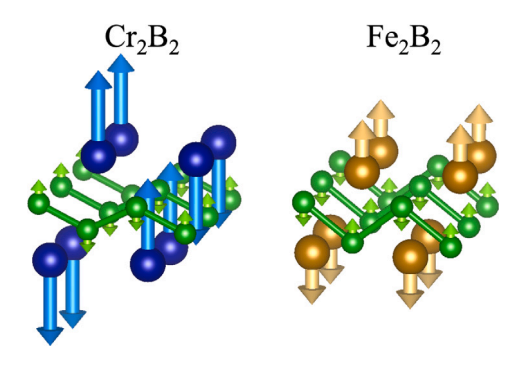


Fig. 2. The ground state antiferromagnetic configurations for Cr_2B_2 (left) and Fe_2B_2 (right). B, Cr and Fe are described by green, blue and gold spheres, respectively. (For interpretation of the references to color in this figure legend, the reader is referred to the web version of this article.)

on top of a metal atom (TopM), on top of a boron atom (TopB), in a bridge position between a metal and a boron atom (Bridge), and over a metal atom with a position on the bottom plane (Hollow).

In the case of the CO molecule, we have considered two different orientations with respect to the monolayer: with either O or C pointing towards the MBene. Moreover, two different starting orientations have also been considered for the diatomic molecules: vertical and horizontal. In total, eleven possible adsorption configurations have been considered in our calculations (Appendix D shows a complete set of results). The most stable sites of the molecules after the optimization (see Figs. 4, 5, and 6) indicate that the adsorption energies are related

Table 2 Adsorption energy (E_{ads} , in eV), charge transfer (Δq , in e), and recovery time (t_{rec}) for each molecule interacting with the MBene surface. Some values for recovery times are highlighted: those in bold are the most suitable for sensing purposes, and those enclosed in boxes are better for capture.

		CO	CO_2	H_2O	NH_3	NO_2	SO_2	O_2	N_2
Cr ₂ B ₂	E_{ads}	-4.76	-0.36	-0.37	-3.78	-5.92	-4.81	-5.83	-0.79
	Δq	-0.33	-0.07	-0.08	-0.02	-0.77	-1.24	-2.67	-0.18
	t_{rec}	years	1.116 μs	1.643 μs	years	years	years	years	18.68 s
Fe_2B_2	E_{ads}	-0.89	-0.20	-0.49	-0.66	-1.94	-1.50	-1.89	-0.25
	Δq	-0.31	-0.05	-0.04	0.03	-0.72	-0.93	-1.26	-0.14
	t_{rec}	14.9 min	2.290 ns	170.5 μs	0.123 s	years	years	years	15.84 ns
$\mathbf{Zr}_{2}\mathbf{B}_{2}$	E_{ads}	-3.37	-3.27	-1.01	-1.11	-11.06	-5.64	-9.01	-2.31
	Δq	-1.97	-2.19	-0.23	-0.07	-4.57	-2.29	-2.38	-1.75
	t_{rec}	years	years	1.07 days	51.36 days	years	years	years	years

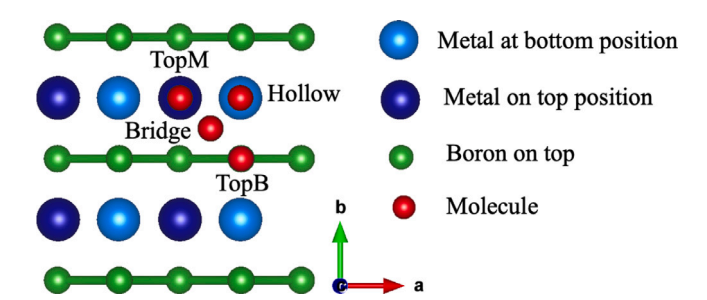


Fig. 3. Starting configurations for the studied molecules on a generic MBene surface.

to the distances between each of them and the MBene and that they are more likely to adsorb on top of the metal ions.

In Table 2, we summarize the adsorption energies of the molecules together with the charge transfers (CTs) and recovery times. From these values, two first observations can be drawn: the adsorption energies are similar to those reported in the literature [17,49,50], and the charge transfer between the MBene and the molecule is related to the strength of the interaction (except for NH₃ for which a small charge transfer is obtained). In the following, chemisorption will be considered when the adsorption energies are larger than 0.2 eV, and the distance between two atoms is less than 3.0 Å [51-53]. In contrast, the rest of the interactions can be considered physisorption. We have observed an enhancement of adsorption energy values after the inclusion of the van der Waals correction, on average, by 0.37, 0.17, and 0.22 eV for the molecules adsorbed on Cr₂B₂, Fe₂B₂, and Zr₂B₂, respectively, although the adsorption trends and final optimal sites remain the same in comparison with standard DFT. A very similar scenario was reported for the adsorption of NH3, NO, NO2, and CO molecules on borophene [54] for which the inclusion of the dispersion correction results in an increase of the adsorption energy ranging between 0.16 and 0.34 eV. The same increase was observed for the adsorption of certain organic molecules on Ag(111) [55] or Fe(100) [56] and water on metals [57].

The reported (see Table 3) values for CO, $\rm CO_2$, $\rm NH_3$, and $\rm NO_2$ adsorbed on other 2D materials like borophene (with adsorption energies of -1.38, -0.36, -1.75, and -2.32 eV, respectively) [58] or borophene/ $\rm MoS_2$ heterostructure (-1.15, -0.64, -1.52, and -2.12 eV, respectively) [59] are in the same order of magnitude, being even higher than the values for graphene (-0.01, -0.05, -0.03, and -0.07 eV, respectively) [60,61], $\rm MoS_2$ (-0.44, -0.33, -0.16, and -0.14 eV, respectively) [62,63], phosphorene (-0.32, -0.41, -0.50, and -0.60 eV, respectively) [64], silicene (-0.18, -0.04, -0.60, and -1.37 eV, respectively) [65], or germanene (-0.16, -0.10, -0.44, and -1.08 eV, respectively) [66]. It is noteworthy the closeness between our results and the values for borophene, not only from a quantitative perspective but also in the behavior, yielding in both cases the $\rm CO_2$ molecule the lowest adsorption energy. This coincides with the experiment [70],

Table 3 Reported adsorption energies, E_{ads} (in eV), for other representative 2D materials.

Material	CO	CO_2	NH_3	NO_2
buckled-B ^j	-0.76	-0.90	-1.96	-2.84
buckled-B ^a	-1.38	-0.36	-1.75	-2.32
β_{12} -B ^{k,l,m}	-1.19	-0.18	-0.94	-1.31
χ_3 -B ^{k,n}	-0.44		-1.11	-1.80
$(\beta_{12} + \chi_3) - B^k$			-1.13	-1.89
			-1.48	-2.14
Boroph./MoS ₂ ^b	-1.15	-0.64	-1.52	-2.12
$MoS_2^{e,f}$	-0.44	-0.33	-0.16	-0.14
Graphene ^{c,d,j}	-0.01	-0.05	-0.03	-0.07
Phosphoreneg	-0.32	-0.41	-0.50	-0.62
Silicene ^h	-0.18	-0.04	-0.60	-1.37
Germanene ⁱ	-0.16	-0.10	-0.44	-1.08

- ^a Ref. [58].
- ^b Ref. [59].
- c Ref. [60].
- ^d Ref. [61].
- e Ref. [62].
- ^f Ref. [63].
 ^g Ref. [64].
- h Ref. [65].
- i Ref. [66].
- ^j Ref. [53].
- ^k Ref. [67].
- ¹ Ref. [68].
- m Ref. [54].
- ⁿ Ref. [69].

which points to a physisorption nature of the interaction, ruled by vdW forces.

In most cases, the highest values of the adsorption energy are achieved for Zr_2B_2 , suggesting that Zr_2B_2 is more suitable as a gas capturer than Fe_2B_2 . Therefore, Fe_2B_2 serves better as a sensor due to the small charge transfer of only 0.05, 0.04, or 0.03 electrons for CO, CO_2 , and NH_3 , an indicator that physisorption takes place. The adsorption trends of the three MBenes are similar due to the ability of the SO_2 and NO_2 molecules to form several bonds with the metal atoms of the surface, leading to larger adsorption energies, which indicate chemisorption.

In general, the original structure of the corresponding MBene is well maintained after the adsorption of the molecule. An exception is Cr_2B_2 whose boron chains, in specific cases (after the adsorption of CO, NH₃, NO₂, and SO₂), become planar instead of keeping the typical zig-zag shape characteristic of the orthorhombic M_2B_2 MBenes, what is visible in the upper row of Fig. 4). Moreover, the arrangement of boron atoms in these particular situations (see bottom row of Fig. 4) resembles the structure of the hexagonal phase of M_2B_2

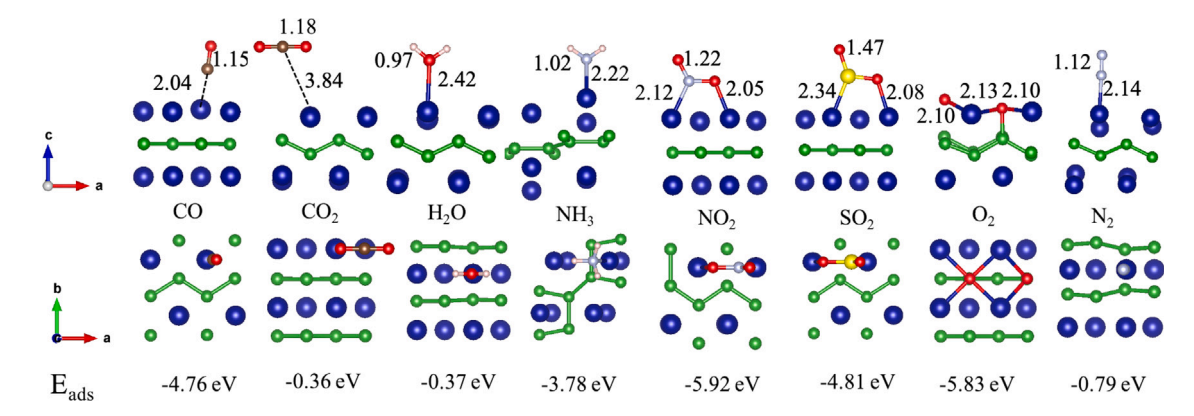


Fig. 4. Side view (top row) and top view (bottom row) of the adsorbed molecules on Cr₂B₂. Bond distances and adsorption energies are indicated.

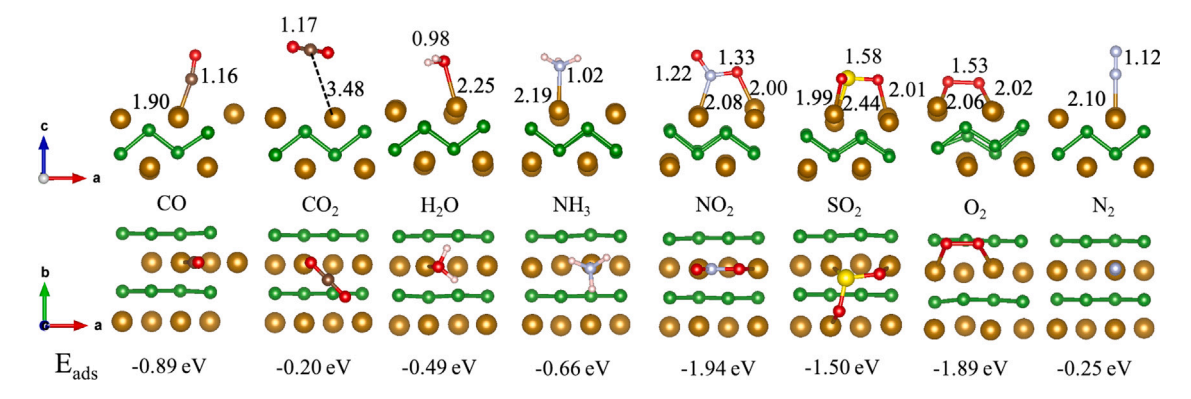


Fig. 5. Side view (upper row) and top view (bottom row) of the adsorbed molecules on Fe₂B₂. Bond distances and adsorption energies are indicated.

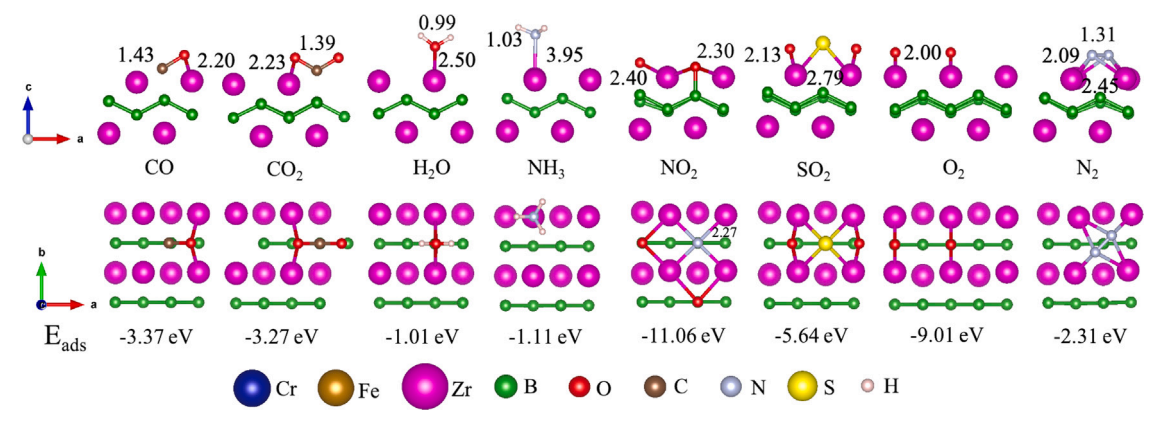


Fig. 6. Side view (upper row) and top view (bottom row) of the adsorbed molecules on Zr₂B₂. Bond distances and adsorption energies are indicated.

MBenes. This deformation reflects the degree of the interaction between the molecules and the MBene, caused by the chemisorption. Also, the oxygen molecule dissociates into two O atoms that bond to two metal and boron atoms on the surface. These cases correlate with very high adsorption energies, indicating a strong interaction. Compared to the other cases, the adsorption energy between the water molecule and this MBene is relatively small, indicating that any device based on the $\rm Cr_2B_2$ MBene will not be significantly affected by humidity.

In the case of the Fe-based MBene, we find a decrease in the adsorption energies with respect to the other studied MBenes, and there are no significant distortions in the structure. The CO molecule has the carbon atom oriented towards the surface. When started vertically, the oxygen molecule aligns to the surface after structural optimization and ends horizontally adsorbed on the substrate. A similar result is obtained for the case of Cr_2B_2 . Finally, the Zr-based MBene behaves differently

from the other two MBenes due to the highest adsorption energies among all and even the dissociation of several molecules, including $NO_2,\,SO_2,$ and $O_2.$ Also, the Zr ion bonds with the oxygen atom of the CO and CO_2 molecules (making this MBene suitable for carbon dioxide capture), whereas Cr and Fe ions tend to interact with their respective carbon atoms, and another difference observed is that the N_2 molecule is adsorbed horizontally on the Zr_2B_2 surface, in contrast to the vertical orientation adopted on Cr_2B_2 and Fe_2B_2 surfaces.

The recovery time gives an idea of the time that the sensor takes, in the absence of the gas, to pass from a certain response (e.g., 90% of the maximum response when the gas is injected) to a certain percentage of it (e.g., 10%) when the gas is removed. It depends on the adsorption energy and, hence, on the interaction strength between the MBene and the molecule. At the same time, the molecules undergo adsorption and desorption processes, which are in dynamic equilibrium. In this sense,

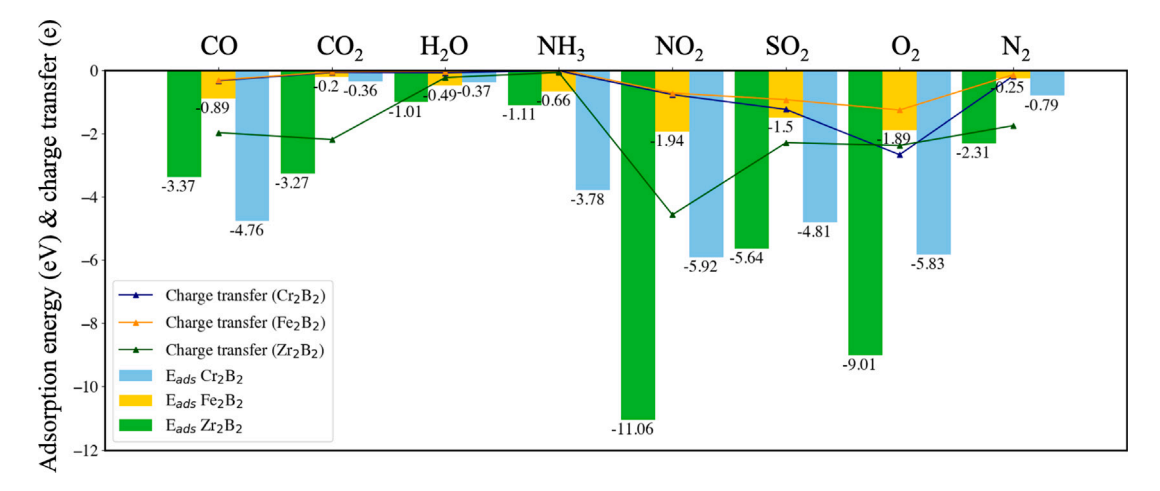


Fig. 7. Adsorption energies compared with the amount of charge transferred from the MBene surface to the molecule. The values of the adsorption energies are given below each bar.

it is a significant parameter for gas sensors that must be considered but always be interpreted carefully because it is only an indicator and does not accurately measure the time required for the sensor to recover. The moderate adsorption energies for Cr₂B₂ and Fe₂B₂ deliver shorter recovery times (in the order of nanoseconds and seconds), a similar order of these observed for MXenes [71,72], making them more suitable as sensors, for specific molecules, than Zr₂B₂, which is more indicated as a gas adsorbent due to its extremely high recovery values (in the order of days and years). The high recovery time values coincide with the strong interaction with the surface and even the dissociation of some of the studied molecules. For example, the surface of Zr₂B₂ causes the rupture of the NO2, SO2, and O2 molecules whose atoms bond with the metal and boron atoms of the surface. Also, the structure of the Cr-based MBene gets severely distorted after adsorbing CO, NH3, NO2, SO₂, and O₂ molecules. Therefore, we can conclude that Zr₂B₂ would be unsuitable as a sensor but could have other useful applications like a gas capturer to remove harmful gases.

3.2.2. Electronic properties

In this section, we examine, using the Bader analysis and the projected density of states (PDOS) (see Fig. D.13), the changes in the electronic structure and the charge transfer after the adsorption of the molecules and the consequent structural distortions. The charge transfer occurs predominantly from the MBene to the gas molecules. The Bader analysis reveals the consistency between the charge transfer and the adsorption strength as it is shown in Fig. 7, with the CO₂ and H2O molecules as weakly bound species on Cr2B2 (with small charge transfer of -0.07 and -0.08 e, respectively) and Fe₂B₂ (with -0.05 and -0.04 e, respectively) and, on the contrary, the NO2 and SO₂ molecules on Cr₂B₂ (with charge transfer -0.77 and -1.24 e) and Fe₂B₂ (with charge transfer -0.72 and -0.93 e) as strongly interacting molecules. For Zr₂B₂, the H₂O and NH₃ molecules show the smallest adsorption energies (-1.00 and -1.11 eV, respectively) and charge transfers (-0.23 and -0.07 e, respectively) among all the molecules involved in this study.

In Fig. 8, we plot the charge difference between the pristine and the pristine+molecule systems, where the yellow areas mean electron gain and the blue areas, electron loss. From the figure, it is clear that the charge is transferred normally from the surface towards the molecule and that the CO, CO_2 , H_2O , and NH_3 molecules show the smallest values of charge transfer, which is consistent with the numerical results from the Bader analysis. A curiosity found in the results is that NH_3 on Fe_2B_2 behaves as a donor, that is, the charge transfer happens from the molecule to the Fe-based MBene, similar to other works [17] and to the interaction of this molecule on similar substrates [67], demonstrating

that the MBene substrate not only behaves like a donor but also like an acceptor of charge.

A general trend in all the MBenes is that the CO2 molecule does not significantly alter the electronic structure of the MBenes since it introduces localized states that are deep in energy (between -10 and -5 eV approximately). For Cr₂B₂, the Fermi level of the pristine structure lies on a minimum in the density of states. However, the system remains metallic since the Fermi energy crosses a nonzero PDOS region (see Fig. 1). The most significant changes at this level are observed for the CO, NH3, NO_2 , SO_2 , and O_2 molecules, while H₂O has an almost negligible effect on the electronic properties around the Fermi level (see Fig. D.13). Except for SO2, such changes consist of a broadening of the PDOS, with respect to the pristine cases, due to hybridization between the boron and the metal atoms because the contributions of the molecules are located deeper in energies (between -5 and -10 eV for CO and NH₃, -1.5 and -12 eV for NO₂, -7 and -12 eV for N₂). This redistribution of states is tightly related to the interaction of the molecules with the MBenes' surface and, hence, with the observed structural distortions (see Fig. 4). SO₂ is the only molecule contributing to the PDOS with states surrounding the Fermi level.

The contribution of molecules to the PDOS is significant for CO, NO_2 , SO_2 , and O_2 interacting with Fe_2B_2 (see Fig. D.13). This correlates with the strongest adsorption energies derived from the multiple bonds between the atoms of the molecules and Fe, leading to the highest values of transferred charge values.

The PDOS of the pristine Zr-based MBene (Fig. 1) shows that the main contribution at the Fermi level comes from the Zr atoms, and it lies near (but not exactly on) a peak. This peak results shifted after the adsorption of each molecule what leads to interesting differences in the conductivity that will be discussed in the next section. The strong interaction between NO_2 , SO_2 , and O_2 molecules and Zr_2B_2 is reflected in the redistribution of states surrounding the Fermi level.

3.2.3. Conductivity

The changes in conductivity, $\sigma = (\sigma_{xx} + \sigma_{yy})/2$ (see Appendix E), after the molecular adsorption, with respect to the pristine MBenes are shown in Fig. 9. The biggest conductivity deviations from pristine Cr_2B_2 correspond to the NO_2 and SO_2 molecules, which have two atoms (nitrogen and oxygen, sulfur and oxygen) bounded to two Cr atoms and produce an enhancement in the resistivity, coming from the backscattering of electrons introduced by the molecules.

The same molecules show the largest deviations when are adsorbed on Fe_2B_2 , and result strongly bonded to this MBene. The hybridization between the orbitals of the SO_2 molecule and the d states of Fe at the Fermi level is evident. Also, the O_2 molecule causes an important drop

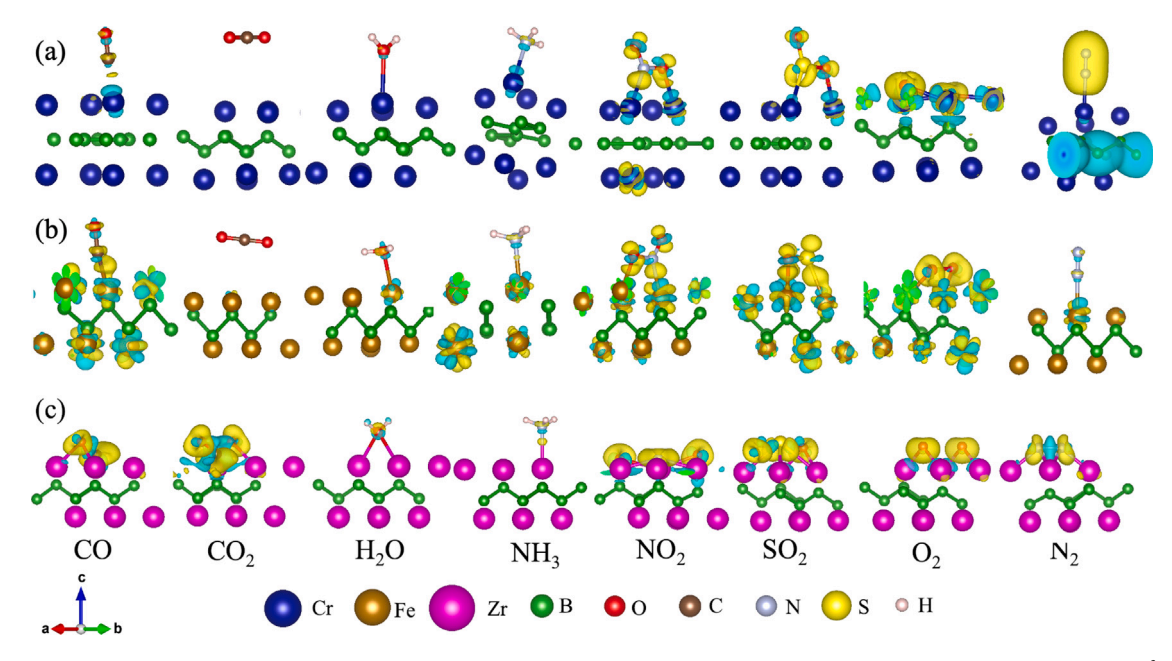


Fig. 8. Charge difference, $\rho_{\text{MBene/molecule}}(\vec{r}) - \rho_{\text{MBene}}(\vec{r}) - \rho_{\text{molecule}}(\vec{r})$, between the pristine and the pristine+molecule systems [the isosurfaces are taken at 0.07 $e/\text{\AA}^3$ (0.01 e/bohr^3)]. (a), (b), and (c) represent the systems $\text{Cr}_2\text{B}_2/\text{molecule}$, $\text{Fe}_2\text{B}_2/\text{molecule}$, and $\text{Zr}_2\text{B}_2/\text{molecule}$, respectively. The yellow areas mean electron gain and the blue areas, electron loss.

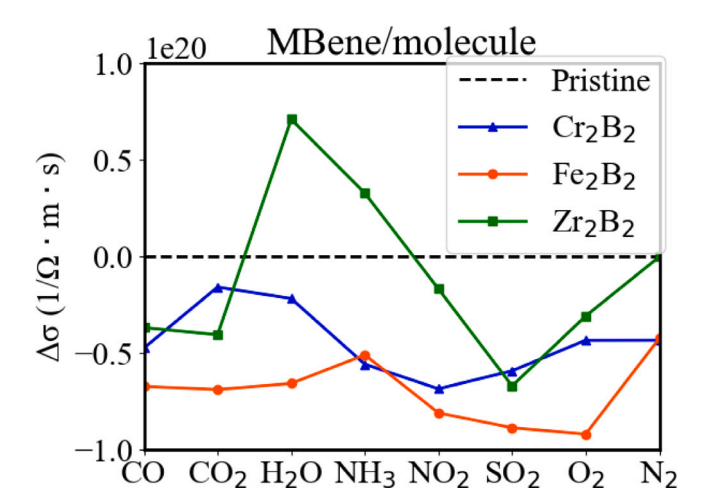


Fig. 9. Variation in conductivity, $\sigma=(\sigma_{xx}+\sigma_{yy})/2$, after the molecule adsorption respect to each pristine value.

in the conductivity due to the double bonding of its constituent atoms to the metals of the surface.

The adsorption of molecules on Zr_2B_2 is causing differences in the contribution of Zr at the Fermi level, which is responsible for the deviations in conductivity with respect to the pristine value. The states at the Fermi level are enhanced after the adsorption of H_2O and NH_3 , which could explain the relative increase in the conductivity. On the other hand, the dissociation of SO_2 on this MBene leads to a drop in the conductivity.

Fig. E.14 shows the components of the conductivity tensor for each system (see Appendix E). As expected, the σ_{zz} component (normal to the surface) is always negligible. Conductivity in $\mathrm{Cr_2B_2}$ is dominated by the σ_{yy} component for both the pristine and the MBene/molecule systems, whereas for $\mathrm{Fe_2B_2}$ the σ_{xx} component is more important. Still, $\mathrm{Zr_2B_2}$ shows an inversion between the pristine sheet (dominated by the σ_{yy} component) and the system MBene/molecule, which always results dominated by the component σ_{xx}).

3.2.4. Magnetism

Now, we will describe the magnetic properties of the studied systems. Magnetism was not always taken into account in similar studies. In the few previous studies that exist in the literature [18,39-42,73], the focus of the attention was to use the MBenes as robust magnets with high Curie Temperatures. Still, considering that Fe, Cr, and Zr are transition metals, we found the description of the magnetic properties of MBenes interesting. As mentioned above, we have started with two different magnetic configurations for each pristine MBene. The ground state of two of our MBenes is AFM, although in different configurations (see Fig. 2), whereas Zr₂B₂ is nonmagnetic. Focusing on the systems with magnetic properties, the electronic configurations of Cr and Fe are [Ar] $3d^4$ $4s^2$ and [Ar] $3d^6$ $4s^2$, respectively. Following the Pauli exclusion principle and Hund's rules, the magnetic moments of the freestanding metals are 4 and 3 $\mu_{\rm B}$ for Cr and Fe, respectively. In contrast, the magnetic moments of Cr and Fe in Cr₂B₂ and Fe₂B₂ are 3.55 and 2.64 $\mu_{\rm B}$, respectively, which are however close to the values for isolated atoms. It is also important to mention that the Bader analysis shows that some charge (more than half of an electron) is transferred from the transition metal to the boron atom. Consequently, some magnetic moment is also localized on the B atoms. This induced spin polarization is around 0.02 and 0.07 μ_B in Cr_2B_2 and Fe_2B_2 , respectively.

Figs. 10a and 10b show isosurface plots for the difference between the electronic densities corresponding to spins up and down for $\text{Cr}_2\text{B}_2/\text{molecule}$ and $\text{Fe}_2\text{B}_2/\text{molecule}$, respectively [the isosurfaces are taken at 0.3 $e/\text{Å}^3$ (0.05 e/bohr^3)]. The blue areas show predominantly minority spin regions, whereas the yellow areas show majority spin regions. Table 4 summarizes the total magnetic moments of the MBene/molecule system (per unit cell) and the resulting magnetic moment on the molecule upon its adsorption on the surface of the MBene. In most cases, the magnetic moment induced in the molecule is small. On the other hand, important changes arise in the magnetism of the MBene/molecule system, with an increase in the values from 0.00 μ_{B} for the AFM pristine MBenes to -0.30, 1.64, -0.28. -0.45 and -0.26 μ_{B} for CO, NH₃, NO₂, SO₂, and O₂, respectively, on the Cr-based MBene and -0.28, 0.33, 0.45, 1.23, 1.30, and 1.68 μ_{B} for CO, H₂O, NH₃, NO₂, SO₂, and O₂, respectively, on the Fe-based MBene.

We have performed spin-polarized calculations of all the isolated molecules, concluding that all the molecules present a net magnetic

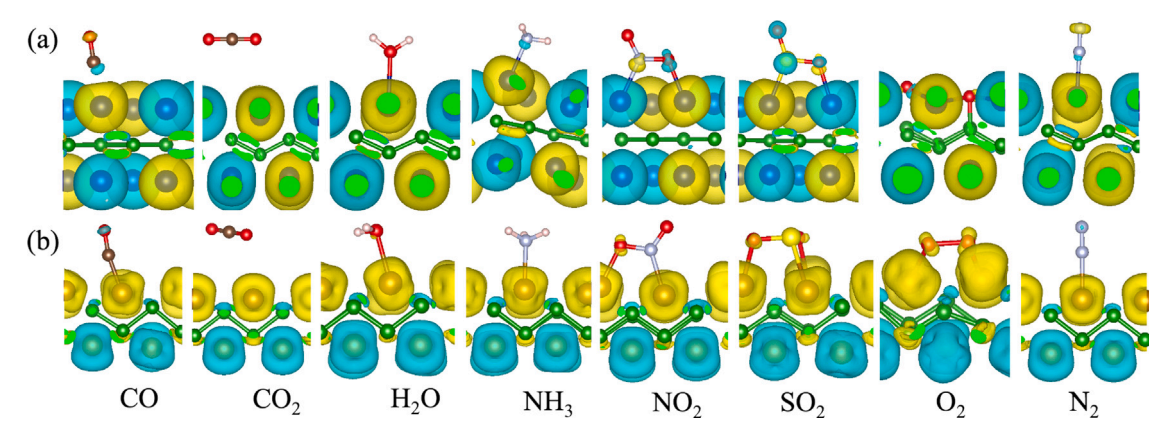


Fig. 10. Spin density difference, $\rho^{\uparrow}(\vec{r}) - \rho^{\downarrow}(\vec{r})$, for (a) $Cr_2B_2/molecule$ and (b) $Fe_2B_2/molecule$ [the isosurfaces are taken at 0.3 e/\mathring{A}^3 (0.05 $e/bohr^3$)].

Table 4 Total magnetic moment, $\mu_{tot.}$, and molecular magnetic moment, $\mu_{mol.}$, in $\mu_{\rm B}$, for each MBene/molecule system.

		CO	CO ₂	H_2O	NH_3	NO_2	SO_2	O ₂	N_2
Cr_2B_2	$\mu_{tot.}$	-0.30	0.00	0.11	1.64	-0.28	-0.45	-0.26	0.09
	$\mu_{mol.}$	0.01	0.00	0.00	-0.01	0.00	-0.2	0.00	0.02
Fe ₂ B ₂	$\mu_{tot.}$	-0.28	-0.01	0.33	0.45	1.23	1.30	1.68	0.00
	$\mu_{mol.}$	-0.04	0.01	0.01	0.01	0.05	0.07	0.15	0.00

moment equal to zero, except NO2 and O2, whose ground states are magnetic (with total magnetic moments of 1 and 2 μ_B for NO₂ and O₂, respectively). On Cr₂B₂, all the molecules show an almost negligible magnetization, with some exceptions like SO2 whose magnetic moment increases from zero to $-0.20~\mu_B$ on the surface of Cr_2B_2 . This type of magnetization induced in a molecule has been reported before, as is the case of the NO molecule on borophene [58]. The magnetic moment of the Cr atom just below the CO molecule has decreased from 3.55 to 3.16 $\mu_{\rm B}$, which is, in turn, the atom that has lost more charge in the transfer towards the molecule. Conversely, C and O show a polarization of -0.02 and $0.02~\mu_{\rm B}$ respectively. The molecular magnetic moment equals zero for NO₂ and O₂ (their behavior changes from paramagnetic to nonmagnetic). In the NO2 molecule, the nitrogen and oxygen atoms bonded to the Cr atoms have 0.05 and $-0.05~\mu_{\rm B}$ respectively, while the remaining atom has only 0.002 μ_B . The total sum results almost null. The same can be said for O2, where each atom in the molecule adopts an opposite sign with respect to the other, canceling the total magnetic moment of the molecule (the starting magnetic moments per atom are aligned in the isolated molecule).

In summary, from the perspective of magnetism, Fe₂B₂ is more interesting than Cr₂B₂ given that not only the resulting total magnetic moments are in most cases larger in absolute value (see Table 4) but also the molecules result more polarized (e.g., $-0.04,\ 0.05,\ 0.07,\$ and 0.15 $\mu_{\rm B}$ for CO, NO₂, SO₂, and O₂, respectively). At a glance at Fig. 10, the most significant differences in magnetism between the pristine systems and the systems after the interaction happen for the molecules showing strong chemisorption to the MBene, a fact that is reflected in Table 4.

4. Summary and conclusions

We have demonstrated that the studied MBenes can be potentially used as sensors or adsorbents for hazardous molecules. The large cohesive energies and dynamical stability of the pristine sheets make them suitable materials for capture, reduction, and sensing purposes. Their metallic nature, mainly derived from the d-orbitals of the metal atoms, makes them ideal for these applications. In most cases, the studied MBenes exhibit high adsorption energies and significant charge transfer

from the surface to the molecule. However, some challenges may arise, such as structural deformation in Cr-based MBenes after the adsorption of specific molecules and large adsorption energies that could limit their reusability as gas sensors. Despite these challenges, our theoretical results could provide valuable insights for future experimental work, as experimental studies in sensing, conversion, and capture using MBenes are still limited.

Regarding magnetic properties, the molecular magnetic moments are almost zero when attached to the MBene surface, except for the SO_2 molecule on Cr_2B_2 . However, the total magnetic moments of the MBene/molecule systems have significantly increased in most cases, particularly in those experiencing a stronger chemisorption.

Based on our findings, Cr/Fe/Zr-based MBenes could be considered as potential substrates for the detection/capture of gas molecules, potentially paving the way for designing sensor nanodevices based on these materials.

CRediT authorship contribution statement

Isabel M. Arias-Camacho: Writing – original draft, Visualization, Validation, Investigation, Conceptualization. **Nevill Gonzalez Szwacki:** Writing – review & editing, Supervision, Investigation, Conceptualization.

Declaration of competing interest

The authors declare that they have no known competing financial interests or personal relationships that could have appeared to influence the work reported in this paper.

Acknowledgments

We acknowledge Polish high-performance computing infrastructure PLGrid for awarding access to the LUMI supercomputer, owned by the EuroHPC Joint Undertaking and hosted by CSC (Finland) and the LUMI consortium through PLL/2023/05/016755. We also acknowledge the use of supercomputers through grant No. GB80-23 at the Interdisciplinary Center for Mathematical and Computational Modelling (ICM) at the University of Warsaw.

Appendix A. Total energy convergence

See Fig. A.11.

Appendix B. Starting magnetic configurations

See Fig. B.12.

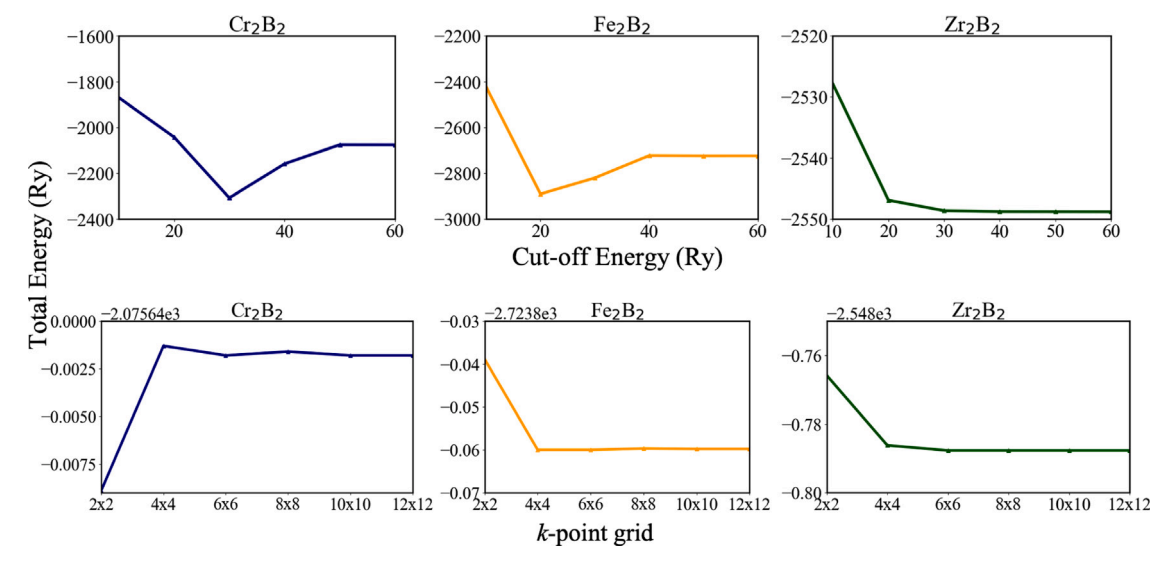


Fig. A.11. Total energy convergence with respect to the cut-off energy (top) and k-point grid (bottom). For all the pristine systems, convergence is achieved with a cut-off energy of 50 Ry and a k-point grid of 6×6 , ensuring that the chosen parameters in the calculations are reliable.

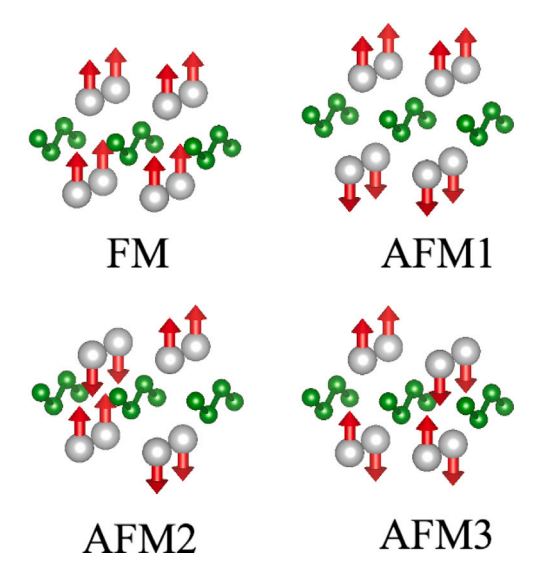


Fig. B.12. Four different starting magnetic configurations have been considered: one ferromagnetic (FM) and three antiferromagnetic (AFM).

 $\begin{tabular}{ll} \textbf{Table C.5} \\ \textbf{Adsorption energies (in eV) of the eight considered molecules on Cr_2B_2 for four different positions. The smallest energy values are highlighted in bold.} \end{tabular}$

Molecule	TopM	TopB	Bridge	Hollow
CO (C facing surface)	-4.76	-0.46	-4.75	-3.75
CO (O facing surface)	-0.09	-0.09	-0.09	-0.09
CO_2	-0.14	-0.02	-0.18	-0.36
H_2O	-0.26	0.12	-0.33	-0.37
NH_3	-3.49	-0.28	-3.49	-3.78
NO_2	-5.90	-1.86	-5.77	-5.92
SO_2	-4.81	-2.07	-4.59	-3.70
O ₂ (vertical)	-5.48	-5.83	-5.27	-5.21
O ₂ (horizontal)	-2.31	-2.57	-2.68	-2.21
N ₂ (vertical)	-0.79	-0.08	-0.10	-0.18
N ₂ (horizontal)	0.08	-0.08	-0.09	-0.09

Appendix C. Adsorption energies for the studied configurations

See Tables C.5-C.7.

Table C.6 Adsorption energies (in eV) of the eight considered molecules on Fe_2B_2 for four different positions. The smallest energy values are highlighted in bold.

Molecule	TopM	ТорВ	Bridge	Hollow
CO (C facing surface)	-0.76	0.15	-0.88	-0.89
CO (O facing surface)	-0.85	-0.03	-0.13	0.00
CO_2	-0.01	-0.15	-0.20	-0.16
H_2O	-0.27	-0.31	-0.49	-0.06
NH_3	-0.50	-0.20	-0.66	-0.61
NO_2	-1.28	-1.60	-1.94	-1.59
SO_2	-0.54	-0.85	-1.50	-0.65
O ₂ (vertical)	-0.35	-1.81	-1.89	-0.11
O ₂ (horizontal)	-0.31	-1.81	-1.34	-1.39
N ₂ (vertical)	-0.05	-0.08	-0.25	-0.02
N ₂ (horizontal)	0.11	-0.11	-0.24	-0.11

 $\begin{array}{l} \textbf{Table C.7} \\ \textbf{Adsorption energies (in eV) of the eight considered molecules on Zr_2B_2 for four different positions. The smallest energy values are highlighted in bold.} \end{array}$

•				
Molecule	TopM	TopB	Bridge	Hollow
CO (C facing surface)	-1.38	-3.36	-3.37	-1.73
CO (O facing surface)	-0.12	-0.07	-3.36	-0.07
CO_2	-2.12	-3.27	-3.22	-2.12
H_2O	-0.78	-0.33	-1.01	-0.46
NH_3	-1.11	-0.85	-1.10	-1.10
NO_2	-2.47	-5.06	-11.06	-3.38
SO_2	-1.38	-5.64	-3.93	-1.40
O ₂ (vertical)	-1.99	-3.07	-8.42	-2.39
O ₂ (horizontal)	-3.21	-9.01	-8.89	-3.96
N ₂ (vertical)	-0.66	-0.07	-0.66	-1.04
N ₂ (horizontal)	-0.24	-1.97	-2.31	-1.04

Appendix D. PDOS for each configuration

Fig. D.13 shows the projected density of states (PDOS) on the M atoms (M = Cr, Fe, or Zr) in blue, boron atoms in green, and the molecules in red. The first column corresponds to Cr_2B_2 , the second to Fe_2B_2 , and the third one to Zr_2B_2 .

Appendix E. Components of the conductivity tensor

Fig. E.14 describes the values of the conductivity tensor components $(\sigma_{xx}, \sigma_{yy}, \text{ and } \sigma_{zz})$ for each MBene/molecule system. In general, the

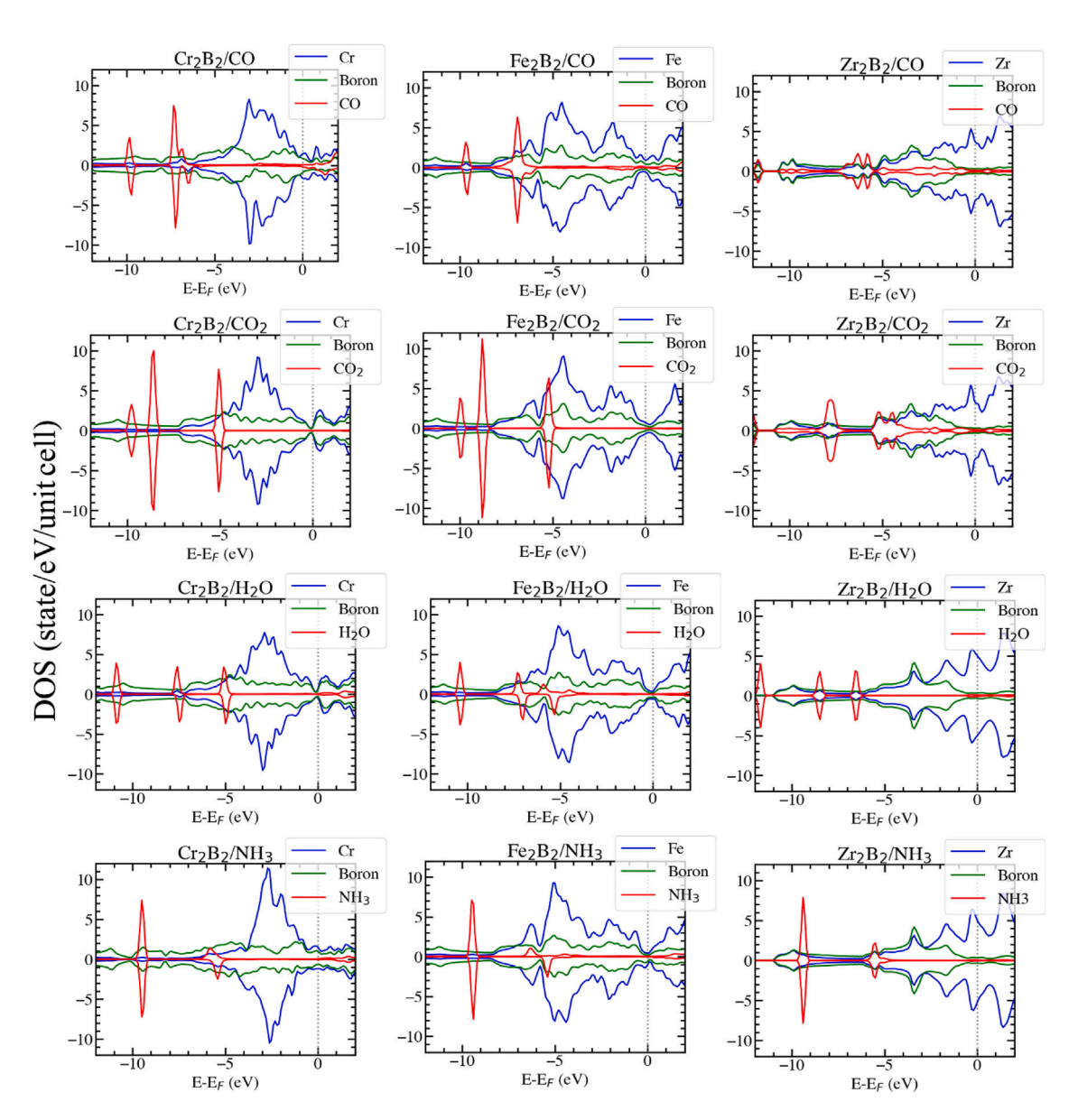
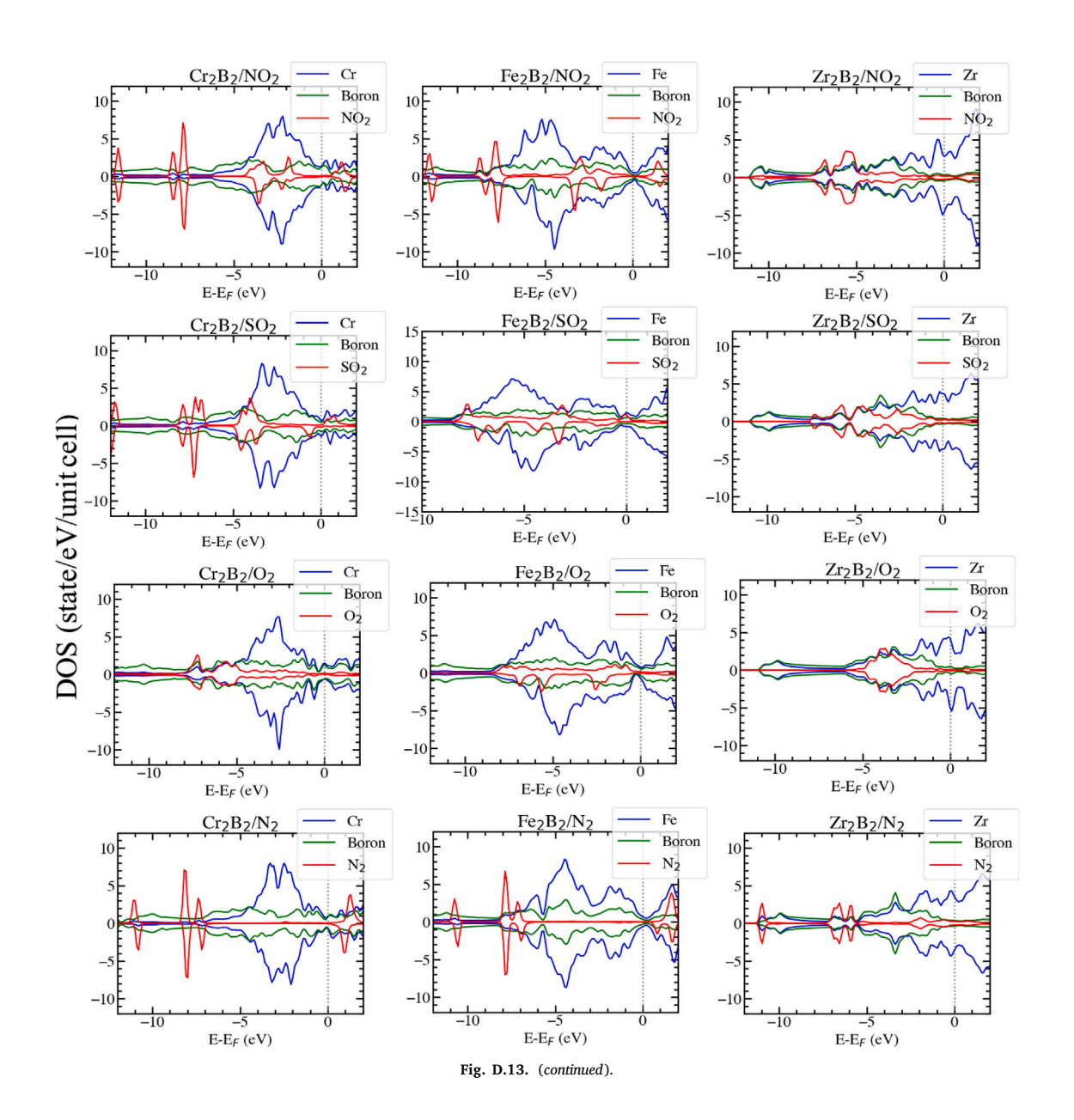


Fig. D.13. Partial density of states (PDOS) of the MBene/molecule systems. The Fermi energy in the PDOS plots has been set to zero.



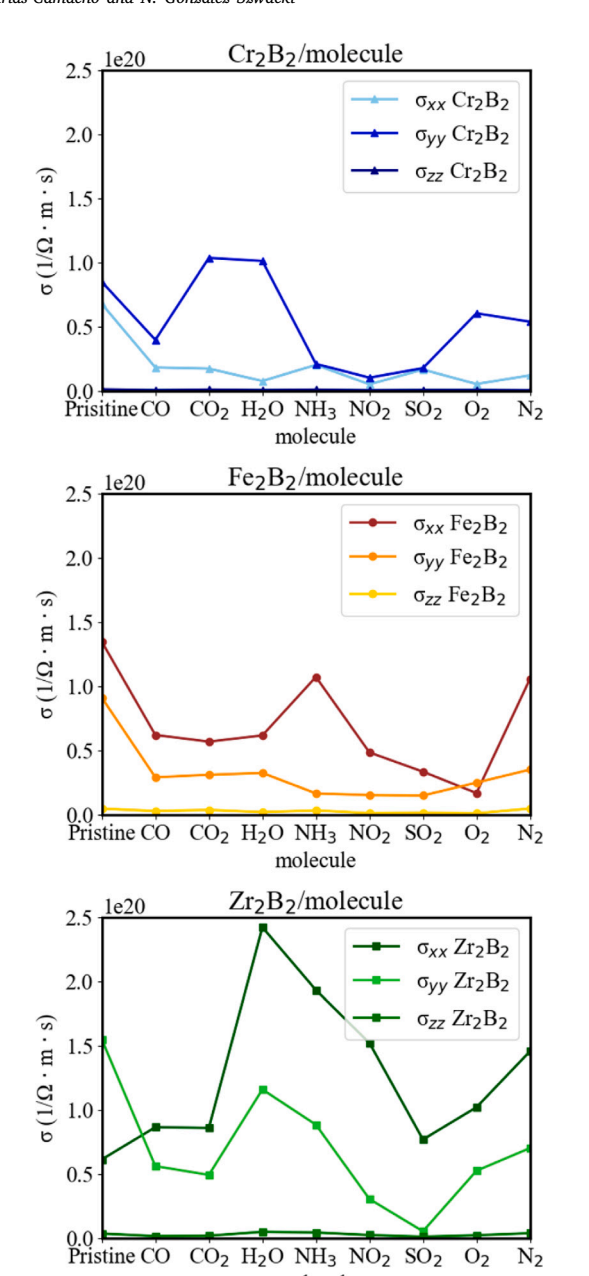


Fig. E.14. Components of the conductivity tensor for the Cr_2B_2/m olecule, Fe_2B_2/m olecule, and Zr_2B_2/m olecule systems in (a), (b), and (c), respectively.

Cr (see Fig. E.14a) and Fe-based (see Fig. E.14b) MBenes maintain the predominance of the σ_{yy} and σ_{xx} components of the conductivity tensor, respectively, before and after the adsorption of the molecules. There is a clear difference between σ_{xx} and σ_{yy} when the carbon dioxide and water molecules interact with the Cr-based MBene, and the same can be said when the ammonia molecule interacts with the Fe monoboride. However, in the case of Zr_2B_2 (see Fig. E.14c) seems to happen an inversion of this behavior, namely the σ_{yy} component, larger in the pristine sheet, is replaced by the σ_{xx} after the molecular adsorption. As expected, the out-of-plane σ_{zz} component is always negligible.

Data availability

Data will be made available on request.

References

- [1] B. Fu, T. Gasser, B. Li, S. Tao, P. Ciais, S. Piao, Y. Balkanski, W. Li, T. Yin, L. Han, X. Li, Y. Han, J. An, S. Peng, J. Xu, Short-lived climate forcers have long-term climate impacts via the carbon-climate feedback, Nature Clim. Change 10 (9) (2020) 851–855, http://dx.doi.org/10.1038/s41558-020-0841-x.
- [2] M.S. Javed, X. Zhang, T. Ahmad, M. Usman, S.S.A. Shah, A. Ahmad, I. Hussain, S. Majeed, M.R. Khawar, D. Choi, C. Xia, W. Al Zoubi, M.A. Assiri, A.M. Hassan, S. Ali, W. Han, MXenes to MBenes: Latest development and opportunities for energy storage devices, Mater. Today 74 (2024) 121–148, http://dx.doi.org/10.1016/j.mattod.2024.01.001.
- [3] X. Zhu, X. Zhou, Y. Jing, Y. Li, Electrochemical synthesis of urea on MBenes, Nature Commun. 12 (1) (2021) 4080, http://dx.doi.org/10.1038/s41467-021-24400-5
- [4] M. Ozkan, MXenes vs MBenes: Demystifying the materials of tomorrow's carbon capture revolution, MRS Energy Sustain. 11 (1) (2024) 181–190, http://dx.doi. org/10.1557/s43581-024-00082-6.
- [5] Y. Xiao, C. Shen, N. Hadaeghi, Quantum mechanical screening of 2D mbenes for the electroreduction of CO₂ to C1 hydrocarbon fuels, J. Phys. Chem. Lett. 12 (27) (2021) 6370–6382, http://dx.doi.org/10.1021/acs.jpclett.1c01499.
- [6] S.H. Mir, V.K. Yadav, J.K. Singh, Efficient CO₂ capture and activation on novel two-dimensional transition metal borides, ACS Appl. Mater. Interfaces 14 (2022) 29703–29710, http://dx.doi.org/10.1021/acsami.2c02469.
- [7] B. Zhang, J. Zhou, Z. Sun, MBenes: progress, challenges and future, J. Mater. Chem. A 10 (2022) 15865–15880, http://dx.doi.org/10.1039/D2TA03482D.
- [8] L.T. Alameda, P. Moradifar, Z.P. Metzger, N. Alem, R.E. Schaak, Topochemical deintercalation of Al from MoAlB: Stepwise etching pathway, layered intergrowth structures, and two-dimensional MBene, J. Am. Chem. Soc. 140 (28) (2018) 8833–8840, http://dx.doi.org/10.1021/jacs.8b04705.
- [9] J. Wang, T.-N. Ye, Y. Gong, J. Wu, N. Miao, T. Tada, H. Hosono, Discovery of hexagonal ternary phase Ti₂InB₂ and its evolution to layered boride TiB, Nature Commun. 10 (1) (2019) 2284, http://dx.doi.org/10.1038/s41467-019-10297-8.
- [10] H. Zhang, H. Xiang, F. zhi Dai, Z. Zhang, Y. Zhou, First demonstration of possible two-dimensional MBene CrB derived from MAB phase Cr₂AlB₂, J. Mater. Sci. Technol. 34 (11) (2018) 2022–2026, http://dx.doi.org/10.1016/j.jmst.2018.02. 024.
- [11] V.G. Nair, M. Birowska, D. Bury, M. Jakubczak, A. Rosenkranz, A.M. Jastrzębska, 2D MBenes: A novel member in the flatland, Adv. Mater. 34 (23) (2022) 2108840, http://dx.doi.org/10.1002/adma.202108840, URL https://onlinelibrary.wiley.com/doi/abs/10.1002/adma.202108840.
- [12] M. Jakubczak, A. Szuplewska, A. Rozmysłowska-Wojciechowska, A. Rosenkranz, A.M. Jastrzębska, Novel 2D MBenes-synthesis, structure, and Biotechnological potential, Adv. Funct. Mater. 31 (38) (2021) 2103048, http://dx.doi.org/10. 1002/adfm.202103048.
- [13] M. Khazaei, J. Wang, M. Estili, A. Ranjbar, S. Suehara, M. Arai, K. Esfarjani, S. Yunoki, Novel MAB phases and insights into their exfoliation into 2D MBenes, Nanoscale 11 (2019) 11305–11314, http://dx.doi.org/10.1039/C9NR01267B.
- [14] R. Khaledialidusti, M. Khazaei, V. Wang, N. Miao, C. Si, J. Wang, J. Wang, Exploring structural, electronic, and mechanical properties of 2D hexagonal MBenes, J. Phys.: Condens. Matter. 33 (15) (2021) 155503, http://dx.doi.org/ 10.1088/1361-648X/abbb0e.
- [15] I. Arias-Camacho, N. Gonzalez Szwacki, Exploring the structural, electronic, magnetic, and transport properties of 2D Cr, Fe, and Zr monoborides, Materials 16 (2023) 5104, http://dx.doi.org/10.3390/ma16145104.
- [16] I.M. Arias-Camacho, Influence of the hubbard U parameter on the structural, electronic, magnetic, and transport properties of Cr/Fe/Zr-Based MBenes, ACS Omega 8 (2023) 45003–45012, http://dx.doi.org/10.1021/acsomega.3c06539.
- [17] A. Shukla, G. Sharma, S. Krishnamurty, Functionalized Mo₂BX₂ (X=H, OH, O) MBenes as a promising sensor, capturer and storage material for environmentally toxic gases: A case study of 1T and 2H phase, Appl. Surf. Sci. 615 (2023) 156299, http://dx.doi.org/10.1016/j.apsusc.2022.156299, URL https://www.sciencedirect.com/science/article/pii/S0169433222038272.
- [18] Z. Guo, J. Zhou, Z. Sun, New two-dimensional transition metal borides for Li ion batteries and electrocatalysis, J. Mater. Chem. A 5 (2017) 23530–23535, http://dx.doi.org/10.1039/C7TA08665B.
- [19] W. Xiong, X. Feng, Y. Xiao, T. Huang, X. Li, Z. Huang, S. Ye, Y. Li, X. Ren, X. Wang, X. Ouyang, Q. Zhang, J. Liu, Fluorine-free prepared two-dimensional molybdenum boride (MBene) as a promising anode for lithium-ion batteries with superior electrochemical performance, Chem. Eng. J. 446 (2022) 137466, http://dx.doi.org/10.1016/j.cej.2022.137466, URL https://www.sciencedirect.com/science/article/pii/S1385894722029540.
- [20] R. Sahu, D. Bogdanovski, J.-O. Achenbach, S. Zhang, M. Hans, D. Primetzhofer, J.M. Schneider, C. Scheu, Direct MoB MBene domain formation in magnetron sputtered MoAlB thin films, Nanoscale 13 (2021) 18077–18083, http://dx.doi. org/10.1039/D1NR05712J.
- [21] P. Giannozzi, S. Baroni, N. Bonini, M. Calandra, R. Car, C. Cavazzoni, D. Ceresoli, G.L. Chiarotti, M. Cococcioni, I. Dabo, A.D. Corso, S. de Gironcoli, S. Fabris, G. Fratesi, R. Gebauer, U. Gerstmann, C. Gougoussis, A. Kokalj, M. Lazzeri, L. Martin-Samos, N. Marzari, F. Mauri, R. Mazzarello, S. Paolini, A. Pasquarello, L. Paulatto, C. Sbraccia, S. Scandolo, G. Sclauzero, A.P. Seitsonen, A. Smogunov, P.

- Umari, R.M. Wentzcovitch, QUANTUM ESPRESSO: a modular and open-source software project for quantum simulations of materials, J. Phys.: Condens. Matter. 21 (39) (2009) 395502, http://dx.doi.org/10.1088/0953-8984/21/39/395502.
- [22] J.P. Perdew, K. Burke, M. Ernzerhof, Generalized gradient approximation made simple, Phys. Rev. Lett. 77 (1996) 3865–3868, https://link.aps.org/doi/10.1103/ PhysRevLett.77.3865.
- [23] P.E. Blöchl, Projector augmented-wave method, Phys. Rev. B 50 (1994) 17953–17979, https://link.aps.org/doi/10.1103/PhysRevB.50.17953.
- [24] A. Dal Corso, (B/Fe/Zr/C/O/N/H/S).pbe-n-kjpaw_psl.1.0.0.UPF, 2018, https://pseudopotentials.quantum-espresso.org/legacy_tables.
- [25] M. Cococcioni, S. de Gironcoli, Linear response approach to the calculation of the effective interaction parameters in the LDA + U method, Phys. Rev. B 71 (2005) 035105, http://dx.doi.org/10.1103/PhysRevB.71.035105.
- [26] I. Timrov, N. Marzari, M. Cococcioni, Hubbard parameters from density-functional perturbation theory, Phys. Rev. B 98 (2018) 085127, http://dx.doi.org/10.1103/PhysRevB.98.085127.
- [27] I. Timrov, N. Marzari, M. Cococcioni, Self-consistent Hubbard parameters from density-functional perturbation theory in the ultrasoft and projector-augmented wave formulations, Phys. Rev. B 103 (4) (2021) 045141, http://dx.doi.org/10. 1103/physrevb.103.045141.
- [28] I. Timrov, N. Marzari, M. Cococcioni, HP A code for the calculation of Hubbard parameters using density-functional perturbation theory, Comput. Phys. Comm. 279 (2022) 108455, http://dx.doi.org/10.1016/j.cpc.2022.108455.
- [29] S. Grimme, J. Antony, S. Ehrlich, H. Krieg, A consistent and accurate ab initio parametrization of density functional dispersion correction (DFT-D) for the 94 elements H-Pu, J. Chem. Phys. 132 (2010) 154104, http://dx.doi.org/10.1063/ 1.3382344.
- [30] J.B.A. Davis, F. Baletto, R.L. Johnston, The effect of dispersion correction on the adsorption of CO on metallic nanoparticles, J. Phys. Chem. A 119 (2015) 9703–9709, http://dx.doi.org/10.1021/acs.jpca.5b05710.
- [31] A. Otero de la Roza, G.A. DiLabio, Chapter 6 a comprehensive overview of the DFT-D3 London-dispersion correction, in: Non-Covalent Interactions in Quantum Chemistry and Physics, Elsevier, 2017, pp. 195–219, http://dx.doi.org/10.1016/ B978-0-12-809835-6.00007-4.
- [32] X. Zhang, Z. Chen, D. Chen, H. Cui, J. Tang, Adsorption behaviour of SO₂ and SOF₂ gas on Rh-doped BNNT: a DFT study, Mol. Phys. 118 (2020) e1580394, http://dx.doi.org/10.1080/00268976.2019.1580394.
- [33] H. Cui, X. Zhang, G. Zhang, J. Tang, Pd-doped MoS₂ monolayer: A promising candidate for DGA in transformer oil based on DFT method, Appl. Surf. Sci. 470 (2019) 1035–1042, http://dx.doi.org/10.1016/j.apsusc.2018.11.230, URL https://www.sciencedirect.com/science/article/pii/S0169433218333087.
- [34] D. Chen, X. Zhang, J. Tang, H. Cui, Y. Li, Noble metal (Pt or Au)-doped monolayer MoS₂ as a promising adsorbent and gas-sensing material to SO₂, SOF₂ and SO₂F₂: a DFT study, Appl. Phys. A 124 (2018) 194, http://dx.doi.org/10. 1007/s00339-018-1629-y.
- [35] G. Henkelman, A. Arnaldsson, H. Jónsson, A fast and robust algorithm for Bader decomposition of charge density, Comput. Mater. Sci. 36 (3) (2006) 354– 360, http://dx.doi.org/10.1016/j.commatsci.2005.04.010, URL https://www. sciencedirect.com/science/article/pii/S0927025605001849.
- [36] G.K. Madsen, J. Carrete, M.J. Verstraete, BoltzTraP2, a program for interpolating band structures and calculating semi-classical transport coefficients, Comput. Phys. Comm. 231 (2018) 140–145, http://dx.doi.org/10.1016/j.cpc.2018.05.010, URL https://www.sciencedirect.com/science/article/pii/S0010465518301632.
- [37] S.H. Mir, V.K. Yadav, J.K. Singh, Recent advances in the carrier mobility of two-dimensional materials: A theoretical perspective, ACS Omega 5 (24) (2020) 14203–14211, http://dx.doi.org/10.1021/acsomega.0c01676.
- [38] K. Momma, F. Izumi, VESTA 3 for three-dimensional visualization of crystal, volumetric and morphology data, J. Appl. Crystall. 44 (6) (2011) 1272–1276, http://dx.doi.org/10.1107/S0021889811038970.
- [39] M. Dou, H. Li, Q. Yao, J. Wang, Y. Liu, F. Wu, Room-temperature ferromagnetism in two-dimensional transition metal borides: A first-principles investigation, Phys. Chem. Chem. Phys. 23 (2021) 10615–10620, http://dx.doi.org/10.1039/ d1cp00052g.
- [40] S. Wang, N. Miao, K. Su, V.A. Blatov, J. Wang, Discovery of intrinsic two-dimensional antiferromagnets from transition-metal borides, Nanoscale 13 (2021) 8254–8263, http://dx.doi.org/10.1039/D1NR01103K.
- [41] B. Zhang, J. Zhou, Z. Guo, Q. Peng, Z. Sun, Two-dimensional chromium boride MBenes with high HER catalytic activity, Appl. Surf. Sci. 500 (2020) 144248, http://dx.doi.org/10.1016/j.apsusc.2019.144248.
- [42] I. Ozdemir, Y. Kadioglu, Y. Yüksel, Ü. Akıncı, O.Ü. Aktürk, E. Aktürk, S. Ciraci, Columnar antiferromagnetic order of a MBene monolayer, Phys. Rev. B 103 (14) (2021) 144424, http://dx.doi.org/10.1103/physrevb.103.144424.
- [43] S. Qi, Y. Fan, L. Zhao, W. Li, M. Zhao, Two-dimensional transition metal borides as highly efficient N_2 fixation catalysts, Appl. Surf. Sci. 536 (2021) 147742, http://dx.doi.org/10.1016/j.apsusc.2020.147742.
- [44] B. Huang, Y.-H. Duan, W.-C. Hu, Y. Sun, S. Chen, Structural, anisotropic elastic and thermal properties of MB (M=Ti, Zr and Hf) monoborides, Ceram. Int. 41 (2015) 6831–6843, http://dx.doi.org/10.1016/j.ceramint.2015.01.132.

- [45] X. Xu, K. Fu, L. Li, Z. Lu, X. Zhang, Y. Fan, J. Lin, G. Liu, H. Luo, C. Tang, Dependence of the elastic properties of the early-transition-metal monoborides on their electronic structures: A density functional theory study, Physica B 419 (2013) 105–111, http://dx.doi.org/10.1016/j.physb.2013.03.018.
- [46] A. Shukla, G. Sharma, S. Krishnamurty, Single-atom-catalyst-implanted mbenes as efficient electrocatalysts for hydrogen evolution reaction as realized through computational screening, ACS Appl. Eng. Mater. 2 (2024) 422–430, http://dx. doi.org/10.1021/acsaenm.3c00732.
- [47] C.C. Yang, S. Li, Cohesive energy: The intrinsic dominant of thermal stability and structural evolution in Sn from size scales of bulk to dimer, J. Phys. Chem. C 113 (2009) 14207–14212, http://dx.doi.org/10.1021/jp904161r.
- [48] B. Akgenc, A. Mogulkoc, E. Durgun, Phase-dependent electronic and magnetic properties of Ti₂C monolayers, J. Appl. Phys. 127 (2020) 084302, http://dx.doi. org/10.1063/1.5140578.
- [49] X. Liu, Z. Liu, H. Deng, Theoretical evaluation of mbenes as catalysts for the CO₂ reduction reaction, J. Phys. Chem. C 125 (2021) 19183–19189, http: //dx.doi.org/10.1021/acs.jpcc.1c02749.
- [50] X. Tan, Z. Na, R. Zhuo, D. Wang, Y. Zhang, P. Wu, Investigation of CrB as a potential gas sensor for fault detection in eco-friendly power equipment, Chemosensors 11 (2023) 371, http://dx.doi.org/10.3390/chemosensors11070371, URL https://www.mdpi.com/2227-9040/11/7/371.
- [51] X. Zhang, X. Pu, Y. Chen, X. Gu, D. Xu, S. Zhang, Characterization of high concentration Ga-doped ZnO nano-powders prepared by sol-gel combustion, Mater. Lett. 112 (2013) 129–132, http://dx.doi.org/10.1016/j.matlet.2013.08.
- [52] H. ping Zhang, X. gang Luo, X. yang Lin, X. Lu, Y. Leng, H. tao Song, Density functional theory calculations on the adsorption of formaldehyde and other harmful gases on pure, Ti-doped, or N-doped graphene sheets, Appl. Surf. Sci. 283 (2013) 559–565, http://dx.doi.org/10.1016/j.apsusc.2013.06.145.
- [53] T. Liu, Y. Chen, M. Zhang, L. Yuan, C. Zhang, J. Wang, J. Fan, A first-principles study of gas molecule adsorption on borophene. AIP Adv. 7 (2017) 125007.
- [54] C.-S. Huang, A. Murat, V. Babar, E. Montes, U. Schwingenschlögl, Adsorption of the gas molecules NH₃, NO, NO₂, and CO on borophene, J. Phys. Chem. C 122 (2018) 14665–14670, http://dx.doi.org/10.1021/acs.jpcc.8b03811.
- [55] J.M. Morbec, P. Kratzer, The role of the van der Waals interactions in the adsorption of anthracene and pentacene on the Ag(111) surface, J. Chem. Phys. 146 (2017) 034702, http://dx.doi.org/10.1063/1.4973839.
- [56] P.O. Bedolla, G. Feldbauer, M. Wolloch, S.J. Eder, N. Dörr, P. Mohn, J. Redinger, A. Vernes, Effects of van der Waals interactions in the adsorption of isooctane and ethanol on Fe(100) surfaces, J. Phys. Chem. C 118 (2014) 17608–17615, http://dx.doi.org/10.1021/jp503829c.
- [57] J. Carrasco, J. Klimeš, A. Michaelides, The role of van der Waals forces in water adsorption on metals, J. Chem. Phys. 138 (2013) 024708, http://dx.doi.org/10. 1063/1.4773901.
- [58] V. Shukla, J. Wärnå, N.K. Jena, A. Grigoriev, R. Ahuja, Toward the realization of 2D borophene based gas sensor, J. Phys. Chem. C 121 (2017) 26869–26876, http://dx.doi.org/10.1021/acs.jpcc.7b09552.
- [59] J. Shen, Z. Yang, Y. Wang, L.-C. Xu, R. Liu, X. Liu, The gas sensing performance of borophene/MoS₂ heterostructure, Appl. Surf. Sci. 504 (2020) 144412, http:// dx.doi.org/10.1016/j.apsusc.2019.144412, URL https://www.sciencedirect.com/ science/article/pii/S0169433219332283.
- [60] O. Leenaerts, B. Partoens, F.M. Peeters, Adsorption of H₂O, NH₃, CO, NO₂, and NO on graphene: A first-principles study, Phys. Rev. B 77 (2008) 125416, http://dx.doi.org/10.1103/PhysRevB.77.125416.
- [61] Y. Liu, J. Wilcox, CO₂ adsorption on carbon models of organic constituents of gas shale and coal, Environ. Sci. Technol. 45 (2011) 809–814, http://dx.doi.org/ 10.1021/es102700c.
- [62] A. Shokri, N. Salami, Gas sensor based on MoS₂ monolayer, Sensors Actuators B 236 (2016) 378–385, http://dx.doi.org/10.1016/j.snb.2016.06.033, URL https://www.sciencedirect.com/science/article/pii/S0925400516308851.
- [63] B. Cho, M.G. Hahm, M. Choi, J. Yoon, A.R. Kim, Y.-J. Lee, S.-G. Park, J.-D. Kwon, C.S. Kim, M. Song, Y. Jeong, K.-S. Nam, S. Lee, T.J. Yoo, C.G. Kang, B.H. Lee, H.C. Ko, P.M. Ajayan, D.-H. Kim, Charge-transfer-based Gas Sensing Using Atomic-layer MoS₂, Sci. Rep. 5 (2015) 8052, http://dx.doi.org/10.1038/srep08052.
- [64] L. Kou, T. Frauenheim, C. Chen, Phosphorene as a superior gas sensor: Selective adsorption and distinct I–V response, J. Phys. Chem. Lett. 5 (2014) 2675–2681, http://dx.doi.org/10.1021/jz501188k.
- [65] J. wen Feng, Y. jie Liu, H. xia Wang, J. xiang Zhao, Q. hai Cai, X. zhang Wang, Gas adsorption on silicene: A theoretical study, Comput. Mater. Sci. 87 (2014) 218–226, http://dx.doi.org/10.1016/j.commatsci.2014.02.025, URL https://www.sciencedirect.com/science/article/pii/S0927025614001190.
- [66] W. Xia, W. Hu, Z. Li, J. Yang, A first-principles study of gas adsorption on germanene, Phys. Chem. Chem. Phys. 16 (2014) 22495–22498, http://dx.doi. org/10.1039/C4CP03292F.
- [67] X. Yu, F. Chen, Z. Yu, Y. Li, Computational study of borophene with line defects as sensors for nitrogen-containing gas molecules, ACS Appl. Nano Mater. 3 (2020) 9961–9968, http://dx.doi.org/10.1021/acsanm.0c01975.
- [68] X. Tan, H.A. Tahini, S.C. Smith, Borophene as a promising material for charge-modulated switchable CO2 capture, ACS Appl. Mater. Interfaces 9 (2017) 19825–19830, http://dx.doi.org/10.1021/acsami.7b03676.

- [69] J.-X. Duan, Y.-P. Tian, C.-B. Wang, L.-L. Zhang, First-principles study of χ_3 -borophene as a candidate for gas sensing and the removal of harmful gases, Nanomaterials 13 (2023) 2117, http://dx.doi.org/10.3390/nano13142117.
- [70] A.K. Mishra, S. Ramaprabhu, Carbon dioxide adsorption in graphene sheets, AIP Adv. 1 (2011) 032152, http://dx.doi.org/10.1063/1.3638178.
- [71] P. Khakbaz, M. Moshayedi, S. Hajian, M. Soleimani, B.B. Narakathu, B.J. Bazuin, M. Pourfath, M.Z. Atashbar, Titanium carbide MXene as NH₃ sensor: Realistic first-principles study, J. Phys. Chem. C 123 (2019) 29794–29803, http://dx.doi.org/10.1021/acs.jpcc.9b09823.
- [72] S. Mehdi Aghaei, A. Aasi, B. Panchapakesan, Experimental and theoretical advances in mxene-based gas sensors, ACS Omega 6 (2021) 2450–2461, http: //dx.doi.org/10.1021/acsomega.0c05766.
- [73] Y.Z. Abdullahi, Z.D. Vatansever, E. Aktürk, Ü. Akıncı, O.Ü. Aktürk, Novel two-dimensional CrXB₂ (X=Cr, Ru) metal for high Néel temperature antiferromagnetic spintronics, J. Solid State Chem. 302 (2021) 122427, http://dx.doi.org/10.1016/j.jssc.2021.122427, URL https://www.sciencedirect.com/science/article/pii/S0022459621004722.



The particular election of the two-dimensional borophene and MBenes is based on the idea that they could exhibit an exceptional sensing potential because their entire surface is exposed to adsorb the gas molecules, maximizing their interaction with the surface. Moreover, their stability in the natural environment, intrinsic metallicity, and large conductivity are advantageous compared with similar materials that are excellent for multiple purposes but limited for sensing applications because of their poor electrical conductivity and Young's modulus, instability under ambient conditions, and high surface energy that provokes a reduction of their electrochemically active sites by restacking.

The novelty of this work lies in the study of selected borophene layers (α -sheet, honeycomb-like) and MBenes (Fe₂B₂ and Zr₂B₂) whose potential as sensors has not yet been explored for such a set of molecules, while some other layers (buckled borophene, Cr₂B₂), with already well-known properties, have been chosen as a reference to reinforce and validate the results.

As has been mentioned throughout this thesis, most of the possible structures of these two-dimensional boron-based materials are theoretically predicted but those experimentally achieved represent only a small subset. Compared with graphene, the fabrication and characterization of these materials is quite expensive and the available funding is, to date, almost negligible. An important challenge to narrow the gap between theory and experiments is the correct selection of the underlying substrate to take advantage

of this richness in structures. It is demonstrated that there is a connection between the substrate morphology and polymorphism, and that control of this circumstance paves the way for tuning the electronic and/or surface properties of these boron-based compounds. In addition, in the particular case of MBenes, the typical etchant used is hydrofluoric acid, which is highly toxic, corrosive, and hazardous to human health. To avoid this impact on the environment, new techniques must be developed, and in this direction, sputtering, chemical vapor deposition, mechanical and chemical exfoliation, thermal fragmentation, and even fluorine-free hydrothermal-assisted alkaline solution etching methods [129] can not only avoid the possible risks associated with their synthesis, but can also reduce manufacturing times and costs [130].

Once their stability and excellent conductivity are out of question, both MBenes and borophenes are ready to be tested as the basis of sensing electronic devices, and in this regard, they have demonstrated an exceptional capability for adsorbing molecules. Yielding the highest adsorption energies among similar 2D materials, their ability to capture and reduce specific harmful molecules has also evidenced that the diversity of these compounds leads to an unexplored range of possible and unexpected applications.

Another drawback that must be addressed is the distortion suffered by some layers after strong interactions with specific molecules, which can limit their reusability as sensors. It is a general trend that the CO_2 molecule manifests physisorption instead of chemisorption and is for this reason easy to detect and track. For example, the α -B and buckled-B sheets are more suitable for sensing purposes than the honeycomb-shaped sheet because they show moderate adsorption energies with the analyte and preserve their original structure better.

Another peculiarity arising from MBenes is their magnetism, which originates in the transition-metal elements. Although it was not the main focus, this work has also dedicated a separate description of their magnetic properties, proving that some of them can behave as robust magnets with high critical temperature. These properties open the window to further investigation in spintronics or memory storage.

Despite these findings, it is not the end, but only the starting point, and there is much room left for further research. This work has shown that the orthorhombic and hexagonal phases are both feasible and close in energy and, according to other works [26, 35], orthorhombic MBenes could transform into hexagonal MBenes by controlling environmental conditions. Although orthorhombic MAB phases have been the subject of study in recent years, the synthesis and characterization of hexagonal MAB phases have undergone notable advancements, with 133 phases predicted as synthesizable, 81 of them that can be potentially exfoliated into 20 stable hex-MBenes [131] and three of them successfully obtained (Hf₂InB₂, Hf₂PbB and V₃PB₄). The next step of this work must then go in the direction of the exploitation of the unique electronic, transport, structural, and magnetic properties of these MBenes with a graphene-like boron layer. The different arrangements of their active sites are expected to lead to substantial differences in comparison with those of the studied ortho-MBenes. Functionalization with several terminal groups (-H, -O, -OH, -Cl, -F) has shown that the robustness of the material [131] improved but also that it is the origin of changes in electronic behavior. Besides, a common way of tuning the chemical and physical properties of 2D materials is the application of strain to the sample, which is justified as most of the materials are grown on a substrate that does not always fit perfectly, which is another line of research. An example of combining the two former effects is that hexagonal TiBF undergoes a transition from a metal to a semiconductor and from a semiconductor to a metal under biaxial compressive strain.

Beyond the dedicated use of these boron-based materials, there is still room to explore their combination in hybrid heterostructures, or even doping: heterojunctions exhibiting a synergistic effect with novel and challenging properties and doping that improves the performance of the electrodes.

- [1] Artem R. Oganov, Jiuhua Chen, Carlo Gatti, Yanzhang Ma, Yanming Ma, Colin W. Glass, Zhenxian Liu, Tony Yu, Oleksandr O. Kurakevych, and Vladimir L. Solozhenko. Ionic high-pressure form of elemental boron. *Nature*, 457:863–867, 02 2009.
- [2] Philip Ball. Magnetic botany. Nat. Mater., 9:470–470, 2010.
- [3] Tomasz Tarkowski, Nevill Gonzalez Szwacki, and Maciej Marchwiany. Structure of porous two-dimensional boron crystals. *Phys. Rev. B*, 104:195423, Nov 2021.
- [4] Evgeni S. Penev, Somnath Bhowmick, Arta Sadrzadeh, and Boris I. Yakobson. Polymorphism of Two-Dimensional Boron. *Nano Lett.*, 12:2441–2445, 05 2012.
- [5] Zhuhua Zhang, Evgeni S. Penev, and Boris I. Yakobson. Polyphony in B flat. *Nat. Chem.*, 8:525–527, 2016.
- [6] Ihsan Boustani. New quasi-planar surfaces of bare boron. *Surf. Sci.*, 370:355–363, 1997.
- [7] Hui Tang and Sohrab Ismail-Beigi. Novel Precursors for Boron Nanotubes: The Competition of Two-Center and Three-Center Bonding in Boron Sheets. *Phys. Rev. Lett.*, 99:115501, Sep 2007.
- [8] Zhuhua Zhang, Yang. Yang, Guoying. Gao, and Boris I. Yakobson. Two-Dimensional Boron Monolayers Mediated by Metal Substrates. *Angew. Chem. Int. Ed.*, 54:13022, 2015.

[9] L. Z. Zhang, Q. B. Yan, S. X. Du, G. Su, and H. J. Gao. Boron Sheet Adsorbed on Metal Surfaces: Structures and Electronic Properties. *J. Phys. Chem. C*, 116:18202–18206, 2012.

- [10] Hongsheng Liu, Junfeng Gao, and Jijun Zhao. From Boron Cluster to Two-Dimensional Boron Sheet on Cu(111) Surface: Growth Mechanism and Hole Formation. *Sci. Rep.*, 3:3238, 2013.
- [11] Yuanyue Liu, Evgeni S. Penev, and Boris I. Yakobson. Probing the Synthesis of Two-Dimensional Boron by First-Principles Computations. *Angew. Chem. Int. Ed.*, 52:3156–3159, 2013.
- [12] W. Li, L. Kong, C. Chen, J. Gou, S. Sheng, W. Zhang, H. Li, L. Chen, P. Cheng, and K. Wu. Experimental realization of honeycomb borophene. *Sci. Bull.*, 63:282–286, 2018.
- [13] Daughty John, Bijoy Nharangatt, and Raghu Chatanathodi. Stabilizing honeycomb borophene by metal decoration: a computational study. *J. Mater. Chem. C*, 7:11493–11499, 2019.
- [14] Zachary A. Piazza, Han-Shi Hu, Wei-Li Li, Ya-Fan Zhao, Jun Li, and Lai-Sheng Wang. Planar hexagonal *B*₃₆ as a potential basis for extended single-atom layer boron sheets. *Nat. Commun.*, 5:3113, 2014.
- [15] A. J. Mannix, X.-F. Zhou, B. Kiraly, J. D. Wood, D. Alducin, B. D. Myers, X. Liu, B. L. Fischer, U. Santiago, and J. R. et al Guest. Synthesis of Borophenes: Anisotropic, Two-Dimensional Boron Polymorphs. *Science*, 350:1513–1516, 2015.
- [16] Baojie Feng, Jin Zhang, Qing Zhong, Wenbin Li, Shuai Li, Hui Li, Peng Cheng, Sheng Meng, Lan Chen, and Kehui Wu. Experimental realization of two-dimensional boron sheets. *Nat. Chem.*, 8:563–568, 2016.
- [17] Pranay Ranjan, Jang Mee Lee, Prashant Kumar, and Ajayan Vinu. Borophene: New Sensation in Flatland. *Adv. Mater.*, 32:2000531, 2020.
- [18] Zhongjian Xie, Xiangying Meng, Xiangnan Li, Weiyuan Liang, Weichun Huang, Keqiang Chen, Jianming Chen, Chenyang Xing, Meng Qiu, Bin Zhang, Guohui Nie, Ni Xie, Xiaobing Yan, and Han Zhang. Two-Dimensional Borophene: Properties, Fabrication, and Promising Applications. *Research*, 2020:2624617, 2020.

[19] Chuang Hou, Guoan Tai, Zenghui Wu, and Jinqian Hao. Borophene: Current Status, Challenges and Opportunities. *ChemPlusChem*, 85:2186–2196, 2020.

- [20] Nevill Gonzalez Szwacki, Arta Sadrzadeh, and Boris I. Yakobson. B₈0 Fullerene: An Ab Initio Prediction of Geometry, Stability, and Electronic Structure. *Phys. Rev. Lett.*, 98:166804, Apr 2007.
- [21] Chuang Hou, Guoan Tai, Yi Liu, Zitong Wu, Xinchao Liang, and Xiang Liu. Borophene-based materials for energy, sensors and information storage applications. *Nano Research Energy*, 2:e9120051, 2023.
- [22] Martin Ade and Harald Hillebrecht. Ternary Borides Cr_2AlB_2 , Cr_3AlB_4 , and Cr_4AlB_6 : The First Members of the Series $(CrB_2)_nCrAl$ with n = 1, 2, 3 and a Unifying Concept for Ternary Borides as MAB-Phases. *Inorg. Chem.*, 54(13):6122–6135, jun 2015.
- [23] Haiming Zhang, Huimin Xiang, Fu zhi Dai, Zhili Zhang, and Yanchun Zhou. First demonstration of possible two-dimensional MBene CrB derived from MAB phase Cr₂AlB₂. *J. Mater. Sci. Technol.*, 34(11):2022–2026, nov 2018.
- [24] Adam Carlsson, Johanna Rosen, and Martin Dahlqvist. Theoretical predictions of phase stability for orthorhombic and hexagonal ternary MAB phases. *Phys. Chem. Chem. Phys.*, 24(18):11249–11258, 2022.
- [25] Junjie Wang, Tian-Nan Ye, Yutong Gong, Jiazhen Wu, Nanxi Miao, Tomofumi Tada, and Hideo Hosono. Discovery of hexagonal ternary phase Ti₂InB₂ and its evolution to layered boride TiB. *Nat. Commun.*, 10(1), may 2019.
- [26] Mohammad Khazaei, Junjie Wang, Mehdi Estili, Ahmad Ranjbar, Shigeru Suehara, Masao Arai, Keivan Esfarjani, and Seiji Yunoki. Novel MAB phases and insights into their exfoliation into 2D MB. *Nanoscale*, 11:11305–11314, 6 2019.
- [27] Rasoul Khaledialidusti, Mohammad Khazaei, Vei Wang, Nanxi Miao, Chen Si, Jianfeng Wang, and Junjie Wang. Exploring structural, electronic, and mechanical properties of 2D hexagonal MBenes. *J. Condens. Matter Phys.*, 33(15):155503, 2 2021.
- [28] Haiming Zhang, Fu-Zhi Dai, Huimin Xiang, Xiaohui Wang, Zhili Zhang, and Yanchun Zhou. Phase pure and well crystalline Cr₂AlB₂:

A key precursor for two-dimensional CrB. *J. Mater. Sci. Technol.*, 35(8):1593–1600, aug 2019.

- [29] Lucas T. Alameda, Parivash Moradifar, Zachary P. Metzger, Nasim Alem, and Raymond E. Schaak. Topochemical Deintercalation of Al from MoAlB: Stepwise Etching Pathway, Layered Intergrowth Structures, and Two-Dimensional MBene. *Journal of the American Chemical Society*, 140(28):8833–8840, jun 2018.
- [30] Lucas T. Alameda, Robert W. Lord, Jordan A. Barr, Parivash Moradifar, Zachary P. Metzger, Benjamin C. Steimle, Cameron F. Holder, Nasim Alem, Susan B. Sinnott, and Raymond E. Schaak. Multi-Step Topochemical Pathway to Metastable Mo₂AlB₂ and Related Two-Dimensional Nanosheet Heterostructures. *Journal of the American Chemical Society*, 141(27):10852–10861, 7 2019.
- [31] V. A. Barinov, G. A. Dorofeev, L. V. Ovechkin, E. P. Elsukov, and A. E. Ermakov. Structure and magnetic properties of the *α*-FeB phase obtained by mechanical working. *Phys. Status Solidi* (*a*), 123(2):527–534, feb 1991.
- [32] Xingbin Zhao, Li Li, Kuo Bao, Pinwen Zhu, Qiang Tao, Shuailing Ma, and Tian Cui. Insight the effect of rigid boron chain substructure on mechanical, magnetic and electrical properties of β -FeB. *J. Alloys Compd*, 896:162767, mar 2022.
- [33] Fernando Igoa Saldaña, Emile Defoy, Daniel Janisch, Gwenaëlle Rousse, Pierre-Olivier Autran, Anissa Ghoridi, Amandine Séné, Marzena Baron, Leopoldo Suescun, Yann Le Godec, and David Portehault. Revealing the Elusive Structure and Reactivity of Iron Boride α-FeB. *Inorg. Chem.*, 62(5):2073–2082, jan 2023.
- [34] Nevill Gonzalez Szwacki. Boron Fullerenes: A First-Principles Study. *Nanoscale Res. Lett.*, 3(2), dec 2007.
- [35] T. Xu, Y Wang, Z. Xiong, Y. Wang, Y. Zhou, and X. Li. A Rising 2D Star: Novel MBenes with Excellent Performance in Energy Conversion and storage. *Nano-Micro Lett.*, 15, 12 2022.
- [36] Siyun Qi, Yingcai Fan, Lanling Zhao, Weifeng Li, and Mingwen Zhao. Two-dimensional transition metal borides as highly efficient N₂ fixation catalysts. *Appl. Surf. Sci.*, 536, 1 2021.

[37] Chaozheng He, Jia Wang, Ling Fu, Chenxu Zhao, and Jinrong Huo. Associative vs. dissociative mechanism: Electrocatalysis of nitric oxide to ammonia. *Chin. Chem. Lett.*, 33(2):1051–1057, 09 2022.

- [38] Y. Xiao and C. Shen. Transition-Metal Borides (MBenes) as New High-Efficiency Catalysts for Nitric Oxide Electroreduction to Ammonia by a High-Throughput Approach. *Small*, 17:2100776, 2021.
- [39] Showkat H. Mir, Vivek K. Yadav, and Jayant K. Singh. Efficient CO₂ Capture and Activation on Novel Two-Dimensional Transition Metal Borides. *ACS Appl. Mater. Interfaces*, 14:29703–29710, 7 2022.
- [40] Michał Jakubczak, Aleksandra Szuplewska, Anita Rozmysłowska-Wojciechowska, Andreas Rosenkranz, and Agnieszka Maria Jastrzębska. Novel 2D MBenes—Synthesis, Structure, and Biotechnological Potential. *Adv. Funct. Mater.*, 31(38):2103048, July 2021.
- [41] Carlos *et al*. Romero-Muñiz. Using a computationally driven screening to enhance magnetocaloric effect of metal monoborides. *J. Phys. Energy*, 5:024021, 05 2023.
- [42] Min Dou, Huan Li, Qingnian Yao, Jiabao Wang, Yunfei Liu, and Fang Wu. Room-temperature ferromagnetism in two-dimensional transition metal borides: A first-principles investigation. *Phys. Chem. Chem. Phys.*, 23:10615–10620, 5 2021.
- [43] S. Wang, N. Miao, K. Su, V. A. Blatov, and J. Wang. Discovery of intrinsic two-dimensional antiferromagnets from transition-metal borides. *Nanoscale*, 13:8254–8263, Mar 2021.
- [44] Ilkay Ozdemir, Yelda Kadioglu, Yusuf Yüksel, Ümit Aklncl, Olcay Üzengi Aktürk, Ethem Aktürk, and Salim Ciraci. Columnar antiferromagnetic order of a MBene monolayer. *Phys. Rev. B*, 103, 4 2021.
- [45] Yusuf Zuntu Abdullahi, Zeynep Demir Vatansever, Ethem Aktürk, Ümit Akıncı, and Olcay Üzengi Aktürk. Novel two-dimensional CrXB₂ (X=Cr, Ru) metal for high Néel temperature antiferromagnetic spintronics. *J. Solid State Chem.*, 302:122427, Oct 2021.
- [46] Shucheng Xing, Jian Zhou, Bikun Zhang, and Zhimei Sun. Magnetic Superexchange Induced Quantum Phase Transition in Cr₂B₂ MBene. *J. Phys. Chem. C*, 126:14275–14282, Aug 2022.

[47] Georgiy Akopov, Michael T. Yeung, and Richard B. Kaner. Rediscovering the Crystal Chemistry of Borides. *Adv. Mater.*, 29(21):1604506, 6 2017.

- [48] Aliasghar Shokri and Nadia Salami. Gas sensor based on MoS₂ monolayer. *Sens. Actuators B: Chem*, 236:378–385, 2016.
- [49] Byungjin Cho, Myung Gwan Hahm, Minseok Choi, Jongwon Yoon, Ah Ra Kim, Young-Joo Lee, Sung-Gyu Park, Jung-Dae Kwon, Chang Su Kim, Myungkwan Song, Yongsoo Jeong, Kee-Seok Nam, Sangchul Lee, Tae Jin Yoo, Chang Goo Kang, Byoung Hun Lee, Heung Cho Ko, Pulickel M. Ajayan, and Dong-Ho Kim. Charge-transferbased Gas Sensing Using Atomic-layer MoS₂. *Sci. Rep.*, 5:8052, 2015.
- [50] O. Leenaerts, B. Partoens, and F. M. Peeters. Adsorption of H₂O, NH₃, CO, NO₂, and NO on graphene: A first-principles study. *Phys. Rev. B*, 77:125416, 3 2008.
- [51] Yangyang Liu and Jennifer Wilcox. CO₂ Adsorption on Carbon Models of Organic Constituents of Gas Shale and Coal. *Environ. Sci. Technol.*, 45:809–814, 2011.
- [52] Tingting Liu, Yuhong Chen, Meiling Zhang, Lihua Yuan, Cairong Zhang, Jing Wang, and Jiajia Fan. A first-principles study of gas molecule adsorption on borophene. *AIP Adv.*, 7:125007, 2017.
- [53] Liangzhi Kou, Thomas Frauenheim, and Changfeng Chen. Phosphorene as a Superior Gas Sensor: Selective Adsorption and Distinct I–V Response. J. Phys. Chem. Lett., 5:2675–2681, 2014.
- [54] Jing wen Feng, Yue jie Liu, Hong xia Wang, Jing xiang Zhao, Qing hai Cai, and Xuan zhang Wang. Gas adsorption on silicene: A theoretical study. *Comput. Mater. Sci.*, 87:218–226, 2014.
- [55] Wenqi Xia, Wei Hu, Zhenyu Li, and Jinlong Yang. A first-principles study of gas adsorption on germanene. *Phys. Chem. Chem. Phys.*, 16:22495–22498, 2014.
- [56] Muhammad Sufyan Javed, Xiaofeng Zhang, Tauqeer Ahmad, Muhammad Usman, Syed Shoaib Ahmad Shah, Awais Ahmad, Iftikhar Hussain, Saadat Majeed, Muhammad Ramzan Khawar, Dongwhi Choi,

Changlei Xia, Wail Al Zoubi, Mohammed A. Assiri, Ahmed M. Hassan, Shafaqat Ali, and Weihua Han. MXenes to MBenes: Latest development and opportunities for energy storage devices. *Mater. Today*, 74:121–148, 2024.

- [57] Jahan Zeb Hassan, Ali Raza, Zaheer Ud Din Babar, Usman Qumar, Ngeywo Tolbert Kaner, and Antonio Cassinese. 2D material-based sensing devices: an update. *J. Mater. Chem. A*, 11:6016–6063, 2013.
- [58] G. Korotcenkov and B.K. Cho. Engineering approaches for the improvement of conductometric gas sensor parameters: Part 1. Improvement of sensor sensitivity and selectivity (short survey). *Sens Actuators B: Chem*, 188:709–728, 2013.
- [59] Lu Zhang, Karim Khan, Jifei Zou, Han Zhang, and Yingchun Li. Recent Advances in Emerging 2D Material-Based Gas Sensors: Potential in Disease Diagnosis. *Adv. Mater. Interfaces*, 6:1901329, 2019.
- [60] G. Korotcenkov. Metal oxides for solid-state gas sensors: What determines our choice? *Mater. Sci. Eng.*, 139:1–23, 2007.
- [61] Hank Wohltjen. Mechanism of operation and design considerations for surface acoustic wave device vapour sensors. *Sensors and Actuators*, 5:307–325, 1984.
- [62] R. Arsat, M. Breedon, M. Shafiei, P.G. Spizziri, S. Gilje, R.B. Kaner, K. Kalantar-zadeh, and W. Wlodarski. Graphene-like nano-sheets for surface acoustic wave gas sensor applications. *Chem. Phys. Lett.*, 467:344–347, 2009.
- [63] A.J. Ricco, S.J. Martin, and T.E. Zipperian. Surface acoustic wave gas sensor based on film conductivity changes. *Sensors and Actuators*, 8:319–333, 1985.
- [64] Wieslaw P. Jakubik, Marian W. Urbańczyk, Stanislaw Kochowski, and Jerzy Bodzenta. Bilayer structure for hydrogen detection in a surface acoustic wave sensor system. *Sens. Actuators B: Chem*, 82:265–271, 2002.
- [65] Wei Yang, Lin Gan, Huiqiao Li, and Tianyou Zhai. Two-dimensional layered nanomaterials for gas-sensing applications. *Inorg. Chem. Front*, 3:433–451, 2016.

[66] B.P Luther, S.D Wolter, and S.E Mohney. High temperature Pt Schottky diode gas sensors on n-type GaN. *Sens. Actuators B: Chem*, 56:164–168, 1999.

- [67] Minkyu Shin, Jinho Yoon, Chanyong Yi, Taek Lee, and Jeong-Woo Choi. Flexible HIV-1 Biosensor Based on the Au/MoS₂ Nanoparticles/Au Nanolayer on the PET Substrate. *Nanomater.*, 9:1076, 2019.
- [68] Wang Z., Dong S, Gui M, Asif M., Wang W., Wang F., and Liu H. Graphene paper supported MoS₂ nanocrystals monolayer with Cu submicron-buds: High-performance flexible platform for sensing in sweat. *Anal Biochem.*, 543:82–89, 2018.
- [69] Bannur Nanjunda Shivananju, Sumeet Yamdagni, Ruknudeen Fazuldeen, Anakkat Koyilothu Sarin Kumar, Shamraju Purushotham Nithin, Manoj M. Varma, and Sundarrajan Asokan. Highly Sensitive Carbon Nanotubes Coated Etched Fiber Bragg Grating Sensor for Humidity Sensing. *IEEE Sens. J.*, 14(8):2615–2619, 2014.
- [70] Mahdi Balali-Mood, Kobra Naseri, Zoya Tahergorabi, Mohammad Reza Khazdair, and Mahmood Sadeghi. Toxic Mechanisms of Five Heavy Metals: Mercury, Lead, Chromium, Cadmium, and Arsenic. Front. Pharmacol., 12, 2021.
- [71] Saikat Mitra, Arka Jyoti Chakraborty, Abu Montakim Tareq, Talha Bin Emran, Firzan Nainu, Ameer Khusro, Abubakr M. Idris, Mayeen Uddin Khandaker, Hamid Osman, Fahad A. Alhumaydhi, and Jesus Simal-Gandara. Impact of heavy metals on the environment and human health: Novel therapeutic insights to counter the toxicity. *J. King Saud Univ. Sci.,,* 34:101865, 2022.
- [72] Qiyuan He, Shixin Wu, Zongyou Yin, and Hua Zhang. Graphene-based electronic sensors. *Chem. Sci.*, 3:1764–1772, 2012.
- [73] Chun-Hua Lu, Huang-Hao Yang, Chun-Ling Zhu, Xi Chen, and Guo-Nan Chen. A Graphene Platform for Sensing Biomolecules. *Angew. Chem.*, *Int. Ed.*, 48:4785–4787, 2009.
- [74] Fei Xing, Gui-Xian Meng, Qian Zhang, Lei-Ting Pan, Peng Wang, Zhi-Bo Liu, Wen-Shuai Jiang, Yongsheng Chen, and Jian-Guo Tian. Ultrasensitive Flow Sensing of a Single Cell Using Graphene-Based Optical Sensors. *Nano Lett.*, 14:3563–3569, 2014.

[75] Phan Thi Kim Loan, Wenjing Zhang, Cheng-Te Lin, Kung-Hwa Wei, Lain-Jong Li, and Chang-Hsiao Chen. Graphene/MoS₂ Heterostructures for Ultrasensitive Detection of DNA Hybridisation. *Adv. Mater*, 26:4838–4844, 2014.

- [76] Dong-Wook Park, Amelia A. Schendel, Solomon Mikael, Sarah K. Brodnick, Thomas J. Richner, Jared P. Ness, Mohammed R. Hayat, Farid Atry, Seth T. Frye, Ramin Pashaie, Sanitta Thongpang, Zhenqiang Ma, and Justin C. Williams. Graphene-based carbon-layered electrode array technology for neural imaging and optogenetic applications. *Nat. Commun.*, 5:5258, 2014.
- [77] Jo I. Lee S., Kang S., Jang B., Moon J., Park J. B., Lee S., Rho S., Kim Y., and Hong B. H. Smart Contact Lenses with Graphene Coating for Electromagnetic Interference Shielding and Dehydration Protection. ACS Nano, 11:5318–5324, 2017.
- [78] Bo Fu, Thomas Gasser, Bengang Li, Shu Tao, Philippe Ciais, Shilong Piao, Yves Balkanski, Wei Li, Tianya Yin, Luchao Han, Xinyue Li, Yunman Han, Jie An, Siyuan Peng, and Jing Xu. Short-lived climate forcers have long-term climate impacts via the carbon–climate feedback. *Nat. Clim. Change*, 10(9):851–855, 2020.
- [79] Richard M. Martin. *Electronic Structure: Basic Theory and Practical Methods*. Cambridge University Press, 2 edition, 2020.
- [80] Frank Jensen. Estimating the Hartree—Fock limit from finite basis set calculations. *Theor. Chem. Acc.*, 113:267–273, 2005.
- [81] Chr. Møller and M. S. Plesset. Note on an Approximation Treatment for Many-Electron Systems. *Phys. Rev.*, 46:618–622, Oct 1934.
- [82] John A. Pople, Martin Head-Gordon, and Krishnan Raghavachari. Quadratic configuration interaction. A general technique for determining electron correlation energies. J. Chem. Phys., 87(10):5968–5975, nov 1987.
- [83] Frank Jensen. *Introduction to Computational Chemistry*. John Wiley and Sons, 2 edition, 2007.
- [84] P. Hohenberg and W. Kohn. Inhomogeneous Electron Gas. *Phys. Rev.*, 136:B864–B871, Nov 1964.

[85] W. Kohn and L. J. Sham. Self-Consistent Equations Including Exchange and Correlation Effects. *Phys. Rev.*, 140:A1133–A1138, Nov 1965.

- [86] David S. Sholl and Janice A. Steckel. *Density Functional Theory: A Practical Introduction*. John Wiley and Sons, Ltd, 2009.
- [87] John P. Perdew, J. A. Chevary, S. H. Vosko, Koblar A. Jackson, Mark R. Pederson, D. J. Singh, and Carlos Fiolhais. Atoms, molecules, solids, and surfaces: Applications of the generalized gradient approximation for exchange and correlation. *Phys. Rev. B*, 46:6671–6687, Sep 1992.
- [88] A. D. Becke. Density-functional exchange-energy approximation with correct asymptotic behavior. *Phys. Rev. A*, 38:3098–3100, Sep 1988.
- [89] David C. Langreth and M. J. Mehl. Beyond the local-density approximation in calculations of ground-state electronic properties. *Phys. Rev. B*, 28:1809–1834, Aug 1983.
- [90] John P. Perdew and Kieron Burke. Comparison shopping for a gradient-corrected density functional. *Int. J. Quantum Chem.*, 57:309–319, 1996.
- [91] John P. Perdew, Kieron Burke, and Matthias Ernzerhof. Generalized Gradient Approximation Made Simple. *Phys. Rev. Lett.*, 77:3865–3868, Oct 1996.
- [92] June Gunn Lee. *Computational materials science: an introduction*. CRC press, Taylor and Francis Group, 1 edition, 2012.
- [93] Thomas M. Henderson, Joachim Paier, and Gustavo E. Scuseria. Accurate treatment of solids with the HSE screened hybrid. *Phys. Status Solidi* (b), 248:767–774, 2011.
- [94] Alejandro J. Garza and Gustavo E. Scuseria. Predicting Band Gaps with Hybrid Density Functionals. *J. Phys. Chem. Lett.*, 7:4165–4170, 2016.
- [95] Peter Deák, Adam Gali, Bálint Aradi, and Thomas Frauenheim. Accurate gap levels and their role in the reliability of other calculated defect properties. *Phys. Status Solidi (b)*, 248:790–798, 2011.
- [96] Wilfried G. Aulbur, Lars Jönsson, and John W. Wilkins. Quasiparticle Calculations in Solids. In *Solid State Physics*, volume 54, pages 1–218. Elsevier, 2000.

[97] Mark S. Hybertsen and Steven G. Louie. Electron correlation in semi-conductors and insulators: Band gaps and quasiparticle energies. *Phys. Rev. B*, 34:5390–5413, Oct 1986.

- [98] Lars Hedin. New Method for Calculating the One-Particle Green's Function with Application to the Electron-Gas Problem. *Phys. Rev.*, 139:A796–A823, Aug 1965.
- [99] Giovanni Onida, Lucia Reining, and Angel Rubio. Electronic excitations: density-functional versus many-body Green's-function approaches. *Rev. Mod. Phys.*, 74:601–659, Jun 2002.
- [100] Stefan Albrecht, Lucia Reining, Rodolfo Del Sole, and Giovanni Onida. Ab Initio Calculation of Excitonic Effects in the Optical Spectra of Semiconductors. *Phys. Rev. Lett.*, 80:4510–4513, May 1998.
- [101] Michael Rohlfing and Steven G. Louie. Electron-Hole Excitations in Semiconductors and Insulators. *Phys. Rev. Lett.*, 81:2312–2315, Sep 1998.
- [102] R. Bader. *Atoms in Molecules: A Quantum Theory*. Oxford University Press, 1 edition, 1990.
- [103] Paolo Giannozzi and Stefano Baroni. *Density-Functional Perturbation Theory*, pages 195–214. Springer Netherlands, 2005.
- [104] Vladimir I. Anisimov, Jan Zaanen, and Ole K. Andersen. Band theory and Mott insulators: Hubbard U instead of Stoner I. *Phys. Rev. B*, 44:943–954, Jul 1991.
- [105] V. I. Anisimov, I. V. Solovyev, M. A. Korotin, M. T. Czyżyk, and G. A. Sawatzky. Density-functional theory and NiO photoemission spectra. *Phys. Rev. B*, 48:16929–16934, Dec 1993.
- [106] I. V. Solovyev, P. H. Dederichs, and V. I. Anisimov. Corrected atomic limit in the local-density approximation and the electronic structure of d impurities in Rb. *Phys. Rev. B*, 50:16861–16871, Dec 1994.
- [107] Matteo Cococcioni and Stefano de Gironcoli. Linear response approach to the calculation of the effective interaction parameters in the LDA + U method. *Phys. Rev. B*, 71:035105, Jan 2005.
- [108] Iurii Timrov, Nicola Marzari, and Matteo Cococcioni. Hubbard parameters from density-functional perturbation theory. *Phys. Rev. B*, 98:085127, Aug 2018.

[109] Iurii Timrov, Nicola Marzari, and Matteo Cococcioni. Self-consistent Hubbard parameters from density-functional perturbation theory in the ultrasoft and projector-augmented wave formulations. *Phys. Rev. B*, 103(4), January 2021.

- [110] S. L. Dudarev, G. A. Botton, S. Y. Savrasov, C. J. Humphreys, and A. P. Sutton. Electron-energy-loss spectra and the structural stability of nickel oxide: An LSDA+U study. *Phys. Rev. B*, 57:1505–1509, Jan 1998.
- [111] R. O. Jones and O. Gunnarsson. The density functional formalism, its applications and prospects. *Rev. Mod. Phys.*, 61:689–746, Jul 1989.
- [112] V. I. Anisimov and O. Gunnarsson. Density-functional calculation of effective Coulomb interactions in metals. *Phys. Rev. B*, 43:7570–7574, Apr 1991.
- [113] Mark S. Hybertsen, Michael Schlüter, and Niels E. Christensen. Calculation of Coulomb-interaction parameters for La₂CuO₄ using a constrained-density-functional approach. *Phys. Rev. B*, 39:9028–9041, May 1989.
- [114] A. K. McMahan, Richard M. Martin, and S. Satpathy. Calculated effective Hamiltonian for La₂CuO₄ and solution in the impurity Anderson approximation. *Phys. Rev. B*, 38:6650–6666, Oct 1988.
- [115] J. F. Janak. Proof that $\frac{\partial E}{\partial n_i} = \epsilon$ in density-functional theory. *Phys. Rev. B*, 18:7165–7168, Dec 1978.
- [116] P. H. Dederichs, S. Blügel, R. Zeller, and H. Akai. Ground States of Constrained Systems: Application to Cerium Impurities. *Phys. Rev. Lett.*, 53:2512–2515, Dec 1984.
- [117] Han Hsu, Koichiro Umemoto, Matteo Cococcioni, and Renata Wentz-covitch. First-principles study for low-spin LaCoO₃ with a structurally consistent Hubbard *U. Phys. Rev. B*, 79:125124, Mat 2009.
- [118] Iurii Timrov, Nicola Marzari, and Matteo Cococcioni. HP A code for the calculation of Hubbard parameters using density-functional perturbation theory. *Comput. Phys. Commun.*, 279:108455, October 2022.
- [119] Lars Goerik. Chapter 6 A Comprehensive Overview of the DFT-D3 London-Dispersion Correction, pages 195–219. Elsevier, 2017.

[120] Stefan Grimme. Semiempirical GGA-type density functional constructed with a long-range dispersion correction. *J. Comput. Chem.*, 27:1787–1799, 2006.

- [121] Stefan Grimme, Jens Antony, Stephan Ehrlich, and Helge Krieg. A consistent and accurate ab initio parametrization of density functional dispersion correction (DFT-D) for the 94 elements H-Pu. *J. Chem. Phys.*, 132:154104, 2010.
- [122] R. N. Euwema, D. J. Stukel, T. C. Collins, J. S. Dewitt, and D. G. Shankland. Crystalline Interpolation with Applications to Brillouin-Zone Averages and Energy-Band Interpolation. *Phys. Rev.*, 178:1419–1423, Feb 1969.
- [123] D. G. Shankland. Fourier transformation by smooth interpolation. *Int. J. Quantum Chem.*, 5:497–500, 1971.
- [124] D.D Koelling and J.H Wood. On the interpolation of eigenvalues and a resultant integration scheme. *J. Comput. Phys.*, 67:253–262, 1986.
- [125] T. J. Scheidemantel, C. Ambrosch-Draxl, T. Thonhauser, J. V. Badding, and J. O. Sofo. Transport coefficients from first-principles calculations. *Phys. Rev. B*, 68:125210, Sep 2003.
- [126] E. Assmann, P. Wissgott, Jan Kunes, A. Toschi, P. Blaha, and K. Held. Woptic: Optical conductivity with Wannier functions and adaptive kmesh refinement. *Comput. Phys. Commun.*, 202, 2015.
- [127] Warren E. Pickett, Henry Krakauer, and Philip B. Allen. Smooth Fourier interpolation of periodic functions. *Phys. Rev. B*, 38:2721–2726, Aug 1988.
- [128] J.M. Ziman. *Electrons and Phonons: The Theory of Transport Phenomena in Solids*. Oxford University Press, 2001.
- [129] Wei Xiong, Xingyu Feng, Yi Xiao, Tao Huang, Xiaoyan Li, Zhencheng Huang, Shenghua Ye, Yongliang Li, Xiangzhong Ren, Xinzhong Wang, Xiaoping Ouyang, Qianling Zhang, and Jianhong Liu. Fluorine-free prepared two-dimensional molybdenum boride (MBene) as a promising anode for lithium-ion batteries with superior electrochemical performance. *Chem. Eng. J.*, 446:137466, 2022.

[130] Mihrimah Ozkan. MXenes vs MBenes: Demystifying the materials of tomorrow's carbon capture revolution. *MRS Energy Sustain.*, 11:181–190, 2024.

[131] Nanxi Miao, Yutong Gong, Huaiyu Zhang, Qing Shen, Rui Yang, Jianping Zhou, Hideo Hosono, and Junjie Wang. Discovery of Two-dimensional Hexagonal MBene HfBO and Exploration on its Potential for Lithium-Ion Storage. *Angew. Chem., Int. Ed.*, 62:e202308436, 2023.